University of Exeter

Doctoral Thesis

Quantum and classical correlations of multiply scattered light

Author:
Illia Starshynov

Supervisors:
Dr. Jacopo Bertolotti
Dr. Janet Anders

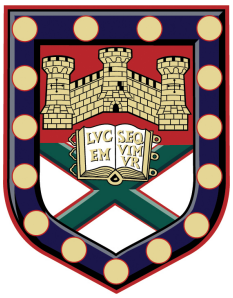

A thesis submitted in fulfilment of the requirements
for the degree of Doctor of Philosophy
in July 2018

Quantum and classical correlations of multiply scattered light

Submitted by Illia Starshynov to the University of Exeter as a thesis for the degree of Doctor of Philosophy in Physics in July 2018.

I certify that all material in this thesis which is not my own work has been identified and that no material has previously been submitted and approved for the award of a degree by this or any other University.

Illia Starshynov

2018

Abstract

Multiple scattering is a very common phenomenon since it occurs any time a wave meets a disordered medium. As almost any natural object has random structure in one form or another, the variety of the processes involving multiple scattering spans from electronic transport in solids to propagation of sound in a forest. In principle, multiple scattering is completely deterministic, and in the absence of absorption also reversible, which means that the information encoded into the incident wave can be perfectly recovered. However, in practice, due to its extreme complexity we often consider this process to be random, which leads to information loss. Within this approach correlations can be an important instrument of information recovery, because they directly quantify the amount of knowledge we get about the wave in a particular point from the measurement performed in a different point.

In the first part of this thesis we study a novel type of mesoscopic correlations between the light intensities at the opposite sides of an opaque scattering slab. We study its dependence on the scattering medium properties and the incoming light beam parameters. In the last chapter of the first part we show how this correlation can be used to retrieve non-invasively the information about the shape of an object placed behind the scattering medium.

In the second part we switch to the quantum aspects of the light propagation inside the scattering materials. We show that certain class of quantum correlations, quantum discord, can be present in the multimode output state of the scattered light even when the input light is in a thermal state, which is commonly considered classical. We propose a non-classicality measure based on the strength of this correlation, applying it to characterize the advantage due to the quantum measurement in discrimination of two coherent states in their mixture.

Contents

Introduction

Most of the information about the surrounding world we obtain by processing electromagnetic or acoustic waves by our body. Indeed, the ability of the waves to carry information is truly remarkable. The light from distant galaxies travels billions of kilometres before reaching the Earth, but we still can observe it. At another extreme is the amount of data that is possible to transfer: at the moment of this thesis completion the fastest optical-fibre cable connecting Northern America with Europe allows a staggering 160 Tb/s data transmission rate [1], through just 8 fibres around a millimetre in diameter. There are multiple ways of how information can be encoded into the light wave. It can be stored into its spatial configuration, temporal dynamics or polarization orientation. Recent developments in the non-classical light generation and manipulation allow for additional degrees of freedom opening the way to encode information directly into its quantum state and retrieve it using higher-order photon statistics measurements [2, 3].

When information is carried by the light intensity spatial distribution in the form of an *image*, any interaction of the wave carrying this distribution with eextraneous objects alters this wave, causing image distortion. However, in many cases information is not lost in this process, unless the carrying wave is absorbed. When the wave transformation can be described deterministically, the resulting distortion may be corrected by post-processing [4, 5] or adaptive optics compensation [6]. However, obviously, this is possible up to a certain limit. Interaction of the light even with a single obstacle of a size of its wavelength leads to a complicated scattered light distribution [7]. When the wave meets a structure containing thousands of such particles, the resulting intensity distribution, called a speckle pattern [8], becomes very complicated, as well as the transformation that relates the incident wave configuration with the outgoing one. Often, despite being completely deterministic this process is treated as random, due to its complexity, which means that we give up the information carried by the incident wave. In the current work we deal exactly with this situation, showing that despite its extreme complexity certain amount of information can survive the multiple scatting process. We also make

steps towards using quantum features of light to increase the amount of the retrieved information.

The problem of quantifying information is well understood [9–11]. For a single random variable A with N possible outcomes $a_i, i = 1 \dots N$, its information capacity is characterized by the entropy

$$H(A) = -\sum p_i \log(p_i), \tag{1}$$

where p_i are the probabilities of each of the outcomes a_i. This quantity is fundamentally important, however in the current context it is useful only to characterize the variation of A (the greater the variation the bigger is H). In most of the practical situations the quantity of interest is rather the *mutual information* between the two variables A and B. Mutual information allows to analyse any kind of relationship between A and B directly quantifying how much knowledge about B it is possible to get from A. Such a simple model of two dependent random variables gives a general description of a variety of physical processes. For example in any communication scenario we can associate A with the transmitted messages and B with the received ones. In that case mutual information between A and B characterizes the quality of the communication channel, imposing a boundary on the achievable information transfer rate [9–11]. In the measurement process we can associate A with the actual physical parameter to be measured, and B with the measurement instrument reading. In that situation the mutual information between A and B characterizes the measurement uncertainty, and is a primary parameter to optimize for the precision improvement [12, 13]. In the context of our problem of the interaction of light with disordered structures, we are interested in the mutual information between the scattered field intensities in different spatial points.

Mutual information provides a complete description of the relations between random processes, however it might be difficult to handle, as it requires full knowledge of their probability distribution [14]. In practice often a simpler criterion of *correlation* is used. For two variables A and B correlation is usually characterized by the quantity

$$C = \frac{\langle AB \rangle - \langle A \rangle \langle B \rangle}{\sqrt{\mathrm{Var}[A]\mathrm{Var}[B]}} = \frac{\langle \delta A \delta B \rangle}{\sqrt{\mathrm{Var}[A]\mathrm{Var}[B]}}, \tag{2}$$

where $\langle \cdot \rangle$ denote ensemble averaging, $\mathrm{Var}[\cdot]$ is variance and $\delta A = A - \langle A \rangle$. It is a part of the mutual information that captures just linear relationships between random processes [9]. While correlation always implies presence of mutual information, the opposite may not always be true. For example, in the case of non-linear (deterministic) relationship between two random variables we might have a complete knowledge of one

of them from another, while their correlation at the same time can be weak. Here we consider the process of elastic light scattering, which is a linear process, therefore we expect correlation to be a suitable criterion to quantify the relationships within the scattered field.

The thesis is organized in the following way: in chapters 1-4 we discuss classical correlations between the reflected and transmitted scattered field intensity patterns upon the disordered medium configuration variation. In chapters 5-7 we discuss quantum features in the statistical fluctuations of light, scattered by a disordered medium with a fixed configuration of scatterers. In more detail:

- In the first chapter we present the results of the experimental measurement of the correlation between the reflected and transmitted multiply scattered light intensities. We start by giving a brief introduction into the topic of coherent multiple scattering and outline the role of the correlations in it. After that we describe the experimental procedure and data processing algorithms that were used to observe the reflection-transmission correlation. Then we discuss the dependence of this correlation on the experiment parameters, such as sample thickness and mean free path, incoming wave angle of incidence and polarization, distance of the observation planes from the sample surface.

- In the second chapter we discuss the numerical simulation of the correlation presented in the first chapter, using the coupled dipoles approximation. We start by describing this method and the main differences between the scattering regimes in the modelling and in the experiment. After that we present the numerical results, comparing them to the experiment.

- The third chapter contains the detailed description of the analytical calculation of the measured correlation function. We start by introducing the necessary concepts from the theory of wave propagation in disordered materials, outline the model, and present calculation of the correlation function in the diffusive regime, which describes one of the contributions observed in the experiment. We also analyse the origin of the other contributions observed in the experiment and in the modelling.

- In the fourth chapter we discuss how the correlation we observed can be used to obtain information about the objects placed behind the scattering layers. For that purpose, we propose a modification of the ghost imaging technique that exploits the correlation between the reflected and transmitted speckle patterns, which we call Blind Ghost Imaging. We analyse the signal-to-noise ratio of the normal ghost imaging technique and extend this analysis to our proposed technique, and

finally make some remarks regarding the possible improvement of the information retrieval using the compressive sensing techniques.

- In the fifth chapter we introduce the background theory required for investigation of the scattered field quantum features. We revise the theory of light quantization, phase-space formulation of quantum mechanics and finally single and multimode non-classicality criteria.

- In the sixth chapter we study quantum correlations between the output modes of the optical beam-splitter, which is a simplified model of the multiple scattering process. It is well known that quantum entanglement may be present between the output modes when the input state is non-classical [15]. We show that weaker form of quantum correlation, *quantum discord* can be present in the output even when the input is a simple mixture of coherent states. We introduce a non-classicality criterion, based on this correlation, which we call discord potential, and compare it to the other single-mode criteria in particular recently introduced coherence monotones [16].

- In the last chapter we finally address the question of the quantum correlations of light scattered by a disordered medium. We extend the model described in the previous chapter to include multiple input and output modes as in the multiple scattering situation. We calculate the output state in that scenario, depending on the properties of the input state and of the scattering medium. We check the non-classicality criteria for the output state, showing that similarly to the beam-splitter case, we can expect entanglement between the output modes if the input is non-classical, but more interestingly quantum discord can be present in the output even if the input is in a thermal state.

Chapter 1

Experimental measurement of the reflection-transmission correlation

1.1 Motivation and previous work

In the current chapter we present the first direct experimental observation of the correlation between the reflected and transmitted speckle patterns during coherent multiple scattering. The results in this, and the following three chapters are obtained in a collaboration with the group of R. Carminati, EPSRC, Paris, where they developed the analytical theory and the framework for the numerical modelling, whereas our group designed and performed the experimental measurements. These results are presented in [17].

Multiple scattering is an omnipresent phenomenon. Almost any natural object contains disordered structures, which upon interaction with a wave cause a complicated recursive interference process, resulting in a complex output field configuration. The parameter responsible for the strength of this effect is the *mean free path*, ℓ. In the absence of absorption it is qualitatively related to the average distance between the scattering events. Different regimes are possible depending on the relations between λ, the wavelength of the incident wave, ℓ, and size of the disordered object along the wave propagation direction, L. In the situation when $L \gg l$ and especially when L is greater than the coherence length of the source, all the interference effects are smoothed by a huge number of scattering events and the transport of intensity is well described by the diffusion equation [18, 19]. In another extreme, when $\ell < \lambda$ [20], the interference effects become so strong that the wave may become "stuck" within a confined region of the disordered sample, which is known as Anderson localization [21]. In this work we are interested in an intermediate situation when $\ell >> \lambda$ and $L \gtrapprox \ell$, but the coher-

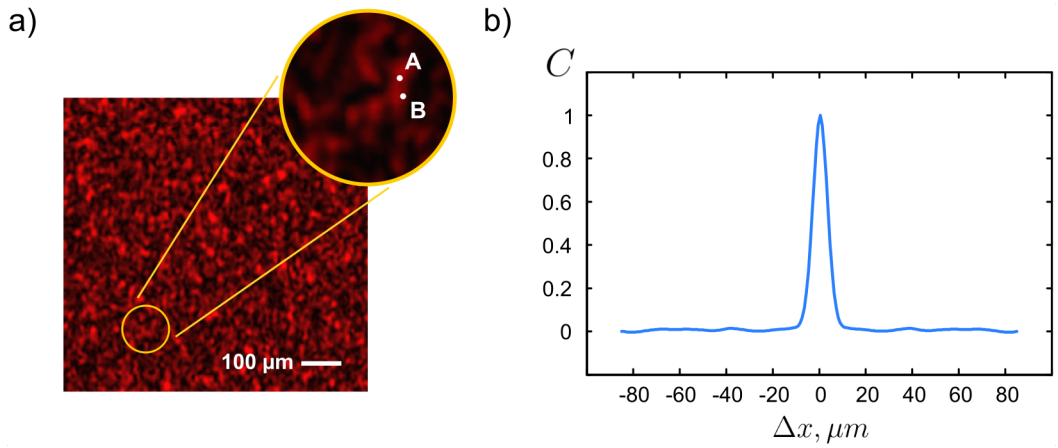

Figure 1.1: a) Example of a speckle pattern in transmission. When intensity in the point A is large, the points in its vicinity are more likely to be bright as well and vice versa. b) Correlation function of this pattern, capturing such behaviour.

ence length of the source is much greater than L. In this scenario, interference effects lead to large spatial (or angular) fluctuations of the reflected and transmitted intensity, called speckle patterns [8], see Fig. 1.1a. At first glance the pattern in Fig. 1.1a seems completely chaotic. However at a closer look it is possible to notice some relationship: it has a granular structure, meaning that when intensity is high at a certain point, it is more likely to be high in the adjacent ones. This fact is captured by the correlation defined in (2),

$$C(\mathbf{r}^A, \mathbf{r}^B) = \frac{\langle \delta I(\mathbf{r}^A) \delta I(\mathbf{r}^B) \rangle}{\langle I(\mathbf{r}^A) \rangle \langle I(\mathbf{r}^B) \rangle}, \tag{1.1}$$

with random variables A and B being field intensities at different spatial points. We note that instead of position we could use any other degree of freedom of the electromagnetic field: propagation direction angle, frequency, time or polarization orientation. The resulting correlation functions would be related to each other and we chose spatial correlations because they are easier for us to measure. In the case of isotropic speckle pattern, correlation in (1.1) does not depend on the absolute positions of the observation points, but only on their relative displacement $\Delta\mathbf{r} = |\mathbf{r}^A - \mathbf{r}^B|$, which leads to the *correlation function*:

$$C(\Delta\mathbf{r}) = \frac{\langle I(\mathbf{r}) I(\mathbf{r} + \Delta\mathbf{r}) \rangle}{\langle I(\mathbf{r}) \rangle \langle I(\mathbf{r} + \Delta\mathbf{r}) \rangle}. \tag{1.2}$$

An example of such function is shown in Fig. 1.1b, where both observation points are behind the scattering sample (in transmission). This correlation is non-zero only for the points within the distance of a speckle spot, or in other words this correlation is a short-range one. However, this type of correlation is not the only possible one. Certain class of interference events within the scattering medium may give rise to long-range correlations

that connect the intensities within the distance of many speckle spots [18–20, 22]. We will discuss in details the physical origin of the short and long-range correlations in Ch. 3. For now, we focus on the experimental observation of the correlation in a particular reflection-transmission geometry.

Correlations between the light on the opposite sides of an opaque scattering slab are interesting from both fundamental and practical points of view. In the former case such geometry allows to probe the validity of the theoretical description of mesoscopic correlations, giving easy access to the contributions that are not described by the standard perturbation theory [22]. On the other hand, the existence of such correlation would mean that we obtain certain amount of information about the pattern on one of the sides of the medium, measuring the pattern on the opposite side, which can be used for imaging of wavefront control purpose.

Despite such apparent benefits, reflection-transmission correlations attracted little attention in the past, being mentioned only in passing [23, 24]. The first detailed study of the correlation function in such a geometry was performed by our collaborators in [25], where they demonstrated the existence of long-range correlations between the reflected and transmitted speckle patterns in the diffusive regime. The main motivation of the current work was to validate these theoretical predictions.

There is usually no problem in observing short-range correlations in either transmitted or reflected light. As we can see from Fig. 1.1, the short range contribution completely dominates the correlation function (1.2) in transmission. In order to measure it we just need to record the speckle and correlate it with itself [26, 27]. It is usually harder to observe the long-range correlation. In the optical domain the long-range correlations in frequency [27, 28] and time [29] were observed by means of total transmission fluctuation measurements. The spatially resolved long-range correlations were experimentally studied in the microwave [30, 31] and in the optical [32, 33] domains only in the waveguide-type geometry. Correlations between reflected and transmitted light were observed indirectly in the experiments on focusing light scattered by random media, where they allowed to control the intensity in the areas much larger than a speckle spot [34, 35]. Here we present a direct measurement of the correlation function for the 3D scattering slabs.

1.2 Measurement set-up and procedure

1.2.1 Set-up description

The experimental apparatus is shown in Fig. 1.2a. A scattering sample is illuminated with a monochromatic wave (2 mW He-Ne $\lambda = 632$ nm laser), incident at an angle that we can vary from 45° to 80°. As a sample we use a suspension of TiO_2 (Rutile) powder in glycerol, placed between two microscope slides. The slab thickness L is controlled using feeler gauge stripes. The mean free path ℓ is controlled by varying the TiO_2 concentration. Typical samples with different optical thickness $b = L/\ell$, from semitransparent to fully opaque are shown in Fig. 1.2b. For a given L and ℓ we record the intensity patterns $R(\mathbf{r})$ and $T(\mathbf{r})$ on the surface of the sample in reflection and transmission respectively, with two identical imaging systems each composed by a 10x

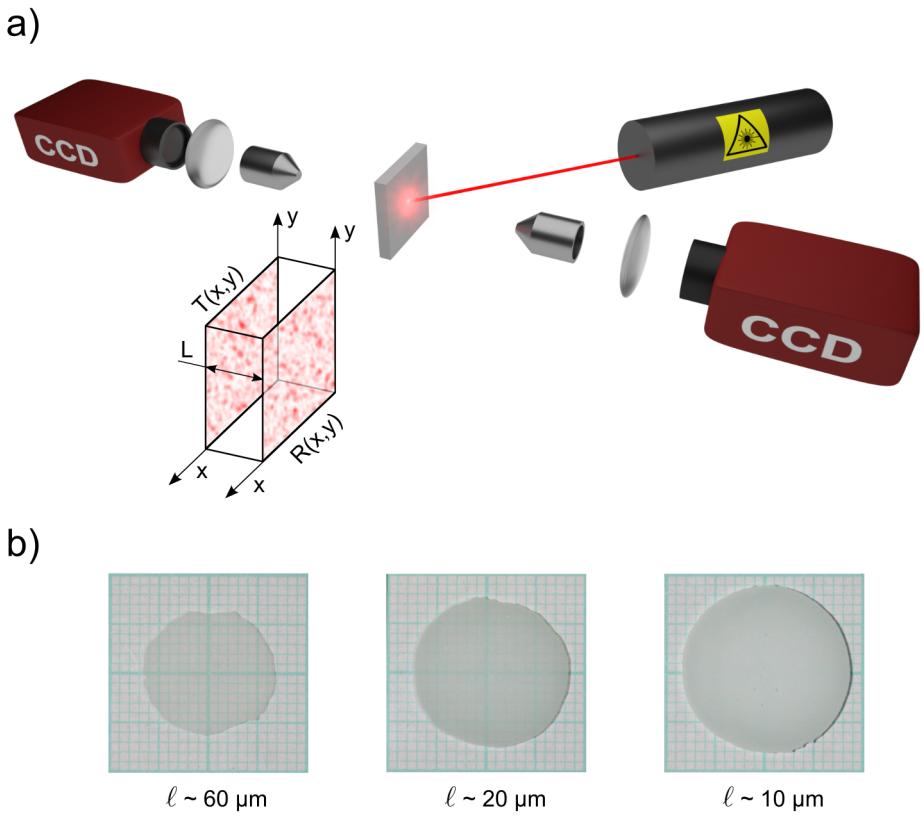

Figure 1.2: a) Experimental setup. A scattering slab, formed by a suspension of TiO_2 particles in glycerol, is illuminated by a laser beam incident at an angle $\sim 45°$. The speckle patterns on the two surfaces, $T(x, y)$ and $R(x, y)$ respectively, are recorded with two identical imaging systems. b) Examples of samples with thickness $L = 20\mu$m but different TiO_2 concentrations: from left to right 5 g/l, 10 g/l and 40 g/l, which correspond to a mean free path of (60, 20.4 and 9.8) $\pm$ 2.5 μm, respectively.

microscope objective, a plano-convex 150 mm lens, and CCD camera (Allied Vision Manta G-146). As the samples are liquid the configuration of the scatterers changes in time due to the Brownian and fluid motion. Therefore the resulting speckle patterns change in time as well, with a decorrelation time τ that depends strongly on the sample thickness, increasing for the thinner ones. Choosing an integration time $< \tau$, and a time interval between successive measurements $> \tau$, allows us to measure speckle images $R(\mathbf{r})$ and $T(\mathbf{r})$ for a large ensemble of configurations of the disordered medium. For the cases when the decorrelation time was significantly larger than interval between successive exposures, the sample was additionally actuated using a piezo-transducer attached to one of the cover slides.

1.2.2 Sample characterization

In order to determine the mean free path of the three samples with different concentrations of the TiO_2 we used the well known Lambert-Beer law $I = I_0 e^{-L/\ell_e}$, where I_0 is the intensity of the incident beam, I is the transmitted intensity, L is the thickness of the sample and ℓ_e the extinction length. This expression describes the attenuation of the ballistic (unscattered) light propagating through a disordered and absorbing medium. Since absorption in the TiO_2-glycerol samples we used is negligible (albeit non zero)

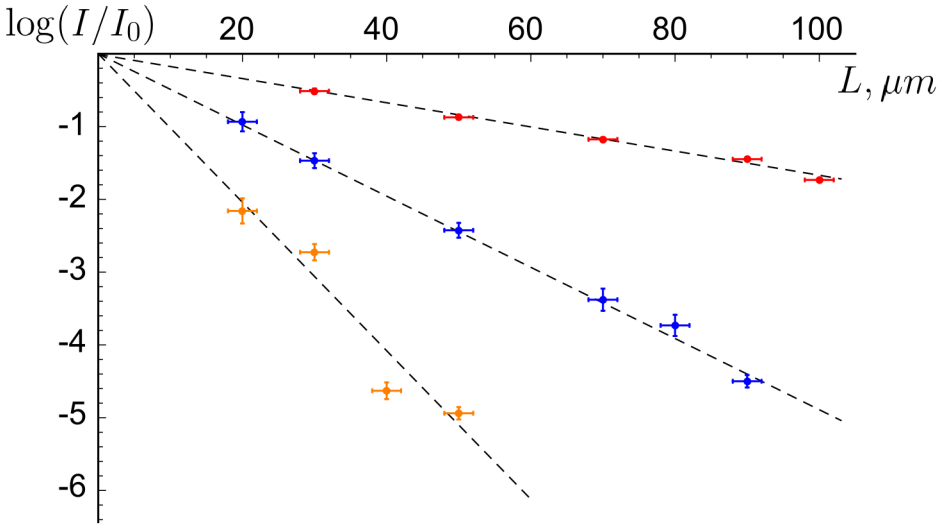

Figure 1.3: Experimental data to determine the mean free path of the three different sample concentrations we used. In red is the data corresponding to the concentration of 50 mg of TiO_2in 10 ml of glycerol, in blue the concentration of 150 mg of TiO_2 in 10 ml of glycerol and in yellow, the data corresponding to the concentration of 400 mg of TiO_2 in 10 ml of glycerol. The black dashed lines represent the Lambert-Beer law fitting to the corresponding experimental data.

compared to scattering, we can consider $\ell_e \approx \ell$. The attenuation of the ballistic light due to scattering follows from the fact that the average Green's function decays exponentially after disorder averaging, see Ch. 3.

We measured the attenuation of the ballistic beam for different thicknesses of the sample and obtained the scattering mean free path of the three different samples by fitting the Lambert-Beer law, as shown in Fig. 1.3.

The scattering mean free paths for the samples with concentrations of 50 mg of TiO_2, 150 mg of TiO_2, and 400 mg of TiO_2 in 10 ml of glycerol were found to be, respectively, 60 $\pm$ 1.3 μm, 20.4 $\pm$ 0.5 μm, and 9.8 $\pm$ 0.7 μm.

1.2.3 Data processing

The correlation function between the reflected and transmitted speckle patterns is defined as

$$C^{RT}(\Delta\mathbf{r}) = \frac{\langle \delta R(\mathbf{r}) \delta T(\mathbf{r}+\Delta\mathbf{r}) \rangle}{\langle R(\mathbf{r}) \rangle \langle T(\mathbf{r}+\Delta\mathbf{r}) \rangle} \tag{1.3}$$

where $\Delta\mathbf{r} = (\Delta x, \Delta y)$ is a transverse shift between the images, and $\delta A = A - \langle A \rangle$, denotes the statistical fluctuation of the speckle intensity around the ensemble (disorder) average. In order to calculate this function we evaluate the correlation product

$$\overline{C^{RT}}(\Delta\mathbf{r}) = \frac{1}{\mathcal{N}_1} \int \delta R(\mathbf{r}) \delta T(\mathbf{r}+\Delta\mathbf{r}) d\mathbf{r} \tag{1.4}$$

for each pair of the recorded speckle patterns, where $\overline{\cdot}$ denotes a spatial average (over $\mathbf{r}$) and $\mathcal{N}_1$ is a normalization factor. After that an ensemble average of $\overline{C^{RT}}(\Delta\mathbf{r})$ is performed, leading to a correlation function $\langle \overline{C^{RT}}(\Delta\mathbf{r}) \rangle$, which is equivalent to $C^{RT}(\Delta\mathbf{r})$ under assumptions that we will discuss below.

Practically $\overline{C^{RT}}(\Delta\mathbf{r})$ is calculated using the convolution theorem

$$\overline{C^{RT}}(\Delta\mathbf{r}) = \mathcal{F}^{-1}[\mathcal{F}[\delta R] \times \mathcal{F}[\delta T]^*], \tag{1.5}$$

where $\mathcal{F}$ denotes the Fourier transform and $\mathcal{F}^{-1}$ its inverse. In the earlier versions of the setup we used a Lab-View script to record the patterns to the disc and calculated this quantity by post-processing the raw data in Mat-Lab. Despite giving flexibility in the data processing, such variant is very slow (due to disk operations) and storage demanding (a typical experiment requires $\sim 10 - 50$ Gb disk space). Therefore we modified the Lab-View script to evaluate the correlation product on-fly without storing the raw images, which allowed to process ~ 5 speckle pairs per second.

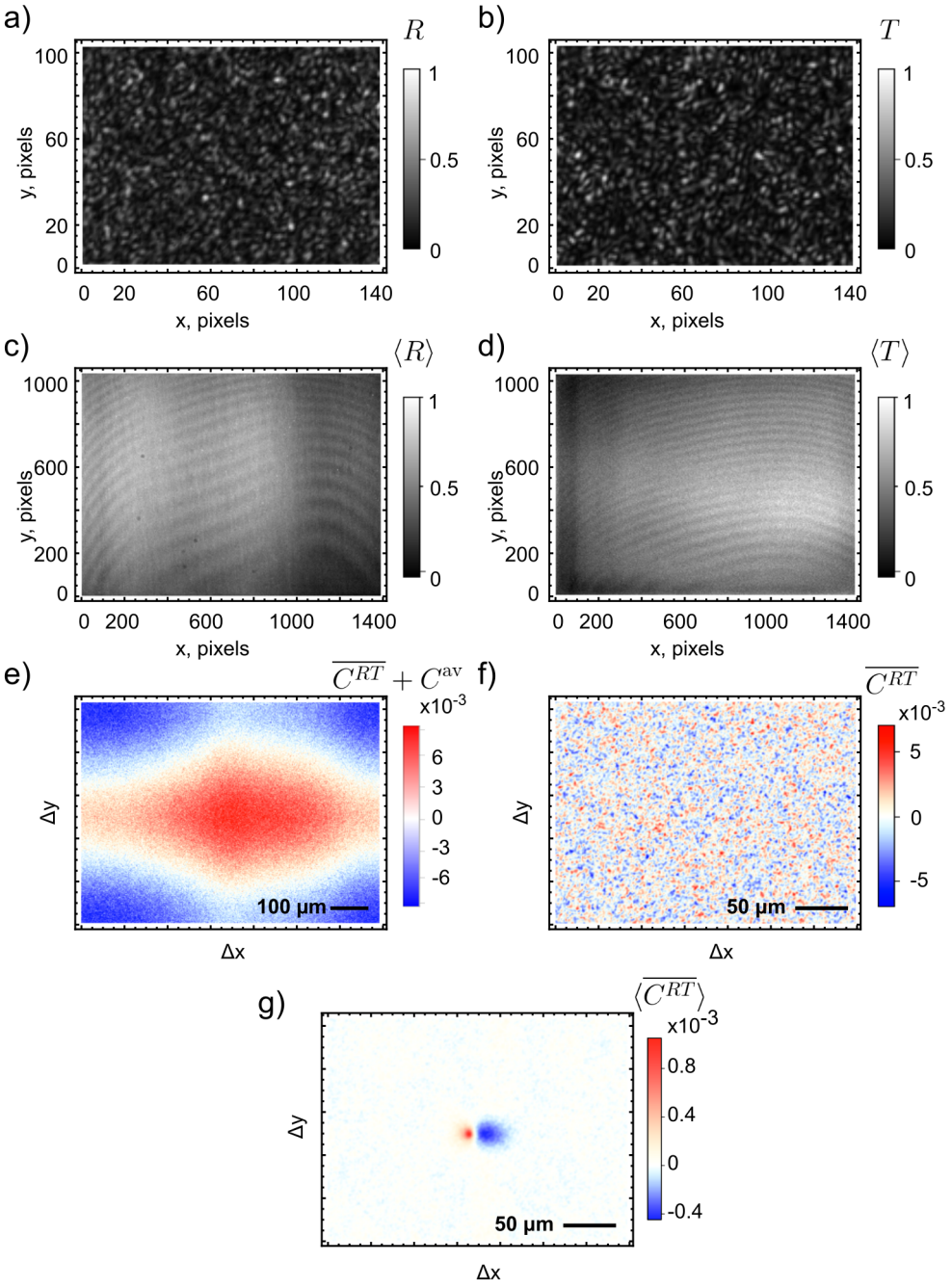

Figure 1.4: Typical raw speckles a) R, in reflection and b) T, in transmission, contain a non-uniform background, which becomes apparent upon averaging, which is shown in c) for reflection and d) in transmission. e) Correlation between the raw speckles, dominated by the cross-product of the average patterns. f) Correlation between a single pair of speckle patterns, $\overline{C^{RT}}$, with the background removed. g) $\langle \overline{C^{RT}} \rangle$, average of $\overline{C^{RT}}$.

The acquisition speed was improved even further by writing the image processing and correlation calculation program in C, for which we used the Vimba acquisition [36] and FFTW [37] libraries, approaching the hardware (camera max. fps) limit of 17 speckle pairs per second.

In the case of the stored data post-processing, the disorder averages $\langle R\rangle$ and $\langle T\rangle$ required to obtain δR and δT is calculated simply by summing the recorded speckles. In the case of on-fly processing a certain number of runs is required to accumulate this quantity prior to the correlation product processing. We note that contrary to the numerical simulation and theory the disorder average subtraction is crucial for the case of experimental measurement of the correlation function since it allows to remove the acquisition artefacts.

In Fig. 1.4a, b we show a pair of typical speckle images in reflection and transmission. It is impossible to notice any similarity between these patterns because the correlation is very weak. It is also hardly visible in the raw speckles but they all lay on an irregular fringed background pattern because of the non-uniformity of the illuminating beam and reflections in the protective glass window in front of the CCD detectors. Performing an ensemble average of the speckles reveals these patterns, shown in Fig. 1.4c, d. In analytical theory $\langle R\rangle$ and $\langle T\rangle$ refer to the uniform background reflected/transmitted intensity. If not subtracted from R or T they will add a constant background to the correlation product, not affecting its shape. In the numerics the situation is almost the same apart from slight non-uniformity of $\langle R\rangle$ and $\langle T\rangle$ due to boundary effects. In the experiment if we don't subtract $\langle R\rangle$ and $\langle T\rangle$ from R and T the resulting correlation product will be dominated by the correlation between $\langle R\rangle$ and $\langle T\rangle$, as we show in Fig. 1.4e, where the correlation product between R and T without average subtraction is shown. The typical correlation product $\overline{C^{RT}}(\Delta\mathbf{r})$ between δR and δT is shown in Fig. 1.4f. It appears random, with a granularity similar to that of a speckle image, because the reflection-transmission correlation we are looking for is too weak to see in one realization of disorder (it would be possible if we had a big enough CCD) and is covered with random noise. Upon ensemble averaging this noise disappears, revealing the shape of the reflection-transmission correlation, as shown in Fig. 1.4g.

The final step in the calculation is the normalization. As $\langle R\rangle$ and $\langle T\rangle$ are dominated by the experimental artefacts, we can't normalize the correlation as in (1.3). Instead we use a normalization factor

$$\mathcal{N}_1 = \overline{\left[\delta R(\mathbf{r}) - \overline{\delta R(\mathbf{r})}\right]^2}^{1/2} \times \overline{\left[\delta T(\mathbf{r}+\Delta\mathbf{r}) - \overline{\delta T(\mathbf{r}+\Delta\mathbf{r})}\right]^2}^{1/2}, \tag{1.6}$$

such that

$$\frac{1}{\mathcal{N}_1}\int \delta T(\mathbf{r})^2 d\mathbf{r} = \frac{1}{\mathcal{N}_1}\int \delta R(\mathbf{r})^2 d\mathbf{r} = 1 \tag{1.7}$$

Substituting $\mathcal{N}_1$ to (1.4) and assuming ergodicity and therefore equivalence of the spatial and disorder averaging we note that $\langle\overline{C^{RT}}(\Delta\mathbf{r})\rangle \simeq \mathcal{N}_2^{-1}\langle\delta R(\mathbf{r})\delta T(\mathbf{r}+\Delta\mathbf{r})\rangle$, with

$$\mathcal{N}_2 = \left\langle[\delta R(\mathbf{r}) - \langle\delta R(\mathbf{r})\rangle]^2\right\rangle^{1/2} \times \left\langle[\delta T(\mathbf{r}+\Delta\mathbf{r}) - \langle\delta T(\mathbf{r}+\Delta\mathbf{r})\rangle]^2\right\rangle^{1/2}. \tag{1.8}$$

As we will discuss later in Ch. 4, the intensity of the speckle patterns in the regime we are working in has a negative exponential distribution [8], according to which $\langle\delta R^2\rangle = \langle R\rangle^2$ and $\langle\delta T^2\rangle = \langle T\rangle^2$, and therefore

$$\langle\overline{C^{RT}}(\Delta\mathbf{r})\rangle \simeq C^{RT}(\Delta\mathbf{r}) = \frac{\langle\delta R(\mathbf{r})\delta T(\mathbf{r}+\Delta\mathbf{r})\rangle}{\langle R(\mathbf{r})\rangle\langle T(\mathbf{r}+\Delta\mathbf{r})\rangle}. \tag{1.9}$$

1.3 Results

In this section we present experimental results showing the dependence of the correlation function on the parameters of the sample and illumination. Later, in the next chapters we will compare these measurements with the numerical simulations and the analytical theory.

1.3.1 Thickness and mean free path dependence

The main parameters that determine the shape of the correlation function are the mean free path of the sample ℓ and its thickness L. We measured $\langle\overline{C^{RT}}(\Delta\mathbf{r})\rangle$ for different values of ℓ and L, covering a full range from single scattering ($L \lesssim \ell$) to the diffusive ($L \gg \ell$) regime. The results are summarized in Fig. 1.5, where both 2D maps $\langle\overline{C^{RT}}(\Delta x, \Delta y)\rangle$ and cross-sections along the line $\Delta y = 0$ (indicated as a dotted line in the 2D maps) are displayed. Both the shape and the sign of the measured correlation substantially depend on L and ℓ. In the single scattering regime (optical thickness $b \lesssim 1$), $\langle\overline{C^{RT}}\rangle$ is dominated by a narrow peak (still much larger than a single speckle spot) with a negative side lobe. In the multiple scattering regime ($b \gg 1$), $\langle\overline{C^{RT}}\rangle$ is dominated by a wide negative dip.

Presence of a negative dip in the $L > \ell$ regime matches the theoretical prediction [25], which confirms non-trivial character of this correlation, arising from the interference between the diffusion paths of the waves travelling through the scattering medium, which we discuss in Ch. 3. This negative correlation implies that for every bright spot

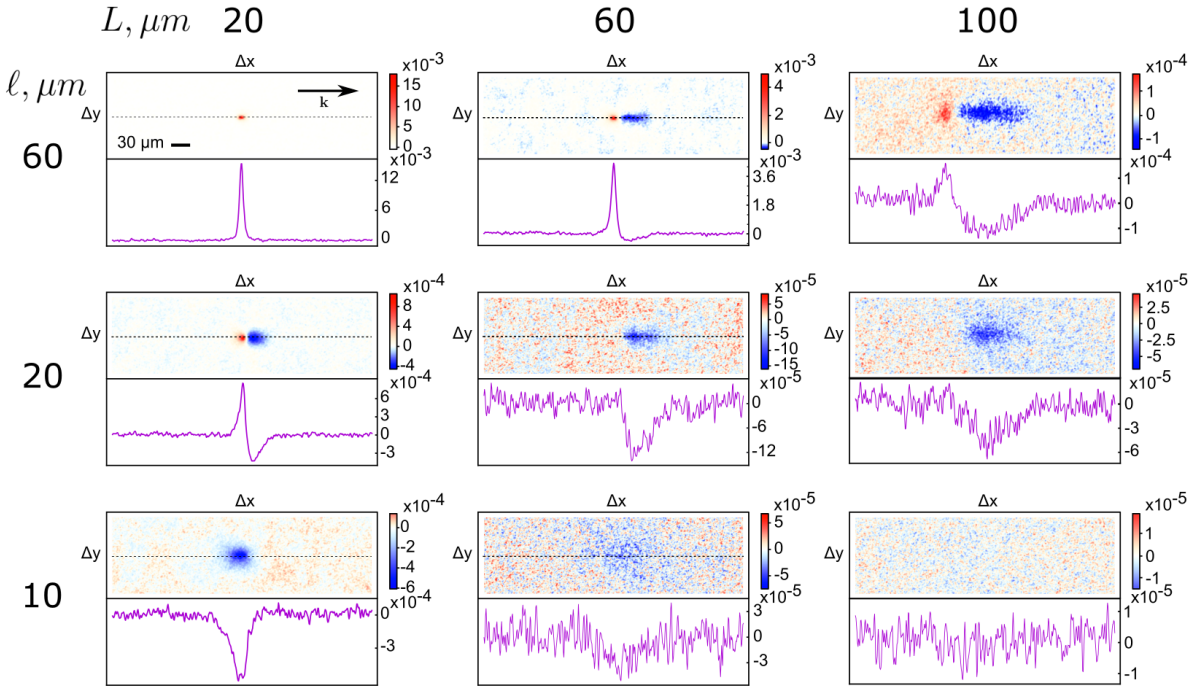

Figure 1.5: Averaged reflection-transmission correlation function $\langle \overline{C^{RT}} \rangle$ for different L and ℓ and the optical thickness $b = L/\ell$. For each L and ℓ, both 2D maps of $\langle \overline{C^{RT}}(\Delta x, \Delta y) \rangle$ and cross-sections along the line $\Delta y = 0$ are displayed. For moderate optical thickness ($b \lesssim 1$), the correlation function is dominated by a narrow peak with a negative side lobe. For large optical thicknesses, ($b > 1$), the correlation function is dominated by a wide negative dip.

in reflection (transmission) the corresponding area in transmission (reflection) is more likely to be darker, and *vice versa*. In Ch. 4 we show how this can be used to retrieve information about the objects hidden behind a scattering medium in the regime in which the methods based on the memory effect [26], are inapplicable.

The origin of the positive contribution present at small and moderate optical thickness is less clear. In Sec. 3.3.1 we present the arguments showing that this can't be a trivial field-field short range correlation, of the same type that normally dominates in the speckle correlation on either side of the medium (in reflection or in transmission). In [17] we suggest that this contribution occurs due to the field exchange between the diffusion paths in the first scattering event near the sample surface. We explain this in more details in Sec. 3.3.3.

To support our argument regarding the origin of these contributions we studied their dependence on the thickness more in detail, see Fig. 1.6. We can see that in the range where both contribution are present, i.e. Fig. 1.6b, e, their interplay complicates the dependence of the total correlation on the sample thickness and it is hard to make any conclusions from that measurement. However, when we isolate one of the contributions

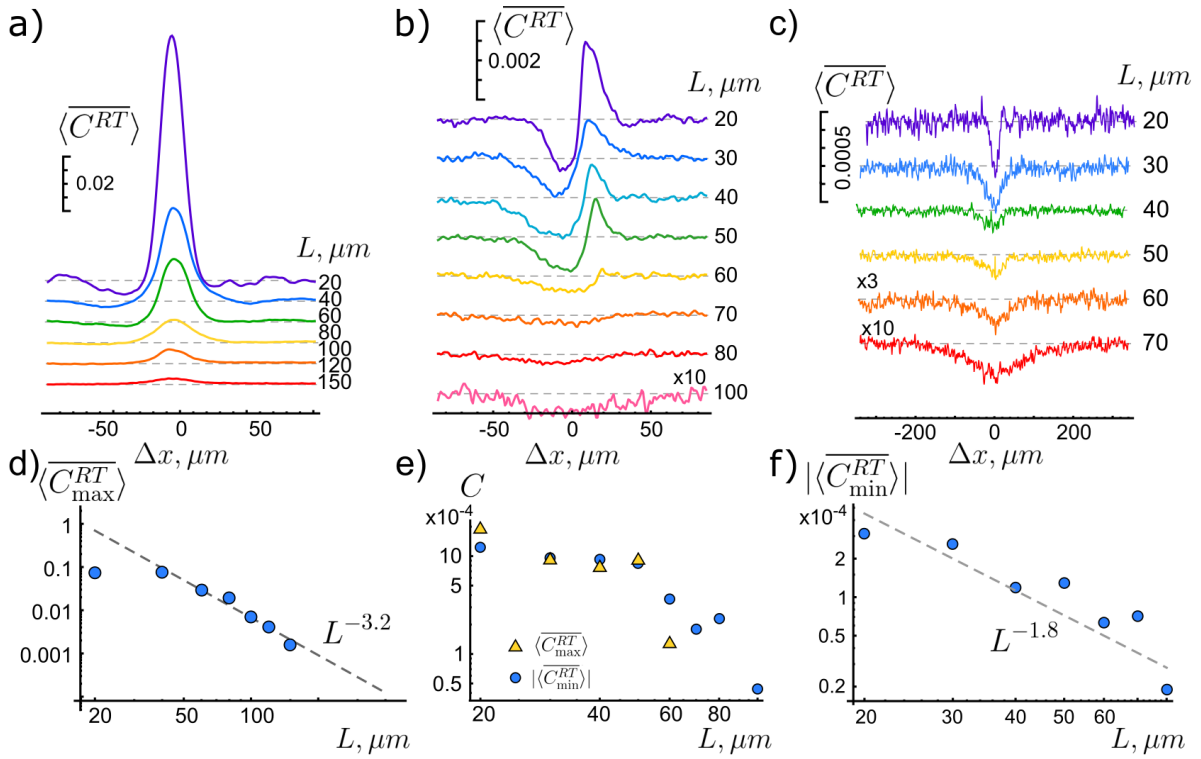

Figure 1.6: Dependence of the correlation function on the sample thickness. a) $\ell = 60\mu m$. b) $\ell = 20\mu m$. c) $\ell = 15\mu m$. d) Thickness dependence of the maximal value of the correlation function for $\ell = 60\mu m$. e) Thickness dependence of the maximal and minimal value of the correlation function for $\ell = 20\mu m$. f) Thickness dependence of the minimal value of the correlation function for $\ell = 15\mu m$.

by choosing an appropriate mean free path, the thickness dependence becomes more apparent. Regarding the negative contribution, the theory predicts $|C^{RT}_{\min}| \propto L^{-2}$. The fit in Fig. 1.6f suggests $\langle\overline{C^{RT}_{\min}}\rangle \propto -L^{-1.8\pm0.2}$, which is quite close to the theoretical prediction. Moreover, introducing a scaling $C^{RT}(\Delta\mathbf{r}/L)/L^{-2}$ according to the theory should remove any thickness dependence of the correlation function, which can be observed in the Fig. 1.7.

As we discuss in Sec. 3.3.3, the mechanism leading to a positive peak implies that it should reduce with the thickness as $C^{RT}_{\max}(\Delta\mathbf{r}) \propto L^{-4}$. In the experiment, see Fig. 1.6a, d, we observe slightly slower decay $\langle\overline{C^{RT}_{\max}}\rangle \propto L^{-3.2\pm0.4}$. This can be attributed to the fact that the negative contribution although invisible in the data, is still present and while reducing (in absolute value) with the thickness somehow balances the quick decay of the peak.

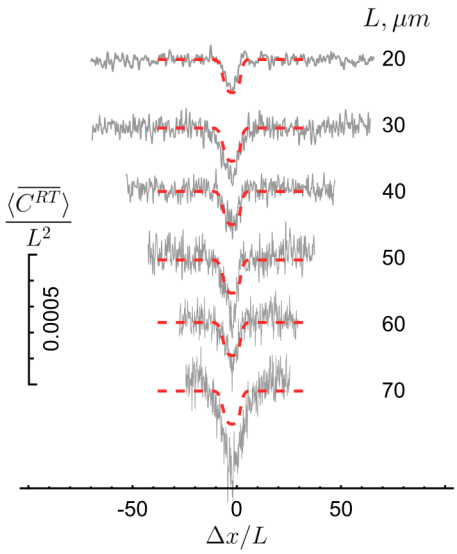

Figure 1.7: Universal scaling of the correlation function. Dividing $\langle \overline{C^{RT}} \rangle$ from Fig. 1.6c by L^2 and rescaling Δr by L leads to elimination of the thickness dependence of the correlation, see Sec. 3.3.2, which agrees with the experimental data.

1.3.2 Dependence on the angle of incidence of the incoming beam

One more argument in favour of the proposed mechanism of the correlation peak formation is its dependence on the incidence angle of the exciting wave. The field exchange occurring at the sample surface, determines the relative phases of the following diffusion paths and in that way can bring the dependence on the initial wave incidence angle in the correlation shape. To support this argument we performed a measurement of the correlation shape dependence on the angle incidence of the incoming light. We show this dependence in Fig. 1.8a. As we can see, the amplitude of the peak reduces with the angle of incidence. Also the relative position of the peak and the dip changes, as can be seen from Fig. 1.8a, but more clearly from Fig. 1.8b, in which correlation is recorded with the incident beam being inclined both in horizontal and vertical planes with respect to the sample surface.

The sample used for this experiment had $\ell = 20\mu m$. According to the theoretical description, the origin of the dip in this configuration is different from the situation of large optical thickness. As we describe in Sec. 3.3.3 the near-surface crossing leads to a complex correlation shape with positive and negative parts, both of which depend on the incidence angle, while the dip occurring due to the diffusion paths crossing in the bulk should not depend on the illumination angle at all. According to the theory, the projection of the incident beam on the sample surface specifies a preferred direction

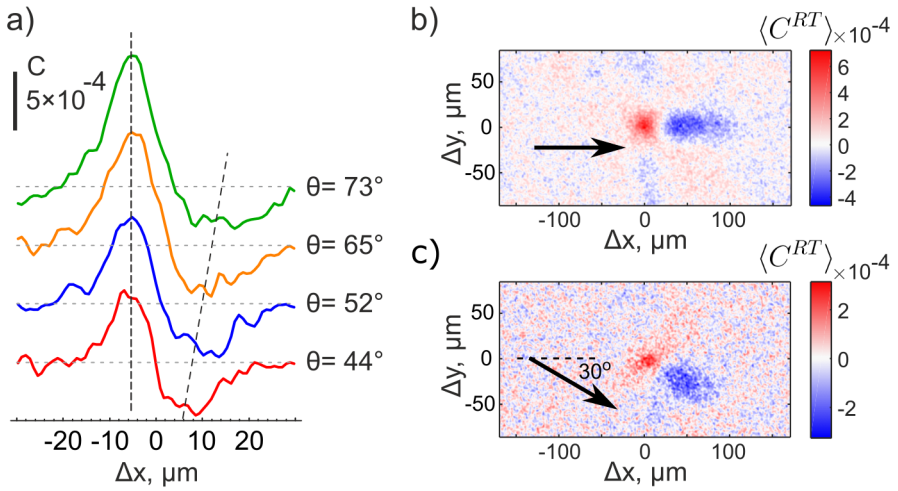

Figure 1.8: Dependence of the correlation function on the exciting light incidence angle. a) The projection of the incident beam on the sample surface is parallel to the camera horizontal axis. b) 2D map of the correlation at $\theta \approx 45°$. c) Correlation function measured after adding an angle of $\sim 30°$ between the beam projection onto the sample surface and camera horizontal axis. Features in the correlation function remain aligned along the incidence beam projection.

along which the peak and the dip are aligned. The correlation shape depends on the angle between the incident beam and its projection on the sample surface, which is qualitatively consistent with the experimental observations. It is hard to go beyond the qualitative comparison since on one hand the ladder approximation, used to describe the diffusive transport after the initial scattering, is hardly valid in the $L \approx \ell$, while at the larger optical density the contribution due bulk crossing should be taken into account, which complicates the analysis.

1.3.3 Correlations between different polarization channels

In the most of the current work we deal with the scalar wave approximation, in which we neglect the vector nature of the electromagnetic field. Such an approach is well justified for the case of strongly scattering samples, where the initial beam polarization state is lost at a distance of $\sim \ell$ within the sample [38]. Good agreement between the theory and experiment, reassures us in the appropriateness of this approximation even for the case of moderate scattering strength. However if we aim for a complete quantitative description, the vector nature of light should be taken into account. The correlations between different polarization channels have been previously studied only theoretically [39–41].

We performed an experiment in which we studied the correlations between the re-

flected and transmitted speckle patterns in different polarization channels. The results are presented in Fig 1.9, in which panel a) refers to the weak scattering situation of $L \approx \ell$ and panel b) refers to a more scattering sample. We assign the subscript $\perp$ to the R or T channels perpendicular to the incident beam polarization and $\parallel$ to the parallel ones, which we can select in the measurement by placing corresponding polarizers before the cameras in reflection or transmission. The upper sub-panels in a) and b) refer to the correlation without polarizers, while the lower ones show the correlation functions for all four possible combinations of $R_\perp$, $R_\parallel$, $T_\perp$ and $T_\parallel$.

In both cases, as expected, the correlation between $R_\parallel$ and $T_\parallel$ is almost identical to $\langle \overline{C^{RT}} \rangle$. When the polarizer in transmission is crossed with the incident beam polarization ($\langle R_\parallel T_\perp \rangle$, $\langle R_\perp T_\perp \rangle$ in Fig 1.9a,b), for both cases the negative part of the correlation disappears and the remaining part is positive. This is not surprising for the weak scattering case, as the positive part is present in the total correlation, however presence of a positive contribution in the strong scattering case is surprising. As we will see in Sec. 3.3.2 the analytic calculation of the correlation function involving diffusion crossing in the bulk of the sample involves evaluation of several terms having different signs. The observed correlation between different polarization channels suggest that these terms may also be separated in polarization.

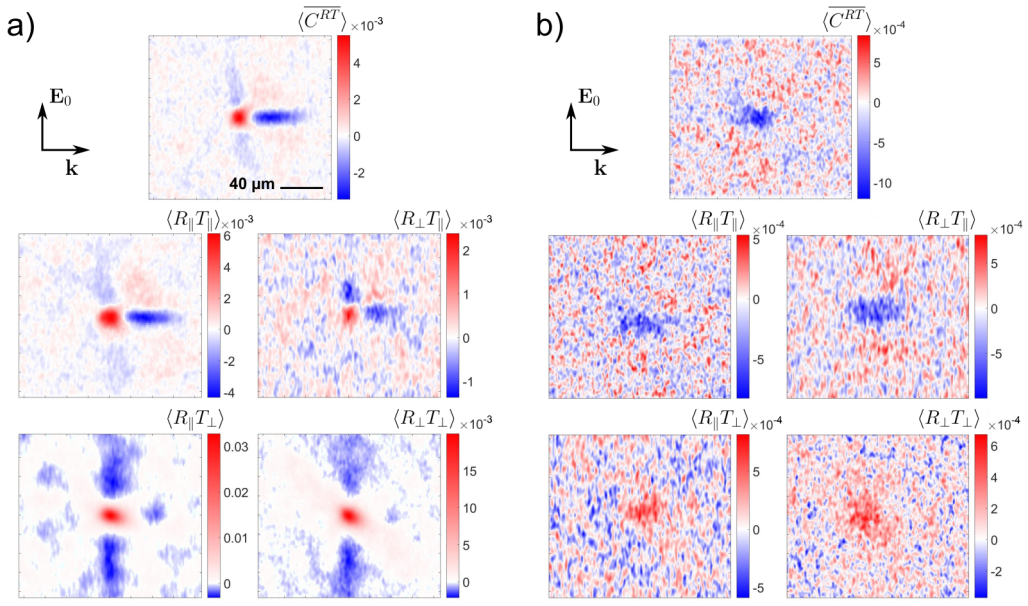

Figure 1.9: Measured correlation function between different polarization orientations in reflection and transmission. Lower index indicates the orientation of the corresponding reflection or transmission registration channel with respect to the incident beam polarization. Arrows indicate the incident beam wave-vector and polarization orientations. a) $\ell = 60\mu m$ sample. b) $\ell = 15um$ sample.

Finally, in the case when the reflection channel is crossed with the incident beam and the transmitted one is aligned with it, the correlation function behaviour is different for the weak and strong scattering case. In the $L \approx \ell$ case the $T_{\parallel}R_{\perp}$ correlation is much weaker than the total one with both positive and negative contributions attenuated by an order of magnitude, while in the strong scattering regime, $T_{\parallel}R_{\perp}$ is almost the same as $\langle\overline{C^{RT}}\rangle$.

In order to explain the observed behaviour we note that in the weak scattering case both reflected and transmitted scattered light is strongly polarized in the same way as the incident beam, while in the strong scattering case the reflected light remains strongly polarized and the transmitted one almost depolarizes. This happens due to the fact that reflection occurs mostly close to the surface and just a small fraction of the reflected light comes from the bulk of the sample. Now, crossing the polarizer in reflection with the incident beam blocks the light that is reflected closer to the surface. As the positive contribution occurs due to the waves involved into a scattering event near the surface, the size of the peak is reduced when we block such single-scattered light from going to the reflection camera. It is hard to go beyond such rough explanation without modifying the analytical theory to account for the vector nature of light, which is a challenging problem for the future.

1.3.4 Behaviour at a distance from the surface

In this section we discuss the dependence of the correlation function on the distance of the registration plane from the sample surface(s). Contrary to the other correlation functions that remain present even in the far field [29–31], $\langle\overline{C^{RT}}\rangle$ exists only near the reflection and transmission surfaces. In the far field $C^{RT}(\mathbf{k}_b, \mathbf{k}_{b'}) \sim \int C^{RT}(\Delta\mathbf{r})\mathrm{d}\Delta\mathbf{r} =$ const. for any pair of observation directions $\mathbf{k}_b$, $\mathbf{k}_{b'}$, as the information content is spread uniformly over all degrees of freedom.

It is hard to estimate theoretically how fast the decorrelation occurs as it involves inclusion of the additional free space propagation terms into the equation for the correlation function. However, this information might be important to assess the limitations of the imaging technique we propose in Ch. 4. In order to get such an estimate, we performed a measurement of $\langle\overline{C^{RT}}\rangle$ changing, d_f the distance of both of the observation planes from the sample surfaces. The resulting correlation functions are presented in Fig. 1.10. In both strong and weak scattering cases the correlation function broadens and reduces in height, when observed farther away from the surface, however surprisingly is still present even at a distance of 150 μm away from them, which is more than $3L$. The rates at which the correlation decays is slightly different for the positive and negative

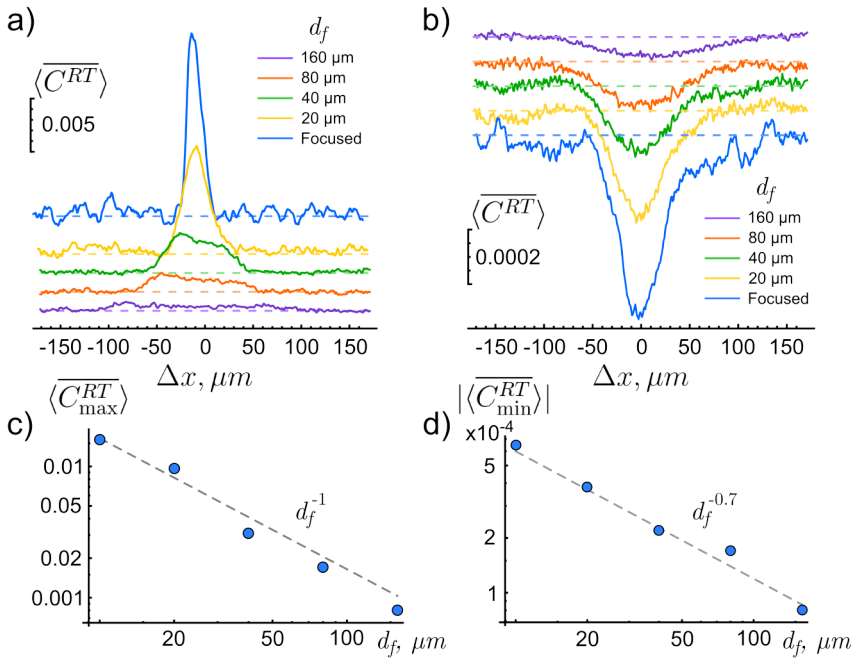

Figure 1.10: Dependence of the average correlation function on the distance from the sample surfaces, d_f. a) Weak scattering case $\ell = 60\mu m, L = 40\mu m$. b) Strong scattering case $\ell = 10\mu m, L = 40\mu m$. c) Dependence of the peak maximal value on d_f for the $\ell = 60\mu m$ sample. d) Dependence of the dip minimal value on d_f for the $\ell = 10\mu m$ sample.

contributions, being bigger for the peak. The size of the dip changes as $\propto d_f^{-0.7\pm0.004}$, while the peak changes as $\propto d_f^{-1\pm0.12}$.

1.4 Summary

We have presented an experimental study of the long-range correlation between the reflected and transmitted speckle patterns. We probed its dependence on the sample parameters, incident beam orientation and collection plane distance from the surface. In the diffusive regime the correlation is dominated by a broad negative dip matching the theoretical prediction [25]. In the ballistic scattering regime the correlation reveals an unforeseen positive contribution. In the intermediate regime, these two terms co-exist leading to a complicated interplay, that depends on the exciting beam angle of incidence and polarization. Both contributions decay with the distance from the surface. In the next two chapters we continue to study this correlation numerically and analytically.

Chapter 2

Numerical simulation of the speckle correlations

In this chapter we present numerical simulation of the reflection-transmission correlation introduced in the previous chapter, using the coupled dipole method [42]. This approach was used to simulate the disordered material slabs in [25]. The author of the thesis extended this approach to include the angle of incidence and polarization of the incoming wave. All the simulations presented here were performed by the author except for those in Fig. 2.3.

2.1 Coupled dipoles approximation

The coupled dipole method is a well established technique for numerical simulation of the fields created or scattered by complex structures [42–44]. In this approach the scattering object is split into discrete blocks and to each block a point dipole is assigned. Assuming that these dipoles interact only through far-field radiation, it is possible to find the effective field exciting each of the dipoles, and when it is known, to calculate the scattered field. There are several difficulties associated with this method [45]. First of all the discretization of the object should be done in such a way that the resulting dipole distribution represents the original object well enough. It means that, at least, there should be sufficient number of the discretization cells, however large numbers of dipoles complicate the calculations. In addition, the polarizability of the dipoles should be chosen in such a way that it reproduces the modelled material refractive index frequency (or position if necessary) dependence. However applying this model to a typical scattering medium we can omit these difficulties.

As we will see later (Sec. 3.1.2), a set of randomly distributed point scatterers,

as in (3.30), is a good model of a typical disordered medium. Moreover, as we are not interested in the exact configurations of the fields, but rather in their statistics, a random distribution of dipoles within some volume is a perfect model of a scattering sample, assuming that they have comparable macroscopic properties (density of scatterers, mean free path, e.t.c). The polarizability of the scatterers can be considered to be constant as in this chapter we consider monochromatic input wave. Moreover, as we are interested in the field correlations, the exact amplitude of the field is not important for us (it is excluded during the correlation normalization) and therefore the polarizability can be arbitrary.

As the polarizability can be arbitrary, we choose $\omega = \omega_0$ or that the scatterers are in resonance, which simplifies further calculations. The polarizability of the scatterers at the frequency close to the resonance in 3D space is

$$\alpha(\omega)\Big|_{\omega\to\omega_0} \approx -\frac{2\pi\mathscr{G}}{k_0^3(\omega-\omega_0+i\mathscr{G}/2)}, \tag{2.1}$$

where ω_0 is their resonant frequency and $\mathscr{G}$ determines the linewidth. In that case $\alpha(\omega) = -4\pi/k_0^3 i$ and the scattering cross-section

$$\sigma(\omega) = \frac{k_0^4|\alpha(\omega)|^2}{4\pi} = \frac{4\pi}{k_0^2}, \tag{2.2}$$

from which we derive the mean-free path

$$\ell = \frac{1}{\rho_s\sigma} = \frac{L\mathcal{S}k_0^2}{4\pi\mathcal{N}_\mathrm{s}}, \tag{2.3}$$

where ρ_s is the density of scatterers, L is the thickness of the sample, $\mathcal{S}$ is the area of the sample surface and $\mathcal{N}_\mathrm{s}$ is the number of scatterers within the sample.

Assuming that the incident field is a wave travelling from left to right along x,

$$E_0(x) = e^{-ik_0x}, \tag{2.4}$$

we can write the expression for the field exciting each scatterer as

$$E_j = E_0(\mathbf{r}_j) + \alpha(\omega)k_0^2\sum_{k=1,k\neq j}^{\mathcal{N}_\mathrm{s}} G_0(k_0|\mathbf{r}_j-\mathbf{r}_k|)E_k, \tag{2.5}$$

where G_0 is the free-space Green's function

$$G_0(\mathbf{r}_0, \mathbf{r}) = -\frac{e^{ik_0|\mathbf{r}_0-\mathbf{r}|}}{4\pi|\mathbf{r}_0-\mathbf{r}|}. \tag{2.6}$$

Here we also neglected the electric field polarization, treating electric field as a scalar wave. We will discuss the effect of polarization later. Considering $\mathcal{E} = \{E_j\}$ to be a vector of unknowns, (2.5) can be treated as a system of linear equations. In the matrix form it is

$$-\mathcal{E}_0 = \alpha(\omega)k_0^2(\mathcal{G}_0 - \mathbb{I})\mathcal{E}, \tag{2.7}$$

where $\mathcal{G}_{0\,jk} = G_0(k_0|\mathbf{r}_j - \mathbf{r}_k|)$. It can be solved for $\mathcal{E}$ by inverting the $\mathcal{G}_0$ matrix, or by approximate methods [46]. When $\mathcal{E}$ is known the field in any point of space is reconstructed as

$$E(\mathbf{r}) = E_0(\mathbf{r}) + \alpha(\omega)k_0^2\sum_{k=1}^{\mathcal{N}_\mathrm{s}} G_0(k_0|\mathbf{r}-\mathbf{r}_k|)E_k. \tag{2.8}$$

When the polarization of the incident and the scattered light is taken into account the problem becomes more complicated. The Green's function takes form

$$\overleftrightarrow{G}_0(\mathbf{r}-\mathbf{r}') = \left(\overleftrightarrow{\mathbb{I}} - \mathbf{u}\otimes\mathbf{u} + \frac{ik_0|\mathbf{r}-\mathbf{r}'|-1}{k_0^2|\mathbf{r}-\mathbf{r}'|^2}\left(\overleftrightarrow{\mathbb{I}} - 3\mathbf{u}\otimes\mathbf{u}\right)\right)\times \\ \times\frac{\exp(ik_0|\mathbf{r}-\mathbf{r}'|)}{4\pi|\mathbf{r}-\mathbf{r}'|^2} - \frac{\delta(|\mathbf{r}-\mathbf{r}'|)}{3k_0^2}\overleftrightarrow{\mathbb{I}}, \tag{2.9}$$

where $\mathbf{u} = (\mathbf{r}-\mathbf{r}')/|\mathbf{r}-\mathbf{r}'|$ and $\overleftrightarrow{(\cdot)}$ means the dyadic function, with $\overleftrightarrow{\mathbb{I}}$ being the dyadic identity. Upon substitution of this Green's function into (2.5) the expression for the field breaks into 3 coupled sets of equations, one for each of the polarization components. The length of the vector $\mathcal{E}$ and correspondingly, the size of the matrix $\mathcal{G}_0$ in (2.7) increases by a factor of 3, but still the resulting system can be solved in the same way as for non-polarized case. Having the values of the three field polarization components at each scatterer we can calculate these components everywhere in space similarly to (2.8).

2.2 Numerical analysis of the speckle correlations

In order to support the experimental observations presented in the previous section, we performed numerical modelling of the reflection-transmission correlation using the coupled dipole method. The program was implemented in MATLAB. $\mathcal{N}_\mathrm{s}$ random scatterers were distributed uniformly within a box of a size $L \times W^2$. The field at the entering and the exit surfaces of the box was calculated (at a distance of 0.1–1λ), assuming the excit-

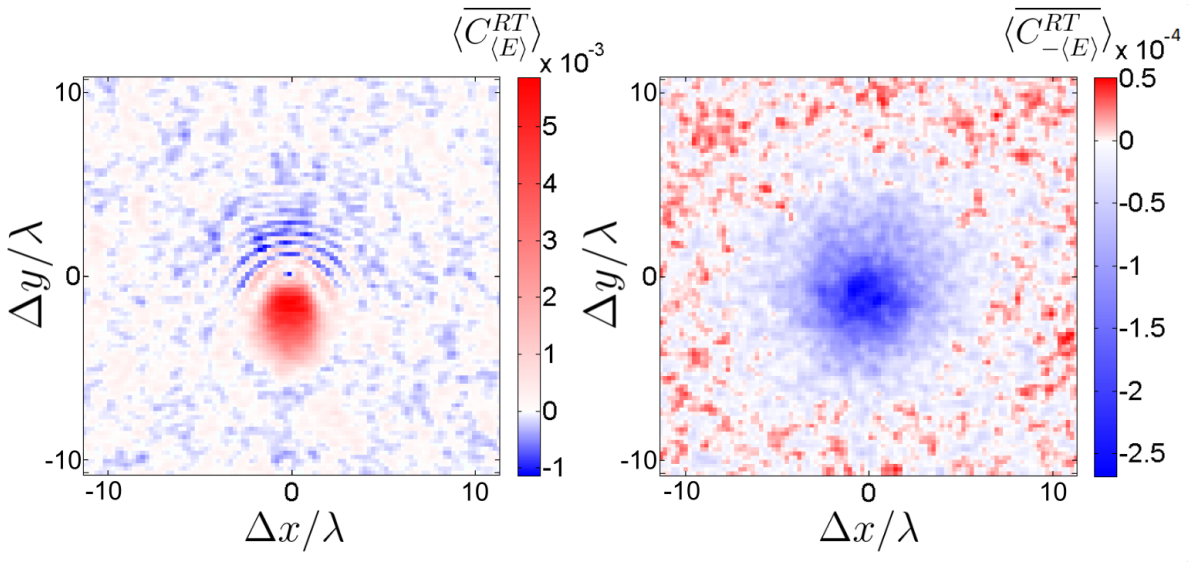

Figure 2.1: The effect of subtraction of the average field at the sample surface on the correlation function. a) Average correlation function without average field subtraction, $L = 2\lambda$, $\ell = \lambda$. b) The same correlation, but subtracting the average field before calculating intensity $R = |E^R - \langle E^R \rangle|^2$ and $T = |E^T - \langle E^T \rangle|^2$.

ing wave travels from left to right along the L side of the box. Most of the simulations were performed with the incident wave entering at 45° to the sample surface, to mimic the experimental conditions. The correlation function was calculated in a way similar to how it was done in the experiment, Sec. 1.2.3, with one additional step of the average field subtraction, which we will discuss below. The rest of the procedure was the same as in the experimental data processing: first the correlation between each pair of the reflected and transmitted patterns was calculated, then the process was repeated $\mathcal{N}_\mathrm{r}$ times and the average correlation was calculated for each configuration of the sample.

Let's note the main differences of the model from the experiment. First of all, in the experiments the incident light wavelength was $\lambda_{\text{He-Ne}} = 632$ nm. It means that even for the thinnest sample $L/\lambda > 30$. In the simulation we need to satisfy the condition $W \gg L$ in order to avoid the boundary effects. Substituting $L/\lambda = 30$ and $W = (10L)^2$ to (2.3), we can estimate the number of scatterers required to model a sample with an optical thickness $b = 1$ to be $\mathcal{N}_\mathrm{s} \approx 10^6$. Such number of scatterers is certainly infeasible for the simulation, therefore we choose the thickness, such that $L/\lambda \approx 1$. With such a choice we can achieve $b \approx 1$ with hundreds of scatterers, however we no longer expect quantitative agreement between the simulation and experiment. One more difference is that in the simulation some near-field components can be present near the sample surface. They do not propagate [47], therefore they are not captured in the experiment, however the calculated correlation may include a contribution from

these components [48], which can lead to a significant mismatch between the modelling and experiment. In the simulation, an easy solution is to calculate the correlation at a certain distance from the surface, however as $\langle\overline{C^{RT}}\rangle$ decays quite quickly with this distance and extensive averaging is required in that case. An alternative solution is to subtract the average fields $\langle E^R(\mathbf{r})\rangle$ and $\langle E^T(\mathbf{r})\rangle$ from $E^R(\mathbf{r})$ and $E^T(\mathbf{r})$ correspondingly before evaluating the intensity of the reflected and transmitted speckles. In Fig. 2.1 we show the effect of the average field subtraction. The correlation function $\langle\overline{C^{RT}_{\langle E\rangle}}\rangle$ between the original calculated speckles without average field subtraction shown in the left panel of the Fig. 2.1, demonstrates a broad positive contribution with fine fringes. However when the corresponding averages are subtracted from the reflected and transmitted field distributions, i.e. $R = |E^R - \langle E^R\rangle|^2$ and $T = |E^T - \langle E^T\rangle|^2$ before putting R and T into (1.3), the resulting correlation, $\langle\overline{C^{RT}_{-\langle E\rangle}}\rangle$, shows a broader negative dip (right panel of Fig. 2.1). Comparing the optical densities of the samples used in the simulation and in the experiment, we note that in the latter the positive part is already absent at $b = 2$, which was used in the modelling, moreover the sharp fringes were never present is the experiments. This supports our guess regarding the necessity of the average field subtraction, therefore, from now on we assume that $\langle\overline{C^{RT}_{-\langle E\rangle}}\rangle$ is equivalent to $\langle\overline{C^{RT}}\rangle$ and in the rest of the chapter we always assume that the average fields are subtracted before calculating the correlation.

2.3 Thickness and mean free path dependence

The dependence of the average correlation function on the mean free path ℓ and sample thickness L in a scalar wave approximation is shown in Fig. 2.2. The first thing we note is that all the contributions, observed in the experiment are present in the simulations as well. We see a broad peak in the low b and low L range, a negative contribution at higher b and their superposition in the intermediate range. The most apparent difference between the experimental and simulated correlation functions is the presence of a sharp $\sim \lambda$, positive contribution at low L, which we attribute to the field-field short-range correlation. We explain the origin of this term in more detail as well as the reason why it is not observed experimentally in Sec. 3.3.1. One more difference is that in the experiment the negative dip becomes elongated in the direction of the incident beam projection on the sample surface, especially at large L, while in the simulation it remains quite symmetric in Δx and Δy. We can refer this discrepancy to the limitations of the scalar wave approximation. As we will see later in this chapter, taking into account the vector character of the incident and scattered field can lead to

an anisotropic shape of both contributions. One more thing to note is that at large optical densities the amplitude of the negative contribution increases with the decrease of the mean free path. This is in striking contrast with the behaviour of the long range correlations in transmission, which linearly depend on the mean free path in the first approximation [22]. Finally we note that apart from the discrepancies in the amplitudes of the positive and negative contributions, there is a good agreement between the simulated and measured correlation functions.

2.4 Dependence on the angle of incidence

In Sec. 1.3.2 we discussed the dependence of the correlation function shape on the incoming beam incidence angle. However, in the experiment the range of possible incidence angles was limited due to mechanical constrains. In the simulation we can study a broader range of angles. In the left panel of Fig. 2.3 we plot the simulated correlation function at different incoming beam incidence angles (counted from the surface normal) and in the right panel we compare the simulation to the experiment. As we can see from this comparison, the amplitude of the positive contribution increases at more grazing angles both in modelling and in the experiment. As we explained in Sec. 1.3.2 and will study more in detail in Sec. 3.3.3 the change of the positive peak amplitude can be explained by the peculiarities of the scattered waves diffusion paths crossing near the reflection surface. In the first instance, the negative contribution should not depend on the specified angle, however as we see from the plots at 73° and 68°, the dip broadens significantly. It might be attributed to the increase of the effective thickness of the medium in which scattering occurs, however the increase in thickness contradicts the fact that the amplitude of the negative contribution grows.

Overall, despite a good agreement between the experiment and simulation, for this particular b and L we are still far from a complete understanding of the underlying physical phenomena. For example, it is not clear if the relative position of the peak and the dip actually changes, or the apparent shift can be explained by the amplitude/width alteration of one or both of the contributions. Also at different ℓ and L there might be quite a big mismatch between the simulation and experiment, which of course can be related to a difference in L/λ ratio, but it is not clear why in some cases it matters and in the others it doesn't. Finally certain mismatch can be due to neglecting the vector nature of light, therefore it is interesting to explore the influence of the incident light polarization on this correlation function.

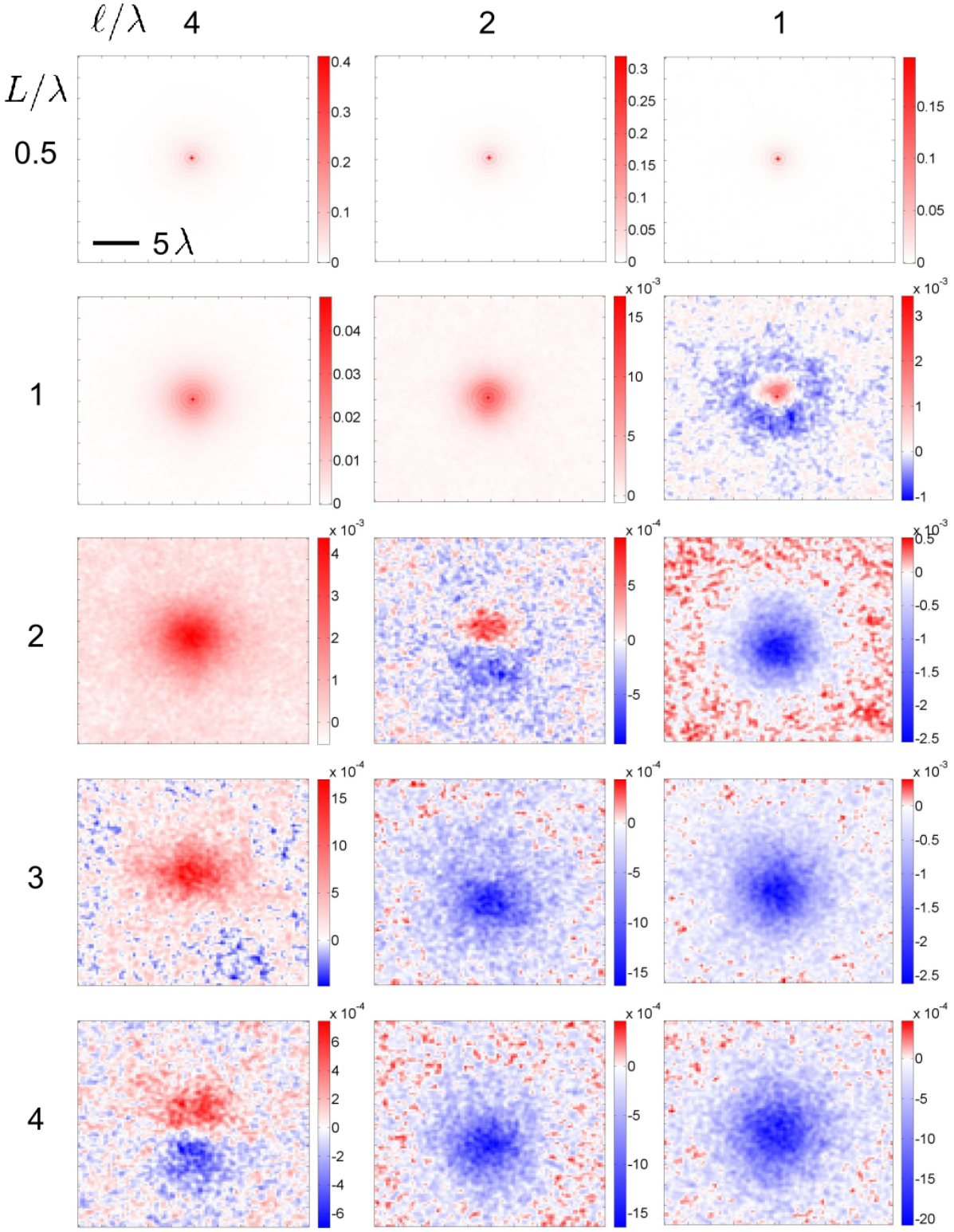

Figure 2.2: The dependence of the average correlation function $\langle \overline{C^{RT}} \rangle$ calculated using the coupled dipole method, on the mean free path, ℓ and the thickness, L of the sample. Number of averages is 5000 for each sample configuration.

2.5 Correlation between different polarization components

In Fig. 2.4 we present the correlation function calculated between different polarization channels in reflection and transmission. Panel a) of this figure refers to a weak disorder scenario, while panel b) refers to a stronger disorder. Analysing these graphs we see that there is no such evident agreement between the experiment and simulation as in the case of incidence angle dependence.

We first note similar features: first of all the correlation of the total scattered intensity in reflection and transmission is not much different from the one calculated in the scalar wave approximation, which justifies its validity for the situation considered here. In the lower optical density case the dip becomes elongated in the direction of the projection of the incident beam on the sample surface, which agrees with the experiment. Also in that case when both analysed channels are crossed with the incident beam polarization, the positive contribution becomes more pronounced. In the bigger optical density case, similarly to the experiment, when only transmitted light aligned in polarisation with

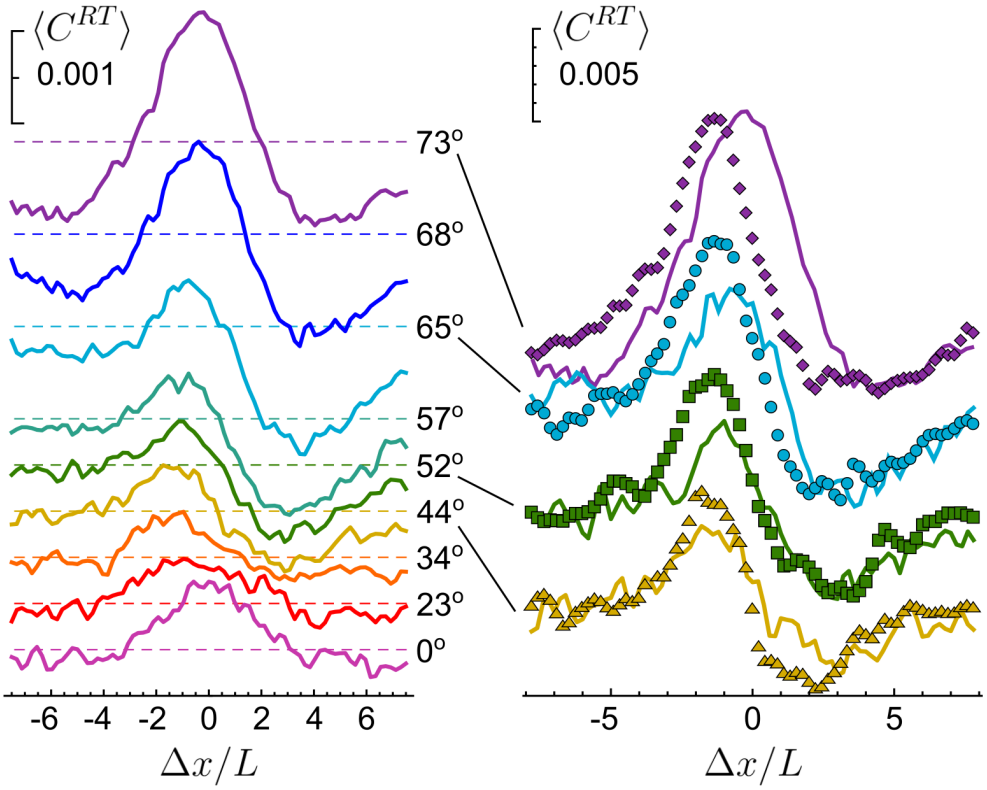

Figure 2.3: Modelled angular dependence of the $\langle \overline{C^{RT}} \rangle$ for $\ell = L = 2.4\lambda$. In right panel we compare modelling to the experiment, see Fig. 1.8 a.

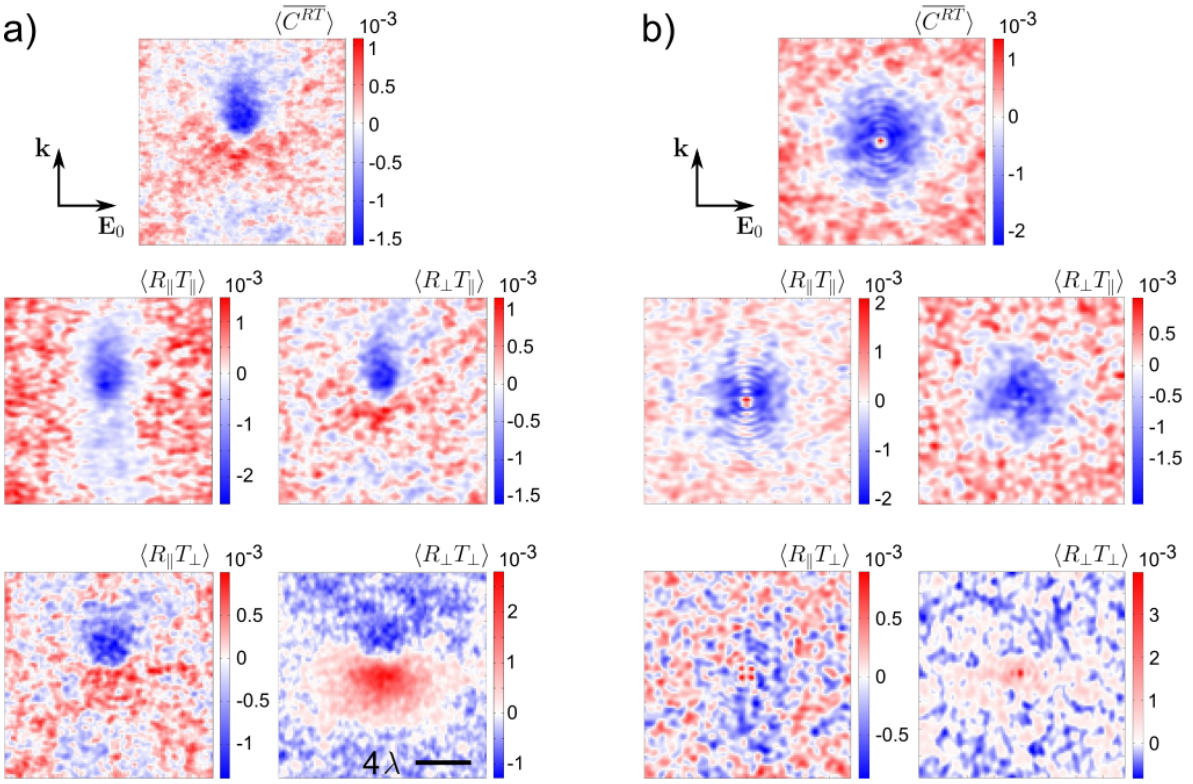

Figure 2.4: Influence of the incident light polarization on the $\langle \overline{C^{RT}} \rangle$ and correlation between different polarization channels. The projection of the incident beam on the sample surface is indicated with an arrow, the angle of incidence $\approx 45°$. The incident light polarization vector is parallel to the sample surface. a) $\ell = 2.67\lambda$, $L = \lambda$. b) $\ell = 1.33\lambda$, $L = \lambda$.

incident beam is taken into account, the correlation shows a broad dip, the same as for the total intensity correlation.

The rest of the features are not matching the experiment. In the lower optical density case in the experiment the dip disappeared when the the polarizer in transmission was crossed with the incident beam, while in the simulation it stays there and the peak present in the opposite situation in experiment is not observed in the simulation. At the same time, for higher optical density the peak observed in $\langle R_{\parallel} T_{\perp} \rangle$ and $\langle R_{\perp} T_{\perp} \rangle$ is not present in the simulation. Also in the stronger scattering case the discrepancy in the negative correlation amplitudes for modelling and experiment is the same as for the scalar wave approximation calculation. This disagreement of the modelling from the experiment stimulates further investigation of the correlation function polarization dependence, including extension of the analytical theory, presented in the next chapter onto the vector wave scenario.

2.6 Summary

We presented a numerical study of the reflection-transmission correlation by means of the coupled dipoles approximation simulation. In this approach we modelled the disordered medium as a set of randomly placed point scatterers. Despite such a simplification, we are able to recover the behaviour observed in the experiment. The simplicity of this method provides a significant advantage over the methods that model the realistic microstructure of the disordered materials [49, 50].

The dependence of the modelled correlation on the thickness and the mean free path is in a good qualitative agreement with the experimental data, apart from presence of a short-range contribution at $L \lessapprox \ell$, which can be explained by a smaller L/λ in the modelling. The angular dependence of the correlation function also matches the experimental data quite well, especially in the $L \sim \ell$ regime, in which even a quantitative agreement is achieved. Certain features of the cross-polarization correlations are reproduced in the modelling, however many details still need clarification, as well as reasons of the disagreement between the correlation amplitudes outside the $L \sim \ell$ regime. The next steps might be to study the dependence of the correlation function on the polarisation orientation with respect to the sample surface (including the circularly polarized light) and to increase the number of modelled scatterers to match the experimental conditions, applying approximate methods [46] to solve the resulting linear system.

Chapter 3

Theoretical analysis of the reflected and transmitted speckle patterns correlations

In this chapter we present the analytical calculation of the reflection-transmission correlation function, based on the diagramatic technique. We first introduce the background theory required to perform such a calculation. We start with discussing the general features of the wave propagation in disordered material: we introduce the most commonly used Gaussian model of such a medium, and show how to obtain the average Green's function and the intensity propagator, which are the building blocks of the considered correlation functions. Then we consider the short and long-range contributions of the intensity correlation function, providing an example of the calculation of these quantities in the transmission geometry. After that we finally apply the outlined techniques to estimate different contributions to the correlation function between the reflected and transmitted intensity.

The material presented in this chapter is based on the work performed by our collaborators from Paris [17, 25].

3.1 Wave propagation in random media

3.1.1 Green's function of the Helmholtz equation in random medium

When a wave of any origin encounters a disordered object, it scatters in random directions and the scattered waves in its turn continuing to interact with the object lead

to a phenomenon we call multiple scattering. Let's consider the formal description of this process for the case of electromagnetic waves. In the current chapter we deal with the situation when the source of incident wave is monochromatic, its amplitude is not changing in time and enough time has passed for all transient processes related to the wave propagation to finish. We also use the scalar wave approximation, as we discussed in Ch. 1, as it significantly simplifies the discussion, still allowing to observe relevant phenomena. In that scenario the field at any point of space is a solution of the Helmholtz equation [51]. Wave propagation in a disordered medium can be modelled by means of including a randomly varying permittivity $\varepsilon(\mathbf{r})$ into that equation

$$\left(\nabla^2 + k_0\varepsilon(\mathbf{r})\right) E(\mathbf{r}) = j(\mathbf{r}), \tag{3.1}$$

where E is the electric field and $k_0 = \omega/c$, with ω being the frequency of the incident field, c is the speed of light and j is source term, here in a form of the electric current distribution. A closed solution of (3.1) is possible only for a number of simple permittivity profiles, but not for a general random ε. In order to get an approximate solution of an inhomogeneous equation we need to build a Green's function for (3.1), which is a solution of the equation

$$\nabla^2 G(\mathbf{r}_0, \mathbf{r}) + \varepsilon(\mathbf{r})\, k_0^2\, G(\mathbf{r_0}, \mathbf{r}) = \delta(\mathbf{r}_0 - \mathbf{r}), \tag{3.2}$$

where $\delta(\mathbf{r_0} - \mathbf{r})$ is a Dirac-delta. When the Green's function is found the field can be expressed as

$$E(\mathbf{r}) = \int G(\mathbf{r}, \mathbf{r}') j(\mathbf{r}') d\mathbf{r}'. \tag{3.3}$$

Equation (3.2) can be rewritten in the form

$$\nabla^2 G(\mathbf{r}_0, \mathbf{r}) + k_0^2\, G(\mathbf{r}_0, \mathbf{r}) = \delta(\mathbf{r}_0 - \mathbf{r}) + \, k_0^2\, (1 - \varepsilon(\mathbf{r})) G(\mathbf{r}_0, \mathbf{r}). \tag{3.4}$$

The right hand side of this expression can be treated as a source term, while the left hand side is a well known free space Helmholtz equation, for which the Green's function in 3D space is

$$G_0(\mathbf{r}_0, \mathbf{r}) = -\frac{e^{ik_0|\mathbf{r}_0 - \mathbf{r}|}}{4\pi|\mathbf{r}_0 - \mathbf{r}|}. \tag{3.5}$$

Using (3.3), the solution of Eq. (3.4) can be written as

$$G(\mathbf{r}_0, \mathbf{r}) = G_0(\mathbf{r}_0, \mathbf{r}) + \int G_0(\mathbf{r}_0, \mathbf{r}_1) V(\mathbf{r}_1) G(\mathbf{r}_1, \mathbf{r}) d\mathbf{r}_1, \tag{3.6}$$

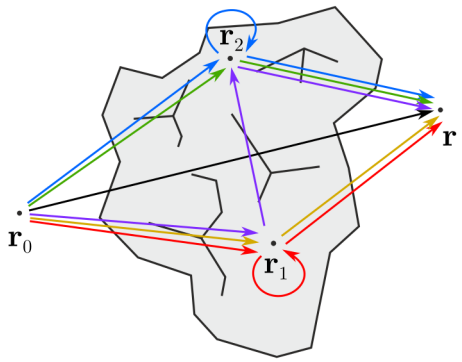

Figure 3.1: Multiple scattering process. The total Green's function is a sum of the terms describing each possible combination of the scattering events, including the recurrent paths (shown by the loops).

where $V(\mathbf{r}) = k_0^2(1 - \varepsilon(\mathbf{r}))$, which is known as the Dyson equation [52]. Assuming that $V(\mathbf{r}) \to 0$, it is possible to obtain a perturbative solution to this equation by an iterative procedure

$$\begin{aligned} G(\mathbf{r}, \mathbf{r}_0) = G_0(\mathbf{r}, \mathbf{r}_0) + \int G_0(\mathbf{r}_0, \mathbf{r}_1) V(\mathbf{r}_1) G_0(\mathbf{r}_1, \mathbf{r}) d\mathbf{r}_1 + \\ + \int G_0(\mathbf{r}_0, \mathbf{r}_1) V(\mathbf{r}_1) G_0(\mathbf{r}_1, \mathbf{r}_2) V(\mathbf{r}_2) G_0(\mathbf{r}_2, \mathbf{r}) d\mathbf{r}_1 d\mathbf{r}_2 + \\ + \int G_0(\mathbf{r}_0, \mathbf{r}_1) V(\mathbf{r}_1) G_0(\mathbf{r}_1, \mathbf{r}_2) V(\mathbf{r}_2) G_0(\mathbf{r}_2, \mathbf{r}_3) V(\mathbf{r}_3) G_0(\mathbf{r}_3, \mathbf{r}) d\mathbf{r}_1 d\mathbf{r}_2 d\mathbf{r}_3 + \dots, \end{aligned} \tag{3.7}$$

where each term has a simple physical interpretation of a scattering path, in which the scattering occurs at the points $\mathbf{r}_1, \mathbf{r}_2, \dots$, as shown in Fig. 3.1. This equation has an infinite number of terms and diagramatic notation is often used to compress the written form of such equations and improve their readability. The free-space Green's function $G_0(\mathbf{r}, \mathbf{r}_0)$ is denoted with a straight thin solid line, and its conjugate is denoted with a thin dashed line[1]

$$G_0(\mathbf{r}, \mathbf{r}_0) \to \text{——} \; ; \quad G_0^*(\mathbf{r}, \mathbf{r}_0) \to \text{- - - -} \tag{3.8}$$

the effective scattering potential $V(\mathbf{r})$ is denoted by a dot

$$V(\mathbf{r}) \to \bullet \; . \tag{3.9}$$

[1]Common convention is that the solid line denotes the retarded Green's function G^R and the dashed denotes the advanced one G^A. When the time evolution is considered G^R is not necessarily equal to G^{A*}. Here we consider stationary picture, therefore $G^R = G^{A*}$ and we omit the upper index, assuming G to describe transport from left to right and G^* is the opposite direction.

When a single scattering event enters the same diagram multiple times a dotted arc is used to denote the same scattering location (here at the point $\mathbf{r}_\mathrm{s}$)

$$V(\mathbf{r}-\mathbf{r}_\mathrm{s})V(\mathbf{r}'-\mathbf{r}_\mathrm{s}) \rightarrow \bullet\overset{\frown}{\bullet}\bullet \,, \tag{3.10}$$

In such a notation (3.7) can be written as

$$G(\mathbf{r},\mathbf{r}_0) = \text{——} + \text{—•—} + \text{—•}\overset{\frown}{\bullet}\text{—} + \text{—•—•—} + \tag{3.11}$$

$$+ \text{—}\overset{\frown}{\bullet}\text{—•—} + \text{—•—}\overset{\frown}{\bullet}\text{—} + \text{—}\overset{\frown}{\bullet}\overset{\frown}{\bullet}\text{—} + \ldots$$

The terms of a type

$$\text{—}\overset{\frown}{\bullet}\text{—} + \text{—}\overset{\frown}{\bullet}\overset{\frown}{\bullet}\text{—} + \text{—}\overset{\frown}{\bullet}\overset{\frown}{\bullet}\overset{\frown}{\bullet}\text{—} + \ldots \tag{3.12}$$

within (3.11) correspond to one scattering event at a certain point. These terms can be arranged into an object called transmission or T-matrix:

$$t(\mathbf{r},\mathbf{r}_0) = \bullet + \bullet\overset{\frown}{\text{——}} + \bullet\overset{\frown}{\text{—•—}} + \ldots \,, \tag{3.13}$$

which in the diagramatic notation is

$$t(\mathbf{r},\mathbf{r}_0) \rightarrow \times. \tag{3.14}$$

This construction describes the interaction of the field with a single scatterer containing all the recursive terms, i. e. the initial scattered field, the scattered field scattered once again and so on. When a single object is considered, (3.11) transforms into

$$G(\mathbf{r},\mathbf{r}_0) = \text{——} + \text{—×—} \,, \tag{3.15}$$

where the first term is again the free space propagation from $\mathbf{r}$ to $\mathbf{r}_0$, and the second term reflects the interaction of the scatterer with the incident field. This equation still has infinitely many terms due to a recurrent nature of this interaction: the scatterer modifies the incident wave, and that, in its turn, modifies the effective field exciting the

scatterer. In terms of the T-matrix (3.11) can be rewritten as

$G(\mathbf{r}, \mathbf{r}_0) =$ 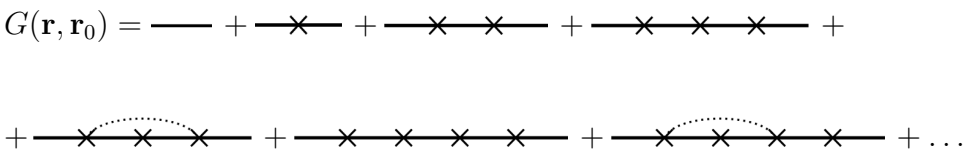 (3.16)

Despite being important for fundamental understanding of the multiple scattering process, the expression above is still far from being practically useful. It is more compact than (3.11), since the terms referring to each single scattering are arranged into the t-matrix, but there is still an infinite number of them, moreover the whole series converges only in the limit of $V(\mathbf{r}) \to 0$ unless special effort is given to ensure its convergence [53]. Secondly, the solution of this equation depends on the position of every scattering event in the medium. As we already mentioned, often we do not have such a knowledge, or even if we do, it is more convenient to assume that these positions are random and consider the statistical properties of the scattered field. In that scenario $G(\mathbf{r}, \mathbf{r}_0)$ becomes random as well, changing from one realization of disorder to another. Although its single realization does not carry important information being effectively a random variable, averaging this function over different realizations of the disorder (positions of the scatterers) is the starting point of the statistical description of the field, which we review in the next section.

3.1.2 Model of the disordered medium

As we mentioned earlier, the disorder is included in (3.16) by means of randomly varying permittivity $\varepsilon(\mathbf{r})$, or the scattering potential $V(\mathbf{r})$. These can be spatially continuous random functions, as in the case of atmospheric turbulence description, in which case the scattering occurs at each point where $\varepsilon(\mathbf{r}) \neq \text{const}$. However, more often multiple scattering occurs in the systems which contain a large number of discrete localized (subwavelength) impurities at random positions. As we will show in the following section the second (discrete) model of the scattering medium is equivalent to the continuous one in a particular limit.

Let's consider $V(\mathbf{r})$ being a continuous Gaussian random potential with 0 mean, and correlation function $\mathcal{B}$

$$\langle V(\mathbf{r}) \rangle = 0,$$
$$\langle V(\mathbf{r}) V(\mathbf{r}') \rangle = \mathcal{B}(\mathbf{r} - \mathbf{r}'), \tag{3.17}$$

where $\langle A\rangle = \int A\mathcal{P}[V(\mathbf{r})]\mathcal{D}V(\mathbf{r})$ and

$$\mathcal{P}[V(\mathbf{r})] = \frac{1}{\mathcal{Z}} e^{-\frac{1}{2}\int V(\mathbf{r})\kappa(\mathbf{r}-\mathbf{r}')V(\mathbf{r}')d\mathbf{r}d\mathbf{r}'} \tag{3.18}$$

is a generalized Gaussian probability distribution function with $\kappa(\mathbf{r}-\boldsymbol{\rho})$ such, that

$$\int \mathcal{B}(\mathbf{r}'-\boldsymbol{\rho})\kappa(\mathbf{r}-\boldsymbol{\rho})d\boldsymbol{\rho} = \delta(\mathbf{r}-\mathbf{r}'), \tag{3.19}$$

and $\mathcal{Z}$ being the normalization constant. The moment generation functional of this probability density is

$$\mathbf{\Phi}_G[f] = e^{-\frac{1}{2}\int f(\mathbf{r})\mathcal{B}(\mathbf{r}-\mathbf{r}')f(\mathbf{r}')d\mathbf{r}d\mathbf{r}'}, \tag{3.20}$$

from which it follows that the cumulants [54]

$$\langle V(\mathbf{r}_1)\dots V(\mathbf{r}_n)\rangle_c = \left.\frac{\delta^n \ln(\mathbf{\Phi}[f])}{\delta f(\mathbf{r}_1)\dots\delta f(\mathbf{r}_n)}\right|_{f=0} \tag{3.21}$$

of any order except $n = 2$ are zero, while the second order cumulant $\langle V(\mathbf{r})V(\mathbf{r}')\rangle_c = \langle V(\mathbf{r})V(\mathbf{r}')\rangle = \mathcal{B}(\mathbf{r}-\mathbf{r}')$. Such a description of the disorder is known as the Gaussian model [55], which refers to the situation of the scattering potential being random continuous function of position. Let's now consider the case in which scattering occurs at the localized microscopic impurities. The scattering potential in this situation is

$$V_p(\mathbf{r}) = \sum_i^{\mathcal{N}_\mathrm{s}} V_0(\mathbf{r}-\mathbf{r}_i), \tag{3.22}$$

where $\mathcal{N}_\mathrm{s}$ is the number of scatterers and V_0 is the scattering potential of each individual impurity. We assume that the positions of the scatterers are distributed according to the Poisson law, for which the moment generation functional is [56]

$$\mathbf{\Phi}_P[f] = \frac{1}{\mathcal{V}}\int \exp\left(\sum_j^{\mathcal{N}_\mathrm{s}}\int f(\mathbf{r}')V_0(\mathbf{r}_j-\mathbf{r}')d\mathbf{r}'\right)d\mathbf{r}_1\dots d\mathbf{r}_{\mathcal{N}_\mathrm{s}}, \tag{3.23}$$

where $\mathcal{V}$ is the volume of the sample. This functional can be written in the form

$$\mathbf{\Phi}_P[f] = \left(\frac{1}{\mathcal{V}}\int e^{\mathscr{F}(\mathbf{r})}d\mathbf{r}\right)^{\mathcal{N}_\mathrm{s}} = \left(1+\frac{n_\mathrm{s}}{\mathcal{N}_\mathrm{s}}\int(e^{\mathscr{F}(\mathbf{r})}-1)d\mathbf{r}\right)^{\mathcal{N}_\mathrm{s}}, \tag{3.24}$$

where $\mathscr{F}(\mathbf{r}) = \int f(\mathbf{r}')V_0(\mathbf{r}_j-\mathbf{r}')d\mathbf{r}'$ and $n_\mathrm{s} = \mathcal{N}_\mathrm{s}/\mathcal{V}$ is the density of the scatterers.

Taking a limit of $\mathcal{V}$ and $\mathcal{N}_\mathrm{s} \to \infty$ (so that n_s remains constant) we obtain

$$\mathbf{\Phi}_P[f] = \exp\left(n_\mathrm{s} \int (e^{\mathscr{F}(\mathbf{r})} - 1) d\mathbf{r}\right), \tag{3.25}$$

from which, using (3.21), we can get the cumulants

$$\langle V_p(\mathbf{r}_1)\rangle_c = n_\mathrm{s} \int V_0(\mathbf{r} - \mathbf{r}_1) d\mathbf{r}, \tag{3.26}$$

$$\langle V_p(\mathbf{r}_1) V_p(\mathbf{r}_2)\rangle_c = n_\mathrm{s} \int V_0(\mathbf{r} - \mathbf{r}_1) V_0(\mathbf{r} - \mathbf{r}_2) d\mathbf{r}, \tag{3.27}$$

$$\langle V_p(\mathbf{r}) \dots V_p(\mathbf{r}_n)\rangle_c = n_\mathrm{s} \int V_0(\mathbf{r} - \mathbf{r}_1) \dots V_0(\mathbf{r} - \mathbf{r}_n) d\mathbf{r}_1 \dots d\mathbf{r}_n, \tag{3.28}$$

If we take a limit of $n_\mathrm{s} \to \infty$ and $V_0(\mathbf{r}) \to 0$, which refers to a high density of weakly scattering impurities, the cumulants of the orders higher than 2 vanish and upon subtracting a constant background we recover the Gaussian model with the effective correlation function

$$\mathcal{B}(\mathbf{r} - \mathbf{r}') = n_\mathrm{s} \int V_0(\boldsymbol{\rho} - \mathbf{r}) V_0(\boldsymbol{\rho} - \mathbf{r}') d\boldsymbol{\rho}, \tag{3.29}$$

Due to the equivalence of these two models we will further assume that even in the case when the refractive index is a random continuous function of position, the scattering of the incoming wave occurs at the spatially separated discrete impurities. In order to further simplify the description we will assume that the single impurity potential is a delta function $V_0(\mathbf{r}) = v_0 \delta(\mathbf{r})$, where v_0 is a constant, characterizing the scattering strength. In that case

$$V_p(\mathbf{r}) = \sum_i^{\mathcal{N}_\mathrm{s}} v_0 \delta(\mathbf{r} - \mathbf{r}_i), \tag{3.30}$$

and the correlation function is

$$\mathcal{B}(\mathbf{r} - \mathbf{r}') = n_\mathrm{s} v_0^2 \delta(\mathbf{r} - \mathbf{r}'). \tag{3.31}$$

Upon the disorder averaging some terms in (3.11) vanish, which can be clearly seen considering Eq. (3.7). Averaging the terms of the series on the right hand side of this expression gives different moments of $V(\mathbf{r})$ under the integrals. The terms containing odd moments vanish due to the properties of the Gaussian function with 0 average. And the moments of the order higher than 2 can be expressed as a sum of products of the

2-nd order moments, for example

$$\langle V(\mathbf{r}_1)V(\mathbf{r}_2)V(\mathbf{r}_3)V(\mathbf{r}_4)\rangle = \langle V(\mathbf{r}_1)V(\mathbf{r}_2)\rangle\langle V(\mathbf{r}_3)V(\mathbf{r}_4)\rangle + \\ + \langle V(\mathbf{r}_1)V(\mathbf{r}_3)\rangle\langle V(\mathbf{r}_2)V(\mathbf{r}_4)\rangle + \langle V(\mathbf{r}_1)V(\mathbf{r}_4)\rangle\langle V(\mathbf{r}_2)V(\mathbf{r}_3)\rangle \tag{3.32}$$

which significantly simplifies the description.

3.1.3 Averaged Green's function

In the diagramatic notation, the expression for the averaged Green's function is

$\langle G(\mathbf{r}, \mathbf{r}_0)\rangle =$ 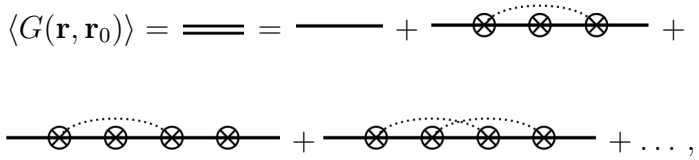 (3.33)

where $\otimes$ is the average of the t matrix. Eq. (3.33) can be written in a more compact form

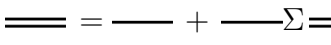 (3.34)

where

$\Sigma =$ 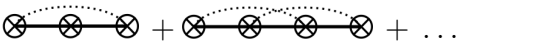 (3.35)

is the sum of the diagrams, which is impossible to break apart without cutting a dotted line (called irreducible). The diagrams that can be cut in such a way are called reducible and can be expressed in terms of irreducible diagrams, which leads to pre-factors in front of the irreducible terms, which are included in the expression for Σ. This quantity is called self-energy and in the context of high energy physics it refers to the part of the particle's energy appearing due to its interaction with the field perturbation created by itself. Here it refers to the part of the electromagnetic field appearing due to the interaction of the scattered light with the scatterers.

Expression (3.35) is another form of the Dyson equation (3.6). This equation can be solved by Fourier transforming both sides, which leads to the expression

$$\langle G(\mathbf{k})\rangle = G_0(\mathbf{k}) + G_0(\mathbf{k})\Sigma(k_0)\langle G(\mathbf{k})\rangle, \tag{3.36}$$

and therefore the Green's function is

$$\langle G(\mathbf{k})\rangle = \frac{1}{G_0^{-1}(\mathbf{k}) - \Sigma(k_0)} \tag{3.37}$$

It means that the problem of finding the averaged Green's function is equivalent to the calculation of the self-energy. This is a very complicated problem, which is intractable in full generality, unless certain approximations are accepted.

Firstly, we neglect all the interference terms between successive collisions in the expression for the self-energy, keeping just the first term $\Sigma \approx \otimes \approx \mathcal{N}_\mathrm{s}\times$ (independent scattering approximation), which can be done assuming the disorder is not too strong. In this approximation the scatterers interact effectively as independent dipoles. As we already know, the disorder strength is characterized by the mean free path, which can be expressed in terms of the properties of the scattering potential

$$\ell = \frac{4\pi}{\langle \mathcal{B}(\mathbf{r} - \mathbf{r}')\rangle}. \tag{3.38}$$

Weak disorder means that the mean free path is much greater than the wavelength of the incident light ($k_0\ell \gg 1$).

One more simplification is that in the expression for the t-matrix we keep only the first two terms, which is called Born approximation. Physically it means that only initially scattered field is taken into consideration during each scattering event, and this initially scattered field does not influence the scatterer any more. The scattering matrix for the potential (3.30) in the Born approximation is

$$t \approx v_0 + \frac{iv_0^2 k_0}{4\pi}. \tag{3.39}$$

Using (3.38) it is possible to relate the t matrix to the macroscopic properties of the scattering medium, i.e. mean free path. In the Born approximation

$$\langle \mathcal{B}(\mathbf{r} - \mathbf{r}')\rangle = 4\pi\mathcal{N}_\mathrm{s}\sigma_\mathrm{B} \tag{3.40}$$

where σ_B is the scattering cross-section, which characterises how much light is deflected from the incident beam into different directions. For the potential (3.30) the scattering cross-section is [56]

$$\sigma_B = \frac{v_0^2}{4\pi} = \frac{\Im(t)}{k_0}, \tag{3.41}$$

where $\Im(t)$ is the imaginary part of (3.39). This expression was obtained taking the limit of $\mathcal{N}_\mathrm{s} \to \infty$ and $v_0 \to 0$, which naturally agrees with the domain of validity of the

Born's approximation and the disorder models introduced in the previous section. The mean free path can be written

$$\ell = \frac{k_0}{\mathcal{N}_\mathrm{s}\Im(t)} = \frac{4\pi}{\mathcal{N}_\mathrm{s}v_0^2}. \tag{3.42}$$

Substitution of t and ℓ to Eq. (3.36) leads to the following expression for the averaged Green's function

$$\langle G(\mathbf{k})\rangle = \frac{1}{k_0^2 - \mathbf{k}^2 - \mathcal{N}_\mathrm{s}t} \approx \frac{1}{k_0^2 - \mathbf{k}^2 - i\frac{k_0}{\ell}}, \tag{3.43}$$

or in the real space

$$\langle G(\mathbf{r}_0, \mathbf{r})\rangle = \frac{e^{iK|\mathbf{r}_0 - \mathbf{r}|}}{4\pi|\mathbf{r}_0 - \mathbf{r}|}, \tag{3.44}$$

where $K = \sqrt{k_0^2 + \mathcal{N}_\mathrm{s}t} \approx \sqrt{k_0^2 + \mathcal{N}_\mathrm{s}v_0} + i/2\ell \approx k_0 + i/2\ell$. This expression resembles the free-space Green's function G_0, however firstly the real part of K acts as a modification of the medium refractive index, and also the imaginary part of K adds an effective field damping, characterized by ℓ, which happens because of the energy transfer from the incident beam to the scattered waves. We also stress that (3.44) describes the average Green's function, and the exponential decay appears only after averaging over disorder, occurring because of the dephasing of the non-averaged Green's functions corresponding to different disorder realizations.

3.1.4 Average intensity

The next step is to calculate the average intensity

$$\langle I(\mathbf{r})\rangle = \langle G(\mathbf{r}_0, \mathbf{r})G^*(\mathbf{r}, \mathbf{r}_0)\rangle, \tag{3.45}$$

which is an average of a product of two Green's functions (3.16). We define an object called intensity propagator as

$$\mathfrak{P}(\mathbf{r}, \mathbf{r}') = \langle G(\mathbf{r}, \mathbf{r}')G^*(\mathbf{r}', \mathbf{r})\rangle. \tag{3.46}$$

An equation for $\mathfrak{P}$ is obtained by multiplying Eq. (3.7) by its complex conjugate and taking the average

$$\begin{aligned}\mathfrak{P}(\mathbf{r}, \mathbf{r}') = \mathfrak{P}_0(\mathbf{r}, \mathbf{r}') + \mathfrak{P}_\mathrm{D}(\mathbf{r}, \mathbf{r}') = \langle G(\mathbf{r}, \mathbf{r}')G^*(\mathbf{r}', \mathbf{r})\rangle + \\ + \int \langle G(\mathbf{r}, \mathbf{r}_1)G^*(\mathbf{r}', \mathbf{r}_2)\rangle \Gamma(\mathbf{r}_1, \mathbf{r}_2, \mathbf{r}_3, \mathbf{r}_4)\langle G(\mathbf{r}, \mathbf{r}_3)G^*(\mathbf{r}', \mathbf{r}_4)\rangle d\mathbf{r}_1 d\mathbf{r}_2 d\mathbf{r}_3 d\mathbf{r}_4,\end{aligned} \tag{3.47}$$

where the first term, $\mathfrak{P}_0$, is the part of the incident beam that travels through the medium without any collision (it deceases exponentially with ℓ), while the second term, $\mathfrak{P}_D$ refers to the intensity of the scattered field, where Γ is a combination of the random potential cumulants called irreducible vertex. In the diagramatic notation it is

$\Gamma =$ 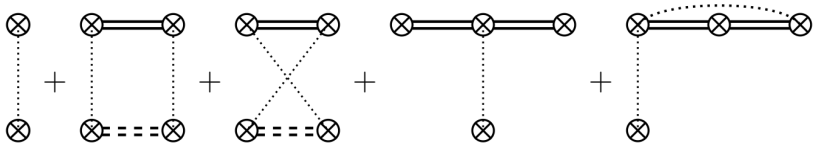 $+ \dots ,$ (3.48)

where double dashed line is $\langle G^*(\mathbf{r}, \mathbf{r}_0)\rangle$, which represents pairing of the diagrams in the advanced and retarded Green's functions expansions, here expressed in terms of the averaged scattering matrix. In addition, the relations between Γ and Σ can be established by means of the Ward identity [52].

The intensity can be calculated as

$$\langle I(\mathbf{r})\rangle = I_0(\mathbf{r}) + I_D(\mathbf{r}) = \mathfrak{P}(\mathbf{r}_0, \mathbf{r}) = \mathfrak{P}_0(\mathbf{r}_0, \mathbf{r}) + \mathfrak{P}_D(\mathbf{r}_0, \mathbf{r}) \tag{3.49}$$

Expression (3.47) is known as the Bethe-Salpeter equation, which in context of high-energy physics describes bound states of a many-body system [52]. As in the situation with Dyson equation, the exact solution of this equation is unattainable and we have to use the independent scattering approximation, i.e. neglect all the successive scattering diagrams, which can be done if the disorder is not too strong. In this approximation all the collisions will be at least ℓ apart, which means that the scattering paths following different sets of scattering events will have a difference in length of at least ℓ. As $\ell \gg \lambda$, such paths will accumulate a phase difference between G and G^* and therefore will vanish upon averaging, while the ones that follow the same scattering sequences will remain (see Fig. 3.2a). The terms remaining in Γ upon this approximation describe such scattering sequences and visually resemble a ladder, that is why this situation is called the *ladder approximation*:

$\Gamma \approx \mathscr{L} =$ 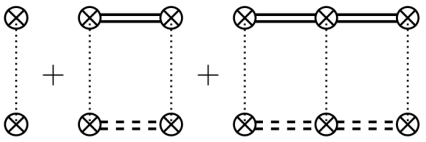 $+ \dots ,$ (3.50)

where $\mathscr{L}$ is called the ladder operator. Under this approximation (3.47) becomes

$$\mathfrak{P}_{\mathrm{D}}(\mathbf{r}, \mathbf{r}') = \int \mathfrak{P}_0(\mathbf{r}, \mathbf{r}_1)\mathscr{L}(\mathbf{r}_1, \mathbf{r}_2)\mathfrak{P}_0(\mathbf{r}_2, \mathbf{r}')d\mathbf{r}_1 d\mathbf{r}_2, \tag{3.51}$$

where the first term under the integral describes the propagation from some point $\mathbf{r}$ to

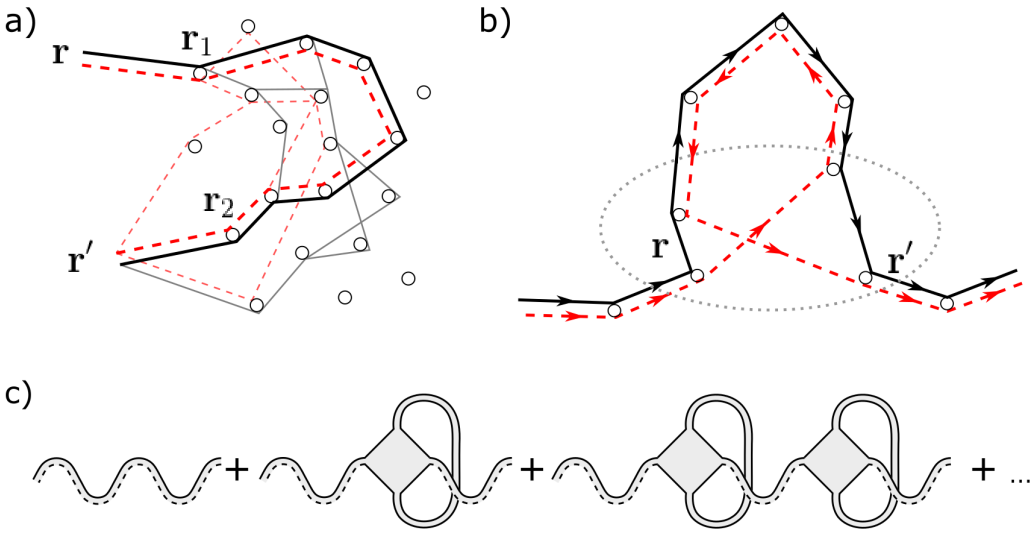

Figure 3.2: a) Propagation of light in a scattering medium in ladder approximation. All the scattering sequences where advanced and retarded Green's functions do not follow the same scattering events (grey and light red lines) accumulate a random phase between these contributions and therefore vanish upon disorder averaging. b) Ladder approximation also allows the paths in which advanced and retarded Green's functions propagate in the opposite directions (shown by errors). A crossing of Green's functions is required for that, which is described by a Hikami vertex (3.57-59). c) Average intensity as a perturbative series. First order term is an average over all possible pairs of paths as in panel a, first order correction involves a crossing as in panel b, higher order terms contain additional crossings.

the point of the first collision $\mathbf{r}_1$, $\mathscr{L}$ takes into account all the possible scattering events between $\mathbf{r}_1$ and $\mathbf{r}_2$ (because we integrate over these points) and finally the last terms describes propagation from $\mathbf{r}_2$ to $\mathbf{r}'$, as in Fig. 3.2a. Diagramatically we denote

$$\mathscr{L}(\mathbf{r}_1, \mathbf{r}_2) = \mathbf{r}_1 \text{ - - - } \mathbf{r}_2. \tag{3.52}$$

In order to complete the intensity transport description we need to specify $\mathscr{L}$, which depends on the disorder model and on the configuration of the experiment. For the case of scattering potential (3.30) we can rewrite (3.51) as

$$\mathscr{L}(\mathbf{r}_1, \mathbf{r}_2) = \frac{4\pi}{\ell}\delta(\mathbf{r}_1 - \mathbf{r}_2) + \frac{4\pi}{\ell}\int \mathfrak{P}_0(\mathbf{r}', \mathbf{r}_2)\mathscr{L}(\mathbf{r}_1, \mathbf{r}')d\mathbf{r}'. \tag{3.53}$$

Now, assuming the number of scattering events in the ladder is large, the spatial variation of $\mathscr{L}$ on the scale of ℓ are small, therefore we can expand $\mathscr{L}(\mathbf{r}', \mathbf{r}_1)$ from (3.53)

around $\mathbf{r}' = \mathbf{r}_2$.

$$\mathscr{L}(\mathbf{r}', \mathbf{r}_1) = \mathscr{L}(\mathbf{r}_1, \mathbf{r}_2) + (\mathbf{r}' - \mathbf{r}_2)\nabla_{\mathbf{r}_2}\mathscr{L}(\mathbf{r}_1, \mathbf{r}_2) + \frac{1}{2}\left[(\mathbf{r}' - \mathbf{r}_2)\nabla_{\mathbf{r}_2}\right]^2 \mathscr{L}(\mathbf{r}_1, \mathbf{r}_2) + \dots . \tag{3.54}$$

Upon substitution back to (3.53) $\mathscr{L}$ no longer depends on the integration variable and can be pulled out of the integral,

$$\begin{aligned} \mathscr{L}(\mathbf{r}_1, \mathbf{r}_2) &= \frac{4\pi}{\ell}\delta(\mathbf{r}_1 - \mathbf{r}_2) + \frac{4\pi}{\ell}\Big[\mathscr{L}(\mathbf{r}_1, \mathbf{r}_2)\int \mathfrak{P}_0(\mathbf{r}', \mathbf{r}_2)d\mathbf{r}' + \\ &+ \nabla_{\mathbf{r}_2}\mathscr{L}(\mathbf{r}_1, \mathbf{r}_2)\int (\mathbf{r}' - \mathbf{r}_2)\,\mathfrak{P}_0(\mathbf{r}', \mathbf{r}_2)d\mathbf{r}' + \\ &+ \frac{1}{2}\nabla^2_{\mathbf{r}_2}\mathscr{L}(\mathbf{r}_1, \mathbf{r}_2)\int (\mathbf{r}' - \mathbf{r}_2)^2\,\mathfrak{P}_0(\mathbf{r}', \mathbf{r}_2)d\mathbf{r}'\Big]. \end{aligned} \tag{3.55}$$

The expressions remaining under the integrals will contain combinations of the average Green's functions as in (3.44) and can be easily calculated leading to [55]

$$-(i\omega + \mathscr{D}\nabla^2_{\mathbf{r}_2})\mathscr{L}(\mathbf{r}_1, \mathbf{r}_2) = \frac{4\pi c}{\ell^2}\delta(\mathbf{r}_1 - \mathbf{r}_2), \tag{3.56}$$

with $\mathscr{D} = c\ell/3$, which is a diffusion equation. $\mathscr{L}$ is therefore a solution of a diffusion equation, the configuration of the scattering target enters this equation in the form of boundary conditions for $\mathscr{L}$ and the properties of the scattering material in the form of the diffusion constant $\mathscr{D}$. In addition as $\mathscr{L}$ varies much slower than $\mathfrak{P}_0$ in (3.51), it can be pulled out of the integral

$$\mathfrak{P}_{\mathrm{D}}(\mathbf{r}, \mathbf{r}') = \mathscr{L}(\mathbf{r}, \mathbf{r}')\int \mathfrak{P}_0(\mathbf{r}, \mathbf{r}_1)\mathfrak{P}_0(\mathbf{r}_2, \mathbf{r}')d\mathbf{r}_1 d\mathbf{r}_2 = \frac{\ell^2}{4\pi}\mathscr{L}(\mathbf{r}, \mathbf{r}'), \tag{3.57}$$

$$I_{\mathrm{D}}(\mathbf{r}) = \frac{\ell^2}{4\pi}\mathscr{L}(\mathbf{r_0}, \mathbf{r}). \tag{3.58}$$

Therefore in the diffusive approximation the intensity propagator and the intensity itself are proportional to the ladder operator.

Independent scattering approximation leading to the ladder diagrams works in a broad range of experimental conditions, however it is easy to find examples of the phenomena going beyond this model. Examples of such phenomena are weak localization [57], coherent backscattering [58], mesoscopic conductance fluctuations [58] and, actually, speckle correlations [20, 22, 55], which are the subject of the current work. The first correction for the ladder approximation involves processes described in Fig. 3.2b. As can be seen from this figure, the conditions following from the independent scatter-

ing approximation are still satisfied, i.e. Green's functions follow the same scattering events, however now the retarded and advanced Green's functions travel in the opposite directions, as indicated by the arrows. Formally such process is described by a set of *maximally crossed* diagrams, which we arrange into an operator

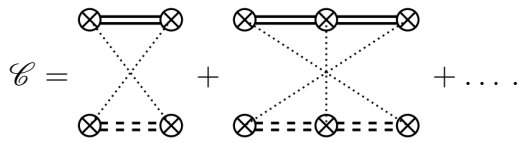

(3.59)

The total intensity can be represented as a series as in Fig. 3.2c. The first term of this expression corresponds to diffusive propagation, while the second contains a crossing of the diffusion path with itself, the loop being a described by (3.59). The volume in which the crossing occurs (dashed oval in the figure) is denoted by a square in the diagrams, and has a name of the Hikami box [59]. The diagrams as in Fig. 3.2c. are important for the case of the amorphous conductors leading to a correction of their electrical resistivity at low temperatures, which is known as weak localization [57]. In the case of the optical fields such corrections are negligible, however interesting effects may occur when two *different* diffusion paths cross entering a Hikami box. This leads to long-range correlations in the light scattered by the disordered materials, which we consider in the next section.

3.2 Correlations in speckle patterns

3.2.1 Correlation function

Diffusive propagation successfully describes the transport of the average intensity through the disordered materials. However, as we know, when a coherent wave interacts with a scattering medium, it forms speckle patterns, in which the intensity can fluctuate dramatically about its average value, dropping almost to 0 or reaching ten times the average in some points. In order to describe that behaviour we need to take into account correlations between the fields in different spatial points.

The starting point of the description of the correlations between the scattered fields is a modification of (3.47) where all the fields are taken in different spatial points.

$$\langle I(\mathbf{r})I(\mathbf{r}')\rangle = \langle G(\mathbf{r},\mathbf{r}_0)G^*(\mathbf{r},\mathbf{r}_0)G(\mathbf{r}',\mathbf{r}_0)G^*(\mathbf{r}',\mathbf{r}_0)\rangle. \tag{3.60}$$

Formally one would need to solve an equation analogous to (3.47) for this quantity, which is again impossible in full generality. Even when the ladder approximation, which

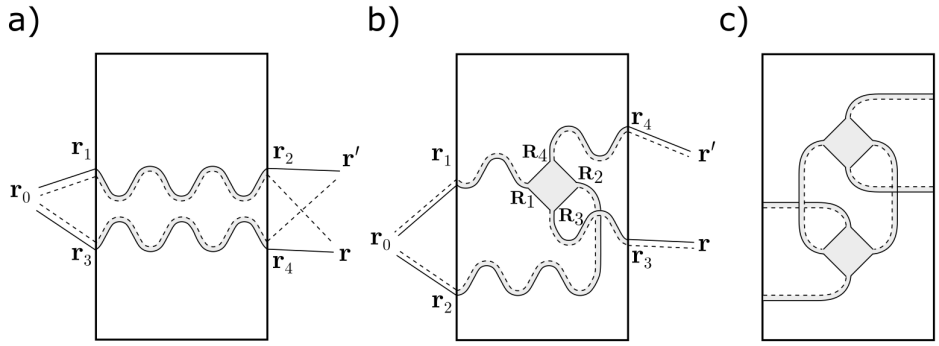

Figure 3.3: Diagrams corresponding to different terms in the correlation function (3.62). a) Short-range C_1 contribution. b) Long-range C_2 contribution. c) One of the diagrams leading to the infinite range C_3 contribution.

we used to obtain the average intensity, is adopted, things do not simplify a lot. The resulting expression involves interaction between two ladder operators, which in its turn depend on the experiment geometry. A common strategy is to identify the contributions relevant for a given experiment configuration and then to get the correlation function evaluating the diagrams referring to them. For that purpose $\langle I(\mathbf{r})I(\mathbf{r}')\rangle$ is conventionally represented as [19]

$$\langle I(\mathbf{r})I(\mathbf{r}')\rangle = \langle I(\mathbf{r})\rangle\langle I(\mathbf{r}')\rangle\left(1 + C_1(\mathbf{r},\mathbf{r}') + C_2(\mathbf{r},\mathbf{r}') + C_3(\mathbf{r},\mathbf{r}')\right). \tag{3.61}$$

The first term in this expression refers to uncorrelated diffusive intensity transport, while the total correlation function

$$C(\mathbf{r},\mathbf{r}') = \frac{\langle I(\mathbf{r})I(\mathbf{r}')\rangle}{\langle I(\mathbf{r})\rangle\langle I(\mathbf{r}')\rangle} - 1 = C_1(\mathbf{r},\mathbf{r}') + C_2(\mathbf{r},\mathbf{r}') + C_3(\mathbf{r},\mathbf{r}') \tag{3.62}$$

is split into three contributions described by different sets of diagrams and relevant in different experimental configurations. The diagrams corresponding to these terms are presented in Fig. 3.3. The first contribution involves an exchange of the Green's functions between the ladder diagrams at the exit of the scattering medium. This contribution is the strongest in the optical scenario and it relates the points that are not far from each other in space. We will discuss this contribution further in this section. The second contribution, C_2 is central to our discussion and it involves crossing of two diffusion paths within the medium. Such correlation is much weaker than C_1 in the transmission/transmission or reflection/reflection geometry and is usually neglected, except for the cases specifically tailored for their observation [27–31]. However as we will show below, such a contribution is dominant in the case of reflection/transmission correlation.

Finally the C_3, involving 2 diffusion crossings correlates effectively any two points in transmission, however the size of the correlation is so weak that it is relevant only for the measurements of total transmission (conductivity) of disordered conductors, being relevant for the universal conductance fluctuation [58], however it will be negligible for the case of speckle correlations.

We will now focus on the examples of the C_1 and C_2 calculation for the transmission/transmission scenario [22, 60], and will compare these contributions.

3.2.2 Short range contribution

To calculate C_1 we compose an expression analogous to (3.47) for $\langle I(\mathbf{r})I(\mathbf{r}')\rangle$ in (3.60) [61]. We will also immediately use the ladder approximation and replace Γ with $\mathscr{L}$ and $\mathfrak{P}$ with $\mathfrak{P}_0$ in that equation to obtain

$$C_1(\mathbf{r},\mathbf{r}') = \frac{1}{\langle I_T(\mathbf{r})\rangle^2}\int |\langle G(\mathbf{r}_0,\mathbf{r}_1)\rangle|^2|\langle G(\mathbf{r}_0,\mathbf{r}_3)\rangle|^2\mathscr{L}(\mathbf{r}_1,\mathbf{r}_2)\mathscr{L}(\mathbf{r}_3,\mathbf{r}_4) \times\langle G(\mathbf{r}_2,\mathbf{r})\rangle\langle G^*(\mathbf{r}_2,\mathbf{r}')\rangle\langle G(\mathbf{r}_4,\mathbf{r})\rangle\langle G^*(\mathbf{r}_4,\mathbf{r}')\rangle d\mathbf{r}_1 d\mathbf{r}_2 d\mathbf{r}_3 d\mathbf{r}_4, \tag{3.63}$$

where

$$\langle I_T(\mathbf{r})\rangle = \int |\langle G(\mathbf{r}_0,\mathbf{r}_1)\rangle|^2\mathscr{L}(\mathbf{r}_1,\mathbf{r}_2)|\langle G(\mathbf{r},\mathbf{r}_2)\rangle|^2 d\mathbf{r}_1 d\mathbf{r}_2 \tag{3.64}$$

is the average transmitted intensity. We first note that the integrals over $\mathbf{r}_1,\mathbf{r}_2$ and over $\mathbf{r}_3,\mathbf{r}_4$ can be separated, leading to

$$C_1(\mathbf{r},\mathbf{r}') = \left[\frac{1}{\langle I_T(\mathbf{r})\rangle}\int |\langle G(\mathbf{r}_0,\mathbf{r}_1)\rangle|^2\mathscr{L}(\mathbf{r}_1,\mathbf{r}_2)\langle G(\mathbf{r}_2,\mathbf{r})\rangle\langle G^*(\mathbf{r}_2,\mathbf{r}')\rangle d\mathbf{r}_1 d\mathbf{r}_2\right]^2,$$

The next step is similar to what we have done in (3.56) and (3.57). We assume that the expression for the ladder operator varies on a much larger scale than the Green's functions and pull it out of the integrals. Taking into account that $\int |\langle G(\mathbf{r}',\mathbf{r}_2)\rangle|^2 d\mathbf{r}_2 \approx \ell/4\pi$ and $\int\langle G(\mathbf{r},\mathbf{r}_2)\rangle\langle G(\mathbf{r}',\mathbf{r}_2)\rangle d\mathbf{r}_2 = \ell\Im(\langle G(|\mathbf{r}-\mathbf{r}_2)|\rangle)/4\pi$ we can write the average intensity as

$$\langle I_T(\mathbf{r})\rangle = \frac{\ell}{4\pi}\int |\langle G(\mathbf{r}_0,\mathbf{r}_1)\rangle|^2\mathscr{L}(\mathbf{r}_1,\mathbf{r})d\mathbf{r}_1 \tag{3.65}$$

and the correlation function as

$$C_1(\Delta r) = \left[\frac{\sin(k_0\Delta r)}{k_0\Delta r}\right]^2 e^{-\Delta r/\ell}. \tag{3.66}$$

This correlation function is shown in Fig. 3.5a, and it is possible to see that it relates points separated by an order of λ. This correlation is responsible for the granular

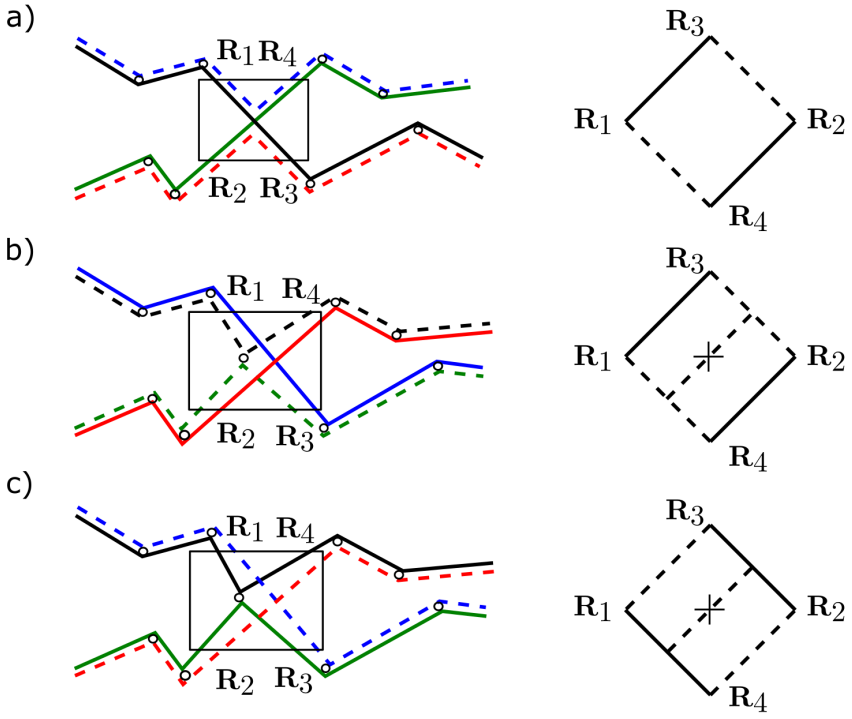

Figure 3.4: Three leading terms in the expression for the Hikami vertex. a) The crossing does not involve a scattering. The diagram corresponds to $\mathscr{H}_A$ (3.67) b) and c) involve one scattering and refer to $\mathscr{H}_B$, (3.68) and $\mathscr{H}_C$, (3.69) respectively.

appearance of the speckle pattern. We also note that this correlation does not depend on the sample configuration, but only on its mean free path.

3.2.3 Long-range correlation

Let's now estimate the C_2 contribution in the same geometry. As we already mentioned C_2 correlation involves crossing of the two diffusion paths. We will consider three variants of how this can happen, as shown in Fig. 3.4. Variant a) does not involve a scattering event during the exchange (the variant when the advanced and retarded Green's functions are exchanged is equivalent), the two other possibilities imply presence of a scatterer, which breaks the symmetry between the advanced and retarded Green's function. As we will see later, each scattering event adds a $1/k_0\ell$ factor in front of the corresponding contribution, therefore the terms involving two or more scattering events are negligible in the weak disorder approximation.

Reading the diagrams in Fig. 3.4a we write the first contribution as

$$\mathscr{H}_A(\{\mathbf{R}_i\}) = \langle G(\mathbf{R}_1,\mathbf{R}_3)\rangle\langle G^*(\mathbf{R}_3,\mathbf{R}_2)\rangle\langle G(\mathbf{R}_2,\mathbf{R}_4)\rangle\langle G^*(\mathbf{R}_4,\mathbf{R}_1)\rangle, \tag{3.67}$$

and the two others are

$$\mathscr{H}_B(\{\mathbf{R}_i\}) = \int \langle G(\mathbf{R}_1,\mathbf{R}_3)\rangle\langle G^*(\mathbf{R}_3,\mathbf{R})\rangle\langle G^*(\mathbf{R},\mathbf{R}_2)\rangle\langle G(\mathbf{R}_2,\mathbf{R}_4)\rangle \times\langle G^*(\mathbf{R}_1,\mathbf{R})\rangle\langle G^*(\mathbf{R},\mathbf{R}_4)\rangle d\{\mathbf{R}_i\}, \tag{3.68}$$

and

$$\mathscr{H}_C(\{\mathbf{R}_i\}) = \int \langle G^*(\mathbf{R}_1,\mathbf{R}_3)\rangle\langle G(\mathbf{R}_3,\mathbf{R})\rangle\langle G(\mathbf{R},\mathbf{R}_2)\rangle\langle G^*(\mathbf{R}_2,\mathbf{R}_4)\rangle \times\langle G(\mathbf{R}_1,\mathbf{R})\rangle\langle G(\mathbf{R},\mathbf{R}_4)\rangle d\{\mathbf{R}_i\}. \tag{3.69}$$

The expression for the C_2 correlation is

$$C_2(\mathbf{r},\mathbf{r}') = \int |\langle G(\mathbf{r}_0,\mathbf{r}_1)\rangle|^2|\langle G(\mathbf{r}_0,\mathbf{r}_2)\rangle|^2\mathscr{L}(\mathbf{r}_1,\mathbf{R}_1)\mathscr{L}(\mathbf{r}_2,\mathbf{R}_2) \tag{3.70}$$

$$\times\mathscr{H}(\{\mathbf{R}_i\})\mathscr{L}(\mathbf{r}_3,\mathbf{R}_3)\mathscr{L}(\mathbf{r}_4,\mathbf{R}_4)|\langle G(\mathbf{r}_3,\mathbf{r})\rangle|^2|\langle G(\mathbf{r}_4,\mathbf{r}')\rangle|^2 d\{\mathbf{r}_i\}d\{\mathbf{R}_i\},$$

where $\mathscr{H} = \mathscr{H}_A + \mathscr{H}_B + \mathscr{H}_C$ is the sum of the Hikami vertex contributions. In this expression the first two Green's function terms under the integral describe free space propagation from the source to the medium boundary, the first pair of ladders describes propagation in the medium before crossing , and the second pair after the crossing, while $\mathscr{H}$ accounts for a crossing. The last two terms describe free space propagation to the observation points.

It is hard to evaluate $\mathscr{H}$ in the real space. In the Fourier space:

$$\mathscr{H}_A(\{\mathbf{q}_i\}) = \delta(\mathbf{q}_1+\mathbf{q}_2+\mathbf{q}_3+\mathbf{q}_4)\int\langle G(\mathbf{p}\rangle\langle G^*(\mathbf{q}_2-\mathbf{p})\rangle \times\langle G(\mathbf{q}_2+\mathbf{q}_3-\mathbf{p})\rangle\langle G^*(\mathbf{p}+\mathbf{q}_1)\rangle d\mathbf{p} \tag{3.71}$$

$$\mathscr{H}_B(\{\mathbf{q}_i\}) = \frac{4\pi}{\ell}\frac{1}{(8\pi)^3}\delta(\mathbf{q}_1+\mathbf{q}_2+\mathbf{q}_3+\mathbf{q}_4)\int\langle G(\mathbf{p}_1\rangle\langle G(\mathbf{p}_2\rangle\langle G^*(\mathbf{q}_1+\mathbf{p}_1)\rangle \times\langle G^*(\mathbf{q}_2-\mathbf{p}_2)\rangle\langle G(\mathbf{p}_2-\mathbf{q}_3-\mathbf{q}_2)\rangle\langle G(\mathbf{p}_1-\mathbf{q}_3-\mathbf{q}_2)\rangle d\mathbf{p}_1 d\mathbf{p}_2 \tag{3.72}$$

and by the symmetry

$$\mathscr{H}_C(\mathbf{r}_1,\mathbf{r}_2,\mathbf{r}_3,\mathbf{r}_4) = \mathscr{H}_B^*(\mathbf{r}_2,\mathbf{r}_3,\mathbf{r}_4,\mathbf{r}_1) \rightarrow \mathscr{H}_C(\mathbf{q}_1,\mathbf{q}_2,\mathbf{q}_3,\mathbf{q}_4) = = \mathscr{H}_B^*(-\mathbf{q}_2,-\mathbf{q}_3,-\mathbf{q}_4,-\mathbf{q}_1) \tag{3.73}$$

In these equations $\mathbf{q}_i$ are the wave vectors of the waves entering the vertex, therefore by

the momentum conservation $\sum_i \mathbf{q}_i = 0$. Using the following approximate expression

$$\langle G(\mathbf{p}+\mathbf{q})\rangle \approx \langle G(\mathbf{p})\rangle - (q^2 + 2\mathbf{p}\cdot\mathbf{q})\langle G(\mathbf{p})\rangle^2 + (2\mathbf{p}\cdot\mathbf{q})\langle G(\mathbf{p})\rangle^3 \tag{3.74}$$

we can transform (3.71) – (3.73) into a set of expressions containing terms:

$$\int \langle G(\mathbf{p})\rangle^n \langle G(\mathbf{p})\rangle^m d\mathbf{p},$$

$$\int \mathbf{p}\cdot\mathbf{q}\langle G(\mathbf{p})\rangle^n \langle G(\mathbf{p})\rangle^m d\mathbf{p},$$

$$\int (\mathbf{p}\cdot\mathbf{q})^2\langle G(\mathbf{p})\rangle^n \langle G(\mathbf{p})\rangle^m d\mathbf{p},$$

which can be evaluated to give

$$\mathscr{H} = h\delta\big(\sum_i \mathbf{q}_i\big)\left[\sum_i q_i^2 + \mathbf{q}_1\cdot\mathbf{q}_2 + \mathbf{q}_2\cdot\mathbf{q}_3 + \mathbf{q}_3\cdot\mathbf{q}_4 + \mathbf{q}_4\cdot\mathbf{q}_1\right], \tag{3.75}$$

with $h = \ell^5/48\pi k^2$. The $\sum_i q_i^2$ term, being a constant in the Fourier space leads to a Dirac-delta function of position in the real space, which is usually neglected, if it does not create divergence [62]. Using the $\sum_i \mathbf{q}_i = 0$ condition we can bring H to the form

$$\mathscr{H} = 2h\delta\big(\sum_i \mathbf{q}_i\big)\mathbf{q}_1\cdot\mathbf{q}_2, \tag{3.76}$$

which after the inverse transform gives

$$\mathscr{H}(\{\mathbf{R}_i\}) = 2h\int \delta(\mathbf{r}-\mathbf{R}_1)\delta(\mathbf{r}-\mathbf{R}_2)\delta(\mathbf{r}-\mathbf{R}_3)\delta(\mathbf{r}-\mathbf{R}_4)\times\nabla_{\mathbf{R}_1}\cdot\nabla_{\mathbf{R}_2}\,d\mathbf{r}, \tag{3.77}$$

containing the gradients to be applied to the incoming ladder operators. It is the final form of H that we substitute to (3.70). In the diffusive limit in (3.70) the exit ladders vary slowly on the scale of ℓ and all the integrals of the single-mode Green's functions $\approx \ell/4\pi$, so using (3.65) Eq. (3.70) can be rewritten as

$$C_2(\mathbf{r},\mathbf{r}') = 2h\int \langle I_T(\mathbf{R})\rangle^2 \nabla_{\mathbf{r}}\mathscr{L}(\mathbf{R},\mathbf{r})\nabla_{\mathbf{r}'}\mathscr{L}(\mathbf{r}',\mathbf{R})d\mathbf{R}. \tag{3.78}$$

The only ingredient we are missing is an expression for the ladder operator $\mathscr{L}$. As we know from (3.56) this operator is the solution of a diffusion equation, so we need to specify the configuration of the scattering target and the boundary conditions. We

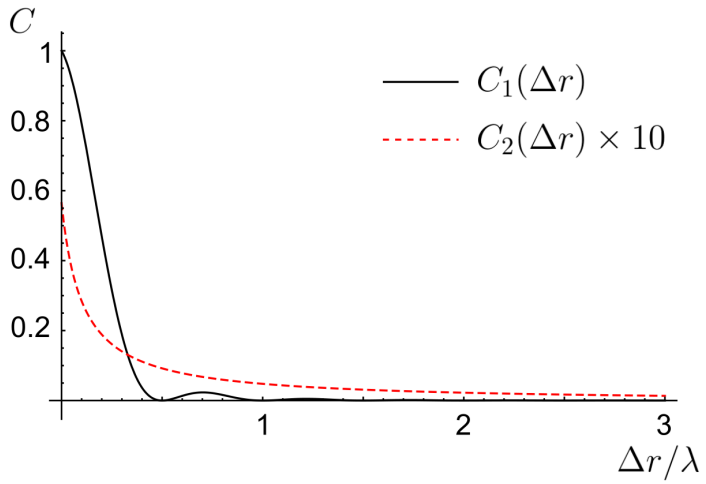

Figure 3.5: Comparison of the short and long-range contributions to the correlation function of the transmitted intensity. The parameters are $L = 10, \ell = 5, \lambda = 1$.

choose the geometry as in Fig. 3.3, a slab of scattering material of the thickness L is illuminated from the left. The boundary conditions impose zero incoming and outgoing flux at left and right, surfaces, which for the purpose of convenience is recast to an equivalent statement of $\mathscr{L} = 0$ at certain distance $z_0 = 2\ell/3$ (extrapolation length) from the slab surfaces. The solution of the diffusion equation for that case is [19]

$$\begin{aligned} &\mathscr{L}(\mathbf{r}_1, \mathbf{r}_2) \to \mathscr{L}(z_1, z_2, \Delta\mathbf{r}) = \mathcal{F}^{-1}\left[\widetilde{\mathscr{L}}(z_1, z_2, \mathbf{k})\right]; \\ &\widetilde{\mathscr{L}}(z_1, z_2, \mathbf{k}) = \frac{12\pi}{\ell^3 \mathbf{k}} \frac{\sinh\left[\mathbf{k}(z_0 + z_1)\right] \sinh\left[\mathbf{k}(z_0 + z_2)\right]}{\sinh\left[\mathbf{k}(L + 2z_0)\right]}, \end{aligned} \tag{3.79}$$

where $\mathcal{F}^{-1}$ is the inverse Fourier transform, $\mathbf{r}_1$ changes only along z direction ($\mathbf{r}_1 \to z_1$) and $\mathbf{r}_2$ is split into z_2, the distance along z and $\Delta\mathbf{r}$, the distance in a perpendicular plane, transformed to $\mathbf{k}$. Substituting the ladder operator to (3.78) and taking into account (3.58) we get

$$C_2(\Delta\mathbf{r}) = \frac{2h}{(2\pi)^2} \int \widetilde{\mathscr{L}}(z, L - \ell, \mathbf{k})^2 \left[\partial z \widetilde{\mathscr{L}}(\ell, z, \mathbf{k}_1)\Big|_{\mathbf{k}_1 = 0}\right]^2 e^{i\mathbf{k}\cdot\Delta\mathbf{r}} dz d\mathbf{k}. \tag{3.80}$$

The scalar product in the exponent $\mathbf{k} \cdot \Delta\mathbf{r} = k\Delta r \cos(\theta)$ integrated over θ leads to a Bessel function $2\pi J_0(\Delta R)$ in (3.80) under the integral, in addition $\widetilde{\mathscr{L}}(z, L - \ell, \mathbf{k}) = \ell \sinh[kz]/\mathscr{D} \sinh[kL]$ and $\partial z \widetilde{\mathscr{L}}(\ell, z, \mathbf{k}_1)\Big|_{\mathbf{k}_1 = 0} = -\ell/L\mathscr{D}$, which leads to the final expression

$$C_2(\Delta\mathbf{r}) = \frac{1}{g} \frac{3}{2\pi L} \left[\frac{L}{\Delta r} + \int_0^\infty \frac{1}{\sinh(k)^2} \left(\frac{\sinh(2k)}{2k} - 1\right)\right] J_0(k\Delta r) dk, \tag{3.81}$$

where $g = \mathcal{N}_s \ell / L = k_0 \ell / 3\pi L$ is the dimensionless conductance. We compare this function to the short-range correlation in Fig. 3.5, from which we can see that it connects the points that are much farther apart, and it also depends on the sample thickness. One more thing to note is that it is much weaker than the C_1 contribution, because of the $1/g$ factor. Each crossing taking part in the correlation diagram reduces its size by a factor of g, which is a large number in the diffusive regime.

3.3 Correlation function between the reflection and transmission

In the previous chapter we presented experimental measurements of the correlation function between the reflected and transmitted speckle patterns. Here our aim is to modify the theory explained in the previous sections to explain (at least qualitatively) the behaviour observed in the experiment.

3.3.1 C_1 in reflection and transmission

We start by computing the C_1-type correlation, given by the diagram in Fig. 3.6a, in order to show that this contribution will be negligible for the conditions in which the experiment was performed. The analytical expression corresponding to the diagram in Fig. 3.6a is

$$\begin{aligned} C_1^{RT}(\mathbf{r}, \mathbf{r}') &= \frac{1}{\langle I_T(\mathbf{r})\rangle \langle I_R(\mathbf{r})\rangle} \int |\langle G(\mathbf{r}_0, \mathbf{r}_1)\rangle|^2 |\langle G(\mathbf{r}_0, \mathbf{r}_3)\rangle|^2 \\ &\times \mathscr{L}(\mathbf{r}_1, \mathbf{r}_2) \mathscr{L}(\mathbf{r}_3, \mathbf{r}_4) \langle G(\mathbf{r}_2, \mathbf{r}^R)\rangle \langle G^*(\mathbf{r}_2, \mathbf{r}^T)\rangle \langle G(\mathbf{r}_4, \mathbf{r}^T)\rangle \langle G^*(\mathbf{r}_4, \mathbf{r}^R)\rangle d\{\mathbf{r}_i\} = \\ &= \frac{1}{\langle I_T\rangle \langle I_R\rangle} \left| \int |\langle G(\mathbf{r}_0, \mathbf{r}_1)\rangle|^2 \mathscr{L}(\mathbf{r}_1, \mathbf{r}_2) \langle G(\mathbf{r}_2, \mathbf{r}^R)\rangle \langle G^*(\mathbf{r}_2, \mathbf{r}^T)\rangle d\mathbf{r}_1 d\mathbf{r}_2 \right|^2 . \end{aligned} \tag{3.82}$$

We already know the expression for the ladder operator, (3.79), so we can calculate the average reflected

$$\langle I_R \rangle = I_0 \left(1 - \frac{5}{3} \frac{\ell}{L + 2z_0} \right) \tag{3.83}$$

and transmitted intensity

$$\langle I_T \rangle = I_0 \frac{5}{3} \frac{\ell}{L + 2z_0}, \tag{3.84}$$

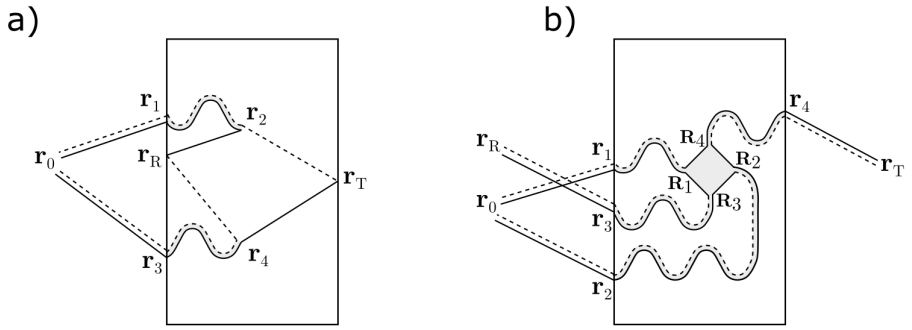

Figure 3.6: Diagrams for the correlation functions between the reflected and transmitted intensity patterns. a) Short-range correlation C_1^{RT} (3.82). b) Long-range C_2^{RT} contribution, (3.92).

where I_0 is the source intensity. Taking into account that $I_0|\langle G(\mathbf{r}_0,\mathbf{r}_1)\rangle|^2 = e^{-z_1/\ell}$ and performing the Fourier transform of the average Green's functions we get

$$C_1^{RT}(\Delta\mathbf{R}) = \frac{1}{\langle I_T\rangle\langle I_R\rangle}\left|\int e^{-\frac{z_1}{\ell}}\widetilde{\mathscr{L}}(z_1,z_2,\mathbf{k})e^{i\mathbf{k}\cdot\Delta\mathbf{R}}\right. \tag{3.85}$$
$$\left.\times\,\langle G(\mathbf{k}_1)\rangle e^{i\mathbf{k}_1|\mathbf{r}_T-\mathbf{r}_2|}\langle G^*(\mathbf{k}_2)\rangle e^{-i\mathbf{k}_2|\mathbf{r}_R-\mathbf{r}_2|}dz_1dz_2\frac{d\mathbf{k}d\mathbf{k}_1d\mathbf{k}_2}{(2\pi)^8}\right|^2,$$

where $\Delta\mathbf{R} = |\mathbf{r}_R - \mathbf{r}_T|$. We need to split $\mathbf{r}_2$ into the distance along z and the transverse one, and do the same with the wave-vectors $\mathbf{k}_1$ and $\mathbf{k}_2$. After doing that, and taking $z(\mathbf{r}^R) = 0$, $z(\mathbf{r}^T) = L$ we get a Dirac-delta term in $\mathbf{k}$ under the integral, which leads to

$$C_1^{RT}(\Delta\mathbf{r}) = \frac{1}{\langle I_T\rangle\langle I_R\rangle}\left|\int e^{-\frac{z_1}{\ell}}\widetilde{\mathscr{L}}(z_1,z_2,0)e^{i\mathbf{q}\Delta\mathbf{r}}\right. \tag{3.86}$$
$$\left.\times\left(\frac{e^{ik_1(L-z_2)}}{k_1^2+|\mathbf{q}|^2-K^2}\right)\left(\frac{e^{ik_2z_2}}{k_2^2+|\mathbf{q}|^2-K^{*2}}\right)dz_1dz_2\frac{d\mathbf{q}dk_1dk_2}{(2\pi)^4}\right|^2,$$

where K is the effective refractive index defined in (3.44). In this equation we used the Fourier representations of the average Green's functions (3.43). Again assuming slow variation of the ladder operator compared to the exponential with ℓ in the denominator, we decouple the integrals over z_1 and z_2. Also, using contour integration, we can take integrals over k_1 and k_2, which leads to

$$C_1^{RT}(\Delta\mathbf{r}) = \frac{\ell\pi^2}{\langle I_T\rangle\langle I_R\rangle}\left|\int\widetilde{\mathscr{L}}(0,z_2,0)e^{i\mathbf{q}\Delta\mathbf{r}}\frac{e^{i\xi L}e^{-i(\xi-\xi')z_2}}{\xi\xi'}dz_2\frac{d\mathbf{q}}{(2\pi)^2}\right|^2, \tag{3.87}$$

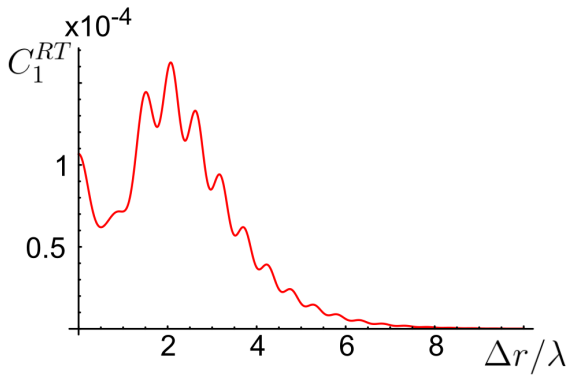

Figure 3.7: Short-range correlation between the reflected and transmitted intensity C_1^{RT}. The values of the parameters are $k_0 = 2\pi$, $L = 2$, $\ell = 1$.

where $\xi = \sqrt{|\mathbf{q}|^2 - K^2}$ and $\xi' = \sqrt{|\mathbf{q}|^2 - K^{*2}}$. Noting that in the $\mathbf{q} \to 0$ limit the ladder operator becomes

$$\widetilde{\mathscr{L}}(0, z, 0) = I_0 \left(\frac{3(\ell + z_0)}{\ell(L + 2z_0)} (L + z_0 - z) - 2e^{-\frac{z}{\ell}} \right), \tag{3.88}$$

we can finally perform the integral over z_2 in (3.87) to get

$$C_1^{RT}(\Delta\mathbf{r}) = \frac{I_0 \ell \pi^2}{\langle I_T \rangle \langle I_R \rangle} \left(\frac{3(\ell + z_0)}{\ell(L + 2z_0)} \right)^2 \tag{3.89}$$
$$\times \left| \int \frac{e^{\xi' L}[1 - i(\xi - \xi')z_0] + e^{\xi L}[i(\xi - \xi')(L + z_0) - 1]}{\xi \xi' (\xi - \xi')^2} e^{i\mathbf{q}\Delta\mathbf{r}} \frac{d\mathbf{q}}{(2\pi)^2} \right|^2 .$$

We plot this expression in Fig. 3.7. From this graph we can see, that although C_1^{RT} is much broader than the correlation in transmission, which is of a size of $\sim \lambda$, it is doubtful that it might be responsible for the positive contribution, observed in the experiment, because of the reasons we discuss below. First of all we can estimate the dependence of this correlation amplitude on L. We can show that

$$C_1^{RT}(0) \sim \frac{e^{\frac{-L}{\ell}}}{k_0^4 \ell^3 L}. \tag{3.90}$$

It means that this contribution decays exponentially with the slab thickness, which contradicts experimental data. In addition, C_1^{RT} contains quickly varying features which were never observed in the experiment. Even taking into account the fact that the resolution of the imaging setup we used, is not enough to resolve these oscillations, they would increase the uncertainty in the lineshape of the positive contribution, which was never observed. We finally note, that in the regime of $\lambda \sim L \sim \ell$, which we probed in

the simulations, additional short-range terms can be present, including the one involving only the free space Green's functions.

3.3.2 Long range correlation between reflection and transmission

We already have an intuitive feeling that the negative part of the correlation function observed in the experiment has a long-range nature, and appear due to the diffusion path interference. Following [17, 25], we support this guess by an analytic expression for the long-range C_2-type correlation function between the reflection and transmission and compare it to the experiment.

All the necessary building blocks of this correlation function were introduced earlier. We need to apply them to the diagram, shown in Fig. 3.6b. The analytical expression for this diagram is

$$C_2^{RT}(\mathbf{r}^R,\mathbf{r}^T) = \int |\langle G(\mathbf{r}_0,\mathbf{r}_1)\rangle|^2 |\langle G(\mathbf{r}_0,\mathbf{r}_2)\rangle|^2 \mathscr{L}(\mathbf{r}_1,\mathbf{R}_1)\mathscr{L}(\mathbf{r}_2,\mathbf{R}_2) \tag{3.91}$$

$$\times \mathscr{H}(\{\mathbf{R}_i\})\mathscr{L}(\mathbf{r}_3,\mathbf{R}_3)\mathscr{L}(\mathbf{r}_4,\mathbf{R}_4)|\langle G(\mathbf{r}_3,\mathbf{r}_R)\rangle|^2 |\langle G(\mathbf{r}_4,\mathbf{r}_T)\rangle|^2 d\{\mathbf{r}_i\}d\{\mathbf{R}_i\},$$

which is similar to (3.70), apart from the coordinates of the enter and exit ladders. Substituting the expression for the ladder operator (3.79), with appropriate enter and exit coordinates and simplified expression for $\mathscr{H}$, (3.77) into (3.91), and performing the integration as we did for $C_2(\Delta\mathbf{r})$, we get the expression for the C_2^{RT}

$$C_2^{RT}(\Delta r) = \frac{-45}{8k_0^2\ell^2}\int \frac{J_0(q\Delta r/L)\sinh(qz_0/L)^2}{q^3\sinh[q\left(1+2\frac{z_0}{L}\right)]^2}$$
$$\times\left(-q\,\mathrm{ch}(q) + \left[1+q^2\left(1+\frac{2z_0}{L}+\frac{2z_0^2}{L^2}\right)\right]\mathrm{sh}(q)\right)\mathrm{d}q, \tag{3.92}$$

In a more detailed analysis we neither can neglect the quadratic in $\mathbf{q}$ terms in the Hikami vertex expression (3.75), nor assume that the gradients applied to the incoming and outgoing ladders give the same contribution. The $\sum_i q_i^2$ term in (3.75), in real space leads to a sum of Laplacians

$$\sum_i q_i^2 \to \sum_i \Delta_{\mathbf{R}_i}, \tag{3.93}$$

and the sum of the dot products can be balanced in such a way that the gradients are applied separately to the incoming and outgoing ladders. The correlation function

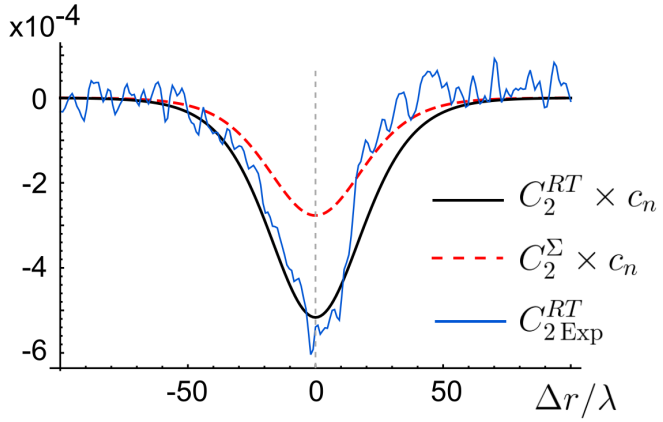

Figure 3.8: Long range correlation function C_2^{RT}: comparison of the theory and experiment. Black solid line represents theoretical model, Eq. (3.92) with $\lambda = 0.63, L = 20, \ell = 10$. Red dashed line total correlation including the other terms (3.94). Blue solid line shows experimentally measured correlation at $L = 20\mu m, \ell = 10\mu m$ (bottom left corner in Fig. 1.5). There is a factor of $c_n \approx 17$ mismatch between the measured and calculated correlation amplitudes, however no additional fitting was used in the horizontal axis.

taking into account these factors is

$$C_2^{\Sigma} = C_2^{\Delta} + \frac{C_2^{\mathrm{in}} + C_2^{\mathrm{out}}}{2}. \tag{3.94}$$

where

$$C_2^{\Delta} = \frac{h}{4} \int |\langle G(\mathbf{r}_0, \mathbf{r}_1)\rangle|^2 |\langle G(\mathbf{r}_0, \mathbf{r}_2)\rangle|^2 \mathscr{L}(\mathbf{r}_1, \mathbf{R}_1)\mathscr{L}(\mathbf{r}_2, \mathbf{R}_2) \tag{3.95}$$

$$\times \left(\sum_i \Delta_{\mathbf{R}_i} \right) \mathscr{L}(\mathbf{r}_3, \mathbf{R}_3)\mathscr{L}(\mathbf{r}_4, \mathbf{R}_4) |\langle G(\mathbf{r}_3, \mathbf{r}_R)\rangle|^2 |\langle G(\mathbf{r}_4, \mathbf{r}_T)\rangle|^2 d\{\mathbf{r}_i\} d\{\mathbf{R}_i\},$$

$$C_2^{\mathrm{in}} = h \int |\nabla_{\mathbf{R}} \langle I(\mathbf{R})\rangle|^2 \mathscr{L}(\mathbf{R}, \mathbf{r}_R)\mathscr{L}(\mathbf{R}, \mathbf{r}_T) d\mathbf{R}, \tag{3.96}$$

and C_2^{out} is equivalent to C_2^{RT} in (3.91) that we calculated using a simplified expression for $\mathcal{H}$, (3.76). In Fig. 3.8 we compare the resulting correlation function with the one, obtained in the experiment. Although there is quite a big mismatch in the correlation magnitude ($\sim$ 17 times) between theory and experiment, when they are normalized to the same magnitude, the shape of the experimentally measured correlation function almost exactly matches the theoretical prediction. There is a slight mismatch on the right side, probably due to the positive contribution present in the experiment.

The qualitative agreement between these functions, confirms our initial assumptions

about the origin of this correlation. Taking additional terms of the Hikami vertex does not improve the magnitude mismatch, as both C_2^{in} and C_2^{Δ} are positive, and only reduce the size of the dip, which means that there might be additional mechanisms, going beyond the Hikami crossing. In the next section we briefly discuss such contributions.

3.3.3 Positive correlation in the semi-ballistic regime

As we have seen in Ch. 1 there are two contributions to the correlation, positive and negative. In the previous chapter we have shown that the negative part is well described by a C_2-type long-range correlation. Before that, we also have shown that the positive part can't be attributed to the C_1 correlation, as its shape is different from the one observed in the experiment and because it decays exponentially with the sample thickness.

The fact that the correlation function depends on the angle of incidence of the incoming beams allows to make a guess about the origin of the positive contribution. None of the correlation functions we considered before show any dependence on this angle. However a contribution called C_0 [63–65], introduced for the case of the point source illumination can show such dependence. The diagrams, corresponding to this contribution are shown in Fig. 3.9. Each diagram involves scattering paths that share

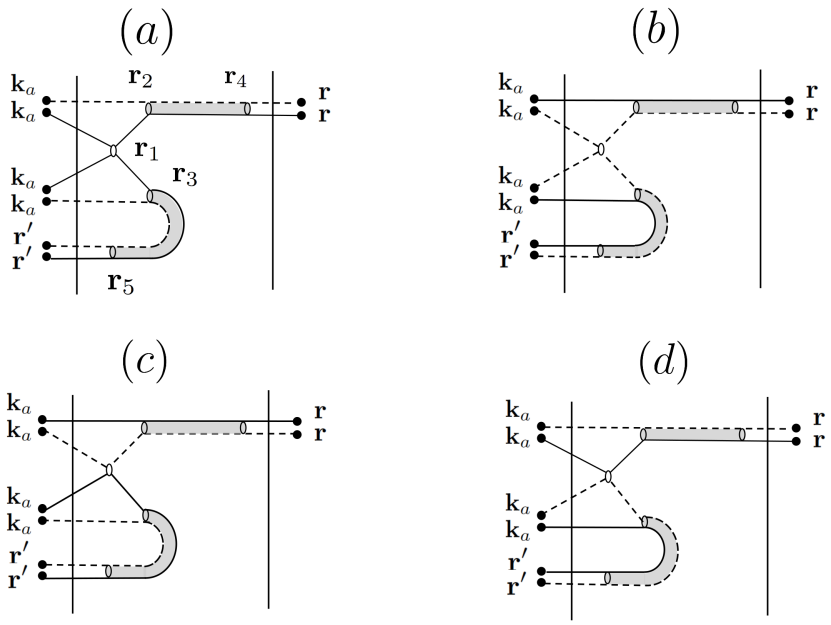

Figure 3.9: Diagrams of the C_0 contribution, responsible for the broad positive peak observed in the experiment at $b \approx 1$. The exchange happens at a single scattering event near the reflection surface, which is described by the $\mathscr{S}$ operator.

a common scatterer close to the front side of the sample. The diagrams that involve a common scatterer in the output paths can be neglected for the same reason as the C_1^{RT} correlation.

The C_0 correlation can be formally written as

$$C_0^{RT}(\Delta\mathbf{r}) = \frac{4\pi}{\ell}\int \mathscr{S}(\mathbf{r}_2,\mathbf{r}_3)\mathscr{L}(\mathbf{r}_2,\mathbf{r}_4)\mathscr{L}(\mathbf{r}_3,\mathbf{r}_5) \times|\langle \mathrm{G}(\mathbf{r}-\mathbf{r}_4)\rangle|^2|\langle \mathrm{G}(\mathbf{r}'-\mathbf{r}_5)\rangle|^2 \mathrm{d}\mathbf{r}_2\mathrm{d}\mathbf{r}_3\mathrm{d}\mathbf{r}_4\mathrm{d}\mathbf{r}_5, \tag{3.97}$$

where $\mathscr{S}(\mathbf{r}_2,\mathbf{r}_3)$ accounts for all of the four possibilities of connecting the input free-space propagating wave to the ladders starting at $\mathbf{r}_2$ and $\mathbf{r}_3$, as shown in Fig. 3.9 [63]. We will not detail here its analytical derivation, just noting that first of all, this contribution manifests in a broad positive peak, which indeed depends significantly on the incident beam orientation. In addition it presents negative side lobes, such that $\int C_0^{RT} = 0$. The amplitude of the C_0^{RT} grows with the increase of the angle of incidence, which due to the zero-integral property leads to broadening of the negative lobes (see Appendix G in [17]), which agrees with the experimental observation, as well at the dependence of the peak hight on L ($C_0^{RT}(0) \propto \text{Ł}^{-4}$).

3.4 Summary

In this chapter we have shown an analytical theory describing the correlation of the reflected and transmitted speckle patterns. This theory qualitatively describes the negative contribution, observed in the diffusive regime, which we consider a strong argument in favour of the non-trivial character of this correlation, arising due to exchange of diffusion partners in the scattering sequences. Moreover, we argue that the positive contribution, observed in the weak scattering regime is not just a field-field short-range correlation, but also appears due to a particular type of (non-universal) interference effects near the reflection surface of the disordered sample.

Despite this initial success we realize that there is still a huge room for improvement, with the final goal being a qualitative agreement in the full disorder strength range.

Chapter 4

Ghost imaging using speckle patterns

In the first instance it might seem that correlations considered in previous chapters are exclusively of fundamental interest. However, as we outlined in the introduction, the existence of correlations always means non-zero mutual information. In context of the problem we consider, it means that measurement of the reflected speckle pattern gives us certain amount of information about the transmitted one [14]. In the current chapter we demonstrate how this knowledge can be used to reconstruct the shape of the objects hidden behind the scattering layers with high optical density.

Our method is based on the ghost imaging technique [66], and since it doesn't require direct access to the imaged object, we call it *blind ghost imaging*. In the beginning of the chapter we review the regular ghost imaging modality, paying particular attention to the case when speckle patterns are used to obtain the ghost image. We calculate the signal-to-noise ratio (SNR) of this technique, showing how it depends on the imaged object transparency. After that we introduce the blind ghost imaging technique and extend the SNR calculation on the scenario of correlated speckle patterns. Then we show the experimental results of the image reconstruction using this method. In the remainder of the chapter we discuss different reconstruction techniques that can improve the SNR (up to perfect reconstruction) keeping the number of measurements the same.

4.1 Regular and computational ghost imaging

The first papers on this subject described this method as relying exclusively on quantum correlations, namely entanglement, between the photons in the two modes [67, 68]. Typical setup used in these experiments is illustrated in Fig. 4.1a. A source produces

photons entangled in position or in momentum going into spatially separated modes. A semi-transparent mask, the object, is placed in one of the beams, and the total transmitted intensity after passing the mask is measured with a single photodiode. In the second beam a scanning photodiode or a CCD is placed. As a consequence of entanglement, when a photon is detected behind the mask, a photon in the second beam can be detected, having the same relative position as the one passing the mask. Therefore, the number of coincidences between the photodiodes in the two arms now gives information about the local transmissivity of the mask. Changing the position of the photodiode in the second beam, or registering coincidences directly with a CCD gives the spatial transmissivity profile, or in other words, the image of an object.

As we will discuss in Ch. 6 it is often hard to decide whether quantum-mechanical description is necessary in particular situations, especially when it comes to light. Ghost imaging is a perfect example of that, as it was soon realized that entanglement is not necessary for this technique [69]. The only requirement for this technique to work is to have correlated light intensity fluctuations in two spatially separated points. One of the ways to get such correlations is to divide a speckle pattern from a dynamically changing scattering medium using a beamsplitter [70]. The modification of the original setup based on the dynamical speckle is illustrated in Fig. 4.1b [71, 72]. Instead of the source of entangled photons, a beam of pseudo-thermal light, often produced by a moving diffuser, is split into two arms. It appears that classical correlation is enough to get the same result as for entangled beams, although quantum correlations provide additional information about the photons in a different beam, thus leading to faster convergence of the method, especially in the case of low total number of photons [73].

In Ch. 6, 7 we show, that some quantum correlations are still possible between the output beams, when a mixed (including thermal) state is incident on a beamsplitter. This fact was noticed by Adesso et al. [74], continuing the discussion about the role of quantum correlations in ghost imaging. The discussion was wrapped up by Shapiro [75], noting that there is a modification of the ghost imaging setup, which does not rely on correlations in any form: computational ghost imaging [76, 77]. The setup for this modification is represented in Fig. 4.1c. Now instead of a source of randomly varying patterns, an image formation device is used, which sends predetermined patterns from an initially prepared set. The reconstruction procedure is analogous to normal ghost imaging: the image is reconstructed as a weighted sum, where the weights are single pixel detector readings. However, in such a configuration there is no randomness in the illuminating patterns, and therefore no correlations are possible.

Computational ghost imaging is considered the most practically useful of the listed

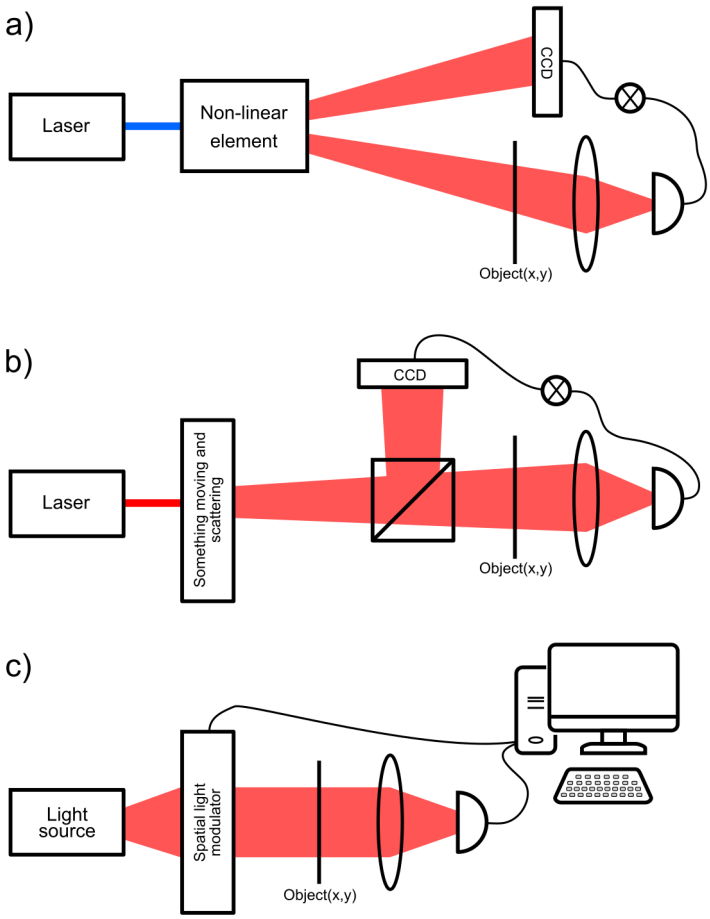

Figure 4.1: Variations of the ghost imaging setup: a) Ghost imaging using non-classical source. b) Ghost imaging using speckle patterns or pseudo-thermal light. c) Computational ghost imaging.

above techniques. All other method still require a camera or a scanning detector, which together with direct accessibility of the imaged object makes them impractical. In computational imaging, the camera is not needed, being replaced with a spatial modulator. This opens a possibility of imaging in the spectral ranges, in which conventional cameras are expensive or unavailable, such as far infrared [77, 78], terahertz [79, 80] or X-ray [81] radiation.

The main limitation of the ghost imaging methods is the signal-to-noise ratio for the correlation-based methods and reconstruction error for the computation-based ones. The SNR depends on the properties of the patterns (random or deterministic), number of measurements and the overall transmissivity of the imaged object [82]. In the next section we consider in details regular ghost imaging technique SNR for the case of the incident patterns following speckle statistics [83].

4.2 Ghost imaging using speckle patterns: statistical approach

4.2.1 Speckle statistics and ghost imaging observable

Let's consider the ghost imaging setup illustrated in Fig. 4.1b with a moving scatterer producing fluctuating speckle patterns as a source. Each pixel of the camera detects the speckle pattern intensity $\mathbf{R} = \{R_{ij}\}$ at a particular point x_j, $j = 0 \dots N_\mathrm{p}$ and the moment of time t_i, $i = 0 \dots N_\mathrm{r}$. Assuming that the random scatterer produces well developed speckle and moves fast enough for it to be independent at different camera exposure events, the distribution of the intensity registered by the camera is

$$P(\mathbf{R}) = \overline{R}^{-N_\mathrm{T}} \prod_{ij}^{N_\mathrm{T}} e^{-R_{ij}/\overline{R}}, \tag{4.1}$$

where $N_\mathrm{T} = N_\mathrm{p} \times N_\mathrm{r}$ and $\overline{R}$ is the average intensity, which we assume to be equal for all of the camera pixels (uniform illumination). Here we also assume that adjacent pixels are uncorrelated, i.e. we neglect the short-range correlation within the speckle, which is automatically true when the pixel size is bigger than the average speckle spot diameter, or can be achieved with pixel binning in the opposite case.

The photodiode readings, c_i are

$$c_i = \sum_{j}^{N_\mathrm{p}} R_{ij} \Lambda_j, \tag{4.2}$$

where $\Lambda_j = \Lambda(x_j)$, is the transmissivity of the object at a position x_j.

Let's consider an observable O_p corresponding to the reconstructed image,

$$O_p = \frac{1}{N_\mathrm{r}} \sum_{i}^{N_\mathrm{r}} R_{ip} c_i. \tag{4.3}$$

As we will show below, the mean value of this observable converges to $\Lambda(x_p)$. We will also calculate the variance of this observable in order to estimate how fast this convergence occurs.

4.2.2 Signal-to-noise ratio

The signal-to-noise ratio will be

$$\mathrm{SNR}_{O_p} = \frac{\langle O_p \rangle}{\sqrt{\Delta O_p}}, \tag{4.4}$$

where $\langle O_p \rangle$ is the mean value and $\Delta O_p = \langle O_p^2 \rangle - \langle O_p \rangle^2$ is the variance of this observable. In order to calculate the $\langle O_p \rangle$ we substitute c_i from (4.2) to (4.3)

$$O_p = \frac{1}{N_\mathrm{r}} \sum_i^{N_\mathrm{r}} \sum_j^{N_\mathrm{p}} R_{ip} R_{ij} \Lambda_j. \tag{4.5}$$

After doing that, the expression for the mean value

$$\langle O_p \rangle = \int_0^\infty O_p P(\mathbf{R}) d\mathbf{R}, \tag{4.6}$$

can be split into two parts

$$\begin{aligned} \langle O_p \rangle &= \frac{1}{N_\mathrm{r}} \int_0^\infty \sum_{ij}^{N_\mathrm{T}} R_{ij} R_{ip} \Lambda_j P(R_{ij}) dR_{ij} = \frac{\Lambda_p}{N_\mathrm{r}} \int_0^\infty \sum_i^{N_\mathrm{r}} R_{ip}^2 \overline{R}^{-1} e^{-R_{ip}/\overline{R}} dR_{ip} + \\ &+ \frac{1}{N_\mathrm{r}} \iint_0^\infty \sum_{i,j \neq p}^{N_\mathrm{T}} R_{ij} R_{ip} \Lambda_j \overline{R}^{-2} e^{-(R_{ij}+R_{ip})/\overline{R}} dR_{ij}\, dR_{ip} = \\ &= \overline{R}^2 \left(1 + \Lambda_p + \sum_{j \neq p}^{N_\mathrm{T}-1} \Lambda_j \right). \end{aligned} \tag{4.7}$$

Let's further assume that the object is a binary transmission mask $\Lambda_j \in \{0, 1\}$, where 0 transmission value refers to black pixels and 1 to white pixels. Also let $\sum_j \Lambda_j = N_\mathrm{w}$. Taking that into account the mean value is

$$\langle O_p \rangle = \begin{cases} \overline{R}^2 \left(1 + N_\mathrm{w}\right), & \text{if } \Lambda_p = 1 \\ \overline{R}^2 N_\mathrm{w}, & \text{if } \Lambda_p = 0. \end{cases} \tag{4.8}$$

As we can see from this expression, the intensity of a ghost image pixel, corresponding to a white pixel in the object, has a mean value bigger by $\overline{R}^2$ than for a black pixel. There is a simple intuitive argument of why this happens. Let's assume that we have just one non-zero pixel in the object $\Lambda = \delta_{j,j'}$. The photodiode measurements become equal to the speckle intensity at this point $c_i = R_{i,j'}$ and the summation in (4.5) becomes

$O_p = \frac{1}{N_\mathrm{r}} \sum_i^{N_\mathrm{r}} R_{ip} R_{ij'}$. When $p \neq j'$, this is a sum of products of uncorrelated positive random numbers, whereas when $p = j'$ it is a sum of squares of a single random variable, which is guaranteed to have a bigger value. From the same argument one can see the biggest limitation of this method. When there are two non-zero pixels, $\Lambda = \delta_{j,j'} + \delta_{j,j''}$, the summation in (4.5) becomes $O_p = \frac{1}{N_\mathrm{r}} \sum_i^{N_\mathrm{r}} R_{ip}(R_{ij'} + R_{ij''})$. It means that for $p = j'$ apart from a sum of $R_{ij'}^2$ there is also a contribution from $R_{ij'} R_{ij''}$, which acts, effectively, as an additional noise, reducing the difference between the intensity of the white and black pixels in the ghost image. Therefore we can expect that the ghost imaging SNR will reduce with the number of white pixels in the object. To see that in more detail, let's calculate the variance of the O_p.

To calculate the variance we need to know

$$\langle O_p^2 \rangle = \int_0^\infty O_p^2 P(\mathbf{R}) d\mathbf{R}. \tag{4.9}$$

The expression for O_p^2 is

$$\begin{aligned} O_p^2 &= \frac{\Lambda_p^2}{N_\mathrm{r}^2} \left[\sum_i^{N_\mathrm{r}} R_{ip}^2 \right]^2 + \frac{2\Lambda_p}{N_\mathrm{r}^2} \left(\sum_i^{N_\mathrm{r}} R_{ip}^2 \right) \left(\sum_k^{N_\mathrm{r}} \sum_{j \neq p}^{N_\mathrm{p}} R_{kj} R_{kp} \Lambda_j \right) + \\ &+ \frac{1}{N_\mathrm{r}^2} \left[\sum_i^{N_\mathrm{r}} \sum_{j \neq p}^{N_\mathrm{p}} R_{ij} R_{ip} \Lambda_j \right]^2 . \end{aligned} \tag{4.10}$$

We can substitute (4.10) into (4.9) and calculate the resulting integrals separately for each term in (4.10) (see Appendix B). Taking into account the formula for the mean value (4.9), we get the variance

$$\Delta O_p = \frac{\overline{R}^4}{N_\mathrm{r}} \begin{cases} (N_\mathrm{w} + 4)^2 - 5, & \text{if } \Lambda_p = 1 \\ \\ N_\mathrm{w}^2 + 2N_\mathrm{w}, & \text{if } \Lambda_p = 0, \end{cases} \tag{4.11}$$

and finally the SNR

$$\mathrm{SNR}_{O_p} = \sqrt{N_\mathrm{r}} \begin{cases} \dfrac{1}{\sqrt{(N_\mathrm{w} + 4)^2 - 5}}, & \text{if } \Lambda_p = 1 \\ \dfrac{1}{\sqrt{N_\mathrm{w}^2 + 2N_\mathrm{w}}}, & \text{if } \Lambda_p = 0, \end{cases} \tag{4.12}$$

As we can see from the expression above, SNR_{O_p} decreases with the number of white

pixels in the object as $O(1/N_{\mathrm{w}})$ and increases as $O(\sqrt{N_{\mathrm{r}}})$ with the number of time averages, see Fig. 4.3a,b.

4.2.3 Average subtraction

The decrease of SNR with the number of white pixels can be partially compensated by a modification of the regular ghost imaging technique called differential ghost imaging [84]. In this method, observable O_p, is modified to

$$O_p^{\mathrm{DGI}} = \frac{1}{N_{\mathrm{r}}} \sum_i^{N_{\mathrm{r}}} R_{ip} c_i - \frac{1}{N_{\mathrm{r}} N_{\mathrm{p}}} \frac{\langle R \rangle}{\langle c \rangle} \sum_{ij} R_{ij} R_{ip}, \tag{4.13}$$

where $\langle R \rangle = \frac{1}{N_{\mathrm{r}} N_{\mathrm{p}}} \sum_{ij} R_{ij}$ is the average total intensity of the speckle patterns and $\langle c \rangle = \frac{1}{N_{\mathrm{r}}} \sum_i c_i$ is the average photodiode signal. This allows to partially overcome the problem of low SNR for objects with large number of white pixels, as SNR of O_p^{DGI} becomes symmetric with respect to the value of $N_{\mathrm{w}} = N_{\mathrm{p}}/2$ (50% of white pixels in the image) [84]. It means that, for example, the reconstructed images of two objects with 99% and 1% white pixels, will have the same signal-to-noise ratio when the differential technique is used. When $N_{\mathrm{w}} \ll N_{\mathrm{p}}$ differential ghost imaging is equivalent to the regular one.

In differential ghost imaging a combination of the average intensities in both arms is subtracted from the normal ghost imaging observable, however even subtraction of the speckle patterns temporal average, $\widetilde{R}_p = \frac{1}{N_{\mathrm{r}}} \sum_i R_{ip}$, can significantly improve SNR. The new observable is

$$O'_p = \frac{1}{N_{\mathrm{r}}} \sum_i^{N_{\mathrm{r}}} R_{ip} c_i - \frac{\langle c \rangle}{N_{\mathrm{r}}} \sum_i R_{ip} = O_p - \langle c \rangle \widetilde{R}_p. \tag{4.14}$$

Its mean value is

$$\langle O_p \rangle = \langle O_p \rangle - \langle c \rangle \langle \widetilde{R}_p \rangle. \tag{4.15}$$

Taking into account that

$$\langle \widetilde{R}_p \rangle = \frac{1}{N_{\mathrm{r}}} \int_0^\infty \sum_i^{N_{\mathrm{r}}} R_{ip} P(\mathbf{R}) d\mathbf{R} = \overline{R},$$

and

$$\langle c \rangle = \frac{1}{N_{\mathrm{r}}} \int_0^\infty \sum_i^{N_{\mathrm{r}}} \sum_j^{N_{\mathrm{p}}} R_{ij} \Lambda_j P(\mathbf{R}) d\mathbf{R} = N_{\mathrm{w}} \overline{R},$$

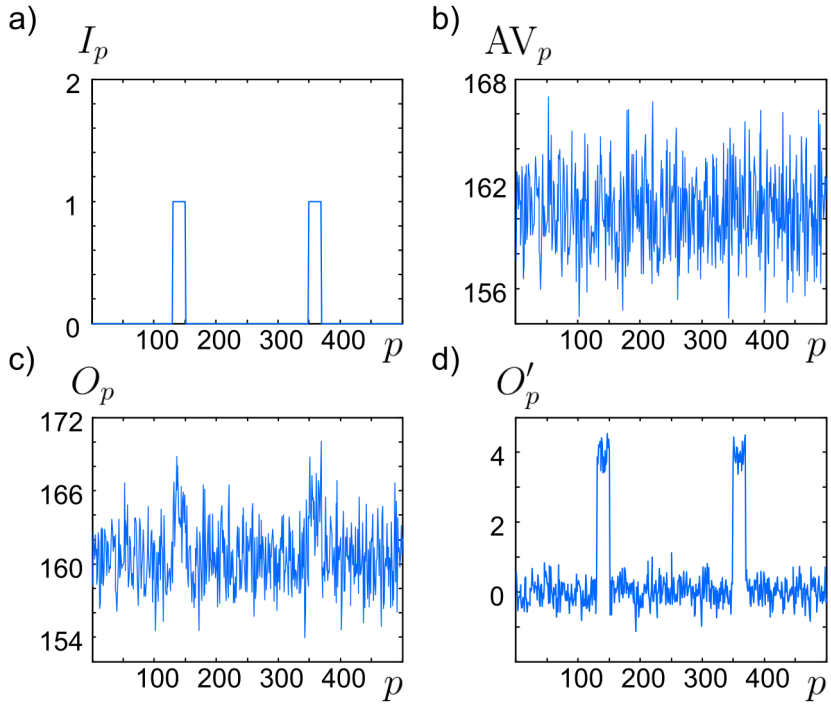

Figure 4.2: a) An object to image, containing $N_{\mathrm{w}} = 20$ white pixels. b) An average of 5000 patterns, distributed according to (4.1). c) Ghost image reconstructed as (4.12) without average subtraction. d) Ghost image reconstructed as (4.21), d) is c) minus b).

from (4.15) we get

$$\langle O'_p \rangle = \begin{cases} \overline{R}^2, & \text{if } \Lambda_p = 1 \\ 0, & \text{if } \Lambda_p = 0, \end{cases} \tag{4.16}$$

which looks similar to (4.8), but now the constant background in black pixels is removed.

The variance $\Delta O'_p$ is

$$\Delta O'_p = \Delta O_p + \langle c \rangle \Delta \widetilde{R}_p - 2\langle c \rangle \mathrm{Cov}\left[O_p, \Delta \widetilde{R}_p\right], \tag{4.17}$$

where Cov[A,B] $= \langle AB \rangle - \langle A \rangle \langle B \rangle$ is the covariance. $\Delta \widetilde{R}_p$ can be calculated similarly to the integral of the first term in (4.10).

$$\langle c \rangle \Delta \widetilde{R}_p = \frac{N_{\mathrm{w}}^2 \overline{R}^4}{N_{\mathrm{r}}} \tag{4.18}$$

The covariance in (4.17) is

$$\mathrm{Cov}\left[O_p, \Delta \widetilde{R}_p\right] = \int_0^\infty O_p \, \widetilde{R}_p \, P(\mathbf{R}) d\mathbf{R} - \langle O_p \rangle \langle \widetilde{R}_p \rangle, \tag{4.19}$$

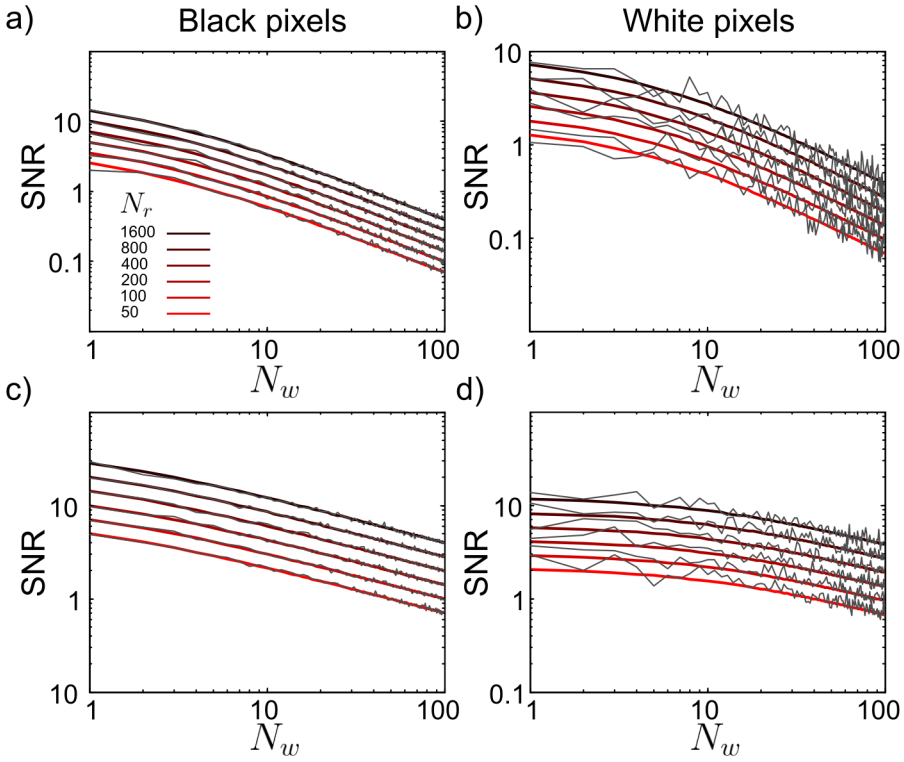

Figure 4.3: SNR of the regular ghost imaging. a), b) SNR of the O_p observable, (4.3), without the subtraction of the average pattern. c), d) SNR of the O'_p observable, (4.14), with subtraction of the average pattern $\widetilde{R}_p = \frac{1}{N_\mathrm{r}} \sum_i R_{ip}$, depending on the number of white pixels in the object, N_w. a) and c) correspond to black pixels, b) and d) to white pixels. Solid lines are analytic expressions, (4.12) for a) and b), and (4.21), black solid lines are numeric simulations.

where the first integral is calculated in Appendix B. Substituting the result into (4.17) we get the variance

$$\Delta O'_p = \frac{\overline{R}^4}{N_\mathrm{r}} \begin{cases} 2N_\mathrm{w} + 11, & \text{if } \Lambda_p = 1 \\ \\ 2N_\mathrm{w}, & \text{if } \Lambda_p = 0, \end{cases} \tag{4.20}$$

and SNR

$$\mathrm{SNR}_{O'_p} = \sqrt{N_\mathrm{r}} \begin{cases} \dfrac{1}{\sqrt{2N_\mathrm{w} + 11}}, & \text{if } \Lambda_p = 1 \\ \dfrac{1}{\sqrt{2N_\mathrm{w}}}, & \text{if } \Lambda_p = 0, \end{cases} \tag{4.21}$$

It is possible to see that subtraction of the temporal average of the speckle pattern improved the ghost imaging SNR, which now scales as $O(1/\sqrt{N_\mathrm{w}})$, see Fig. 4.3c,d. To illustrate the improvement, in Fig. 4.2 we compare the ghost images with and without temporal average subtraction.

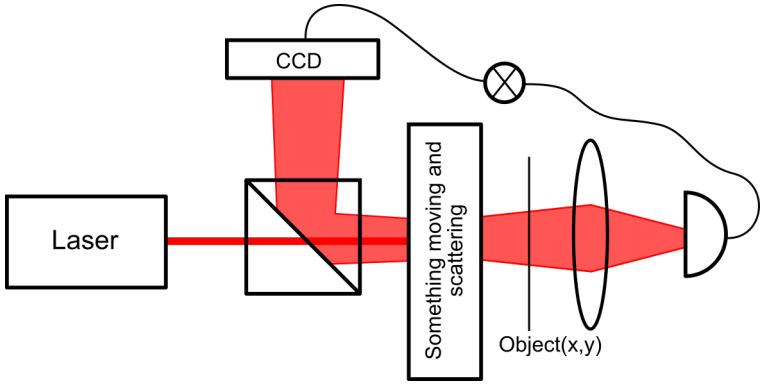

Figure 4.4: Principle schematics of the blind ghost imaging setup. The object to be imaged is hidden behind a scattering layer. In case when the object is fluorescent, we don't need the bucket detector to be behind the object, as we can collect the fluorescence signal from the reflection side.

The statistical approach to ghost imaging has an advantage of relatively high stability against instrumental noise (in the cameras or in the detector), however it does not allow perfect reconstruction of the object. At the end of this chapter we will consider deterministic approach, in which it is possible to achieve perfect reconstruction.

4.3 Blind ghost imaging

4.3.1 Description of the technique

Ghost imaging relies on the spatial correlations between the light intensities in the bucket detector and resolving detector paths of the imaging system. For example in the setup in Fig. 4.1b, the patterns passing the object and registered by the resolving detector are the same, which implies perfect spatial correlation. But what happens when this correlation is imperfect? Statistically reconstructed ghost images have quite poor signal-to-noise ratio even in the case of the perfect correlation, especially for semi-transparent objects. Imperfect correlation acts as an additional effective noise in one of the patterns. Therefore, in the first instance it might seem that this additional nose reduces the SNR so much, that the reconstruction becomes impossible. However, as we show below, we are able to reconstruct the object even when the correlation is as weak as the one described in Ch. 1–3 ($\sim 10^{-3}$–10^{-4}).

A modification of the ghost imaging technique that exploits reflection-transmission correlations we call the *blind ghost imaging*. A schematic setup description for this method is given in Fig. 4.4. A laser beam illuminates a scattering sample, that produces a dynamically changing speckle pattern. The reflection speckle is registered with a

camera, and the transmitted speckle illuminates the object placed behind the scattering material. Total transmitted light is registered by a photodiode placed behind the object and the scattering slab. In this configuration transmitted speckle patterns are inaccessible for direct measurement, but since reflected and transmitted patterns are correlated, the reconstruction is still possible if we modify the corresponding observable.

4.3.2 Signal-to-noise ratio

By analogy to (4.3), an observable for the object reconstruction is

$$G_p = \sum_i^{N_\mathrm{r}} R_{ip} t_i, \tag{4.22}$$

where t_i are the readings of the photodiode registering the total transmitted intensity.

$$t_i = \sum_j^{N_\mathrm{p}} T_{ij} \Lambda_j, \tag{4.23}$$

where $\mathbf{T} = \{T_{ij}\}$ are the transmitted speckle patterns.

As we have seen in Sec. 4.2, average subtraction can significantly improve the reconstruction SNR, therefore we consider an observable

$$G'_p = \sum_i^{N_\mathrm{r}} R_{ip} t_i - \langle t \rangle \widetilde{R}_p, \tag{4.24}$$

where $\langle t \rangle = \frac{1}{N_\mathrm{r}} \sum_i t_i$.

The signal-to-noise of this observable can be calculated in a way similar to (4.21), however to do that we need to know the joint distribution of the reflected and transmitted speckle intensities. This distribution was estimated in [14]:

$$P(\mathbf{RT}) = \frac{1}{(\overline{R}\overline{T})^{N_\mathrm{T}}} \prod_{ij}^{N_\mathrm{T}} e^{-(R_{ij}+T_{ij})/\overline{R}\overline{T}} \left(\frac{C^{RT} \left(\frac{R_{ij}}{\overline{R}} - 1 \right) \left(\frac{T_{ij}}{\overline{T}} - 1 \right)}{\overline{R}\overline{T}} + 1 \right), \tag{4.25}$$

under the assumption of small C^{RT}, correlation coefficient between the reflected and transmitted intensities. Here we also neglect the spatial shape of the correlation, assuming that it connects only it adjacent pixels in reflection and transmission (it is of a size of one pixel). This can always be achieved practically by binning the pixels within the correlation range. When finite size of the correlation is taken into account the reconstructed image becomes a convolution of the original object profile with the correlation

line-shape, which is shown in Appendix C.

Now we can calculate the mean value of G'_p

$$\langle G'_p \rangle = \int_0^\infty G'_p P(\mathbf{RT})\, d\mathbf{R} d\mathbf{T} = \begin{cases} C^{RT}, & \text{if } \Lambda_p = 1 \\ 0, & \text{if } \Lambda_p = 0, \end{cases} \tag{4.26}$$

its variance

$$\Delta G'_p = \frac{(\overline{R}\overline{T})^2}{N_\mathrm{r}} \begin{cases} \frac{8C^{RT}(1+N_\mathrm{w})}{\overline{R}\overline{T}} + 2N_\mathrm{w} + 3, & \text{if } \Lambda_p = 1 \\ \\ 2N_\mathrm{w}, & \text{if } \Lambda_p = 0, \end{cases} \tag{4.27}$$

and signal-to-noise ratio

$$\mathrm{SNR}_{G'_p} = C^{RT}\sqrt{N_\mathrm{r}} \begin{cases} \frac{1}{\sqrt{\frac{8C^{RT}(1+N_\mathrm{w})}{\overline{R}\overline{T}} + 2N_\mathrm{w} + 3}}, & \text{if } \Lambda_p = 1 \\ \\ \frac{1}{\sqrt{2N_\mathrm{w}}}, & \text{if } \Lambda_p = 0, \end{cases} \tag{4.28}$$

when C^{RT} the term with C^{RT} in the denominator of (4.28) can be neglected, which means that the SNR linearly reduces with the correlation strength.

4.3.3 Numerical modelling

In order to check the validity of the method we performed numerical modelling of this imaging technique applying a set of numeric mask with different N/N_w ratio to the transmitted speckle patterns within the reflection-transmission correlation measurement setup (Fig. 1.2). Ghost images were calculated using (4.24). The modelling results are demonstrated in Fig. 4.5, showing the feasibility of reconstruction and also qualitatively confirming the dependence of the signal-to-noise ratio on the number of transparent pixels in the object.

4.3.4 Experimental results

The experimental setup is shown in Fig. 4.6a, it is very similar to the one used in the correlations measurements. The laser was Thorlabs He-Ne (632 nm). The sample was the same as for correlation measurement (TiO_2 in glycerol), its thickness was $L = 40\mu m$ and the mean free path $\ell \approx 16 \pm 2.5\,\mu m$. In order to speed up the sample movement a piezo transducer was used at a frequency ~ 9 kHz. As an object we used a negative

1951 USAF resolution test chart. Instead of a photodiode we used the same camera as in the correlation measurement (Allied Vision Manta-146GB), integrating its readings. An identical camera was used to measure the reflected patterns.

The reconstructed image is shown in Fig. 4.6. Panel b) shows the original object and panel c) is the reconstructed one. After $N_r = 2.7 \times 10^6$ measurements the signal to noise ratio is 2.9.

The blind ghost imaging technique can be modified to be fully non-invasive for the case of fluorescent objects. In Fig. 4.6a we show the setup modification for the fluorescent blind ghost imaging. Behind the transparency mask we place a slab of fluorescent material, YAG:Ce^{3+}. We replace the He-Ne laser with a blue photodiode one (FP-D-450-5P-C-C; Flexpoint, 450nm, 5mW). The typical fluorescent spectrum of this material is shown in Fig. 4.6e. The fluorescent light is collected in reflection using a beam-splitter and a 500 nm long-pass color filter to separate it from the reflected laser light. In

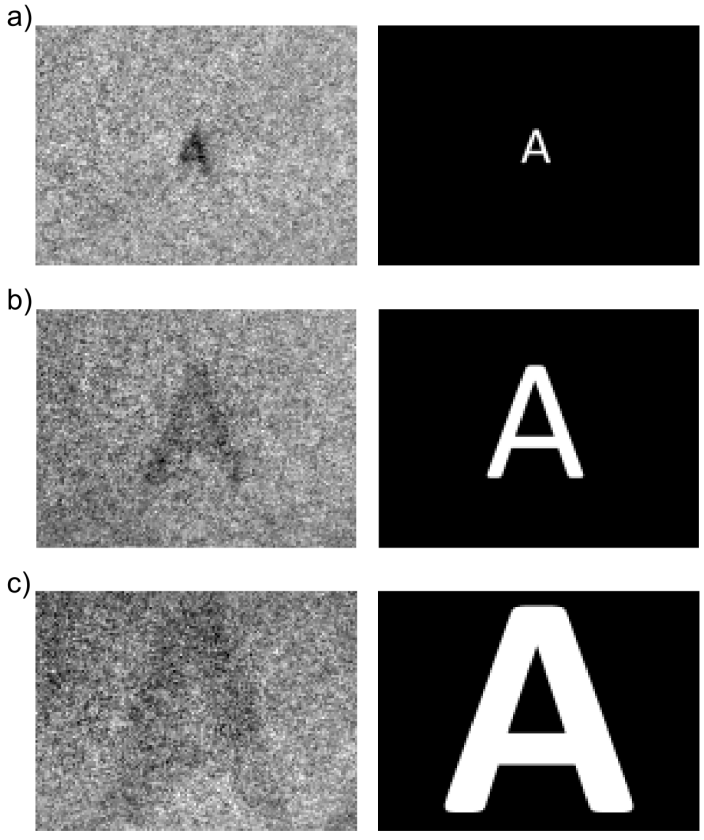

Figure 4.5: Numerical simulation of the blind ghost imaging technique. Right column represents numerical masks applied to the data collected in the correlation function measurement, left column contains reconstructed images for different N_w/N_p: a) $N_w/N_p = 0.0045$, SNR =3.1. b) $N_w/N_p = 0.05$, SNR =1.22. c) $N_w/N_p = 0.24$, SNR =0.57.

Fig. 4.6b we show the original object (top left), the measured correlation function (top right), the convolution of the original object with the measured correlation function (bottom left) and finally the reconstructed object after $N_r = 4.3 \times 10^6$ measurements (bottom right). As we discussed earlier and in the Appendix C the shape of the reconstructed object is the convolution of the original object with the correlation function and that is what we see in the experimental data. This also becomes the main limitation of our method. As we discussed in Sec. 1.3.4, the correlation broadens and decreases in hight as $\sim \frac{1}{L^2}$. It means that firstly more averages is needed to get the same SNR, and more importantly that the reconstructed image resolution is degraded with the increase of the scattering layer thickness.

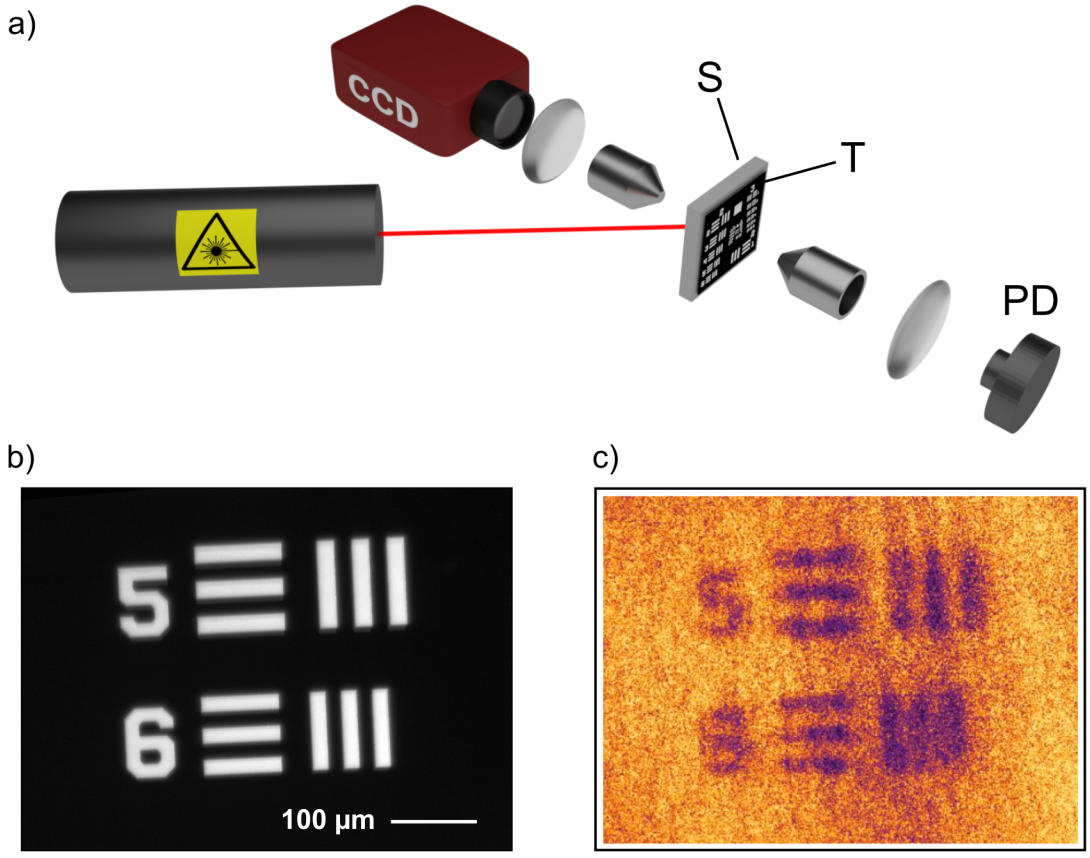

Figure 4.6: Blind ghost imaging. a) Experimental setup is similar to the one used for the correlation measurements (See Fig. 1.2). A semitransparent object (T) (USAF negative target) is placed behind the scattering layer (S). The camera behind the sample collects only integrated intensity acting as a photodiode (PD). The sample has $L = 40\mu m$ and $\ell = 16 \pm 2\mu m$. b) Original object (part of the USAF target). c) Reconstructed image after $N_{\mathrm{r}} \approx 2.27 \times 10^6$ averages, SNR ≈ 2.9.

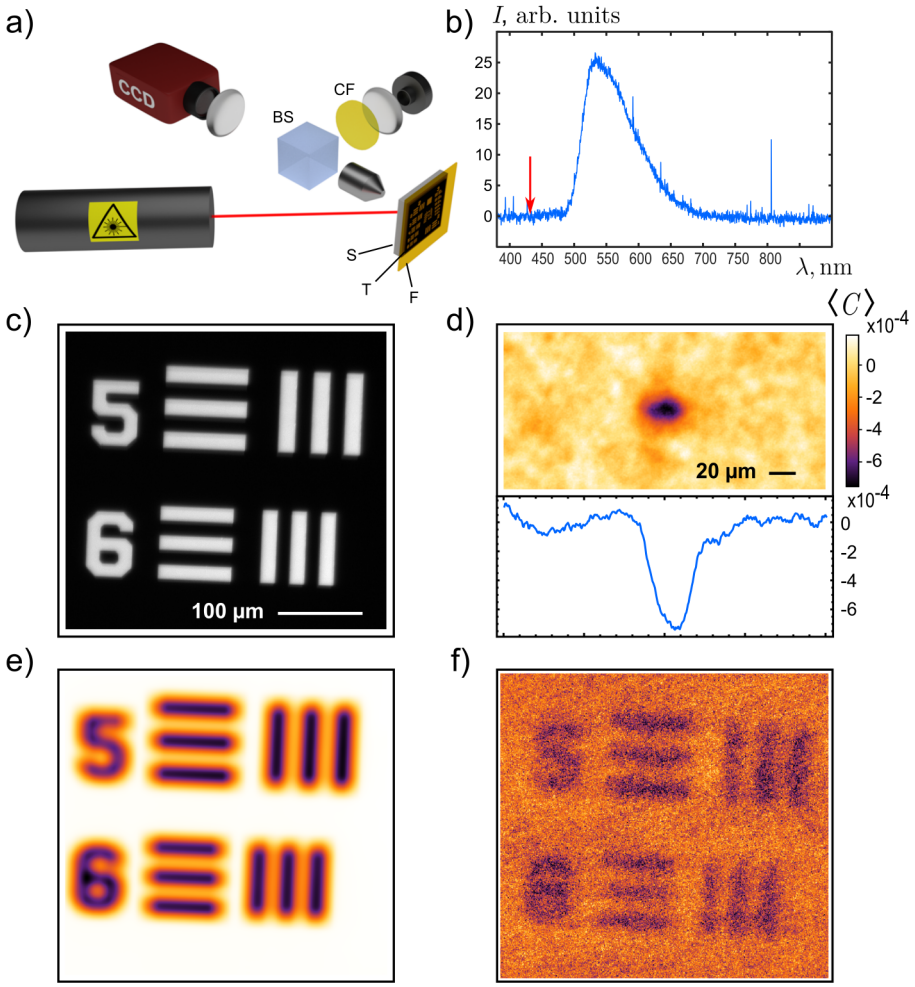

Figure 4.7: Non-invasive blind ghost imaging using of a fluorescent object. a) Experimental setup is similar to the one presented in Fig. 4.6a. Instead a photodiode behind the scattering sample (S) and the target (T), we put a layer of fluorescent material (F) just behind them. Being illuminated by the transmitted speckle, it produces a fluorescence signal, detected by the photodiode decoupled from the pump light by a beam-splitter (BS) and colourfilter (CF). b) YAGCe^{3+} fluorescence spectrum, pump wavelength indicated by a red arrow. c) Original object. d) Correlation function between the reflected and transmitted speckles for the sample used in a). e) Convolution (calculated) between the correlation function and the original object in c. f) Image reconstructed using blind ghost imaging technique after $N_{\mathrm{r}} \approx 4 \times 10^6$ averages.

4.4 Deterministic approach to ghost imaging. Compressive sensing

Let's consider the image reconstruction problem from a different perspective. We can rewrite the expression for the photodiode readings, (4.2), in a matrix form:

$$\mathbf{c} = \mathbf{R} * \mathbf{\Lambda}, \tag{4.29}$$

where $\mathbf{c} = \{c_i\}$, $\mathbf{R} = \{R_{ij}\}$ and $\mathbf{\Lambda} = \{\Lambda_j\}$. Now we can treat this as a system of linear equations, and assuming that $N_\mathrm{r} \geq N_\mathrm{p}$ and that there is no noise in c_i and R_{ij}, we can get an exact solution of this system

$$\mathbf{\Lambda} = \mathbf{R}^{-1} * \boldsymbol{c}, \tag{4.30}$$

by inverting $\mathbf{R}$. This, in principle, allows to perfectly reconstruct the object, however the performance of this method is severely degraded by the photodiode or the imaging device (that captures the speckle) noise. In Fig. 4.8a we compare the performance of the statistical (left column) and matrix inversion (right column) approaches. We add zero mean random Gaussian noise with variance s to the c_i. It is possible to see that in the absence of noise matrix inversion gives perfect reconstruction, however already at the level of the photodiode SNR ≤ 2, the inversion method stops working. At the same time in the statistical approach such noise just averages out, almost not affecting the reconstructed image.

When $N_\mathrm{r} \leq N_\mathrm{p}$ the inversion problem becomes underdefined. It is still possible to use a generalized pseudoinverse [85] of $\mathbf{R}$, however this again leads to an error in the reconstruction. In Fig. 4.8b we compare the deterministic and statistical reconstruction performance at different numbers of averages N_r. In the statistical method, as we figured out in the previous section, SNR reduces as $\frac{1}{\sqrt{N_\mathrm{r}}}$. The inversion method starts from a better SNR, however it decays faster and the two methods give comparable results at $N_\mathrm{r} \approx N_\mathrm{p}/2$.

It is possible to improve significantly the reconstruction quality of the deterministic method in the $N_\mathrm{r} < N_\mathrm{p}$ domain using some prior information about the object. The technique that allows to do that is called *compressive sensing* [86, 87]. One can use optimization methods to find an approximate solution of a linear system (4.29), using prior information about the object in a form of a set of optimization constraints. There are two conditions that should be satisfied during the reconstruction procedure.

- The reconstructed object should be sparse in some basis [88]. In other words, there should be a basis, in which it is described only by a few non-zero coefficients. Mathematically sparsity is characterized by the generalized norm of the vector

$$||\mathbf{x}||_n, \quad n = 0, 1 \ldots \infty \tag{4.31}$$

  Finding the sparsity basis is often a challenging task. For most of the natural images the basis of the discrete Fourier transform harmonics is a good choice [89]. However if a particular set of images to reconstruct is given, an optimal basis

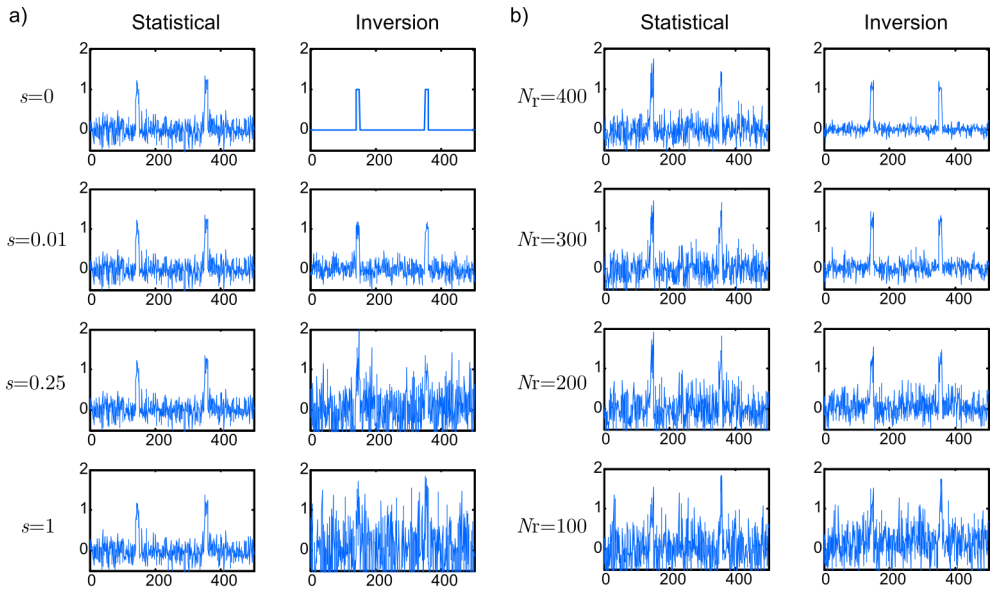

Figure 4.8: Performance of the statistical and inversion reconstruction in the situation when a) white noise with the variance s is added to the bucket detector readings b) when $N_\mathrm{r} < N_\mathrm{p}$ and pseudoinverse is used.

can be constructed using the machine learning algorithms [90] in terms of the generalized wavelet functions [91].

- The measurement basis should be incoherent with the object's sparsity basis [88]. The formal definition of the basis coherence is:

$$\Xi = \max_{k,j}(\langle \phi_k \psi_j \rangle), \tag{4.32}$$

where $\{\phi_k\}$ and $\{\psi_k\}$ are the measurement and object sparsity basis respectively. The lower Ξ the better is the reconstruction, because in such a situation a measurement covers many coefficients in the sparsity basis simultaneously.

We can apply compressive sensing to improve the quality of the speckle pattern ghost imaging. The most natural sparsity assumption follows from the conditions of the ghost imaging best performance $N_\mathrm{w} \ll N_\mathrm{p}$, which means that there are a few non-zero pixels in the image and it is sparse in the canonical (pixel) basis. With such a choice of the sparsity basis, the second requirement of the compressive sensing applicability is automatically fulfilled, as speckle basis, being the measurement basis, is incoherent with the canonical one. Another fair sparsity assumption for a binary object is minimal total variation, or in other word small amount of sharp edges. We will explore this variant as well.

For the canonical basis sparsity assumption, the mathematical formulation of the

problem is the following: given a measurement matrix $\mathbf{R}$ constructed of the speckle patterns and a vector of photodiode readings $\mathbf{c}$, find a vector $\mathbf{\Lambda}_{\text{rec}}$:

$$\min ||\mathbf{\Lambda}_{\text{rec}}||_n \quad \text{subject to} \quad \mathbf{c} = \mathbf{R} * \mathbf{\Lambda}_{\text{rec}}. \tag{4.33}$$

For n=0 the problem is shown to be NP hard [89], whereas for n=2, although being simpler, the optimization gives effectively the same result as (4.30) with $\mathbf{R}$ pseudoiversed. When $n = 1$ the problem is known as the basis pursuit [92]. There are multiple ways of solving that problem, such as LASSO regression [93], conjugate gradient [46], or primal-dual algorithms [94]. We use the l_1-MAGIC package for Matlab [95], which in its turn uses the log-barrier iterative method for a quadratically constraint l_1 minimization problem:

$$\min ||\mathbf{\Lambda}_{\text{rec}}||_1 \quad \text{subject to} \quad ||\mathbf{c} - \mathbf{R} * \mathbf{\Lambda}_{\text{rec}}||_2 \leq s, \tag{4.34}$$

which is equivalent to (4.33), but additionally accounts for the photodiode readings noise. The primal-dual reconstruction is also available within this package. We also use TMSBL package [96], based on sparse Bayesian learning algorithm exploiting correlations in the reconstructed signal. In Fig. 4.9a we show the images of an object in Fig. 4.3 reconstructed using the log-barrier algorithm at $N_{\text{r}} < N_{\text{p}}$, to be compared with Fig. 4.8b. As we can see, almost perfect reconstruction is possible even at $N_{\text{r}} = N_{\text{p}}/7$. In Fig. 4.9b we compare the performance of 3 different compressive sensing algorithms: primal-dual, log-barrier and sparse Bayesian learning in the presence of photodiode noise. We plot the reconstruction error

$$\text{ER} = ||\mathbf{\Lambda} - \mathbf{\Lambda}_{\text{rec}}||_2, \tag{4.35}$$

as a function of N_{r} and s. The first thing that we see is that there is a threshold in the number of measurements, $N_r \approx 65$, under which the reconstruction is infeasible. In the region of large N_r the noise degrades the reconstruction quality for both algorithms, however, as we can see the log-barrier algorithm is more efficient. This means that contrary to the statistical approach additional noisy measurements do not improve the reconstruction quality and for a given amount of noise there is an optimal number of measurements, which is almost the same for both algorithms.

Finally we apply the log-barrier and total variation minimization reconstruction methods to a 2D object. The variation is defined as

$$\text{TV} = \int ||\nabla \Lambda(x, y)||_2 \, dxdy, \tag{4.36}$$

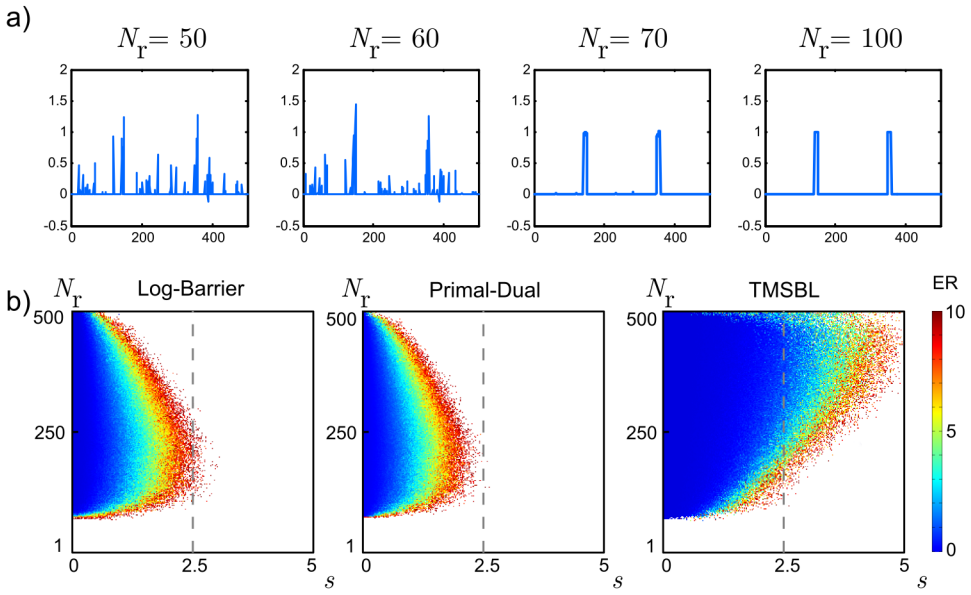

Figure 4.9: Compressive sensing algorithms performance. a) Object reconstruction at $N_r \ll N_p$ (to be compared with Fig. 4.8). b) Recnotruction error ER (4.35) as a function of number of measurements N_r and the bucket detector noise s for three different reconstruction algorithms: log-barrier, primal-dual and TMSBL.

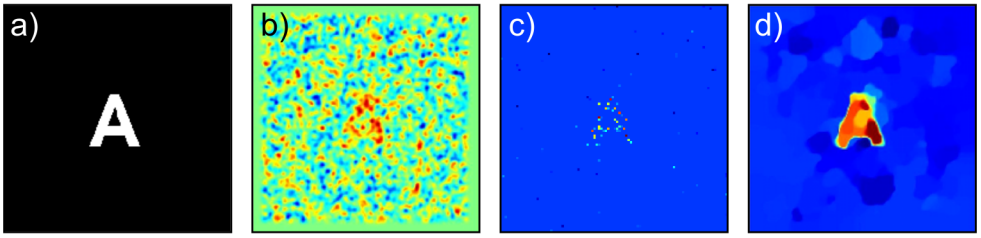

Figure 4.10: 2D image reconstruction using different sparsity assumptions. a) Original image. b) Statistically reconstructed image. c) Pixel basis sparsity assumption. d) Total variation sparsity assumption. In all of the reconstructed images $N_r = 100$.

where $\Lambda(x, y)$ is a 2D object and ∇ is the gradient operator. The resulting reconstructed images are shown in Fig. 4.10, from which it is possible to see that the total variation minimization gives a reasonable reconstruction from only 100 measurements of a 200x200 image.

4.4.1 Summary and outlook

In this chapter we introduced a novel imaging technique that we call blind ghost imaging. It is a modification of the normal ghost imaging method that exploits mesoscopic correlation between the reflected and transmitted speckle patterns. We analysed the signal-to-noise ratio of the normal ghost imaging technique and extended this analysis

to the blind ghost imaging. In contrast to the previous attempts to apply regular ghost imaging to retrieve the shape of the objects hidden inside or behind the scattering media [97–99], our method allows to do that in highly scattering media (OD$\gg 1$). Its only limitation is the loss of resolution with the increase of the scattering layer thickness.

We explored the possibilities to reduce the number of measurements in regular ghost imaging using compressive sensing. The next step is to apply the compressive sensing methods to the blind ghost imaging, however it is a challenging task, because the low reflection-transmission correlation in blind ghost imaging setup is equivalent to a severe (of an order of $1/C^{RT}$) photodiode noise in normal ghost imaging. None of the compressive sensing algorithms considered here is able to work with such a noise, therefore a custom optimization algorithm is required.

Chapter 5

Quantum description of the electromagnetic field

With this chapter we start the discussion of the quantum correlations in multiply scattered fields. In order to do that we first need to introduce theoretical concepts related to the analysis of the quantum states of light, non-classicality and quantum correlations, which is the main purpose of this chapter.

We start with the theory of the second quantization and describe the transition from the field dynamical variables to the corresponding quantum-mechanical operators. Being a quantum object the field itself is described by a *state* in an abstract Hilbert space. We identify the subspace of the Hilbert space suitable for the field description and introduce several classes of states relevant for the further discussion. As quantum physics contains classical physics as a limiting case, some of the states of the field might not actually require quantum description. In the final part of this chapter we revise the methods that allow to check if a given state requires quantum mechanical description or the classical one is sufficient.

5.1 Quantization of electromagnetic field

In most cases light can be described as a classical wave obeying a set of Maxwell's equations. However, in certain situations such description is not sufficient. The idea of light consisting of tiny discrete particles existed since the times of Newton or even earlier, since ancient philosophers introduced it [100]. This idea was revisited in more recent times to address numerous evidence of the light discreteness, such as photoelectric effect, atoms stability and resolution of the ultraviolet catastrophe by means of Planck's summation approach, leading to the development of quantum mechanics. Despite its

success in the description of many physical phenomena, in its early days this theory suffered from a lot of issues. One of them was difficulty to describe the effects involving more than one particle within the wavefunction approach. In particular, in context of the electromagnetic field, while it was clear that it is carried by the discrete quanta, it was not less clear how and why they appear. This problem was resolved by P. Dirac, who developed the rigorous theory of the electromagnetic radiation quantization [101], named *second quantization*. Since then, his approach is a standard method of the field theory, that allows transition from classical to quantum picture for various systems.

For the case of the electromagnetic field,the procedure of the 2nd quantization consists of the following steps [102, 103]:

- Write the Hamiltonian of the system (field) and identify the canonical conjugate variables.
- Assign operators to these quantities and figure out their commutation relations.
- Identify the creation and annihilation operators and their commutation relations.
- Construct the state space using the creation and annihilation operators.

The classical expression for the energy (Hamiltonian) of the electromagnetic field is:

$$\mathcal{H} = \frac{1}{2}\int \left(\epsilon_0 \mathbf{E}^2(\mathbf{r},t) + \frac{1}{\mu_0}\mathbf{B}^2(\mathbf{r},t)\right) dV. \tag{5.1}$$

Its first term stands for the kinetic energy of the field, while the second is the potential energy, therefore the Lagrangian of the system is:

$$\mathcal{L} = \frac{1}{2}\int \left(\epsilon_0 \mathbf{E}^2(\mathbf{r},t) - \frac{1}{\mu_0}\mathbf{B}^2(\mathbf{r},t)\right) dV. \tag{5.2}$$

It is convenient to replace the electric and magnetic field in these expressions with the vector potential $\mathbf{A}$, which satisfies:

$$\mathbf{B}(\mathbf{r},t) = \nabla \times \mathbf{A}(\mathbf{r},t), \quad \mathbf{E}(\mathbf{r},t) = -\partial \mathbf{A}(\mathbf{r},t)/\partial t\,. \tag{5.3}$$

The Lagrangian becomes:

$$\mathcal{L} = \frac{1}{2}\int \left(\epsilon_0 \left(\frac{\mathbf{A}(\mathbf{r},t)}{\partial t}\right)^2 - \frac{1}{\mu_0}\left(\nabla \times \mathbf{A}(\mathbf{r},t)\right)^2\right) dV. \tag{5.4}$$

If we take $\mathbf{A}$ as one of the canonical variables, its conjugate pair is

$$\mathbf{\Pi}(\mathbf{r},t) = \frac{\partial \mathcal{L}}{\partial(\partial \mathbf{A}(\mathbf{r},t)/\partial t)} = \epsilon_0 \partial \mathbf{A}(\mathbf{r},t)/\partial t. \tag{5.5}$$

According to the canonical quantization scheme we can replace the classical canonically conjugate fields with the corresponding quantum-mechanical operators, $\mathbf{A} \mapsto \hat{\mathbf{A}}$, $\mathbf{\Pi} \mapsto \hat{\mathbf{\Pi}}$, satisfying the commutation relations:

$$\begin{aligned} \left[\hat{\mathrm{A}}_n(\mathbf{r},t),\, \hat{\Pi}_k(\mathbf{r}',t)\right] &= i\hbar\delta_{nk}\delta_\perp(\mathbf{r}-\mathbf{r}'), \\ \left[\hat{\mathrm{A}}_n(\mathbf{r},t),\, \hat{\mathrm{A}}_k(\mathbf{r}',t)\right] &= \left[\hat{\Pi}_n(\mathbf{r},t),\, \hat{\Pi}_k(\mathbf{r}',t)\right] = 0, \end{aligned} \tag{5.6}$$

where $\hat{\mathrm{A}}_n$ and $\hat{\Pi}_k$ are components of $\hat{\mathbf{A}}$ and $\hat{\mathbf{\Pi}}$, δ_{nk} is the Kronecker-delta, and $\delta_\perp$ is the transverse delta function

$$\delta_\perp(\mathbf{r}-\mathbf{r}') = \delta^3(\mathbf{r}-\mathbf{r}') + \frac{1}{4\pi}\nabla\times\nabla\frac{1}{|\mathbf{r}-\mathbf{r}'|}. \tag{5.7}$$

Commutation relations (5.6) are useful for general understanding of the field configuration, however they depend on the spatial coordinates, which complicates their practical use. One of the ways to address this problem is the monochromatic mode expansion. The fields $\mathbf{A}$ and $\mathbf{\Pi}$ are decomposed over an orthogonal mode basis. In that decomposition, the amplitudes of the expansion become the canonical variables. Their commutation relations do not depend on the spatial coordinates, because it is transfered into the mode configuration.

In order to perform the mode decomposition, equations of motion of the system should be specified. This can be easily done by substituting (5.4) into the Euler-Lagrange equations of motion, which gives the regular wave equation for the vector potential (assuming Coulomb gauge, $\nabla\cdot\mathbf{A}=0$)

$$\nabla^2\mathbf{A}(\mathbf{r},t) = \frac{1}{c^2}\frac{\partial^2\mathbf{A}(\mathbf{r},t)}{\partial t^2} \tag{5.8}$$

The solution of this equation in free space can be written in the form of a plane wave decomposition

$$\mathbf{A}(\mathbf{r},t) = \sum_{\mathbf{k}} \left(\mathcal{A}_{\mathbf{k}}(t)e^{i\mathbf{kr}} + \mathcal{A}^*_{\mathbf{k}}(t)e^{-i\mathbf{kr}}\right). \tag{5.9}$$

Substituting this expression into the wave equation (5.8) we obtain the equation of

motion for $\mathcal{A}_{\mathbf{k}}(t)$:

$$\left(\frac{\partial^2}{\partial t^2} + \omega_{\mathbf{k}}^2\right) \mathcal{A}_{\mathbf{k}}(t) = 0, \quad (\omega_{\mathbf{k}} = \mathbf{k}c), \tag{5.10}$$

which has a solution:

$$\mathcal{A}_{\mathbf{k}}(t) = \mathcal{A}_{\mathbf{k}} e^{-i\omega_{\mathbf{k}} t}\,. \tag{5.11}$$

The full solution to the wave equation is

$$\mathbf{A}(\mathbf{r}, t) = \sum_{\mathbf{k}} \sum_{\nu} \left(a_{\mathbf{k}\nu} \mathbf{e}_{\nu} e^{i\mathbf{k}\mathbf{r} - i\omega_{\mathbf{k}} t} + a^*_{\mathbf{k}\nu} \mathbf{e}^*_{\nu} e^{-i\mathbf{k}\mathbf{r} + i\omega_{\mathbf{k}} t} \right), \tag{5.12}$$

where $\mathbf{e}_\nu$ are the polarization unit vectors. Now for each mode with a wave vector $\mathbf{k}$ and polarization $\mathbf{e}_\nu$ we can introduce a pair of real variables:

$$\begin{aligned} x_{\mathbf{k}\nu}(t) &= a_{\mathbf{k}\nu} e^{-i\omega_{\mathbf{k}} t} + a^*_{\mathbf{k}\nu} e^{i\omega_{\mathbf{k}} t}, \\ p_{\mathbf{k}\nu}(t) &= -i\omega_{\mathbf{k}} (a_{\mathbf{k}\nu} e^{-i\omega_{\mathbf{k}} t} - a^*_{\mathbf{k}\nu} e^{i\omega_{\mathbf{k}} t}), \end{aligned} \tag{5.13}$$

that form canonically conjugate pairs

$$\begin{aligned} \frac{\partial x_{\mathbf{k}\nu}}{\partial t} &= p_{\mathbf{k}\nu}, \\ \frac{\partial p_{\mathbf{k}\nu}}{\partial t} &= -\omega_{\mathbf{k}}^2 x_{\mathbf{k}\nu}, \end{aligned} \tag{5.14}$$

The Hamiltonian of the field is

$$\mathcal{H} = \frac{1}{2} \sum_{\mathbf{k}} \sum_{\nu} \left(p^2_{\mathbf{k}\nu} + \omega^2 x^2_{\mathbf{k}\nu} \right), \tag{5.15}$$

which is a sum of the energies of individual independent modes with wave vectors $\mathbf{k}$ and polarizations $\mathbf{e}_\nu$. By the same procedure as in (5.6) we can assign operators to x and p

$$x_{\mathbf{k}\nu} \mapsto \sqrt{\frac{\hbar}{2\epsilon_0 \omega_{\mathbf{k}}}} \hat{x}_{\mathbf{k}\nu}, \quad p_{\mathbf{k}\nu} \mapsto \sqrt{\frac{\hbar}{2\epsilon_0 \omega_{\mathbf{k}}}} \hat{p}_{\mathbf{k}\nu}, \tag{5.16}$$

obeying commutation relations:

$$[\hat{x}_{\mathbf{k}\nu}, \hat{p}_{\mathbf{k}\nu}] = \frac{i}{2} \delta_{\mathbf{k}\mathbf{k}'} \delta_{\nu\nu'}\,, \tag{5.17}$$

$$[\hat{x}_{\mathbf{k}\nu}, \hat{x}_{\mathbf{k}\nu}] = 0\,, \tag{5.18}$$

$$[\hat{p}_{\mathbf{k}\nu}, \hat{p}_{\mathbf{k}\nu}] = 0. \tag{5.19}$$

Operators $\hat{x}_{\mathbf{k}\nu}$ and $\hat{p}_{\mathbf{k}\nu}$ have a distinct physical meaning. The electric field (5.3) us-

ing (5.12) can be expressed in terms of these variables

$$E(\mathbf{r},t)=\sum_{\mathbf{k}}\sum_{\nu}\left(x_{\mathbf{k}\nu}\sin\left(\omega_{\mathbf{k}}t-\mathbf{kr}\right)-p_{\mathbf{k}\nu}\cos\left(\omega_{\mathbf{k}}t-\mathbf{kr}\right)\right), \tag{5.20}$$

which shows that x and p are the amplitudes of the two components of the field shifted by 90° in phase. They are called quadratures and $\hat{x}_{\mathbf{k}\nu}$ and $\hat{p}_{\mathbf{k}\nu}$ are called quadrature operators. These quantities are analogous to the position and momentum of a harmonic oscillator and can be measured experimentally.

Now we can start building the state space for the electromagnetic field. The most natural choice of that space is the set of the eigenstates of the field Hamiltonian, which also becomes an operator in the quantized picture. It is convenient to introduce a pair of conjugate operators

$$\hat{a}_{\mathbf{k}\nu} = \omega_{\mathbf{k}}\hat{x}_{\mathbf{k}\nu}+i\hat{p}_{\mathbf{k}\nu} \tag{5.21}$$

$$\hat{a}^{\dagger}_{\mathbf{k}\nu} = \omega_{\mathbf{k}}\hat{x}_{\mathbf{k}\nu}-i\hat{p}_{\mathbf{k}\nu}. \tag{5.22}$$

called creation and annihilation operators. As $\hat{a}\neq\hat{a}^{\dagger}$, they do not represent any observable quantities, however they are useful in calculations. Their commutation relations can be derived from (5.17) – (5.19).

$$\left[\hat{a}_{\mathbf{k}\nu},\hat{a}^{\dagger}_{\mathbf{k}\nu}\right]=\delta_{\mathbf{k}\mathbf{k}'}\delta_{\nu\nu'}\,, \tag{5.23}$$

$$\left[\hat{a}_{\mathbf{k}\nu},\hat{a}_{\mathbf{k}\nu}\right]=0\,, \tag{5.24}$$

$$\left[\hat{a}^{\dagger}_{\mathbf{k}\nu},\hat{a}^{\dagger}_{\mathbf{k}\nu}\right]=0. \tag{5.25}$$

The Hamiltonian (5.15) can be expressed in terms of these operators

$$\hat{\mathcal{H}}=\sum_{\mathbf{k}}\sum_{\nu}\hbar\omega_{\mathbf{k}}\left[\hat{a}_{\mathbf{k}\nu}\hat{a}^{\dagger}_{\mathbf{k}\nu}+\frac{1}{2}\right]=\sum_{\mathbf{k}}\sum_{\nu}\hat{\mathcal{H}}_{\mathbf{k}\nu}\,, \tag{5.26}$$

where $\hat{\mathcal{H}}_{\mathbf{k}\nu}$ is a Hamiltonian of each of the modes with a wave vector $\mathbf{k}$ and polarization $\mathbf{e}_{\nu}$. Let's denote the eigenvectors of $\hat{\mathcal{H}}_{\mathbf{k}\nu}$ as $|n_{\mathbf{k}\nu}\rangle$. The eigenvalues of this operator, $\mathcal{E}_{n\mathbf{k}\nu}$,

$$\hat{\mathcal{H}}_{\mathbf{k}\nu}|n_{\mathbf{k}\nu}\rangle=\mathcal{E}_{n\mathbf{k}\nu}|n_{\mathbf{k}\nu}\rangle, \tag{5.27}$$

correspond to the allowed energy levels of each mode. Substituting $\hat{\mathcal{H}}_{\mathbf{k}\nu}$ from (5.15) into (5.27), multiplying both side with $\hat{a}^{\dagger}_{\mathbf{k}\nu}$ and using the commutation relations (5.23)

gives

$$\hat{\mathcal{H}}_{\mathbf{k}\nu}\hat{a}^\dagger_{\mathbf{k}\nu}|n_{\mathbf{k}\nu}\rangle = (\mathcal{E}_{n\mathbf{k}\nu} + \hbar\omega_{\mathbf{k}})\hat{a}^\dagger_{\mathbf{k}\nu}|n_{\mathbf{k}\nu}\rangle, \tag{5.28}$$

which means that $\hat{a}^\dagger_{\mathbf{k}\nu}|n_{\mathbf{k}\nu}\rangle$ is also an eigenvector of the mode's Hamiltonian with an eigenvalue $\mathcal{E}_{n\mathbf{k}\nu} + \hbar\omega_{\mathbf{k}}$. Repeating this multiple times we can see that the energy of the mode changes in discrete portions equal to $\hbar\omega_{\mathbf{k}}$. This is exactly what we were aiming for, as it captures the discrete nature of light and these energy portions are the quanta of electromagnetic radiation called photons.

The operator $\hat{a}^\dagger_{\mathbf{k}\nu}$ increases the energy of the mode by one portion, or in other words, it adds a photon to the mode. To capture that, we can assign a different eigenvector to the increased eigenvalue

$$\hat{a}^\dagger_{\mathbf{k}\nu}|n_{\mathbf{k}\nu}\rangle = \sqrt{n_{\mathbf{k}\nu}+1}|n_{\mathbf{k}\nu}+1\rangle, \tag{5.29}$$

where the $\sqrt{n_{\mathbf{k}\nu}+1}$ prefactor is added for the normalization purpose. This is where the name "creation operator" comes from. The adjoint of the creation operator reduces the number of photons in the mode:

$$\hat{a}_{\mathbf{k}\nu}|n_{\mathbf{k}\nu}\rangle = \sqrt{n_{\mathbf{k}\nu}}|n_{\mathbf{k}\nu}-1\rangle, \tag{5.30}$$

that is why it is called "annihilation" operator.

Acting on $|n_{\mathbf{k}\nu}\rangle$ consecutively with the annihilation and then with the creation operator results in

$$\hat{a}^\dagger_{\mathbf{k}\nu}\hat{a}_{\mathbf{k}\nu}|n_{\mathbf{k}\nu}\rangle = n_{\mathbf{k}\nu}|n_{\mathbf{k}\nu}\rangle, \tag{5.31}$$

therefore the operator $\hat{a}^\dagger_{\mathbf{k}\nu}\hat{a}_{\mathbf{k}\nu} = \hat{n}_{\mathbf{k}\nu}$ is called a number operator. It is similar, apart from a constant factor, to the Hamiltonian of the EM field and its eigenvalues correspond to the number of photons in the mode. Using (5.20) the electric field operator can be written as

$$\hat{E}_{\mathbf{k}\nu}(\mathbf{r},t) = \hat{E}^+_{\mathbf{k}\nu}(\mathbf{r},t) + \hat{E}^-_{\mathbf{k}\nu}(\mathbf{r},t), \tag{5.32}$$

where

$$\hat{E}^+_{\mathbf{k}\nu}(\mathbf{r},t) = \sqrt{\frac{\hbar\omega_{\mathbf{k}}}{2\epsilon_0}}\hat{a}_{\mathbf{k}\nu}e^{-i\omega_{\mathbf{k}}t - i\mathbf{kr}}, \quad \hat{E}^-_{\mathbf{k}\nu}(\mathbf{r},t) = \sqrt{\frac{\hbar\omega_{\mathbf{k}}}{2\epsilon_0}}\hat{a}^\dagger_{\mathbf{k}\nu}e^{i\omega_{\mathbf{k}}t + i\mathbf{kr}} \tag{5.33}$$

are the positive and negative frequency components of the field. From this expression follows, that when a classical field is represented as a positive frequency Fourier series over the spatial harmonics, in order to switch to the quantum description and get the field operator, we just need to replace the amplitudes of the modes by the corresponding annihilation operators. Now we have all the instruments to explore the space of

the possible states of the EM radiation, but before doing that, let's make a couple of important remarks.

First of all, due to the proposed quantization scheme the commutation relations between the mode operators do not depend on the spatial coordinates. It means that in the considered situation of the free EM field its spatial configuration is fully determined by classical mechanics. In other words, the interference patterns and the speckle produced by the exotic quantum states of light will be the same as for classical field. However the dynamics of the field depends on the state of modes, which can be observed by measuring the photon statistics of light using homodyne detection [104] or other techniques [105]. Finally this argument can break for the systems where the separation of spatial and time dependence of the field is impossible, such as nonlinear or inhomogeneous media[106]. Propagation of non-classical light in such media can lead to some interesting features of the output field spatial distribution [107, 108].

5.2 Quantum states of light

In the previous chapter we outlined a basis in the Hilbert space of the states of the EM field. For a given mode with a wave vector $\mathbf{k}$ and polarization ν, such a basis is formed by a set of the eigenvectors of the number operator $\hat{n}$ of this mode (for simplicity we skip the $\mathbf{k}$ and ν indices)

$$\hat{n}|n\rangle = n|n\rangle. \tag{5.34}$$

Any other pure state of the EM field of this mode can be expressed as a linear combination of the basis vectors

$$|\Psi\rangle = \sum_n c_n|n\rangle, \quad c_n \in \mathbb{C}, \quad \sum_n |c_n|^2 = 1. \tag{5.35}$$

To get a complete description of the field we need to consider also statistical mixtures of arbitrary pure states $|\Psi_n\rangle$

$$\rho = \sum_n p_n|\Psi_n\rangle\langle\Psi_n|, \quad 0 \geq p \geq 1, \quad \sum_n p_n = 1 \tag{5.36}$$

There is a whole multitude of ways to construct a valid physical state specifying c_n and p_n. We now introduce the states that are relevant for the following discussion and outline their most important properties.

- The vacuum, $|0\rangle$, is the ground state of the EM field. It is defined as such a state

for which

$$\hat{a}|0\rangle = 0. \tag{5.37}$$

Despite being minimal, the energy of the field in a vacuum state, $\langle 0|\mathcal{H}|0\rangle$ is non-zero, which is in a drastic contradiction to the classical theory. The mean number of photons of the field in this state is 0, however the variances of its quadratures are non-zero, indicating presence of fluctuations. These quantum fluctuations are responsible for such phenomena as spontaneous emission, Casimir force and Lamb shift and establish an uncertainty limit on the simultaneous measurement of the non-commuting field observables.

- Fock states

  The basis vectors $|n\rangle$ themselves are appropriate states of the field called Fock states. Any of these states can be obtained from the vacuum as

$$|n\rangle = \frac{1}{\sqrt{n!}} \left(\hat{a}^\dagger\right)^n |0\rangle \tag{5.38}$$

  The mode in such a state has a fixed number of photons per unit interval, equal to n, however as it follows from the Heisenberg indeterminacy principle the uncertainty in the time of emission of these photons is maximal. Returning to the wave picture of EM radiation, a mode in such a state will have fixed amplitude, but a completely randomized phase. Fock states exhibit features that are unavailable for regular waves, demonstrating their genuinely quantum nature. It is captured by various non-classicality criteria that will be discussed in the nest sections.

- Coherent states were introduced by Glauber [109] and Sudarshan [110], to explain the photon statistics of the ideal shot noise limited laser radiation as the eigenstates of the annihilation operator

$$\hat{a}|\alpha\rangle = \alpha|\alpha\rangle. \tag{5.39}$$

  In the Fock basis a coherent state can be written as

$$|\alpha\rangle = e^{-\frac{|\alpha|^2}{2}} \sum_n \frac{\alpha^n}{\sqrt{n!}}|n\rangle, \tag{5.40}$$

  where parameter α corresponds to the classical amplitude of the electric field of

the light mode. This expression, using (5.38) can be rewritten as

$$|\alpha\rangle = e^{-\frac{|\alpha|^2}{2}} \sum_n \frac{\left(\alpha\hat{a}^\dagger\right)^n}{n!}|0\rangle = e^{\left(\alpha\hat{a}^\dagger - \frac{|\alpha|^2}{2}\right)}|0\rangle = \\ = e^{\left(\alpha\hat{a}^\dagger - \alpha^*\hat{a}\right)}|0\rangle = \hat{D}(\alpha)|0\rangle, \tag{5.41}$$

where $\hat{D} = e^{\left(\alpha\hat{a}^\dagger - \alpha^*\hat{a}\right)}$ is the displacement operator.

A set of coherent states with the amplitude α being a parameter, also form a basis in the Hilbert space of the states of the mode. However in contrast to the Fock basis, the coherent state basis is overcomplete, i. e.

$$\langle\alpha|\beta\rangle = e^{-\frac{1}{2}\left(|\alpha|^2 + |\beta|^2 - 2\alpha^*\beta\right)} \neq 0. \tag{5.42}$$

These states have equal and minimal possible uncertainty in the quadratures or in the phase and the amplitude.

- Squeezed states

  In certain conditions it is possible to reduce or "squeeze" the uncertainty in one of the quadratures, amplitude or phase of the mode [111, 112]. This can be achieved when the light is emitted in the result of the nonlinear process, such as spontaneous parametric down-conversion or optical parametric amplification or alternatively second harmonic generation. Such states of the light field are called squeezed and in the Fock basis they can be expressed as

$$|\zeta\rangle = \sqrt{\cosh r} \sum_{n=0}^{\infty} \frac{\sqrt{2n!}}{n!} \left(\frac{e^{i\theta}\tanh r}{2}\right)^n |2n\rangle, \tag{5.43}$$

  where r is the squeezing parameter and θ is the squeezing phase. Density matrix approach is not the best way of description for such states, a more natural description will be given by the phase-space formulation.

- Thermal states

  By now all the states we considered were pure. However, for example, a black body equilibrium radiation can't be described by a pure state. The state of the field of the mode in that case is mixed and it is described by a density matrix

$$\rho_{\text{th}} = \frac{1}{\bar{n}} \sum_{n=0}^{\infty} \left(\frac{\bar{n}}{1+\bar{n}}\right)^{1+n} |n\rangle\langle n|, \tag{5.44}$$

where $\bar{n}$ is the average number of photons it the mode. The uncertainties in the quadratures for this state are defined by the average number of photons $\bar{n}$ in it.

- Superpositions vs. mixtures of coherent states

  Ability to form superpositions is considered a genuinely quantum feature. The difference between a superposition and a mixture of two states is often illustrated by the following example. Let's consider two states:

$$|\Psi_{\text{sup}}\rangle = \frac{1}{\sqrt{2}}\left(|\psi_1\rangle + |\psi_2\rangle\right) \tag{5.45}$$

  and

$$\rho_{\text{mix}} = \frac{1}{2}\left(|\psi_1\rangle\langle\psi_1| + |\psi_2\rangle\langle\psi_2|\right). \tag{5.46}$$

  When a projective measurement is performed in $\{|\psi_1\rangle, |\psi_2\rangle\}$ basis, both for $|\Psi_{\text{sup}}\rangle$ and for ρ_{mix} the probability to observe either $|\psi_1\rangle$ or $|\psi_2\rangle$ is 1/2. However for $|\Psi_{\text{sup}}\rangle$ there will be a particular basis

$$\{\frac{|\psi_1\rangle + |\psi_2\rangle}{\sqrt{2}}, \frac{|\psi_1\rangle - |\psi_2\rangle}{\sqrt{2}}\} \tag{5.47}$$

  in which there will be no uncertainty in the measurement results and the outcome related to the first basis vector will occur with 100% probability. At the same time, for the state ρ_{mix} any projective measurement basis within the space spanned by $|\psi_1\rangle, |\psi_2\rangle$ will result in 1/2 probability to get either of the outcomes.

  Similar argumentation can be used to distinguish between the superposition

$$|\Psi_{\text{coh sup}}\rangle = c_s|\alpha\rangle + \sqrt{1-c_s^2}|\beta\rangle \tag{5.48}$$

  and a mixture

$$\rho_{\text{coh mix}} = c_m|\alpha\rangle\langle\alpha| + (1-c_m)|\beta\rangle\langle\beta|, \tag{5.49}$$

  of coherent states (5.40), where c_s and c_m are normalization constants. However basis manipulation in the Fock space is less straightforward and the measurement in which $|\Psi_{\text{coh sup}}\rangle$ gives only a particular outcome is hard to interpret.

  Another way to check if a particular state is a superposition is to examine the non-diagonal elements of its density matrix. In our example the density matrix of $|\Psi_{\text{sup}}\rangle$ is

$$\rho_{\text{sup}} = |\Psi_{\text{sup}}\rangle\langle\Psi_{\text{sup}}| = \frac{1}{2}\begin{pmatrix} 1 & 1 \\ 1 & 1 \end{pmatrix}, \tag{5.50}$$

while

$$\rho_{\text{mix}} = \frac{1}{2}\begin{pmatrix} 1 & 0 \\ 0 & 1 \end{pmatrix}. \tag{5.51}$$

As expected, the non-diagonal elements of the second matrix are zeros. However, it is always possible to write the density matrix of a given state in its eigenbasis, in which it is diagonal. In order to quantify the non-classical features using the density matrix non-diagonal elements one either needs to specify a preferred basis (usually the energy basis of the problem), or to consider a full basis set as in the case of the so-called coherence monotones, which will be discussed later in this chapter.

5.3 Phase-space formulation and quasi-probability distributions

In the early days of quantum mechanics, various interpretations of its formalism were proposed, sometimes to complement the mainstream formulation, but more often to oppose it and suggest a better explanation of the physical reality. Although many of these alternative formulations were later shown to be equivalent to each other and to the standard one, leading to the same predictions in similar conditions, some of them still remain useful. Often developed to address a particular system/problem they provide a more convenient way to approach it compared to the other interpretations. For example, path integral formulation [113] is particularly useful for calculating the transition probabilities between different states and the Bohmian formulation [114] allows to get rid of the counterintuitive non-unitary dynamics suggested by the Born rule [115]. The phase-space formulation [116–119], which we introduce in the current chapter is one of these alternative approaches. It uses a well developed apparatus of the probability theory to treat quantum fluctuations within the same framework as stochastic randomness due to incomplete description of the system.

As we figured out in the previous chapter, the states of the EM radiation of a particular mode occupy a space spanned by the basis vectors $|n\rangle$. This is an infinitely dimensional set, therefore a generic state of the mode is described by an infinite dimensional density matrix. The joint state of two modes will reside in the Hilbert space, which is a tensor product of the Hilbert spaces of the individual modes. The density matrix of such a state is not an easy object to handle and the situation gets even worse when additional modes are taken into account.

In phase space, instead of a density matrix, a mode of light is described by a function of two variables, usually the field quadratures. The value of this function is related to the probability to observe certain quadrature values in a measurement. However, since Heisenberg uncertainty relation poses constraints on the simultaneous knowledge of these values, this function might have some features inappropriate for a normal probability distribution (negative or singular values). This is a reason why such functions are called quasiprobability distributions. When additional modes are taken into account, the number of arguments of the quasiprobability distribution increases by two per mode, which makes it convenient to handle using the normal methods of multivariate calculus.

In order to see how it works in details, let's consider a set of N modes with creation operators $\hat{a}_k$, $k = 1 \dots N$, obeying commutation relations similar to (5.23) - (5.25)

$$\left[\hat{a}_k, \hat{a}_l^\dagger\right] = \delta_{kl}, \quad [\hat{a}_k, \hat{a}_l] = 0, \quad \left[\hat{a}_k^\dagger, \hat{a}_l^\dagger\right] = 0. \tag{5.52}$$

Let's arrange the quadrature operators, $\hat{x}_k$ and $\hat{p}_k$ of these modes into a vector

$$\hat{\mathbf{R}} = \{\hat{x}_1, \hat{p}_1, ..., \hat{x}_N, \hat{p}_N\} \tag{5.53}$$

The commutation relation of the elements of $\hat{\mathbf{R}}$ are

$$[\hat{R}_k, \hat{R}_l] = i\Omega_{kl}, \tag{5.54}$$

where Ω_{kl} are the elements of the symplectic matrix

$$\Omega = \begin{pmatrix} 0 & 1 \\ -1 & 0 \end{pmatrix}^{\oplus N} = \begin{pmatrix} 0 & 1 & 0 & 0\dots & 0 & 0 \\ -1 & 0 & 0 & 0\dots & 0 & 0 \\ 0 & 0 & 0 & 1\dots & 0 & 0 \\ 0 & 0 & -1 & 0\dots & 0 & 0 \\ \vdots & \vdots & \vdots & \ddots & \vdots & \vdots \\ 0 & 0 & 0 & 0\dots & 0 & 1 \\ 0 & 0 & 0 & 0\dots & -1 & 0 \end{pmatrix}. \tag{5.55}$$

The first step to get the quasiprobability distributions of a state ρ is to compute its characteristic function

$$\chi_\kappa(\boldsymbol{\xi}) = \mathrm{Tr}[\rho\, \hat{\mathbf{D}}(\boldsymbol{\xi})]\, e^{\frac{1}{2}\kappa||\boldsymbol{\xi}||^2}, \quad \kappa \in \{-1, 0, 1\}, \tag{5.56}$$

where $\hat{\mathbf{D}}(\boldsymbol{\xi}) = \{\hat{D}_k(\xi_k)\}$ is a multimode generalization of the displacement opera-

tor (5.41)

$$\hat{D}_k(\xi_k) = e^{(\xi_k \hat{a}_k^\dagger - \xi_k^* \hat{a}_k)} \tag{5.57}$$

and $\boldsymbol{\xi}$ is a $2N$-dimensional vector of phase-space variables, $\boldsymbol{\xi} \in \mathbb{R}^{2N}$. After writing (5.57) in a more compact form

$$\hat{\mathbf{D}}(\boldsymbol{\xi}) = e^{i\hat{\mathbf{R}}^{\mathrm{T}}\Omega\boldsymbol{\xi}}, \tag{5.58}$$

the κ parametrized set of the quasiprobability distributions is obtained from the characteristic function via a complex Fourier transform [120],

$$W_\kappa(\mathbf{R}) = \frac{1}{(2\pi^2)^N} \int e^{i\boldsymbol{\zeta}^{\mathrm{T}}\Omega\mathbf{R}} \chi_\kappa(\boldsymbol{\zeta}) d^{2N}\boldsymbol{\zeta}, \tag{5.59}$$

where $\mathbf{R} = \{x_1, p_1, ..., x_N, p_N\}$ in analogy to (5.53). Depending on the value of κ we get the following distributions:

- Wigner function [116]: $\kappa = 0$

  It is the most commonly used quasiprobability distribution. For a single mode and $\kappa = 0$ (5.59) simplifies to

  $$W(x,p) = \frac{1}{2\pi} \int \langle x + \frac{\hbar y}{2} | \rho | x - \frac{\hbar y}{2} \rangle e^{iyp} dy. \tag{5.60}$$

  This expression gives some context about the physical meaning of W: the marginal distributions of this function coincide with the quadrature distributions of the mode, which are available for a direct measurement via the homodyne technique [104]

  $$\int W(x,p) dx = \langle p | \rho | p \rangle \tag{5.61}$$

  $$\int W(x,p) dp = \langle x | \rho | x \rangle \tag{5.62}$$

  Despite this, the Wigner function can't be considered as a joint distribution of the field quadratures. As, already mentioned, in quantum mechanics these values are not measurable simultaneously and this leads to negative values of the Wigner function. This negativity, actually is often used as a criterion for non-classicallity. When a given state has a positive Wigner function, it is considered classical. In the next chapter we will discuss the limitation of such argumentation.

- Glauber-Sudarshan P-function [109, 110]: $\kappa = 1$

  The P-function is the most straightforward way of mapping from the density op-

erators in Hilbert space to the real-valued functions [109]. It appears that any density matrix ρ can be diagonalized in the coherent state basis:

$$\rho = \int P(\alpha)|\alpha\rangle\langle\alpha| d^2\alpha, \tag{5.63}$$

where $|\alpha\rangle$ are coherent states (5.40) and $d^2\alpha$ means $d\mathrm{Re}(\alpha)d\mathrm{Im}(\alpha)$. The real-valued function (because ρ is Hermitian) P is equivalent to the one obtained from (5.59) by taking $\kappa = 1$.

P-function is related to the Wigner function as

$$W(\alpha, \alpha^*) = \frac{2}{\pi} \int P(\beta, \beta^*) e^{-2|\beta-\alpha|^2} d^2\beta, \tag{5.64}$$

from which a relation between the P-function and the density matrix of a state can be derived

$$P(\alpha, \alpha^*) = \frac{e^{|\alpha|^2}}{\pi} \int \langle -\beta|\rho|\beta\rangle e^{|\beta|^2 - \beta\alpha^* + \beta^*\alpha} d^2\beta. \tag{5.65}$$

As well as the Wigner function, the P function can become negative, and it is also considered as a non-classicallity signature. In addition to that whenever Wigner function has any features less than $\hbar/2$ in width, the P function becomes singular ($\sim$ derivative of a delta function). This makes it inaccessible for direct observation.

- Husimi Q-function [121]: $\kappa = -1$

  The Q-function is the easiest to calculate of all the distributions. Given the density matrix ρ

  $$Q(\alpha) = \langle\alpha|\rho|\alpha\rangle. \tag{5.66}$$

  It is also the most well-behaved of the quasiprobabilities, being always positive, $Q(\alpha) \geq 0$. The non-classicality of ρ is captured by some details of its variation. It is also accessible for direct measurement, however due to the sharp dependence of the state properties of fine features of its shape, it is highly sensitive to the noise and measurement imperfections [122].

One of the key features of the phase space formulation that determined its success is the optical equivalence theorem [103]. It provides a intuitive and straightforward way to calculate expectation values of the observables for a system described by a quasiprobability distribution. Let's consider an observable $\hat{O}$ represented by an function of operators $\hat{a}$ and $\hat{a}^\dagger$: $\hat{O} = f(\hat{a}, \hat{a}^\dagger)$. The optical equivalence theorem states that

the expected value of this observable for a state ρ with a Wigner function W can be calculated as

$$\mathrm{Tr}[\rho\,\hat{O}] = \int W(x,p)\,O_S(x,p)\,dx\,dp, \tag{5.67}$$

where $O_S(x,p)$ is a Wigner representation of $\hat{O}_S = f^{(S)}(\hat{a},\hat{a}^\dagger)$, a symmetrically ordered version of $f(\hat{a},\hat{a}^\dagger)$

$$O_S(x,p) = \frac{1}{2\pi}\int \langle x + \frac{\hbar y}{2}|\hat{O}_S|x - \frac{\hbar y}{2}\rangle e^{iyp}dy. \tag{5.68}$$

Expressions equivalent to (5.67) can be obtained by replacing the Wigner function by the P-function and using the normally ordered version of $\hat{O}$, $\hat{O}_N = f^{(N)}(\hat{a},\hat{a}^\dagger)$ or by replacing it with the Q-function and using the antinormally ordered version of $\hat{O}$, $\hat{O}_A = f^{(A)}(\hat{a},\hat{a}^\dagger)$.

Having set a general framework of the phase-space formalism, we are now ready to explore particular examples of the states within this interpretation. The set of all possible states is divided into two classes: Gaussian and non-Gaussian states. It appears that for Gaussian states the phase space formalism significantly simplifies any calculations, which is due to the properties of the Gaussian functions. For non-Gaussian states usually the advantage is not that apparent, therefore a combination of different approaches might be required.

5.3.1 Gaussian states

The states for which characteristic function $\chi_\kappa(\boldsymbol{\xi})$, (5.56) is a Gaussian distribution, are called Gaussian states [120, 123, 124]. Any multivariate Gaussian distribution can be written in a vector form

$$F_{\mathrm{G}}(\mathbf{x}) = Ae^{-\frac{1}{2}\mathbf{x}^{\mathrm{T}}\mathbf{B}\mathbf{x}+\mathbf{c}^{\mathrm{T}}\mathbf{x}}, \tag{5.69}$$

where $\mathbf{x} \in \mathbb{R}^N$ is a vector of variables, $\mathbf{B} \in \mathbb{R}^N \times \mathbb{R}^N$ is a real-valued matrix that characterizes the variances of the random variables and their correlations, $\mathbf{c} \in \mathbb{R}^N$ is a vector of mean values and C is a normalization constant.

In the expression for the characteristic function vector $\boldsymbol{\xi}$ has a particular structure (it consists of pairs of x and p quadratures of the modes) therefore there are additional constraints on the elements of the matrix $\mathbf{B}$. The Gaussian form of the characteristic function is

$$\chi_\kappa(\boldsymbol{\xi})\big|_{\kappa=0} = \chi(\boldsymbol{\xi}) = e^{\frac{1}{2}\boldsymbol{\xi}^{\mathrm{T}}\Omega\sigma\Omega^{\mathrm{T}}\boldsymbol{\xi}-i\boldsymbol{\xi}^{\mathrm{T}}\Omega\mathbf{d}}, \tag{5.70}$$

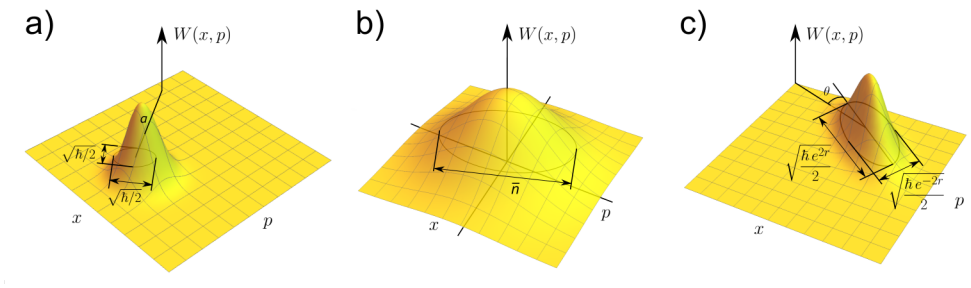

Figure 5.1: Examples of the quasiprobability distributions (Wigner functions) of Gaussian states: a) coherent state (5.40). b) thermal state (5.44). c) squeezed state (5.43).

where σ is a covariance matrix

$$\sigma_{\mu,\nu} = \frac{1}{2}\langle \hat{R}_\mu \hat{R}_\nu + \hat{R}_\nu \hat{R}_\mu \rangle + \langle \hat{R}_\mu \rangle \langle \hat{R}_\nu \rangle \tag{5.71}$$

and $\mathbf{d}$ is a vector of displacements. The uncertainty relation, derived from the commutation relations (5.17) - (5.19) put additional constraints on the elements of σ

$$\sigma + i\Omega \geq \frac{1}{2}. \tag{5.72}$$

For a Gaussian state covariance matrix and the displacement vector fully describe the system. Performing the Fourier transform (5.59) it is possible to find the Wigner function (and other quasiprobability distributions) of a Gaussian state

$$W(\mathbf{R}) = \frac{1}{(2\pi)^N \sqrt{\det(\sigma)}} e^{-(\mathbf{R}-\mathbf{d})^{\mathrm{T}} \sigma^{-1} (\mathbf{R}-\mathbf{d})}, \tag{5.73}$$

from which a conversion to the density matrix formalism is possible.

Let's now look at the particular examples of the Gaussian states:

- Coherent states and Vacuum

  Coherent states are the simplest of the Gaussian states. Their covariance matrix $\sigma_{coh} = \frac{1}{2}\mathbb{I}$ is just an identity matrix $(N \times N)$ multiplied by $1/2$, and the displacement vector

  $$\mathbf{d}_{coh} = \{\mathrm{Re}(\alpha_1), \mathrm{Im}(\alpha_1) \ldots \mathrm{Re}(\alpha_N), \mathrm{Im}(\alpha_N)\} \tag{5.74}$$

  is determined by the field amplitudes of each of the modes. Particularly, for the vacuum state $\mathbf{d} = 0$.

  For a single mode coherent state Wigner function is a 2D Gaussian with the

variance of $1/2$ centered at (x_0, y_0), where $\alpha = x_0 + iy_0$ is the complex amplitude of the field (see Fig. 5.1a).

- Squeezed states

  Squeezed states are described by multivariate Gaussian distributions with a certain structure. A single mode squeezed state has a covariance matrix

$$\sigma_{sq} = \begin{pmatrix} \cosh r + \sinh r \cos\theta & \sinh r \sin\theta \\ \sinh r \sin\theta & \cosh r - \sinh r \cos\theta \end{pmatrix} \tag{5.75}$$

  This matrix corresponds to a Gaussian distribution elongated along an axis that makes an angle of θ with respect to the positive direction of the x-quadrature (see Fig. 5.1b). The variances of the widest and the narrowest projections of this 2D Gaussian are $e^r/2$ and $e^{-r}/2$ respectively. The second variance can go beyond $1/2$, which is the shot noise limit. That is the reason why this class of states is considered to be non-classical.

- Thermal states

  As we already mentioned, thermal states are mixed. In contrast with coherent and squeezed states, where the only source of uncertainty in the quadrature (or amplitude and phase) measurements is quantum indeterminacy in the form of shot noise, thermal states describe chaotic fluctuations of the field. These fluctuation are, in principle, deterministic, but as they depend on the position of each emitting atom, their full description is inaccessible. Instead, as is usual in statistical physics, they are treated as a random process, for which the phase space formalism is convenient, since in naturally unifies stochastic randomness with the one from quantum indeterminacy [116]. The covariance matrix associated with one mode thermal light is $\sigma_{th} = (1/2 + \bar{n})\mathbb{I}$. Wigner function of these states is a symmetric Gaussian with a variance $\bar{n} + 1/2$ and, normally, centred at 0 (see Fig. 5.1c) (in the case of regular black-body radiation). Although non-zero displacement $\mathbf{d} \neq 0$ is also possible. Thermal states with non-zero $\mathbf{d}$ are called displaced [125].

The most general Gaussian state is a squeezed and displaced multimode thermal state [126]. Covariance matrix σ of such a state is a $2N \times 2N$ real valued symmetric matrix that may contain pretty much arbitrary entries, as long as they satisfy the uncertainty relation (5.72). In addition, this matrix has a particular block structure

$$\sigma = \begin{pmatrix} \boldsymbol{\alpha} & \boldsymbol{\gamma} \\ \boldsymbol{\gamma}^{\mathrm{T}} & \boldsymbol{\beta} \end{pmatrix}, \tag{5.76}$$

where the 2×2 blocks along the diagonal refer to the properties of the individual modes and the off-diagonal elements describe the correlations between different modes. All the possible types of classical or quantum correlations can be described by these submatrices. In the next section we will examine different methods and criteria for their analysis, but now let's briefly discuss the states for which Gaussian formalism is not applicable.

5.3.2 Non-Gaussian states

A state for which characteristic function $\chi_\kappa(\boldsymbol{\xi})$, (5.56) is anything rather than a Gaussian distribution is called non-Gaussian. As any state that has negative values of the Wigner function (and therefore is non-classical by that criterion) belongs to that class, non-Gaussianity is often linked to non-classicality. Indeed, such non-Gaussian states as Fock states [127], photon added or photon subtracted states [128], Yurke states [129], superpositions of coherent states [130], are all highly non-classical. However mixtures of coherent states, that are often considered to be completely classical, are also non-Gaussian. In Fig 5.2 we compare the Wigner functions of a mixture of two coherent states $(|\alpha\rangle\langle\alpha| + |-\alpha\rangle\langle-\alpha|)/2$, with a Wigner function of their superposition $(|\alpha\rangle + |-\alpha\rangle)/\sqrt{2}$. The side lobes of both function represent the two states $|\alpha\rangle$ and $|-\alpha\rangle$. The fringes in the center of the second graph are due to quantum interference of $|\alpha\rangle$ and $|-\alpha\rangle$ and they are responsible for the non-classicality of this superposition, as the Wigner function becomes negative within that region. When the distance between the peaks of the superposition increases (or in other words when the amplitude α grows), the fringes become sharper and more fine. The Wigner function of the mixture remains positive at any value of α, however, as we will show in the next chapter, some quantum features are present within that mixture. In order to reveal them we need to develop a non-classicality criterion that can capture that type of non-classicality, but before doing that we will review the currently known criteria.

5.4 Non-classicality criteria

It is often not obvious whether a given system requires a quantum-mechanical description or not. On the one hand there are examples of phenomena, such as the Hanbury Brown and Twiss effect [131] or ghost imaging [132], that originally were considered to have quantum nature [67, 74, 133], but were later described classically [71, 75, 103]. On the other hand even such undoubtedly quantum features as entanglement can be mimicked by completely classical systems [134, 135].

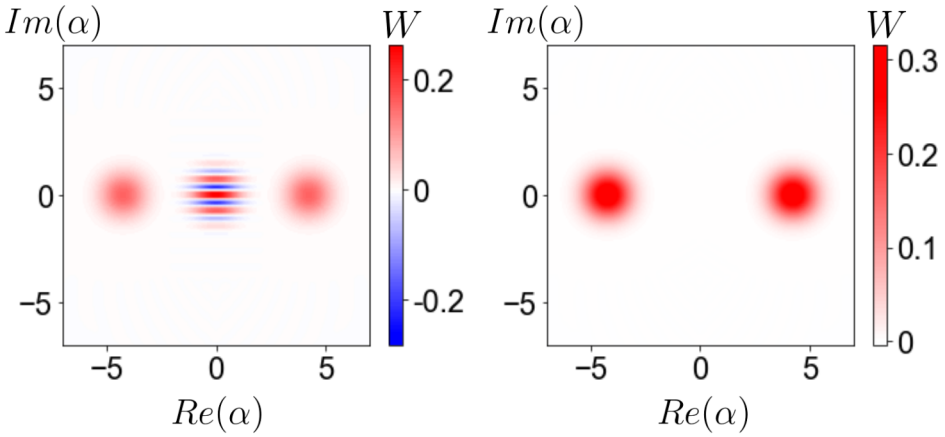

Figure 5.2: Wigner functions of a superposition $|\alpha\rangle + |-\alpha\rangle$, left panel and a mixture $|\alpha\rangle\langle\alpha| + |-\alpha\rangle\langle-\alpha|$ of two coherent states.

The most evident non-classicality criteria are related to the Bell's inequality violation. In his work addressing the famous EPR paradox [136], Bell suggested a test of completeness of the quantum theory [137]. This test was based on an inequality relating the properties of two particular correlated systems and having a tight bound for a classical "hidden-variable" variant of the system description. Getting a value beyond that bound (violation of the inequality) would mean that the theories based on the classical picture are not able to explain the experimental results. On the other hand quantum theory accepted such a possibility, giving a higher value of the bound. The Bell's test was performed numerous times, eliminating any possible "loopholes" or experimental imperfections that questioned the validity of the final result and each time the violation of the classical prediction was achieved [138]. As the validity of quantum theory that was tested by the Bell's inequalities is now reliably confirmed, they can be a criterion for the state non-classicality: any state that violates them is definitively non-classical.

As Bell's inequalities are formulated for the systems of at least two spatially separated parties and rely on the correlations between their properties, we first review the features of such multimode systems that make them non-classical.

5.4.1 Multimode state non-classicality: entanglement and discord

In order to violate the Bell's inequality a state must be entangled. Entanglement is a property of a quantum system, which is responsible for the situation when two or more spatially separated parts of such a system act as a whole. In particular, the outcome of a measurement performed on one of the parts of an entangled state will depend on the

outcome of a measurement on the other part.

The entanglement criteria are well understood for the pure states. For a pure state there are only two options: it can either be a product state of two subsystems and they are completely independent in that case, or the state is entangled. Let's consider an example of two qubitss, A and B.

The general pure state of the first qubit is

$$|\Psi^A\rangle = \alpha_1|\psi_1\rangle + \beta_1|\psi_2\rangle; \tag{5.77}$$

where $|\psi_1\rangle$, $|\psi_2\rangle$ is a pair of orthonormal vectors and $\alpha_1, \beta_1 \in \mathbb{C}$. By analogy, the state of the second qubit

$$|\Phi^B\rangle = \alpha_2|\phi_1\rangle + \beta_2|\phi_2\rangle, \tag{5.78}$$

Their product state is of the form

$$\begin{aligned} |\Psi^A\Phi^B\rangle &= (\alpha_1|\psi_1\rangle + \beta_1|\psi_2\rangle) \otimes (\alpha_2|\phi_1\rangle + \beta_2|\phi_2\rangle) \\ &= \alpha_1\alpha_2|\psi_1\phi_1\rangle + \alpha_1\beta_2|\psi_1\phi_2\rangle + \alpha_2\beta_1|\psi_2\phi_1\rangle + \beta_1\beta_2|\psi_2\phi_2\rangle, \end{aligned}$$

However a general state in a 2-qubit Hilbert space

$$|\Psi^A\Phi^B\rangle = u_1|\psi_1\phi_1\rangle + u_2|\psi_1\phi_2\rangle + u_3|\psi_2\phi_1\rangle + u_4|\psi_2\phi_2\rangle \tag{5.79}$$

doesn't necessarily has such a form. It can be easily shown that a state

$$|\Psi\Phi\rangle_{\text{Bell}} = \frac{|\psi_1\phi_1\rangle + |\psi_2\phi_2\rangle}{\sqrt{2}} \tag{5.80}$$

can't be written as a product, therefore it is entangled. The states of a type as in (5.80) are called Bell states as they are used to violate Bell's inequalities.

The general criterion for the entanglement of bipartite pure states is based on the Schmidt decomposition [139]. To check if such a state is entangled it is necessary to check if the reduced states of each of the parties are mixed. In case they are, the bipartite state is entangled, if they are pure, the joint state is a product. This procedure also can be generalized to multipartite systems, however multipartite generalization of the Schmidt decomposition works well only for case in which if one of the parts is traced out, the rest is fully separable [140]. In a general case one needs to check the purity of all possible bipartite reductions [141].

For mixed states the situation is more complex: a multicomponent system that is

not entangled is not necessarily in a product state. Mixed states of a form

$$\rho_{\text{sep}} = p_i \rho_i^1 \otimes \cdots \otimes \rho_i^n, \quad p_i > 0, \quad p_i \in \mathbb{R} \tag{5.81}$$

are not entangled and are called separable. A general criterion of multidimensional entanglement of arbitrary quantum systems should be able to tell if a given state can be written in a form (5.81). Such criterion has not been developed yet. Moreover it has been shown that such a problem is NP hard [142]. A procedure called positive partial transpose (PPT) criterion exists for the systems with dimensions $2 \otimes 2$ and $2 \otimes 3$ [143, 144]. If we write the density matrix of a joint state as:

$$\rho = \sum_{ijkl} \rho_{ijkl} |\psi_i\rangle\langle\psi_j| \otimes |\phi_k\rangle\langle\phi_l| \tag{5.82}$$

the partial transpose is defined as follows:

$$\rho^{T_B} = \sum_{ijkl} \rho_{ijkl} |\psi_i\rangle\langle\psi_j| \otimes |\phi_l\rangle\langle\phi_k|. \tag{5.83}$$

If all of the eigenvalues of the partial transpose of the density matrix ρ^{T_B} are positive, this density matrix describes a separable state, while if at least one of the eigenvalues is negative the state is entangled. For $2 \otimes 2$ and $2 \otimes 3$ systems this criterion gives necessary and sufficient condition of the separability of the joint density matrix. For higher dimensions it gives only the necessary condition.

The PPT criterion can be generalized to the case of Gaussian states. This generalization is called Simon criterion [145]. One can notice that the partial transpose operation in the regular PPT criterion corresponds to a mirror reflection of the corresponding state within its Hilbert space. For a continuous variable system such an operation is analogous to a time reversal, which in its turn changes the sign of the p quadrature of the transposed mode. If the covariance matrix obtained after such an operation corresponds to a physical state (i.e. it is positive and satisfies Heisenberg uncertainty relation (5.72)), the considered state is separable, if not it is entangled. As in the case of two-level systems, Simon criterion is applicable only for two modes and in several special generalizations of this case [146, 147]. The Simon criterion is formulated in terms of the symplectic eigenvalues of the state η_+, η_- as [148]:

$$\eta^{\pm} := \left[\frac{1}{2} \left(\Delta' \pm \sqrt{\Delta'^2 - 4 \det(\sigma')} \right) \right]^{1/2} \geq 1/2, \tag{5.84}$$

where $\Delta' = \det(\boldsymbol{\alpha}) + \det(\boldsymbol{\beta}) + 2\det(\boldsymbol{\gamma'})$. $\boldsymbol{\alpha}$, $\boldsymbol{\beta}$ and $\boldsymbol{\gamma}$ are the sub-matrices of the full

covariance matrix written in a special form:

$$\sigma = \begin{pmatrix} \boldsymbol{\alpha} & \boldsymbol{\gamma} \\ \boldsymbol{\gamma}^{\mathrm{T}} & \boldsymbol{\beta} \end{pmatrix} = \begin{pmatrix} a & 0 & \gamma_x & 0 \\ 0 & a & 0 & \gamma_p \\ \gamma_x & 0 & b & 0 \\ 0 & \gamma_p & 0 & b \end{pmatrix}. \tag{5.85}$$

σ' and $\boldsymbol{\gamma}'$ are matrices referring to the time reversed system, which are obtained from Eq. (5.85) by changing the sign of γ_p, i.e. $\gamma_p \to -\gamma_p$. Their determinants together with the determinant of the full covariance matrix are the invariants of the states.They are not changed by local operations and actually characterize its entropic and correlation properties [149]. There exist a couple of alternative criteria to characterize entanglement in Gaussian states [150], however the Simon criterion is usually enough for any practical situation.

For the case when the PPT criterion does not work, the only way to verify the presence of entanglement is construction of a so called entanglement witness [151]. An entanglement witness is an observable $\hat{W}$ whose expectation value $W = Tr(\hat{W}\rho)$ is negative when the state is entangled and positive otherwise. Entanglement witness is usually specific to a particular class of states and building it can be a difficult problem.

For a pure bipartite entangled state a measurement of the property in which the parties are entangled on one of them completely determines the result of a measurement on the second and for product states measurement on either of the parties are completely independent. For a mixed state separability, however does not imply absence of correlation between the sub-parts of the whole system. The measurement of one of the parties can influence the other in a probabilistic sense [152], moreover an interplay between classical and quantum correlations can exist. A measure called *quantum discord* allows to separate quantum correlations from the classical ones [153].

For a random process X, its informational capacity is defined by its Shannon informational entropy H:

$$H(X) = -\sum_n p_n^X \log(p_n^X), \quad p_i > 0, \quad p_i \in \mathbb{R} \tag{5.86}$$

where p_n^X are the probabilities of different possible outcomes of the process. If we consider the results of the measurements on a classical system consisting of two parts A and B as two random processes, the mutual information $I^{cl}(A, B)$ is defined as the difference between the amount of information contained in the individual subsystems

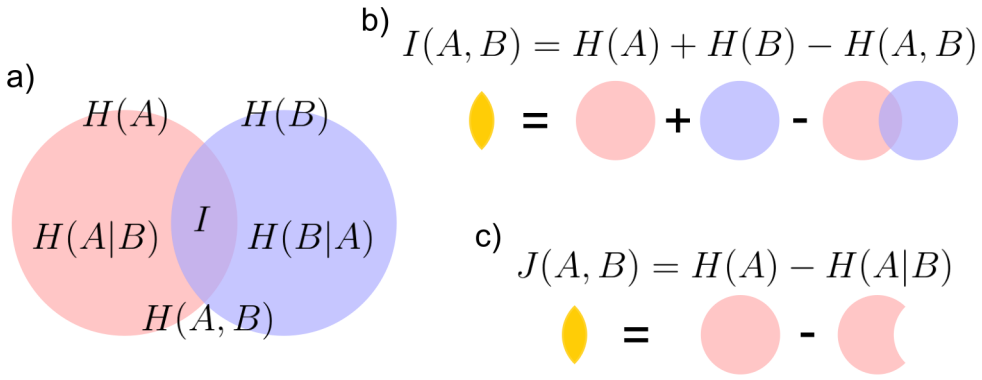

Figure 5.3: The two ways to define mutual information. a) Definitions: entropy of the marginals $H(A)$, $H(B)$, entropy of the joint system, $H(A,B)$, conditional entropies, $H(A|B)$, $H(B|A)$, and mutual information $I(A,B)$. b) Mutual information as a sum of entropies of the marginals minus entropy of the joint system. c) Mutual information as the entropy of one of the marginals minus the conditional entropy (5.88)

and those contained in the whole system (see Fig. 5.3b):

$$I^{cl}(A,B) = H(A) + H(B) - H(A,B) \tag{5.87}$$

where $H(A)$ and $H(B)$ are the entropies of the individual systems and $H(AB)$ is the entropy of the whole system: $H(AB) = \sum_n p_n^A p_n^B \log(p_n^A p_n^B)$. On the other hand, we can define this mutual information in another way, using the conditional entropy

$$H(A|B) = \sum_n (p^A|B_n) \log(p^A|B_n) \tag{5.88}$$

where $p^A|B_n$ are the conditional probabilities. The amount of mutual information is

$$J^{cl}(A,B) = H(A) - H(A|B) = H(B) - H(B|A). \tag{5.89}$$

For any classical system the definitions given by Eq. (6.55) and (5.89) are equivalent, i.e. $I^{cl} = J^{cl}$ as a consequence of the Bayes' rule, see Fig. 5.3. For a quantum system these two ways to define the mutual information can lead to different results. Let's now define I and J for quantum systems.

For a quantum system described by a density matrix ρ the Shannon informational entropy should be replaced by the Von-Neumann entropy [139]:

$$S(\rho) = -\sum_n \lambda_n \log(\lambda_n), \tag{5.90}$$

where λ_n are the eigenvalues of the density matrix ρ. The quantum analogue of the

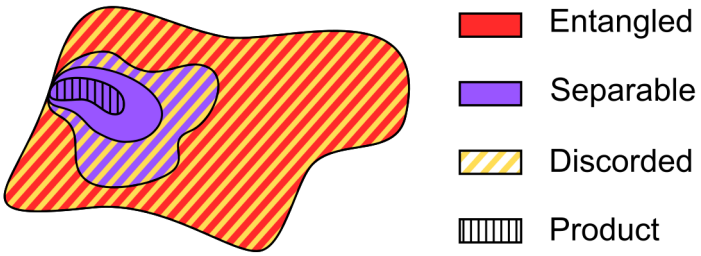

Figure 5.4: Venn diagram of the correlation properties. All non-separable states are entangled. All entangled states have non-zero discord. There are some separable states that have non-zero discord, and, in principle, there are some non-product states with zero discord.

quantity I from Eq. (6.55) is obtained by replacing the Shannon entropy in this equation by the Von-Neumann one:

$$I^q(\rho^{AB}) = S(\rho^A) + S(\rho^B) - S(\rho^{AB}), \tag{5.91}$$

where $S(\rho^{AB})$ is the entropy of the whole system ρ^{AB}, and $S(\rho^A)$, $S(\rho^B)$ are the entropies of the reduced density matrices of the corresponding subsystems. In order to define the quantum analogue of the quantity J form Eq. (5.89) we need to determine the conditional entropy in the quantum case. The conditional entropy can be defined as:

$$S_{\{\Pi_j\}}(\rho^{A|B}) = \sum_j p_j S(\rho^{A|\Pi_j}), \tag{5.92}$$

where $p_j = Tr[\rho^{AB}(\mathbb{I}^A \otimes \Pi_j^B)]$, $\rho^{A|\Pi_j} = Tr_B[\rho^{AB}(\mathbb{I}^A \otimes \Pi_j^B)]/p_j$ and $\{\Pi_j^B\}$ is a complete set of orthogonal projectors. The expression (5.89) for the mutual information becomes:

$$J_j^q(\rho^{AB}) = S(\rho^A) - S_{\{\Pi_j\}}(\rho^{A|B}), \tag{5.93}$$

and now it depends on the particular choice of the measurement operator Π_j. The quantum discord $D(\rho^{AB})$ is defined [152, 153] as the difference between Eq. (5.91) and Eq. (5.93) minimized over all possible measurement operators Π_j:

$$D(\rho^{A|B}) = S(\rho^B) - S(\rho^{AB}) + \inf_{\{\Pi_j\}} S_{\{\Pi_j\}}(\rho^{A|B}). \tag{5.94}$$

The procedure of minimization is quite challenging and therefore a closed formula for the discord can be found just in the simplest cases. In Appendix A we provide several examples of its calculation. The discord is limited from beneath for an entangled state, which means that all entangled states have non-zero discord. It is limited from above for

separable states and the states for which it is zero are considered to have no quantum correlations and are called classical. It can be shown that they have a specific form [154]:

$$\rho_{cl} = \sum_i \alpha'_i \Psi_1^i \otimes \cdots \otimes \Psi_n^i \tag{5.95}$$

where $\Psi_1, \ldots \Psi_n$ are complete sets of orthogonal projectors, and α'_i are positive numbers such that $\sum_i \alpha'_i = 1$. The map of the correlation properties of the quantum states is shown on the figure 5.4.

For two-mode Gaussian states quantum discord is defined in the same way as for the discrete systems [152, 153]. However the general projective measurement operators Π_j in (5.94) may have complicated structure in the infinite-dimensional Hilbert space, having infinitely many free parameters. This makes the optimization procedure used in the definition of the discord impossible. However, in the case when the studied state is Gaussian, the optimization may be constrained to a particular type of measurements called Gaussian [155]. Such measurements are projections onto Gaussian states and practically refer to modifications of the optical homodyne detection techniques [156]. In this case is possible to derive a closed expression for the discord of a bipartite Gaussian state depending on its covariance matrix. In order to do that we are missing just a few ingredients: the expression for the entropy of the Gaussian states and the phase space analogue of the Born's rule. The entropy of a Gaussian state can be expressed as:

$$S(\sigma) = \sum_i f_{\text{ent}}(\eta_i), \tag{5.96}$$

where η_i are the symplectic eigenvalues of the state of σ and $f_{\text{ent}}(x) = (x + 1/2)\ln(x + 1/2) + (x - 1/2)\ln(x - 1/2)$ [157]. The state after a projective measurement onto another Gaussian state is given as [156]:

$$\boldsymbol{\alpha}' = \boldsymbol{\alpha} - \boldsymbol{\gamma}(\boldsymbol{\beta} + \sigma^M)^{-1}\boldsymbol{\gamma}^{\mathrm{T}}, \tag{5.97}$$

where σ^M is the covariance matrix of the state, corresponding to the measurement operator. Now we can derive the formula for Gaussian (referring to Gaussian measurements) discord [158, 159]:

$$\begin{aligned} D(\sigma) &= f_{\text{ent}}(\sqrt{\det(\boldsymbol{\beta})}) - f_{\text{ent}}(\eta^-) - f_{\text{ent}}(\eta^+) + \\ &+ f_{\text{ent}}\left(\frac{\sqrt{\det(\boldsymbol{\alpha})} + 2\sqrt{\det(\boldsymbol{\alpha})\det(\boldsymbol{\beta})} + 2\det(\boldsymbol{\gamma})}{1 + 2\sqrt{\det(\boldsymbol{\beta})}}\right). \end{aligned} \tag{5.98}$$

5.4.2 Single mode non-classicality criteria

For the case of a single quantum object the criteria of non-classicality are less straightforward. For the continuous variable systems one of the first attempts to introduce a non-classicality criterion was done by Mandel [160], who introduced the q-parameter

$$\mathrm{q} = \frac{\langle(\Delta\hat{n})^2\rangle - \langle\hat{n}\rangle}{\langle\hat{n}\rangle} = \langle\hat{n}\rangle(g^{(2)}(0) - 1), \tag{5.99}$$

$g^{(2)}(0)$ is the degree of second-order coherence. This parameter shows how far the photon statistics of a mode is from the Poissonian. Negative values of this parameter indicated non-classicality, reaching a minimum of -1 for the Fock states [103].

At the same time it was early realized that negative values of the Wigner function can be an indicator of non-classicality [161]. Indeed such obviously non-classical states as Fock, photon added/subtracted and coherent state superpositions have negative values of the Wigner function. However this criterion didn't capture the squeezed states, which are widely considered non-classical as well. An improved version of the Wigner function negativity criterion, that treated squeezed states as non-classical was the P-function criterion, which stated that a P-function of a classical state is a well defined probability distribution and this function being negative or ill-defined (singular) is a criterion for non-classicality [162]. However all these criteria suffered from the following problems:

- They didn't quantify the non-classicality, being effectively a binary indicator, which can partly be solved by quantifying the volume of the negative part of the Wigner function [163].

- None of these criteria could be directly observed experimentally. Moreover, Wigner function is usually reconstructed from the quadrature measurements via a tomographic transform [104], therefore its fine features are highly affected by measurement noise and imperfections.

- Characterization of some the measures, such as trace distance of a given state from the nearest classical one, represented a computationally hard problem [164].

The criterion that resolves these problems is the entanglement potential. It is defined as the amount of two-mode entanglement that can be generated from the field using linear optics, auxiliary classical states, and ideal photodetectors [165]. In most of the cases it is just the amount of entanglement one can get splitting the studied state on a symmetric lossless beam-splitter. As in most practical applications the aim of non-classical state preparation is to produce entanglement, which in its turn is used to achieve

quantum advantages in various tasks, the entanglement potential is beneficial over the previously mentioned criteria, since it directly quantifies how useful is a given state for such a procedure.

Finally one of the most recent advancement in the attempts to characterize non-classicality of a generic single mode states are the coherence monotones [16, 166]. The key idea behind this class of measures is, as already mentioned, that non-classicality is closely related to superposition. Coherence monotones quantify how far a given state is away from a maximal superposition available in its Hilbert space. In order to be a coherence monotone, a map $C : \rho \to \mathbb{R}$ should satisfy the following properties:

- **I**. Positivity.

  $C(\rho) \geq 0 \quad \forall \rho. \quad C(\rho) = 0$ for a set, $\mathfrak{I}$ of so called incoherent states $\rho_{inc} = \sum p_k |k\rangle\langle k| \subset \mathfrak{I}, \quad p_k > 0, \quad p_k \in \mathbb{R}$

- **II**. Monotonicity.

  The most general operation, Λ that can be performed on a quantum ρ system is the following [167]

  $$\Lambda[\rho] = \mathrm{Tr}_{\rho'}[U(\rho \otimes \rho')U^\dagger] \tag{5.100}$$

  i. e. the system ρ is brought together with an auxiliary system ρ' and their resulting product state is transformed by some global unitary U, and after that the ρ' is traced out. Such operation can be represented as a sum

  $$\Lambda[\rho] = \sum_k K_k \rho K_k^\dagger \tag{5.101}$$

  where K_k are so-called Kraus operators. The incoherent Kraus operator $K^{\mathfrak{I}}$ is the one that maps an incoherent state onto a set of incoherent ones $K^{\mathfrak{I}} \rho_{inc} K^{\dagger\mathfrak{I}} \subset \mathfrak{I}$. In its turn, an incoherent map $\Lambda^{\mathfrak{I}}$ is the one that can be represented in a form

  $$\Lambda^{\mathfrak{I}}[\rho] = \sum_k K_k^{\mathfrak{I}} \rho K^{\mathfrak{I}\dagger_k} \tag{5.102}$$

  Finally the monotonicity criterion implies that

  $$C(\Lambda^{\mathfrak{I}}[\rho]) \leq C(\rho) \tag{5.103}$$

- **III**. Strong monotonicity.

  The state ς_k after the action of a Kraus operator K_k on ρ is $\varsigma_k = K_k \rho K_k^\dagger / z_k$, where $z_k = \mathrm{Tr}[K_k \rho K_k^\dagger]$. There is a special class of operations when the next of the

operators K_k is chosen depending on the results of the previous measurements. Such operations are called selective. The strong monotonicity implies that C does not increase on average under selective incoherent operations

$$\sum_k z_k^{\mathfrak{I}} C(\varsigma_k^{\mathfrak{I}}) \leq C(\rho), \tag{5.104}$$

where $\varsigma_k^{\mathfrak{I}} = K_k^{\mathfrak{I}} \rho K_k^{\mathfrak{I}\dagger} / z_k^{\mathfrak{I}}$ and $z_k^{\mathfrak{I}} = \mathrm{Tr}[K_k^{\mathfrak{I}} \rho K_k^{\mathfrak{I}\dagger}]$

- **IV**. Convexity.

  Finally, C should not increase under classical mixing.

$$\sum_k p_k C(\rho_k) \geq C\left(\sum_k p_k \rho_k\right), \quad p_k \in \mathbb{R}, \quad p_k \geq 0. \tag{5.105}$$

The most common examples of coherence monotones are the l_1 norm of coherence [166]

$$C_{l_1}(\rho) = \sum_{n \neq k} |\rho_{nk}| \tag{5.106}$$

and the relative coherence entropy [166]

$$C_{RE}(\rho) = S(\rho_{\mathrm{diag}}) - S(\rho), \tag{5.107}$$

where $S(\rho)$ is the Von-Neumann entropy (5.90) of ρ and $S(\rho_{\mathrm{diag}})$ is the entropy of the matrix obtained by putting all non-diagonal elements of ρ to 0.

Coherence monotones for various systems are currently an area of active research, however there are several problems regarding these measures. First of all they are basis dependent: let's consider, for example, the state (5.45). In $\{|\psi_1\rangle, |\psi_2\rangle\}$ basis it is a maximal superposition, however in the basis given by (5.47), the non-diagonal elements of the density matrix of this state will be 0. Often the energy eigenbasis of the system is the preferred one, however in many cases it is not clear why one should prefer one basis over another. Also extra care should be taken when extrapolating the coherence monotones onto the continuous variable systems [168]. As we will show in the next chapter, they can diverge even for completely classical coherent states.

Chapter 6

Discord potential of a coherent state mixture

In this chapter we consider the problem of generation of quantum correlations in the output state of a lossless beam-splitter. This problem is relevant not only as a simplified version of the multiple scattering scenario, but also because quantum correlations of the beam splitter output can be used as an indicator of its input state non-classicality [165]. It is well known, that when the state of one of the input modes of a beam splitter has an ill-defined or negative P-function, its output modes will be entangled [15, 148]. Here we consider quantum discord [152, 153], which is a type of quantum correlations weaker than entanglement, in the beam splitter output state.

We start this chapter by an example from the theory of quantum state discrimination [12, 169], in which we show that it is possible to discriminate between two coherent states in a mixture more efficiently by exploiting quantum features of such a state. As this discrimination advantage is not captured by any of the previously mentioned non-classicality criteria, we introduce a new measure, which we call *discord potential* (by an analogy to the entanglement potential [165]), based on the discord of the beam splitter output with the characterized state being one of the inputs. We calculate the discord potential of a mixture of two coherent states and show that it is non-zero in the same conditions (in terms of the mixture elements overlap) as when the advantage in the discrimination is maximal. The procedure of the beam-splitter output state quantum discord estimation using the conditional Wigner functions was developed in [170], followed by an experimental measurement [171, 172]. However, all of these works dealt with the Gaussian states, giving only estimates for the non-Gaussian ones. Here we show a method of the quantum discord potential calculation for a certain class (positive P-representation) of non-Gaussian states. Finally we compare the discord potential with

the phase-space non-classicality measures and coherence monotones [16, 166], showing that the former provides a better characterization of the non-classical features of the coherent state mixture.

The material presented in this chapter is a part of a manuscript submitted to J. Phys. A. [173]

6.1 Quantum advantage in coherent state discrimination

The problem of quantum state discrimination is fundamental for quantum communication and quantum metrology. In quantum communication, two parties agree on an alphabet, which is encoded by some predetermined set of quantum states. The transmitting party sends a state corresponding to one of the symbols of the alphabet to the receiving party, which should decide which symbol has been sent based on the outcomes of some measurements. The key problem is to construct the best possible measurement for a given set of encoding states and a priori probabilities of their occurrence. In metrology the situation is similar: different values of the measured parameter are associated with different states from a set, and discriminating between these states gives the information about the parameter.

The figure of merit for the discrimination quality varies depending on the exact discrimination strategy. However the most straightforward one is the average probability to make an error in the discrimination. The measurement which minimizes this error is considered the optimal one. When the discriminated states are orthogonal, this error can, in principle, be reduced to zero. However, when the sates are non-orthogonal, the non-zero error probability follows from the generalized uncertainty principle [174]. Finding an optimal measurement for the state discrimination is an area of active research [175–178].

Let's consider the simplest scenario of the state discrimination. We wish to discriminate between the states $|\psi_0\rangle$ and $|\psi_1\rangle$ with prior probabilities p_0 and $p_1 = 1 - p_0$. We can introduce an orthogonal basis $\{|0\rangle, |1\rangle\}$ within the subspace spanned by $|\psi_0\rangle$ and $|\psi_1\rangle$. In that subspace all possible projective measurements are parametrized just by an angle θ

$$\begin{aligned} \hat{\Pi}_0 &= (\cos(\theta)|0\rangle + \sin(\theta)|1\rangle)(\cos(\theta)\langle 0| + \sin(\theta)\langle 1|) \\ \hat{\Pi}_1 &= (\cos(\theta)|0\rangle - \sin(\theta)|1\rangle)(\cos(\theta)\langle 0| - \sin(\theta)\langle 1|). \end{aligned} \tag{6.1}$$

Being projectors, both of these observables have just two outcomes: $0_0, 1_0$ for $\hat{\Pi}_0$ and $0_1, 1_1$ for $\hat{\Pi}_1$. Moreover, as $\hat{\Pi}_0$ and $\hat{\Pi}_1$ are orthogonal, $0_0, 0_1$ and $1_0, 1_1$ are mutually exclusive. Therefore there are just two possible outcomes, let's denote them $0 = 1_0 \wedge 0_1$ and $1 = 0_0 \wedge 1_1$ and associate the occurrence of 0 with the detection of the state $|\psi_0\rangle$ and 1 of the state $|\psi_1\rangle$. In simple terms, measurement of $\hat{\Pi}_0$ just answers the question "is the measured state $|\psi_0\rangle$?" (0 – yes 1 – no) and the same for $\hat{\Pi}_1$ "is the measured state $|\psi_1\rangle$?" (1 – yes 0 – no). As an error we can treat the event when 0 is observed and the measured state is $|\psi_1\rangle$ or 1 is observed when the measured state is $|\psi_0\rangle$. Its probability is

$$\begin{aligned} P_{\text{err}} &= p_0\langle\psi_0|\hat{\Pi}_1|\psi_0\rangle + p_1\langle\psi_1|\hat{\Pi}_0|\psi_1\rangle = \\ &= p_0 - \text{Tr}[(p_0|\psi_0\rangle\langle\psi_0| - p_1|\psi_1\rangle\langle\psi_1|)\hat{\Pi}_0] = p_0 - \text{Tr}[\hat{O}_p\hat{\Pi}_0]. \end{aligned} \tag{6.2}$$

P_{err} will be minimal, when $\text{Tr}[\hat{O}_p\hat{\pi}_0]$ is maximal. This is achieved when $\hat{\Pi}_0$ is a projector onto a positive eigenstate of the operator $\hat{O}_p = p_0|\psi_0\rangle\langle\psi_0| - p_1|\psi_1\rangle\langle\psi_1|$ with the eigenvalue

$$\lambda_+ = \frac{1}{2}(p_0 - p_1 + \sqrt{1 - 4p_0p_1|\langle\psi_0|\psi_1\rangle|^2}), \tag{6.3}$$

which leads to the expression for the minimal error

$$P_{\text{err}} = \frac{1}{2}(1 - \sqrt{1 - 4p_0p_1|\langle\psi_0|\psi_1\rangle|^2}), \tag{6.4}$$

This expression is known as the Helstrom bound [12, 169]. It specifies the minimal possible error in discriminating between the two states depending on their overlap $|\langle\psi_0|\psi_1\rangle|^2$.

In the case of discrimination between two mixed states ρ_0 and ρ_1 with prior probabilities p_0 and p_1 respectively the optimal measurement is just a projective measurement in a subspace spanned by the eigenvectors of an operator $p_0\rho_0 - p_1\rho_1$, which is similar to $\hat{O}_p$. Finally in the most general case of discrimination between multiple mixed states ρ_i with prior probabilities p_i the optimal measurement is not necessarily projective [179]. The optimal measurement in that case is some POVM $\{\pi_j\}$ on a Hilbert space spanned by the eigenvectors of ρ_i. The error, in analogy to (6.2) is the overlap of the probabilities to observe the element of the POVM not associated with the state being actually measured

$$P_{\text{err}} = \sum_i p_i \sum_{j \neq i} \text{Tr}[\rho_i\hat{\pi}_j]. \tag{6.5}$$

The problem of finding the optimal set of operators $\hat{\pi}_j$ is challenging, and allows a closed solution only in simple situations [169].

Now let us consider the problem of distinguishing two coherent states $|\alpha_0\rangle$ and $|\beta_0\rangle$

that occur with probabilities $0 < a < 1$ and $1 - a$, respectively, i.e. the corresponding mixed state is

$$\rho_0 = a\,|\alpha_0\rangle\langle\alpha_0| + (1-a)\,|\beta_0\rangle\langle\beta_0|. \tag{6.6}$$

The error probability of an optimal measurement, according to (6.4) is

$$P_{\text{Hel}} = \frac{1}{2}\left[1 - \sqrt{1 - 4a(1-a)e^{-d_0^2}}\right], \tag{6.7}$$

where d_0 is related to the states' overlap $d_0^2 := |\alpha_0 - \beta_0|^2 = -\ln|\langle\alpha_0|\beta_0\rangle|^2$. When d_0 decreases, the two coherent states become identical and the system is not a mixture anymore. The error probability in that case tends to 1/2. For large separations, the two coherent states have less and less overlap and thus become almost orthogonal. In that case $\lim_{d_0\to\infty} P_{\text{Hel}} = 0$, see Fig 6.2 a. The optimal measurement is given by the operators [180] (in the $\{|\alpha\rangle, |\beta\rangle\}$ basis)

$$\Pi_\alpha = \frac{1}{2(1-d_e^2)}\begin{pmatrix} 1-\sqrt{1-d_e^2} & -d_e \\ -d_e & 1+\sqrt{1-d_e^2}\end{pmatrix}, \qquad \Pi_\beta = \mathbb{I} - \Pi_\alpha, \tag{6.8}$$

where $d_e = e^{-d_0^2/2}$. Although these operators satisfy all the requirements of the observable quantities, it is hard to associate them with a particular experimental procedure. This is a common feature of any operators obtained in the optimization process: the measurement they correspond to, can be very difficult to implement. There are several practical methods that approach the Helstrom bound, such as Dolinar receiver [181], Kennedy receiver [182], feed forward strategy [176], and some more [177, 178, 183], however the search of procedures of optimal coherent state discrimination that are easy to implement is still ongoing [184].

In order to identify the advantages given by quantum features, let's consider a classical strategy for discriminating between $|\alpha_0\rangle$ and $|\beta_0\rangle$. By an appropriate displacement and phase shift the state (6.6) can be transformed into

$$\rho_0' = a\,|\gamma_0\rangle\langle\gamma_0| + (1-a)\,|-\gamma_0\rangle\langle-\gamma_0|, \tag{6.9}$$

where $\gamma_0 = (\alpha_0 - \beta_0)/2)$, see Fig 6.1 a. Now a homodyne measurement along the x quadrature can be performed on the state ρ_0', and based on whether its outcome is greater of less than a certain threshold x_t, the decision whether $|\alpha_0\rangle$ or $|\beta_0\rangle$ occurred is

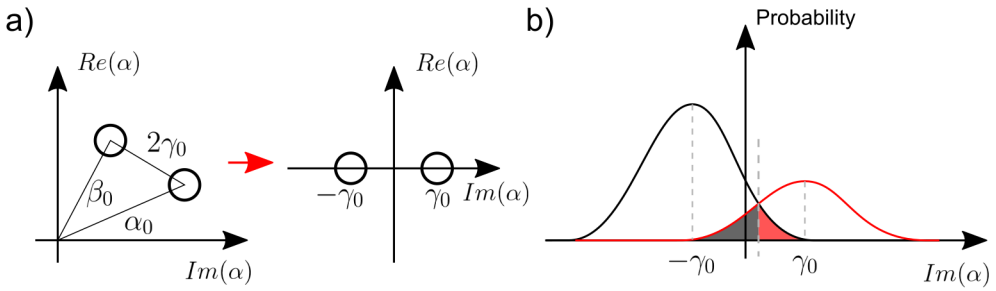

Figure 6.1: a) A mixture of coherent states with arbitrary amplitudes, $\rho_0 = a\,|\alpha_0\rangle\langle\alpha_0| + (1-a)\,|\beta_0\rangle\langle\beta_0|$, is displaced and phase shifted into a state $\rho_0' = a\,|\gamma_0\rangle\langle\gamma_0| + (1-a)\,|-\gamma_0\rangle\langle-\gamma_0|$. b) When $a \neq 1/2$ in ρ_0', the optimal discrimination threshold shifts towards the less probable of the coherent states in the mixture.

made, see Fig 6.1 a. The error rate, similarly to (6.2), is

$$P_{\text{Hom}} = \frac{1}{2}\left(1 - a\,\text{Erf}\left(\frac{d_0/2 - x_t}{\sqrt{2}}\right) + (a-1)\,\text{Erf}\left(\frac{d_0/2 + x_t}{\sqrt{2}}\right)\right), \tag{6.10}$$

When $a = 1/2$, the optimal strategy is simply to check if the measured quadrature value is greater or less than 0, which leads to a simple expression for the error rate

$$P_{\text{Hom}}(1/2, d_0) \;=\; \frac{1}{2}\left[1 - \text{Erf}(d_0/\sqrt{2})\right], \tag{6.11}$$

but when $a \neq 1/2$ the threshold position shifts, see Fig. 6.1b. The optimal position is derived from the condition $\partial P_{\text{Hom}}/\partial x_t = 0$.

$$\widetilde{x}_t = \frac{\log(\frac{1}{a} - 1)}{d_0} \tag{6.12}$$

The dependence of P_{Hom} on a and d_0 is shown in Fig 6.2 b, it behaves similarly to P_{Hel}, Fig 6.2 a, despite the difference of the forms of these expressions. As expected $P_{\text{Hom}} \geq P_{\text{Hel}}$ for any a and d_0, which can be clearly seen from Fig 6.2 c, d, where also the difference, ΔP, between P_{Hom} and P_{Hel} is plotted. ΔP characterizes the "advantage" of a quantum measurement over the classical one. As shown in the figure, this advantage is zero for $d_0 \to 0$ and $d_0 \to \infty$, and has a maximum at an intermediate separation. As pointed out in [180] this advantage is due to the quantum interference of the measured state with the ancillary states used in the measurement process. This fact, however, is not captured by most of the existing non-classicality criteria, except the coherence monotones described in Ch. 5, which, as we show further diverge at large d_0.

In order to address these issues we combine two existing criteria - quantum discord, and entanglement potential. As mentioned in Ch. 5, the entanglement potential is a

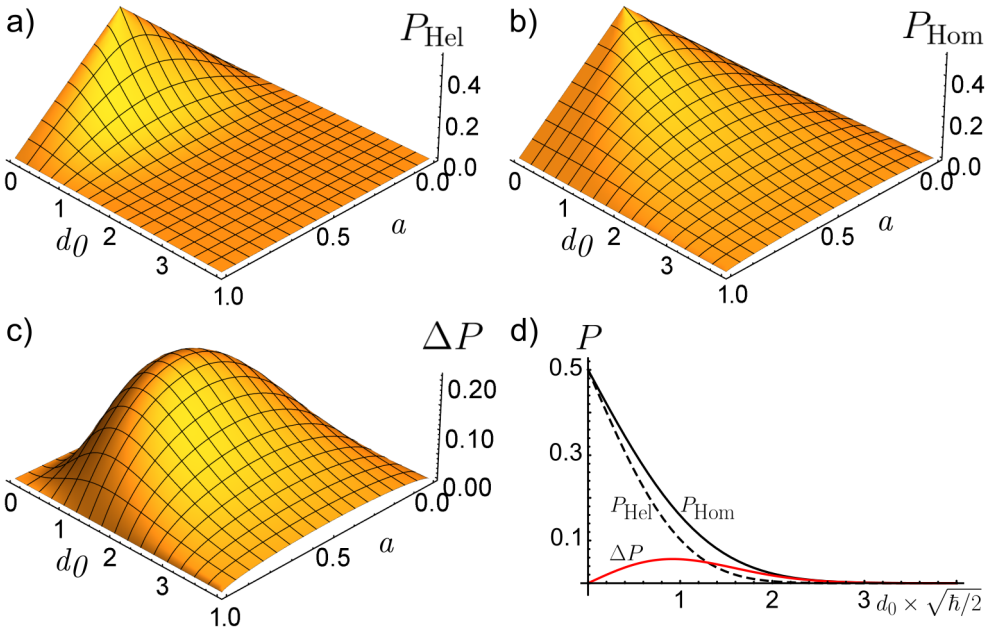

Figure 6.2: The dependence on the parameters a and d_0 of a) minimal possible error rate P_{Hel} in binary coherent state discrimination. b) P_{Hom}– error rate of a classical homodyne measurement; c) $\Delta P = P_{\mathrm{Hom}} - P_{\mathrm{Hel}}$, the difference in error rate of a classical and quantum measurement. d) Cross-sections of a, b and c at $a = 1/2$: $\Delta P(1/2, d_0)$, $P_{\mathrm{Hom}}(1/2, d_0)$, $P_{\mathrm{Hel}}(1/2, d_0)$.

single-mode non-classicality measure based on the amount of entanglement between the output modes of a balanced lossless beam splitter, when the investigated state is one of the inputs and the other input is vacuum. As we will see in the next sections, if quantum discord between the output modes is taken instead of entanglement in this situation, the resulting non-classicality measure is able to capture the quantum advantage in the state discrimination, described above. However, first we need to review more in detail the quantum-mechanical description of a beam-splitter.

6.2 Beam splitter operation

Despite its apparent simplicity a beam splitter is a key instrument in quantum optics. This device is an essential tool in such seminal experiments as Hanbury Brown - Twiss and Hong-Ou-Mandel effect observation [131, 185]. Overall, it is hard to imagine a quantum optics experiment, that does not use a beam splitter of any kind. There are several reasons for this. First of all, any discrete unitary operator in a finite-dimensional Hilbert space can be experimentally realized by a set of generalized (the ones that allow to tune the phase between the output beams) beam splitters [186, 187]. Secondly, a

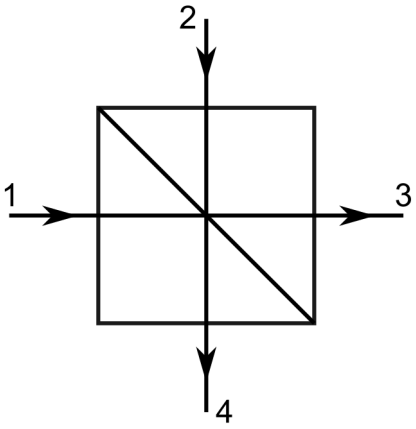

Figure 6.3: Schematic representation of a beam splitter.

beam splitter can be used to observe interference, not only in purely optical, but in quantum-mechanical sense, being a complete analogy of the famous Feynman double slit-setup [188]. Finally, from a theoretical point of view the beam splitter operation is closely related to the abstract rotations of angular momenta on a sphere [189]. In particular, the operation of a symmetric beam splitter is described by the displacement operator $\hat{D}$, (5.41) [190].

One more reason to consider in detail the beam splitter operation is that it is a simple limiting case of a linear multiply scattering medium. When the size of scattering matrix is equal to 2, which means that there are only 2 input and output modes, this expression effectively describes the classical beam splitter operation. Therefore a medium described by a $N \times N$ scattering matrix can be treated as a N-port beam splitter. Quantum optical description of such devices will be considered in the next section.

There are two variants of quantum optical description of the beam splitter operation. The first takes as an input the density matrix of a two-mode input state in the Fock basis and treats the action of a beam splitter as a unitary operator in an appropriate Hilbert space [189]. Despite being completely general, this approach has a disadvantage of dealing with infinite-dimensional matrices. As it is common for the continuous variable systems, phase space approach is more convenient in this situation. The beam splitter operation within this approach is described by a linear mapping between the input and output coherent state amplitudes applied to the variables of the input state quasiprobability distribution [185].

Let's consider a 2-mode beam splitter, with the input modes indexed 1 and 2, and the output modes 3 and 4, as in Fig. 6.3. The amplitudes of the input and output modes are related as

$$\begin{pmatrix} a_3 \\ a_4 \end{pmatrix} = \begin{pmatrix} \mathcal{T} & \mathcal{R} \\ \mathcal{R} & \mathcal{T} \end{pmatrix} \begin{pmatrix} a_1 \\ a_2 \end{pmatrix} \tag{6.13}$$

where $\mathcal{T}$ and $\mathcal{R}$ are the complex reflection and transmission coefficients of the beam splitter. From the unitarity of the scattering matrix it follows that:

$$|\mathcal{R}|^2 + |\mathcal{T}|^2 = 1 \qquad \text{and} \qquad \mathcal{R}\mathcal{T}^* + \mathcal{R}^*\mathcal{T} = 0 \tag{6.14}$$

As we discussed in the previous chapter, in order to switch to the quantum mechanical description we can replace the modes' amplitudes with corresponding annihilation operators. This leads to the following relations between the input and output modes

$$\hat{a}_3 = \mathcal{R}\hat{a}_1 + \mathcal{T}\hat{a}_2 \qquad \text{and} \qquad \hat{a}_4 = \mathcal{T}\hat{a}_1 + \mathcal{R}\hat{a}_2 \tag{6.15}$$

Now in order to find the relations between the input and output we demand that

$$\mathrm{Tr}[f(\hat{a}_3, \hat{a}_4)\rho_{\mathrm{out}}] = \mathrm{Tr}[f(\mathcal{R}\hat{a}_1 + \mathcal{T}\hat{a}_2, \mathcal{R}\hat{a}_1 + \mathcal{T}\hat{a}_2)\rho_{\mathrm{in}}] \tag{6.16}$$

for any function f of the annihilation operators. Using the optical equivalence theorem and the P-function state representations of ρ_{in} and ρ_{out} we can rewrite (6.16) in the integral form

$$\int f(\alpha_3, \alpha_4) P_{\mathrm{out}}(\alpha_3, \alpha_4)\, d^2\alpha_3\, d^2\alpha_4 = \int f(\mathcal{R}\alpha_1 + \mathcal{T}\alpha_2, \mathcal{R}\alpha_1 + \mathcal{T}\alpha_2) P_{\mathrm{in}}(\alpha_1, \alpha_2)\, d^2\alpha_1\, d^2\alpha_2, \tag{6.17}$$

where α_i are complex amplitudes of the corresponding BS channels and P_{in} and P_{out} are the P-functions of the beam splitter input and output states respectively. After a change of variables

$$\alpha_1 \to \mathcal{T}\alpha_3 - \mathcal{R}\alpha_4 \qquad \alpha_2 \to \mathcal{R}\alpha_3 + \mathcal{T}\alpha_4, \tag{6.18}$$

expression (6.21) is rewritten as

$$\int f(\alpha_3, \alpha_4) P_{\mathrm{out}}(\alpha_3, \alpha_4)\, d^2\alpha_3\, d^2\alpha_4 = \int f(\alpha_3, \alpha_4) P_{\mathrm{in}}(\mathcal{T}\alpha_3 - \mathcal{R}\alpha_4, \mathcal{R}\alpha_3 + \mathcal{T}\alpha_4)\, d^2\alpha_3\, d^2\alpha_4, \tag{6.19}$$

as this expression should hold for any f

$$P_{\text{out}}(\alpha_3, \alpha_4) = P_{\text{in}}(\mathcal{T}\alpha_3 - \mathcal{R}\alpha_4, \mathcal{R}\alpha_3 + \mathcal{T}\alpha_4) \tag{6.20}$$

By taking into account the relations between the phases of $\mathcal{R}$ and $\mathcal{T}$ that follow from (6.14), the expression above can be simplified to

$$P_{\text{out}}(\alpha_3, \alpha_4) = P_{\text{in}}(\sqrt{|\mathcal{T}|}\alpha_3 - i\sqrt{|\mathcal{R}|}\alpha_4, -i\sqrt{|\mathcal{R}|}\alpha_3 + \sqrt{|\mathcal{T}|}\alpha_4), \tag{6.21}$$

Now we are ready to implement the non-classicality criterion that can characterize the quantum advantage discussed in the previous section.

6.3 Discord potential

The advantage ΔP indicates a non-trivial quantum property in the state ρ_0, (6.6) which we want to capture with a suitable measure of non-classicality. It is clear that most of the measures listed in Sec. 5.4 are not able to capture these non-classical features. Indeed, the photon statistics of such a state is just a mixture of two Poissonian distributions, and any of its quasiprobability distributions are positive and well defined, therefore the measure able to capture these features should be more sensitive than the others. For multimode states quantum discord is a proper candidate, since it grasps subtle non-classical correlations beyond entanglement. However, in order to apply this criterion, we need some technique that maps single mode non-classicality to a multimode one. Such a technique was developed to implement the entanglement potential (See sec. 5.4.2). Entanglement potential $EP(\rho)$ is formally defined as

$$EP(\rho) = E_{\mathcal{N}}(\rho_{BS}) \tag{6.22}$$

where $E_{\mathcal{N}}$ is the logarithmic negativity [139], the most common measure of entanglement and ρ_{BS} is a two-mode state obtained by impinging ρ on a balanced beam splitter, as shown in Fig. 6.4. Formally, this output state can be written as

$$\rho_{BS} = U_{BS}\left(\rho \otimes |0\rangle\langle 0|\right) U_{BS}^{\dagger}, \tag{6.23}$$

and $E_{\mathcal{N}}$ can be expressed as

$$E_{\mathcal{N}}(\rho_{BS}) = \log ||\rho_{BS}^{T_A}||, \tag{6.24}$$

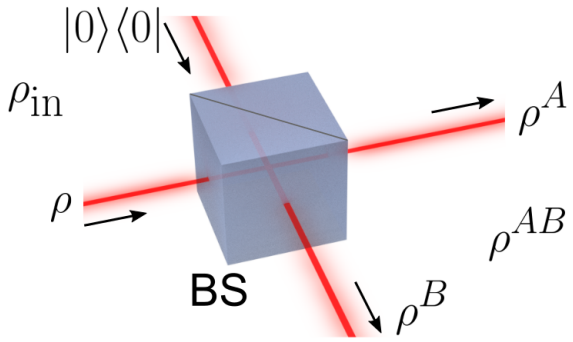

Figure 6.4: A beam splitter transforms a state ρ and the vacuum state $|0\rangle\langle 0|$ into a two-mode state ρ_{BS}. ρ_A and ρ_B are the reduced states of ρ^{BS}.

where $||\cdot||$ denotes the trace norm and $\rho_{BS}^{T_A}$ is the partially transposed state (5.83).

We note that the entanglement potential was constructed as a measure of quantumness that explicitly identifies proper mixtures of coherent states as classical [165]; i.e. it does not capture the advantage in coherent state discrimination. Here we are looking for a measure C that characterises the non-classicality of any state, with the following properties:

- it is positive-defined,
- it is non-zero for all states that have a non-zero entanglement potential,
- it vanishes for the coherent state mixtures ρ_0 when $d_0 \to 0$ and when $d_0 \to \infty$,
- and it is strictly positive for intermediate distances d_0 for mixtures ρ_0.

We define the *discord potential* C_D as a measure of non-classicality of any state ρ in analogy to (6.22)

$$C_D(\rho) \equiv D(\rho_{BS}), \tag{6.25}$$

where $D(\rho_{BS})$ is the quantum discord, (5.94) and ρ_{BS} is given by (6.23). In order to verify if C_D satisfies the desired properties, we now calculate it for a mixture of coherent states (6.6).

6.4 Discord potential of a coherent state mixture

6.4.1 Beam splitter output state

The first step in the calculation of the discord potential of a state ρ_0 (6.6), is to obtain the two-mode output state ρ_{BS} (6.23). In order to do that we use the relations between

the quasi-probability distributions of the input and output of a lossless balanced beam splitter outlined in Sec.6.2. Specifically, for a one-mode state ρ the P-function is a distribution over a complex amplitude given by the Eq. (5.63). Then, according to (6.21), the P-function of a two-mode BS output state is related to the P-function of the two-mode input state as

$$P_{\rho_{BS}}(\xi', \zeta') = P_{\rho_0 \otimes |0\rangle\langle 0|}\left(\frac{\xi' - i\zeta'}{\sqrt{2}}, \frac{\zeta' - i\xi'}{\sqrt{2}}\right). \tag{6.26}$$

For the input state $\rho_0 \otimes |0\rangle\langle 0|$ the P-function is:

$$P_{\rho_0 \otimes |0\rangle\langle 0|}(\xi, \zeta) = \left[a\,\delta^2(\xi - \alpha_0) + (1-a)\,\delta^2(\xi - \beta_0)\right] \cdot \delta^2(\zeta). \tag{6.27}$$

Substituting (6.27) into (6.26) gives the output P-function, from which we obtain the density matrix of the output state:

$$\rho_{BS} = a\,|\alpha\rangle\langle\alpha| \otimes |i\alpha\rangle\langle i\alpha| + (1-a)\,|\beta\rangle\langle\beta| \otimes |i\beta\rangle\langle i\beta|, \tag{6.28}$$

where $\alpha = \alpha_0/\sqrt{2}$, $\beta = \beta_0/\sqrt{2}$. The reduced state ρ^A of the mode A is then:

$$\rho^A = a|\alpha\rangle\langle\alpha| + (1-a)|\beta\rangle\langle\beta|, \tag{6.29}$$

with ρ^B taking exactly the same form.

We are now ready to calculate the discord $D(\rho_{BS})$. The first problem we encounter in this calculation is that coherent states, such as in (6.6), are elements of the infinite dimensional Hilbert space spanned by the Fock basis. At first this makes the direct calculation of the entropies in (5.94) tricky, as one would need to find the eigenvalues of an infinite matrix. In the next section we develop a straightforward method to calculate these entropies for a particular set of states considered here.

6.4.2 Calculating entropies of (non-Gaussian) coherent state mixtures

While calculations in the infinite dimensional Hilbert space can be challenging and are usually limited to Gaussian states [155, 158, 159], the entropies of the states like ρ_0 can be obtained by moving to the Hilbert space spanned by the non-trivial pure state elements of the considered mixture and establishing an orthonormal basis in this smaller

sub-space. For a general proper mixture of coherent states

$$\rho = \sum_{j=1}^{N} p_j \, |\alpha_j\rangle\langle\alpha_j|, \tag{6.30}$$

with $p_j > 0$, this subspace can be spanned by the $|\alpha_j\rangle$ for $j = 1, \ldots, N$, the orthonormal basis $|u_j\rangle$ can be built using the Gram-Schmidt procedure:

$$|u_1\rangle \quad = |\alpha_1\rangle, \tag{6.31}$$

$$|u_j\rangle \;\; = \tfrac{|v_j\rangle}{||v_j||}, \quad |v_j\rangle \;\; = |\alpha_j\rangle - \sum_{k}^{N-1} \frac{\langle v_k|\alpha_j\rangle}{\langle v_k|v_k\rangle}. \tag{6.32}$$

In such a basis the only non-zero elements of ρ will be:

$$\rho_{jk} = \langle u_j|\rho|u_k\rangle. \tag{6.33}$$

This is a finite dimensional matrix of size $N \times N$, where N is the number of pure state elements in Eq. (6.30). This finite-dimensional matrix is straightforwardly diagonalized allowing the calculation of the eigenvalues and entropy of the state ρ.

For example, for the reduced state ρ^A in Eq. (6.29) an orthonormal basis in the subspace spanned by $|\alpha\rangle$ and $|\beta\rangle$ is given by:

$$|u_1\rangle = |\alpha\rangle; \qquad |u_2\rangle = \frac{|\beta\rangle - k|\alpha\rangle}{\sqrt{1-|k|^2}}, \tag{6.34}$$

where $k = \langle\alpha|\beta\rangle$. In this basis ρ^A can be written as:

$$\rho^A = \begin{pmatrix} a + (1-a)k^2 & \frac{k(1-a)(1-|k|^2)}{\sqrt{1-k^2}} \\ \frac{k^*(1-a)(1-|k|^2)}{\sqrt{1-k^{*2}}} & (1-a)(1-k^2) \end{pmatrix}. \tag{6.35}$$

The eigenvalues and the entropy, $S(\rho^A)$, are now readily calculated. The resulting entropy $S(\rho^A)$ is shown in Fig 6.5, as a function of the mixing parameter a and the separation d, which measures the overlap between the coherent states $|\alpha\rangle$ and $|\beta\rangle$ in the reduced state of the output mode A, ρ^A (6.6). d is directly related to the separation d_0 between $|\alpha_0\rangle$ and $|\beta_0\rangle$ as $d_0 = \sqrt{2}d$, since $\alpha_0 = \sqrt{2}\alpha$ and $\beta_0 = \sqrt{2}\beta$. When d is large, the coherent states in the mixture ρ^A are almost orthogonal and the mode acts effectively as a classical system with two possible outcomes: either $|\alpha\rangle$ or $|\beta\rangle$. The entropy $S(\rho^A)$ is maximal when they are equiprobable and reduces to 0 when the probability of either of them tends to 0. However as d decreases, an additional source of uncertainty appears

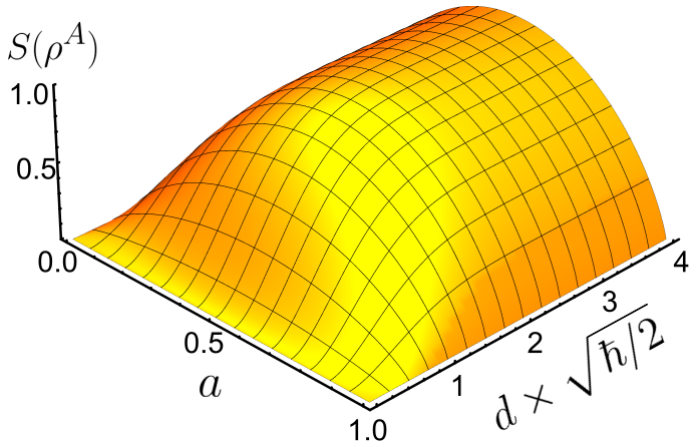

Figure 6.5: The entropy $S(\rho^A)$ as a function of the mixing ratio a and separation d.

from non-orthogonality of $|\alpha\rangle$ and $|\beta\rangle$, which reduces the maximal entropy of the state. When d approaches 0, the entropy also reduces to 0 indicating that the mode A tends more and more to a pure state.

To calculate the entropy of the two-mode state $S(\rho^{AB})$ in Eq. (6.28) one has to introduce an analogous pair of basis vectors for the second mode and then diagonalize a four-dimensional matrix to obtain the entropy. The last term in the expression for the discord (5.94) is the entropy of a single reduced mode, but requires the optimization over all possible measurement operators for the other mode. In the subspace spanned by $|\alpha\rangle$ and $|\beta\rangle$ the general set of projective measurement operators is:

$$\Pi_1^A = (\cos\theta\,|u_1\rangle + e^{i\phi}\,\sin\theta\,|u_2\rangle)(\cos\theta\,\langle u_1| + e^{-i\phi}\,\sin\theta\,\langle u_2|) \tag{6.36}$$

$$\Pi_2^A = (\sin\theta\,|u_1\rangle - e^{-i\phi}\,\cos\theta\,|u_2\rangle)(\sin\theta\,\langle u_1| - e^{i\phi}\,\cos\theta\,\langle u_2|) \tag{6.37}$$

Using these operators it is then possible to calculate the conditional entropy, $S(\sigma^{B|\{\Pi_j^A\}})$ and minimize this entropy over all θ and ϕ, see Appendix A.

For the more general case that the input state is a mixture of more than two pure state elements, i.e. $N > 2$, the Gram-Schmidt diagonalization can still be used to calculate the entropies for $N \otimes N$ reduced states. But the optimization procedure for obtaining the conditional entropies becomes complicated and has so far been shown to be possible using the linear entropy approximation for $2 \otimes N$ systems [191].

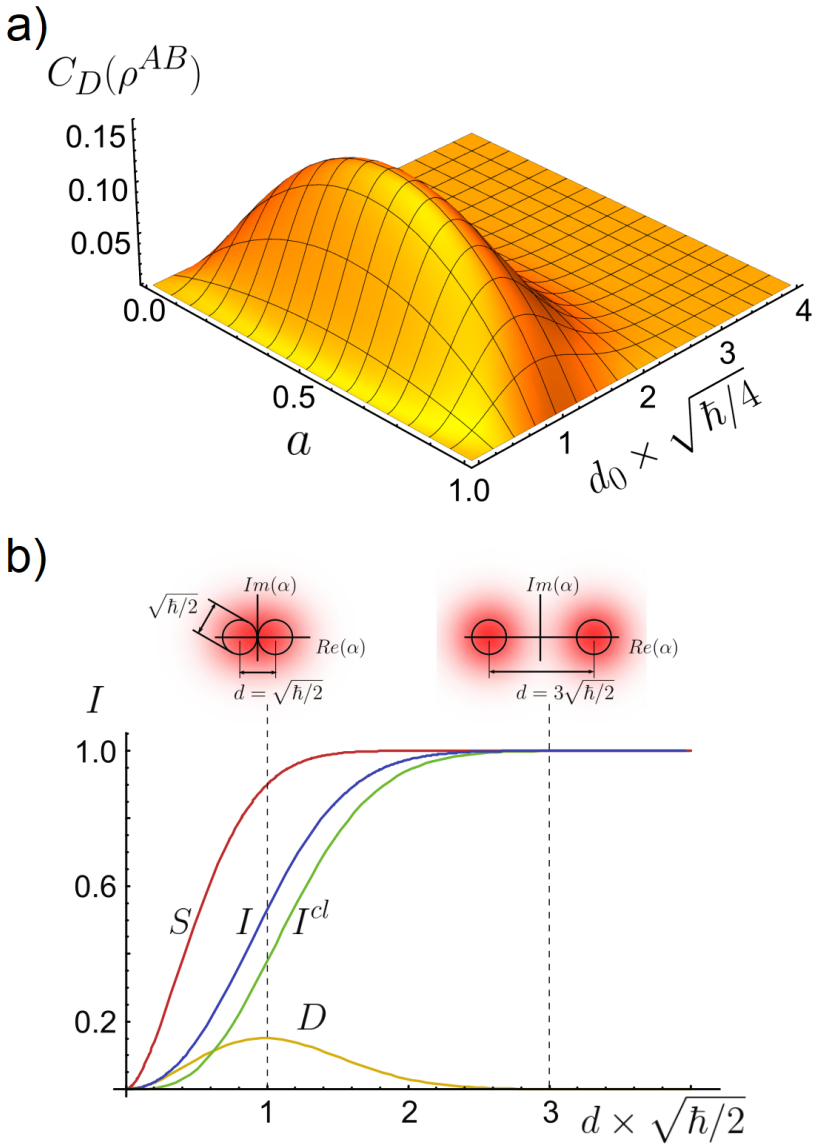

Figure 6.6: a) Discord potential C_D of ρ_0, see Eq. (6.6), as a function of mixing probability a and overlap d_0. b) Output state's total entropy $S(\rho^{AB})$ (red line), its mutual information $I(\rho^{AB})$ (blue line), classical contribution to the mutual information $I^{cl}(\rho^{AB})$ (green line) and quantum contribution to the mutual information, i.e. discord, $D(\rho^{AB})$ (yellow line) as a function of d. The upper panel illustrates the overlap between the two coherent states $|\alpha\rangle$ and $|\beta\rangle$ in ρ^{AB}.

6.4.3 Dependence of the discord potential on the coherent state separation

The discord of the two-mode output state, $D(\rho^{AB})$, and thus the discord potential $C_D(\rho_0)$ of the input state, shown in Fig. 6.6a, vanishes for $d_0 \to 0$, $d_0 \to \infty$, $a \to 0$ and $a \to 1$, as we required for our non-classicality measure.

Fig. 6.6b shows the output state discord $D(\rho^{AB})$, its entropy $S(\rho^{AB})$, its mutual information $I(\rho^{AB}) = S(\rho^A) + S(\rho^B) - S(\rho^{AB})$, and the "classical" contribution to the mutual information, $I^{cl}(\rho^{AB}) = I(\rho^{AB}) - D(\rho^{AB})$, as a function of $d = |\alpha - \beta|$, with d directly related to the separation in the input state, as $d = d_0/\sqrt{2}$. As can be seen from the figure, the discord reaches a maximum for $d = \sqrt{\hbar/2}$. This is the distance at which the peaks of the input state Wigner-function is equal to half of the value of the coherent state quadrature uncertainty, which is equivalent to the Rayleigh criterion for peak resolution [192]. Interestingly, for $d <\approx \sqrt{\hbar/8}$ the quantum discord contribution to I becomes larger than the classical contribution.

6.5 Comparison with the coherence monotones

Alternative candidates that may satisfy our requirements for a measure of non-classicality are the coherence monotones [16, 166], which quantify the coherence of a quantum state with respect to a chosen basis. In quantum information theory quantum coherences have been shown to be a resource for creating non-classical correlations [193, 194], for enhancing quantum measurement precision [195] and for performing certain quantum computational tasks [196]. Coherences can be quantified by the l_1 *norm of coherence*

$$C_{l_1}(\rho) = \sum_{n \neq k} |\rho_{n,k}|, \tag{6.38}$$

where $\rho_{n,k}$ are the coefficients of the state in a basis $\{|n\rangle\}$, and the *relative entropy of coherence*

$$C_{RE}(\rho) = S(\rho_{\text{diag}}) - S(\rho), \tag{6.39}$$

where ρ_{diag} is the state obtained by removing the non-diagonal elements of ρ in the chosen basis.

We first evaluate the large α asymptotes of the coherence monotone C_{l_1} for a coherent state $|\alpha\rangle$ in the Fock basis $\{|n\rangle\}$ with $n = 0, 1, 2, ...$, and then conclude with stating the asymptotic behaviour of a mixture of two coherent states.

Using Eq. (6.38) the l_1 norm of coherence for a coherent state in the Fock basis is:

$$\begin{aligned} C_{l_1}(|\alpha\rangle) &= e^{-|\alpha|^2} \sum_{k \neq n} \frac{|\alpha|^{n+k}}{\sqrt{k!\, n!}} \\ &= e^{-|\alpha|^2} \left(\left[1 + \sum_{k=1}^{\infty} \frac{|\alpha|^k}{\sqrt{k!}} \right]^2 - \sum_{k=0}^{\infty} \frac{|\alpha|^{2k}}{k!} \right). \end{aligned} \tag{6.40}$$

The resulting summation contains a square root of a factorial, and does not have a closed form. However, its asymptotic behaviour at large $A := |\alpha|$ can be estimated using the following procedure:

We introduce

$$f(A) = \sum_{k=1}^{\infty} \frac{A^k}{\sqrt{k!}} \quad \text{and} \quad g(A) = \frac{A}{f(A)} \left(\frac{\mathrm{d}f}{\mathrm{d}A}\right), \tag{6.41}$$

so that

$$C_{l_1}(|\alpha\rangle) \;\; = e^{-A^2} \; (1 + 2f(A) + f^2(A)) - 1. \tag{6.42}$$

Using that the ratio of two power series in x with coefficients p_k and q_k for large x is asymptotically determined by the ratio of the coefficients of the largest power,

$$\lim_{x\to\infty} \frac{\sum_{k=1}^{\infty} p_k \, x^k}{\sum_{k=1}^{\infty} q_k \, x^k} = \lim_{k\to\infty} \frac{p_k}{q_k}, \tag{6.43}$$

the asymptote of $g(A)/A^2$ for large A is:

$$\lim_{A\to\infty} \frac{g(A)}{A^2} = \lim_{A\to\infty} \frac{\sum_{k=0}^{\infty} \frac{(k+1)A^k}{\sqrt{(k+1)!}}}{\sum_{k=2}^{\infty} \frac{A^k}{\sqrt{(k-1)!}}} = \lim_{k\to\infty} \frac{(k+1)\sqrt{(k-1)!}}{\sqrt{(k+1)!}} = 1, \tag{6.44}$$

and thus $g(A) = A^2 + o(A^2)$. The next order of the approximation is given by

$$\lim_{A\to\infty} \left(g(A) - A^2\right) = \lim_{A\to\infty} \frac{\sum_{k=2}^{\infty} \frac{(k-1)A^k}{\sqrt{(k-1)!}} - \sum_{k=4}^{\infty} \frac{A^k}{\sqrt{(k-3)!}}}{\sum_{k=2}^{\infty} \frac{A^k}{\sqrt{(k-1)!}}} \tag{6.45}$$

$$= \lim_{k\to\infty} \left((k-1) - \sqrt{(k-1)(k-2)}\right) = \frac{1}{2}, \tag{6.46}$$

and thus $g(A) = A^2 + \frac{1}{2} + o(1)$.

This leads to the following differential equation for $f(A)$:

$$\left(\frac{\mathrm{d}f}{\mathrm{d}A}\right) = \left(A^2 + \frac{1}{2} + o(1)\right) \frac{f(A)}{A}, \tag{6.47}$$

which in the asymptotic limit of large A has the solution

$$f(A) \approx e^{\frac{A^2}{2}} \sqrt{cA} \tag{6.48}$$

with c a constant which can be evaluated numerically, resulting in $c \approx 5$. Further terms of the approximation will lead to multipliers of the form $\exp[\frac{1}{A^k}]$ with $k > 1$ in $f(A)$, which quickly converge to 1 for large A. This allows one to conclude that the l_1 norm of coherence of a coherent state in the Fock basis for large α asymptotically becomes

$$C_{l_1}(|\alpha\rangle) \quad = e^{-|\alpha|^2} + 2e^{\frac{-|\alpha|^2}{2}}\sqrt{c|\alpha|} + c|\alpha| - 1 \approx c|\alpha| \tag{6.49}$$

i.e. that C_{l_1} diverges for $|\alpha| \to \infty$.

We now return to a proper mixture of two coherent states, $\rho = a|\alpha\rangle\langle\alpha| + (1-a)|\beta\rangle\langle\beta|$ with $0 < a < 1$. This state's coefficients in the Fock basis are

$$\rho_{k,n} = \frac{a\, e^{-|\alpha|^2}\alpha^k\alpha^{*n} + (1-a)e^{-|\beta|^2}\beta^k\beta^{*n}}{\sqrt{k!\, n!}}. \tag{6.50}$$

One can see that these coefficients imply that the l_1 norm of coherence, Eq. (6.38), will depend on the absolute values of α and β, not just their relative displacement, in contrast to the discord potential which only depends on the relative displacement.

To illustrate the behaviour of the l_1 norm of coherence on the separation of the elements of the mixture we here choose $\beta = -\alpha$ and also $a = 1/2$. The mixed state coefficients then simplify to

$$\rho_{k,n} = \frac{\alpha^k\alpha^{*n}}{\sqrt{k!\, n!}}\, e^{-|\alpha|^2} \quad \text{for} \quad k + n = \text{even}. \tag{6.51}$$

Thus, the coefficients of the mixture of coherent states are identical to those for the coherent state $|\alpha\rangle$, but only when $k + n$ is an even number. As a consequence the coherence monotone $C_{l_1}(\rho)$ has almost identical asymptotic behaviour for large $|\alpha|$ as the monotone for the coherent state $C_{l_1}(|\alpha\rangle)$, with $C_{l_1}(\rho) = \frac{1}{2}C_{l_1}(|\alpha\rangle) \approx \frac{c}{2}|\alpha|$. The diverging asymptotic behaviour of $C_{l_1}(\rho)$ for large α is indicated in Fig. 6.7.

6.5.1 Asymptotic behaviour of C_{RE} for coherent states in the Fock basis

We first evaluate the large α asymptotes of the relative entropy of coherence C_{RE} for a coherent state $|\alpha\rangle$ in the Fock basis $\{|n\rangle\}$ with $n = 0, 1, 2, ...$, and then conclude with stating the asymptotic behaviour of a mixture of two coherent states.

The second term in Eq. (6.39) is 0 since the coherent state is pure, which leaves us

with

$$\begin{aligned} C_{RE}(|\alpha\rangle) &= -e^{-|\alpha|^2} \sum_{k=0}^{\infty} \frac{|\alpha|^{2k}}{k!} \ln\left(e^{-|\alpha|^2} \frac{|\alpha|^{2k}}{k!} \right) \\ &= |\alpha|^2 (1 - 2\ln|\alpha|) + e^{-|\alpha|^2} \sum_{k=0}^{\infty} \frac{|\alpha|^{2k}}{k!} \ln k!. \end{aligned} \tag{6.52}$$

For large $A := |\alpha|$ the high powers are important and we use the Stirling approximation $\ln k! \approx k \ln k - k + \frac{1}{2}\ln(2\pi k) + \ldots$, to transform the above expression to:

$$\begin{aligned} C_{RE}(|\alpha\rangle) &= \tfrac{1}{2} e^{-A^2} \textstyle\sum_{k=1}^{\infty} \frac{A^{2k}}{k!} \ln k + A^2 e^{-A^2} \sum_{k=0}^{\infty} \frac{A^{2k}}{k!} \ln(k+1) - \\ &\qquad - A^2 \ln A^2 + \tfrac{\ln(2\pi)}{2}. \end{aligned} \tag{6.53}$$

Now we need to establish the asymptotic behaviour for large A of the functions

$$h_0(A) = e^{-A^2} \sum_{k=1}^{\infty} \frac{A^{2k}}{k!} \ln k \quad \text{and} \quad h_1(A) = e^{-A^2} \sum_{k=0}^{\infty} \frac{A^{2k}}{k!} \ln(k+1). \tag{6.54}$$

After substituting the Laplace transform identity $\ln k = -k \int_0^{\infty} e^{-kt} \ln t \, \mathrm{d}t - \gamma$, in Eq. (6.54), where γ is the Euler – Mascheroni constant, $h_0(A)$ becomes:

$$\begin{aligned} h_0(A) &= -e^{-A^2} \textstyle\int_0^{\infty} \sum_{k=1}^{\infty} \frac{A^{2k} e^{-kt}}{k!} k \ln t \, \mathrm{d}t - \gamma \left(1 - e^{-A^2}\right) \\ &= -e^{-A^2} A^2 \textstyle\int_0^{\infty} e^{-t + A^2 e^{-t}} \ln t \, \mathrm{d}t - \gamma \left(1 - e^{-A^2}\right) \\ &= -A^2 \textstyle\int_0^1 e^{A^2(x-1)} \ln\left(\ln \frac{1}{x}\right) \mathrm{d}x - \gamma \left(1 - e^{-A^2}\right) \end{aligned}$$

where $x = e^{-t}$ and the integral kernel is $I(A, x) = e^{A^2(x-1)} \ln\left(\ln \frac{1}{x}\right)$.

The kernel $I(A, x)$ diverges at the points $x = 0$ and $x = 1$, i.e. $I(A, 0) \to \infty$ and $I(A, 1) \to -\infty$, and these points will give maximal contribution to the integral. Also at $x = 1/e$ the kernel vanishes, i.e. $I(A, 1/e) = 0$. Splitting the integral into two parts,

$$\int_0^1 I(A, x) \, \mathrm{d}x = \int_0^{1/e} I(A, x) \, \mathrm{d}x + \int_{1/e}^1 I(A, x) \, \mathrm{d}x \,, \tag{6.55}$$

we bound the asymptotic behaviour of the first integral using the Cauchy–Schwarz inequality

$$0 \le \int_0^{1/e} I(A, x) \, \mathrm{d}x \le \frac{\text{const.}}{\sqrt{2}A} \, e^{-A^2\left(1 - \frac{1}{e}\right)}, \tag{6.56}$$

where const. is a number arising from integrating $\left(\ln(-\ln x)\right)^2$ and taking the square root. This shows that the first integral decays exponentially with $A \to \infty$.

In order to find the asymptotic behaviour of the second integral we change variables $x-1=-p$,

$$\int_{1/e}^{1} I(A,x)\,\mathrm{d}x = \int_{0}^{1-1/e} e^{-pA^2}\ln(-\ln(1-p))\,\mathrm{d}p. \tag{6.57}$$

Now we can expand the function $\ln(-\ln(1-p))$ around the point $p=0$,

$$\begin{aligned}\int_{1/e}^{1} I(A,x)\,\mathrm{d}x &= \textstyle\int_0^{1-1/e} e^{-pA^2}\left(\ln p + \sum_{k=1}^{\infty}\frac{(-1)^{n+1}}{n}\left[\sum_{k=2}^{\infty}\frac{p^{k-1}}{k}\right]^n\right)\mathrm{d}p \\ &= \textstyle\int_0^{1-1/e} e^{-pA^2}\left(\ln p + \frac{p}{2} + \frac{5p^2}{24} + \frac{90p^3}{720} + \ldots\right)\mathrm{d}p \\ &= \textstyle\int_0^{1-1/e} e^{-pA^2}\ln p\,\mathrm{d}p + \sum_{j=1}\lambda_j\int_0^{1-1/e} e^{-pA^2}p^j\,\mathrm{d}p\,.\end{aligned}$$

where λ_j are the expansion coefficient of the logarithm for powers of p. The leading contribution to the first of these integrals is

$$\int_{0}^{1-1/e} e^{-pA^2}\ln p\,\mathrm{d}p \approx -\frac{\gamma+\ln A^2}{A^2}, \tag{6.58}$$

plus some exponentially decaying terms in A. The second integral gives

$$\begin{aligned}\sum_{j=1}\lambda_j\int_{0}^{1-1/e} e^{-pA^2}\,p^j\,\mathrm{d}p &= \sum_{j=1}\lambda_j\frac{\Gamma(1+j)-\Gamma(1+j,A^2(1-\frac{1}{e}))}{A^{2(1+j)}} = \\ &= O\left(\frac{\mathrm{const}}{A^4}\right),\end{aligned} \tag{6.59}$$

where $\Gamma(k)$ and $\Gamma(k,A)$ are the Gamma and incomplete Gamma functions, respectively. Therefore for large A, when dropping decaying terms, one finds

$$\begin{aligned}h_0(A) &= -A^2\int_0^1 I(A,x)\,\mathrm{d}x - \gamma\,(1-e^{-A^2}) \\ &\approx -A^2\left(-\frac{\gamma+\ln A^2}{A^2}\right) + O\left(\frac{\mathrm{const}}{A^4}\right) - \gamma \approx \ln A^2.\end{aligned} \tag{6.60}$$

Using similar arguments one finds

$$h_1(A) \approx \ln A^2 + \frac{1}{2A^2} + o\left(\frac{\mathrm{const}}{A^2}\right). \tag{6.61}$$

Finally, the asymptotic behavior of C_{RE} of a coherent state for large $|\alpha| = A$ is

$$\begin{aligned}C_{RE}(|\alpha\rangle) &= \tfrac{1}{2}\,h_0(A) + A^2\,h_1(A) - A^2\ln A^2 + \tfrac{\ln(2\pi)}{2} \\ &\approx \ln A + \tfrac{1}{2} + \tfrac{\ln(2\pi)}{2} + o\,(\mathrm{const})\,,\end{aligned} \tag{6.62}$$

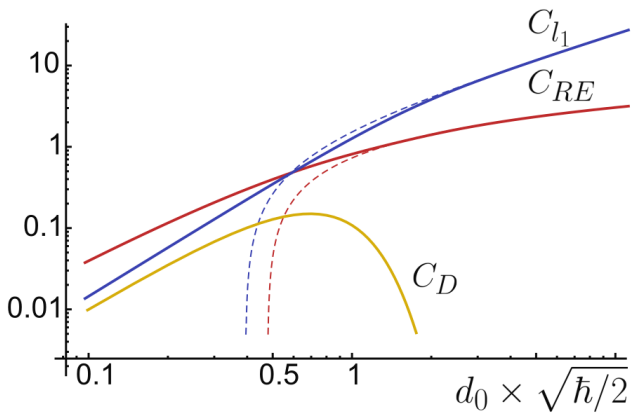

Figure 6.7: Discord potential C_D (solid yellow) and coherence monotones for ρ_0 as a function of $d_0 = \sqrt{2}\,d$. The l_1 norm of coherence C_{l_1} (solid blue) and relative entropy of coherence C_{RE} (solid red) are shown together with their asymptotic behaviour (dashed lines) for large d_0.

which diverges logarithmically as $A \to \infty$.

We return again to the mixture of two coherent states $|\alpha\rangle$ and $|-\alpha\rangle$, $\rho = \frac{1}{2}|\alpha\rangle\langle\alpha| + \frac{1}{2}|-\alpha\rangle\langle-\alpha|$ which allows us to illustrate the behaviour of the relative entropy of coherence C_{RE} on the separation $d = 2|\alpha|$. Since the diagonal coefficients of the mixed state, $\rho_{n,n}$, are identical to those for the coherent state $|\alpha\rangle$ its coherence monotone $C_{RE}(\rho)$ is identical to the coherent state one $C_{RE}(|\alpha\rangle)$ apart from the fact that the entropy $S(\rho)$ is now non-zero and rises to $\ln 2$ for large $|\alpha|$. Hence $C_{RE}(\rho) \approx C_{RE}(|\alpha\rangle) - \ln 2 \approx \ln|\alpha|$ for large $|\alpha|$ and this diverging asymptotic behaviour of $C_{RE}(\rho)$ is indicated in Fig. 6.7.

C_{RE} and $C_{l_1}(\rho)$ are plotted in Fig 6.7 for the mixture of two coherent states ρ_0 with $a = 1/2$ and $\beta_0 = -\alpha_0$ as a function of separation d_0. One can see that both, the l_1 norm of coherence and the relative entropy of coherence, increase monotonously with d_0. Notably they diverge for $d_0 \to \infty$, which contrasts with the properties we require for our non-classicality measure. Indeed, the l_1 norm of coherence has already been shown to diverge for a certain class of states in the infinite-dimensional case [168]. Here we have shown that actually both measures diverge for the coherent state mixtures. Moreover, both coherence monotones depend not only on the separation between the coherent states in the mixture d_0, but they also depend on the absolute amplitude of each coherent state $|\alpha_0|$ and $|\beta_0|$. In contrast, $C_D(\rho)$ depends only on d_0, tends to zero at both small and large values of d_0, and quantifies the state's non-classicality at intermediate separations, as can be seen in Fig. 6.6a,b. Thus the discord potential satisfies all our requirements. In addition, C_D does not require to choose a basis, in contrast to the coherence monotones.

6.6 Summary and outlook

As quantum mechanics contains classical theory as a limiting case, it can be hard to determine if a given system requires a full quantum-mechanical description or not, especially if it is infinite-dimensional. There exist a variety of non-classicality criteria, however they are often inconsistent, indicating non-overlapping sets of states as non-classical [197]. In particular, mixtures of coherent states are often considered classical, but there is a quantum advantage when discriminating between overlapping coherent states in the mixture, suggesting that a quantum-mechanical description is necessary to fully capture the system properties. We proposed a new criterion for non-classicality, based on the quantum discord of the output of a balanced beam splitter. This measure, which we name the discord potential, identifies as non-classical all states with non-zero entanglement potential, but it is also positive for mixtures of coherent states when the quantum advantage in discrimination is positive and vanishes otherwise. We also showed that the discord potential has several advantages over another set of commonly used non-classicality measures: the coherence monotones. First of all, the discord potential does not imply the existence of a preferred basis choice and secondly it stays always finite for mixtures of coherent states, in contrast to two coherence monotones. We have also shown a simple method to calculate the entropy of any state with positive P-function, which is an intermediate step of the discord potential calculation. We conclude that the discord potential can be a more sensitive indicator of non-classicality than the entanglement potential [165] or the of the P-function [162], capturing a wider class of states that show quantum advantages. In addition, the methods developed in the current chapter help to deal with the case of multimode scattering, considered in the next chapter.

Chapter 7

Quantum correlations of multiply scattered light

In the previous chapter we considered quantum correlations of the output state of a beam splitter and pointed out, that a linear multiply scattering medium can be considered as a multimode generalization of this device. In this chapter we finally approach the problem of identifying quantum features in the output state of light scattered by a disordered medium.

This chapter is based on the material presented in our paper [198], and follows its structure. We start by introducing the problem and pointing out why it is not possible to simply apply the results of the previous chapter in the multimode case. Then we apply the theory described in Ch. 5 to determine the quantum state of the output modes of the multiply scattering medium. In its general form it depends on the photon statistics of the input state and on the properties of the scattering medium, through the scattering matrix. After that we study in what situation quantum correlations can be present between an arbitrary pair of the output modes, by checking continuous variable entanglement [145, 199] and discord [158, 159] criteria for the quantum state of this pair. Next, we consider a number of different input state examples identifying what correlations in the output we can expect for each of them, paying more attention to the surprising case of the thermal state producing quantum discord in the output. Finally we evaluate the intensity correlations function in terms of the output covariance matrix, showing that it can't be a reliable criterion of the output state non-classicality.

7.1 Problem formulation and overview

The framework for the investigation of quantum features of multiply scattered light was established in [200], where the statistics of thermal noise interacting with a disordered material was studied. This approach was further developed in [201], and finally applied to study the propagation of squeezed radiation through random media [202], which is, to our knowledge, the first work on the interaction of non-classical light with the disordered materials. Later in a series of works [203–208] Lodahl et al. performed a systematic investigation of the non-classical properties of the multiply scattered light. Starting with the theoretical treatment [204], similar to [202], predicting the existence of a long-range quantum correlation in the reflected or transmitted light, they performed a series of experiments, confirming the existence of such correlation [206] and furthermore demonstrating quantum interference and entanglement in this situation [207, 208]. These pioneering works stimulated further interest to the quantum aspects of multiple scattering. Generation of quantum correlations in random waveguide lattices was studied from the perspective of the Anderson localization [106, 209]. Bi-photon speckle patterns as a manifestation of quantum correlations were investigated theoretically [210] and experimentally [211].

Further interest to this topic was motivated by the related problem of boson sampling [212], which attracted massive attention in recent years [213]. In this problem the output of a multimode linear interferometer is considered. It is relatively easy to predict the output state of such a device and therefore the probability to detect a photon in each of the output arms for an arbitrary input state. However, for a certain set of (non-classical) input states sampling from this probability distribution becomes a computationally hard task for a classical computer [214]. Despite being unable to perform a universal set of tasks, boson sampling is considered an accessible test model for quantum computation advantage demonstration. Normally, in the experiments on boson sampling, the key element, a multimode interferometer, is a predesigned device employing a waveguide [215] or photonic chip [216] architecture. Multiply scattering medium is a natural equivalent of such structures. The only prerequisite for using it as a multimode interferometer is the ability to control precisely the state of the incident light and its propagation within the scattering medium. Significant progress, achieved in recent years in this area, allowed to perform a series of experiments on the control of non-classical light propagation in the scattering media [217–220], enabling novel application far beyond boson sampling.

Despite substantial progress in understanding the non-classical light interaction with

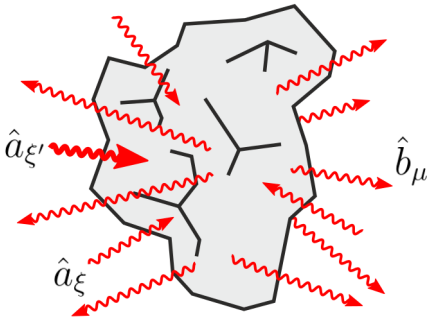

Figure 7.1: The disordered medium is scattering N input modes $\hat{a}_\xi$ into N output modes $\hat{b}_\mu$. The scattering process is described by a scattering matrix S. The only non-empty input mode is $\hat{a}_{\xi'}$, the others are assumed to be in a vacuum state.

disordered materials there are still points that need clarification. First of all, most of the works listed above use particular features of the output photon statistics, such as antibunching [204], or sub-shot-noise quantum fluctuations [206] as non-classicality criteria. Being only sufficient criteria these indicators can miss certain sets of non-classical states, as we discussed in the previous chapter. In our approach, for the first time to our knowledge, we use rigorous quantum information criteria [145, 158, 159] to address the problem of non-classical correlations generation during the multiple scattering process. As a result of that we are able to capture more subtle features beyond entanglement, which can be present even if the input state is regarded as classical. The drawback of this approach is that in the case of an arbitrary input state the multimode output state becomes complicated and therefore we have to limit ourselves to a set of Gaussian input states, that allow analytical treatment.

As we pointed out earlier, the process of multiple scattering can be described by a scattering matrix, that relates all the input modes to the output ones. In addition, as we know from Ch. 5, the transition from the classical to the quantum description can be done by replacing the amplitudes of the modes of the electromagnetic field by corresponding annihilation operators.

$$\hat{b}_\mu = \sum_{\xi}^{N} S_{\mu,\xi}\, \hat{a}_\xi, \quad \xi, \mu = 1, \ldots, N. \tag{7.1}$$

Here $\hat{a}$ and $\hat{b}$ are the annihilation operators related to, respectively, the input and the output modes as shown in Fig. 7.1.

If the scattering matrix is known, any observable quantity of the output state of light can be expressed as an expected value of some function $f(\hat{a}_\xi, \hat{a}_\xi^\dagger, S)$ over the quantum state of the input modes ρ_{in}. Moreover, in principle, the quasiprobability distributions

of the output modes can be obtained using a procedure analogous to the one used in Sec. 6.2 for a beam-splitter. In practice, however, this problem can be extremely difficult. As we have seen in the example of boson sampling [212] it can't be solved efficiently using classical computation.

However, while a beam-splitter is described by a 2x2 scattering matrix (see Sec. 6.2), for a typical disordered medium the size of the scattering matrix can be enormous [18]. As a consequence of that, the results of the previous chapter can't be directly extrapolated to the situation of multimode scattering. The main reasons preventing us from doing that are:

- The number of modes emerging in the multiple scattering process is so large, that often, despite being completely deterministic, this process is treated as random due to the multitude of possibilities of the initial state evolution. This leads to additional source of randomness in the output states of light emerging from such media, apart form quantum or classical dynamic fluctuations. The quantities characterizing the output state for a single fixed configuration of scatterers within the disordered medium could not be predicted, and the only practical way of analysing this situation is to replace them by the "disorder averages" as in Ch. 3.

- One more problem, somewhat related to the first one is that due to large number of output modes it is often impossible to keep track of all of them in the experiment. Therefore in any realistic scenario only a limited amount of the output modes is taken into account. However, as the scattering coefficients from a given input mode to any of the output ones are usually non-zero [221, 222], exclusion of some of the output modes leads to the behaviour described within the framework of open quantum systems [167], with the excluded modes serving as a lossy "environment".

- Finally, the argument raised in the previous point applies also to the input modes. It is impossible (and often not desirable) to populate all of them. While in the classical picture, it is possible just to exclude completely all the unoccupied modes from consideration, in the quantum version one has to include the vacuum contributions from all these input modes.

In order to take into account these points, in the current chapter we modify the general model of multiple scattering outlined in Ch. 3 to account for quantum features of the input and output light.

7.2 Covariance matrix of the output state

The covariance matrix together with a displacement vector provide a complete description of any Gaussian state within the infinite-dimensional Hilbert space, see Sec. 5.3.1. In this section our goal is to obtain the covariance matrix of the output state of light scattered by a disordered medium described by a scattering matrix S.

The first step is to substitute the expressions for the quadrature operators

$$\begin{aligned} \hat{x}_\mu &= \frac{(\hat{b}_\mu + \hat{b}_\mu^\dagger)}{\sqrt{2}} \\ \hat{p}_\mu &= \frac{\hat{b}_\mu - \hat{b}_\mu^\dagger}{i\sqrt{2}} \end{aligned} \tag{7.2}$$

into the expression for the covariance matrix (5.71). After that, we can express the elements of the output state covariance matrix as:

$$\begin{aligned} \sigma_{2\mu-1,2\nu-1} &= \frac{1}{2}\left(\delta_{\mu,\nu} + \Delta\hat{b}_\mu^\dagger\hat{b}_\nu + \Delta\hat{b}_\nu^\dagger\hat{b}_\mu + \Delta\hat{b}_\mu\hat{b}_\nu + \Delta\hat{b}_\mu^\dagger\hat{b}_\nu^\dagger\right) \\ \sigma_{2\mu,2\nu} &= \frac{1}{2}\left(\delta_{\mu,\nu} + \Delta\hat{b}_\mu^\dagger\hat{b}_\nu + \Delta\hat{b}_\nu^\dagger\hat{b}_\mu - \Delta\hat{b}_\mu\hat{b}_\nu - \Delta\hat{b}_\mu^\dagger\hat{b}_\nu^\dagger\right) \\ \sigma_{2\mu-1,2\nu} &= \frac{1}{2i}\left(\Delta\hat{b}_\mu\hat{b}_\nu - \Delta\hat{b}_\mu^\dagger\hat{b}_\nu^\dagger + \Delta\hat{b}_\mu^\dagger\hat{b}_\nu - \Delta\hat{b}_\nu^\dagger\hat{b}_\mu\right) \\ \sigma_{2\mu,2\nu-1} &= \frac{1}{2i}\left(\Delta\hat{b}_\mu\hat{b}_\nu - \Delta\hat{b}_\mu^\dagger\hat{b}_\nu^\dagger - \Delta\hat{b}_\mu^\dagger\hat{b}_\nu + \Delta\hat{b}_\nu^\dagger\hat{b}_\mu\right), \end{aligned} \tag{7.3}$$

where

$$\Delta AB = \langle AB\rangle - \langle A\rangle\langle B\rangle$$

In order to express the output covariance matrix in terms of the input mode properties, we substitute (7.1) into (7.3).

If any quantum features are present in the output when there is only one input mode, they will certainly persist when more input modes are added [223]. Therefore, for simplicity, we assume that all the input modes except one, ξ', are in vacuum state, as in Fig.7.1. Taking that into account, the general expressions for the output covariance matrix elements are

$$\begin{aligned} \sigma_{2\mu-1,2\nu-1} &= \frac{\delta_{\mu,\nu}}{2} + W_{\mu,\nu}\,\Delta\hat{n}_{\xi'} + Y_{\mu,\nu}\,\Delta\hat{a}_{\xi'}\hat{a}_{\xi'} + Y_{\mu,\nu}^*\,\Delta\hat{a}_{\xi'}^\dagger\hat{a}_{\xi'}^\dagger, \\ \sigma_{2\mu,2\nu} &= \frac{\delta_{\mu,\nu}}{2} + W_{\mu,\nu}\,\Delta\hat{n}_{\xi'} - Y_{\mu,\nu}\,\Delta\hat{a}_{\xi'}\hat{a}_{\xi'} - Y_{\mu,\nu}^*\,\Delta\hat{a}_{\xi'}^\dagger\hat{a}_{\xi'}^\dagger, \\ \sigma_{2\mu-1,2\nu} = \sigma_{2\mu,2\nu-1} &= \frac{1}{2i}\left[Z_{\mu,\nu}\,\Delta\hat{n}_{\xi'} + Y_{\mu,\nu}\,\Delta\hat{a}_{\xi'}\hat{a}_{\xi'} - Y_{\mu,\nu}^*\,\Delta\hat{a}_{\xi'}^\dagger\hat{a}_{\xi'}^\dagger\right], \end{aligned} \tag{7.4}$$

where

$$W_{\mu,\nu} = \left(S^*_{\mu,\xi'}S_{\nu,\xi'} + S^*_{\nu,\xi'}S_{\mu,\xi'}\right),$$
$$Z_{\mu,\nu} = \left(S^*_{\mu,\xi'}S_{\nu,\xi'} - S^*_{\nu,\xi'}S_{\mu,\xi'}\right),$$
$$Y_{\mu,\nu} = S_{\mu,\xi'}S_{\nu,\xi'},$$

This expression gives the general N-mode output state of the scattered light, for the case of one input mode. We can now select an arbitrary pair of the output modes and characterize their correlation properties, i. e. entanglement or quantum discord, but first we need to evaluate the state of this arbitrary pair depending on the properties of the input mode.

Coherent state: If the input mode is in a coherent state $|\alpha\rangle$ we have: $\langle\alpha|\hat{a}|\alpha\rangle = \alpha$, where α is the amplitude of the coherent state, also $\langle\alpha|\hat{a}^\dagger|\alpha\rangle = \alpha^*$, $\langle\alpha|\hat{a}\hat{a}|\alpha\rangle = \alpha\alpha$, $\langle\alpha|\hat{a}^\dagger\hat{a}^\dagger|\alpha\rangle = \alpha^*\alpha^*$, $\langle\alpha|\hat{a}^\dagger\hat{a}|\alpha\rangle = \alpha^*\alpha$. Thus the expectation value of all the operators in Eq. (7.2) is 0. Therefore the covariance matrix will be

$$\sigma^{\text{coh}} = \frac{1}{2}\mathbb{I}^{\oplus 2}. \tag{7.5}$$

This means that any two output modes will also be in a joint coherent state.

Thermal state: For a thermal state ρ_{th} we have: $Tr(\hat{a}\rho_{\text{th}}) = Tr(\hat{a}^\dagger\rho_{\text{th}}) = Tr(\hat{a}\hat{a}\rho_{\text{th}}) = Tr(\hat{a}^\dagger\hat{a}^\dagger\rho_{\text{th}}) = 0$ and $Tr(\hat{a}^\dagger\hat{a}\rho_{\text{th}}) = \bar{n}$, where $\bar{n}$ is the average number of photons in the input mode. The covariance matrix of the two output modes μ and ν is

$$\sigma^{\text{th}} = \begin{pmatrix} \sigma_a^{\text{th}} & 0 & \sigma_{t_1}^{\text{th}} & \sigma_{t_2}^{\text{th}} \\ 0 & \sigma_a^{\text{th}} & -\sigma_{t_2}^{\text{th}} & \sigma_{t_1}^{\text{th}} \\ \sigma_{t_1}^{\text{th}} & -\sigma_{t_2}^{\text{th}} & \sigma_b^{\text{th}} & 0 \\ \sigma_{t_2}^{\text{th}} & \sigma_{t_1}^{\text{th}} & 0 & \sigma_b^{\text{th}} \end{pmatrix} \tag{7.6}$$

with $\sigma_a^{\text{th}} = |S_{\mu,k'}|^2\bar{n} + \frac{1}{2}$, $\sigma_b^{\text{th}} = |S_{\nu,k'}|^2\bar{n} + \frac{1}{2}$, $\sigma_{t_1}^{\text{th}} = \frac{\bar{n}}{2}(S^*_{\mu,k'}S_{\nu,k'} + S^*_{\nu,k'}S_{\mu,k'})$ and $\sigma_{t_2}^{\text{th}} = \frac{\bar{n}}{2}(S^*_{\mu,k'}S_{\nu,k'} - S^*_{\nu,k'}S_{\mu,k'})$, where $\bar{n}$ is the average number of photons in the input mode.

Squeezed state If the input mode is in a squeezed state with the squeeze parameter r, and angle θ, see Sec. 5.3.1, than the relevant expectation values are: $\Delta\hat{a}_{k'} = -e^{i\theta}\sinh(r)\cosh(r)$, $\Delta\hat{a}^\dagger_{k'} = -e^{-i\theta}\sinh(r)\cosh(r)$, and $\Delta\hat{n}_{k'} = \sinh^2(r)$. We can express the coefficients of the scattering matrix, corresponding to the transition from the input mode k' to the output modes μ and ν as: $S_{\nu,k'} = s_\mu e^{i\varphi_\mu}$ and $S_{\nu,k'} = s_\nu e^{i\varphi_\nu}$, and setting

$\theta = 0$ we can express the covariance matrix for the modes μ and ν as:

$$\sigma^{\mathrm{sq}} = \begin{pmatrix} \sigma^{\mathrm{sq}}_{a_1} & \sigma^{\mathrm{sq}}_{a_3} & \sigma^{\mathrm{sq}}_{c_1} & \sigma^{\mathrm{sq}}_{c_3} \\ \sigma^{\mathrm{sq}}_{a_3} & \sigma^{\mathrm{sq}}_{a_2} & \sigma^{\mathrm{sq}}_{c_4} & \sigma^{\mathrm{sq}}_{c_2} \\ \sigma^{\mathrm{sq}}_{c_1} & \sigma^{\mathrm{sq}}_{c_4} & \sigma^{\mathrm{sq}}_{b_1} & \sigma^{\mathrm{sq}}_{b_3} \\ \sigma^{\mathrm{sq}}_{c_3} & \sigma^{\mathrm{sq}}_{c_2} & \sigma^{\mathrm{sq}}_{b_3} & \sigma^{\mathrm{sq}}_{b_2} \end{pmatrix}, \tag{7.7}$$

where:

$$\begin{aligned} \sigma^{\mathrm{sq}}_{a_1} = \frac{1}{2} - s_\nu^2(q\cos(2\varphi_\nu) - t); \quad \sigma^{\mathrm{sq}}_{a_2} = \frac{1}{2} + s_\nu^2(q\cos(2\varphi_\nu) + t); \\ \sigma^{\mathrm{sq}}_{b_1} = \frac{1}{2} - s_\mu^2(q\cos(2\varphi_\mu) - t); \quad \sigma^{\mathrm{sq}}_{b_2} = \frac{1}{2} + s_\mu^2(q\cos(2\varphi_\mu) + t); \\ \sigma^{\mathrm{sq}}_{a_3} = -s_\nu^2 q\sin(2\varphi_\nu); \qquad \sigma^{\mathrm{sq}}_{b_3} = -s_\mu^2 q\sin(2\varphi_\mu); \\ \sigma^{\mathrm{sq}}_{c_1} = s_\nu s_\mu(t\cos(\varphi_\nu - \varphi_\mu) - q\cos(\varphi_\nu + \varphi_\mu)); \\ \sigma^{\mathrm{sq}}_{c_2} = s_\nu s_\mu(t\cos(\varphi_\nu - \varphi_\mu) + q\cos(\varphi_\nu + \varphi_\mu)); \\ \sigma^{\mathrm{sq}}_{c_3} = s_\nu s_\mu(t\sin(\varphi_\nu - \varphi_\mu) - q\sin(\varphi_\nu + \varphi_\mu)); \\ \sigma^{\mathrm{sq}}_{c_4} = -s_\nu s_\mu(t\sin(\varphi_\nu - \varphi_\mu) + q\sin(\varphi_\nu + \varphi_\mu)); \\ t = \sinh^2(r); \quad q = \sinh(2r)/2. \end{aligned}$$

We have evaluated the output states for various inputs now we can check what correlations we get between the output modes for each of them.

7.3 Entanglement between the modes

An entanglement criterion, suitable for the continuous variable systems was introduced in Sec. 5.4.1. In order to check which of the output states evaluated above satisfy this criterion and to visualize the result, we first determine the region of valid states within the parameter space of the covariance matrix elements.

The covariance matrix for a two-mode state is a 4x4 real valued symmetric matrix, however not all 16 elements of this matrix are relevant for estimation of the correlations. Some of these parameters can be changed by local transformations (displacements and phase shifts) on each of the modes and therefore the global correlation properties do not depend on them. The minimal configuration of the covariance matrix, where all the parameters are relevant for evaluating the correlations between the two modes is given

by (5.85)

$$\sigma = \begin{pmatrix} \boldsymbol{\alpha} & \boldsymbol{\gamma} \\ \boldsymbol{\gamma}^{\mathrm{T}} & \boldsymbol{\beta} \end{pmatrix} = \begin{pmatrix} a & 0 & \gamma_x & 0 \\ 0 & a & 0 & \gamma_p \\ \gamma_x & 0 & b & 0 \\ 0 & \gamma_p & 0 & b \end{pmatrix}. \tag{7.8}$$

The determinants of the submatrices $\boldsymbol{\alpha}$, $\boldsymbol{\beta}$, $\boldsymbol{\gamma}$ and the covariance matrix σ itself are invariant under local transformations and therefore completely determine the correlations of the state [124]. We also note that for Gaussian states, correlations do not depend on the displacement vector. Therefore, overall there are 4 independent parameters that determine the correlations properties: a and b are related to the variances of the x and p quadratures of each of the two modes, and γ_x and γ_p are the correlation coefficients between the quadratures.

These parameters are not completely independent. As it was mentioned in Sec. 5.4.1 a valid covariance matrix should satisfy the Heisenberg uncertainty relations 5.72, which implies that the eigenvalues

$$\lambda^{\mathrm{CM}}_{1,2,3,4} = \frac{1}{2}\left(a + b \pm \sqrt{\pm 2\sqrt{\varepsilon_{xp}} + (a-b)^2 + 2\gamma_x^2 + 2\gamma_p^2 + 1}\right), \tag{7.9}$$
$$\varepsilon_{xp} = (a-b)^2 + (\gamma_x + \gamma_p)^2\left((\gamma_x - \gamma_p)^2 + 1\right)$$

of the matrix $\sigma + i\Omega/2$ should all be positive. This puts constraints on the values of a, b, γ_x and γ_p [124]. In (7.9) two eigenvalues with a plus sign outside the square root are always positive. Out of the remaining two the most strict constrains are due to the eigenvalue with a minus sign outside the square root and with a plus sign inside the square root.

$$\frac{1}{2}\left(a + b - \sqrt{2\sqrt{\varepsilon_{xp}} + (a-b)^2 + 2\gamma_x^2 + 2\gamma_p^2 + 1}\right) \geq 0, \tag{7.10}$$

which can be rewritten in a form of a set of constrains

$$4\left(a\,b - \gamma_x^2\right)\left(a\,b - \gamma_p^2\right) \leq a^2 + b^2 + 2\gamma_x\gamma_p - \frac{1}{4}, \tag{7.11}$$

$$a, b \geq 1/2, \quad \gamma_x \leq a\,b, \quad \gamma_p \leq a\,b.$$

From these inequalities it is apparent that while there is no upper bound for a and b, γ_x and γ_p are bounded from above. In other words, (7.11) define a closed region within the γ_x, γ_p parameter space, which contains all the values of these parameters, corresponding to the valid 2-mode covariance matrices. The shape of this region is shown in Fig. 7.2a,b, depending on the parameters a and b, related to the quadrature variances of the individual modes. Any class of states, i.e. entangled, discorded and

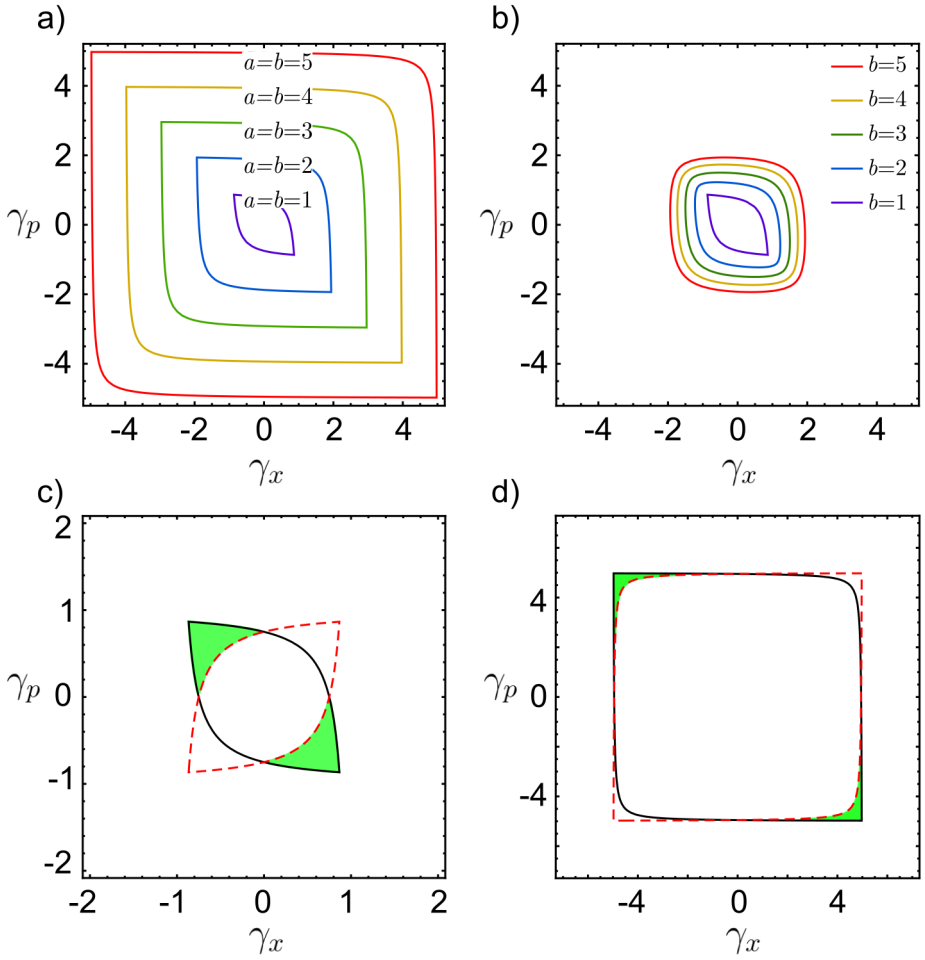

Figure 7.2: The shape of the regions of valid covariance matrix parameters. In each of the panels a black solid line encloses a set of γ_x, γ_p, quadrature correlation coefficients values, that upon substitution in (7.8) give a valid covariance matrix. The shape of this region depends on a and b, the other two parameters in σ. a) Valid γ_x, γ_p regions for symmetric states $a = b$. b) For asymmetric states, $a = 1$, b changes in steps of 1 from 1 to 5. c) Subregion corresponding to entangled states (green) for $a = b = 1$. d) for $a = b = 5$.

product, will occupy some subregion of the regions illustrated in Fig. 7.2a,b.

Let's figure out what subregion of those parameter sets fulfilling (7.11) correspond to the entangled states. According to Simon criterion [145], see Ch. 5, if the matrix obtained by a partial transpose of the global state violates the Heisenberg uncertainty relations (5.72), such state is entangled. As we discussed in Sec. 5.4.1, partial transpose in phase space corresponds to a change of sign of one of the quadratures, say the p quadrature. The matrix obtained from (7.8) after this operation is different from the

original only by the sign of γ_p parameter, i.e.

$$\sigma^{\mathrm{PPT}} = \begin{pmatrix} a & 0 & \gamma_x & 0 \\ 0 & a & 0 & -\gamma_p \\ \gamma_x & 0 & b & 0 \\ 0 & -\gamma_p & 0 & b \end{pmatrix} \tag{7.12}$$

The condition $\sigma^{\mathrm{PPT}} + i\Omega/2 < 0$ leads to a set of constrains similar to (7.11)

$$4\,\left(a\,b - \gamma_x^2\right)\left(a\,b - \gamma_p^2\right) > a^2 + b^2 - 2\gamma_x\gamma_p - \frac{1}{4}, \tag{7.13}$$

$$a, b \geq 1/2, \quad \gamma_x \leq a\,b, \quad |\gamma_p| \leq a\,b,$$

which graphically corresponds to the exterior of the region defined by (7.11), but mirror reflected along γ_p. The overlap of the regions defined by (7.11) and (7.13) illustrated in Fig. 7.2c,d, contains entangled states. The configuration of this region agrees with a well-known fact that the p quadratures of Gaussian entangled states are strongly anti-correlated [15, 148].

Obviously, the covariance matrix σ^{coh} that we get for coherent state input, with $\gamma_x = \gamma_p = 0$ can never lead to entanglement. The 2-mode output covariance matrix for the thermal state input (7.6) can be rewritten as

$$\sigma^{\mathrm{th}}_{l,m} = \begin{pmatrix} \sigma^{\mathrm{th}}_a & 0 & \sigma^{\mathrm{th}}_\gamma & 0 \\ 0 & \sigma^{\mathrm{th}}_a & 0 & \sigma^{\mathrm{th}}_\gamma \\ \sigma^{\mathrm{th}}_\gamma & 0 & \sigma^{\mathrm{th}}_b & 0 \\ 0 & \sigma^{\mathrm{th}}_\gamma & 0 & \sigma^{\mathrm{th}}_b \end{pmatrix} \tag{7.14}$$

with $\sigma^{\mathrm{th}}_\gamma = \bar{n}|S_{l,k'}||S_{m,k'}|$. The values of γ_x and γ_p in this case are equal. In Fig. 7.2 all the possible output states for the thermal state input lie on the line $\gamma_x = \gamma_p$ and thus no entanglement is possible. In fact, in order for the modes to be entangled, γ_x and γ_p should at least have different signs [145]. Although these states do not show entanglement, as we show in the next section, weaker quantum correlations in the form of quantum discord are still possible.

Finally for a squeezed state input, if we set $\theta = 0$, for which we expect maximal entanglement [148], the output covariance matrix (7.7) written in the Simon normal

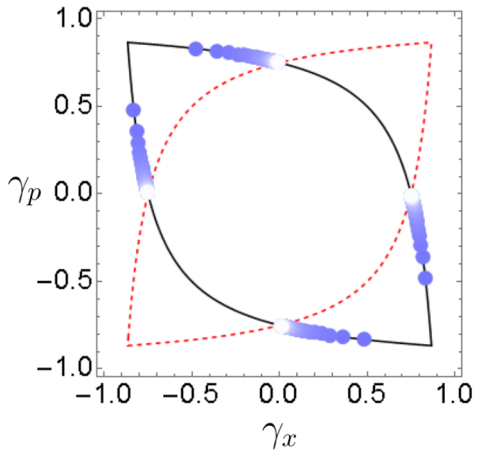

Figure 7.3: Position of the output states (blue dots) in the region of allowed states from Fig. 7.2 for the case of squeezed state input. The color corresponds to the degree of squeezing, r, which changes in steps of 0.05 from 0 (light blue) to 3 (dark blue).

form is

$$\sigma^{\mathrm{sq}} = \begin{pmatrix} \sigma_a^{\mathrm{sq}} & 0 & \sigma_{\gamma_x}^{\mathrm{sq}} & 0 \\ 0 & \sigma_a^{\mathrm{sq}} & 0 & \sigma_{\gamma_p}^{\mathrm{sq}} \\ \sigma_{\gamma_x}^{\mathrm{sq}} & 0 & \sigma_b^{\mathrm{sq}} & 0 \\ 0 & \sigma_{\gamma_p}^{\mathrm{sq}} & 0 & \sigma_b^{\mathrm{sq}} \end{pmatrix} \tag{7.15}$$

where $\sigma_a^{\mathrm{sq}} = \frac{1}{4}\left(2|S_{l,k'}|^2 t + 1\right)^2 - q^2|S_{l,k'}|^4$, $\sigma_b^{\mathrm{sq}} = \frac{1}{4}\left(2|S_{m,k'}|^2 t + 1\right)^2 - q^2|S_{m,k'}|^4$, and $\sigma_{\gamma_x}^{\mathrm{sq}}$, $\sigma_{\gamma_p}^{\mathrm{sq}}$ satisfy a set of equations

$$\sigma_{\gamma_x}^{\mathrm{sq}}\sigma_{\gamma_p}^{\mathrm{sq}} = -\sinh(r)^2|S_{l,k'}|^2|S_{m,k'}|^2$$

$$\sigma_a^{\mathrm{sq}\,2}\sigma_b^{\mathrm{sq}\,2} - \sigma_a^{\mathrm{sq}}\sigma_b^{\mathrm{sq}}(\sigma_{\gamma_x}^{\mathrm{sq}\,2} + \sigma_{\gamma_p}^{\mathrm{sq}\,2}) + \sigma_{\gamma_x}^{\mathrm{sq}\,2}\sigma_{\gamma_p}^{\mathrm{sq}\,2} =$$
$$= \frac{1}{16}\left[\left(1 + 2t\left(|S_{l,k'}|^2 + |S_{m,k'}|^2\right)\right)^2 - 4q^2\left(|S_{l,k'}|^2 + |S_{m,k'}|^2\right)^2\right]$$

From these expressions we can derive the entanglement criterion, which reads

$$\sinh(r)^2|S_{l,k'}|^2|S_{m,k'}|^2 > 0 \tag{7.16}$$

This is always true if r and both scattering matrix elements are non-zero. This means that we will get entanglement for any non-zero degree of squeezing r [224]. This is illustrated in Fig. 7.3, in which position of the states with a covariance matrix σ^{sq} is shown. These states always fall into the region corresponding to entangled states and

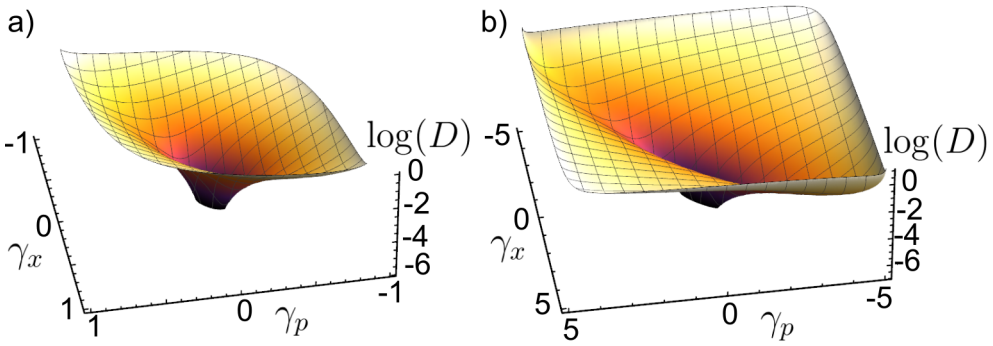

Figure 7.4: Quantum discord of a generic quantum state with a covariance matrix σ (7.8) depending on the parameters γ_x and γ_p, for symmetric states a) $a = b = 1$, b) $a = b = 5$.

the degree of entanglement increases with r. It is also remarkable that the degree of entanglement, measured by the logarithmic negativity [139] does not depend on the phases of transmission coefficients of the scattering matrix, but only on their moduli.

7.4 Discord between the modes

Let's now apply the procedure described in Sec. 5.4.1 to calculate the discord of the output state of a pair of modes. For that we need to substitute the covariance matrix (7.8) into the expression for the Gaussian discord (5.98). The dependence of the discord on the correlation coefficients between the x and p quadratures is shown in Fig. 7.4. From this figure it is apparent that maximal discord, as expected, is achieved for entangled states, however, what is surprising, it is non-zero for almost any other state except for the one with $\gamma_x = \gamma_p = 0$. Therefore we can make a conclusion, that discord between the output modes of the scattered light will be present for any state of the input mode except the coherent one.

It is not surprising that squeezed light can produce non-classical correlations in the output state of the scattered modes. It is considered non-classical by any reasonable criterion, and it is well known that non-classical states can produce entanglement between the output modes of a beam splitter, being one of the inputs [15, 148, 224]. However it is interesting that, for example thermal input states can produce quantum discord between two output modes.

We calculate the discord of the output covariance matrix for the case of thermal input mode by substituting the output covariance matrix Eq. (7.6) into the formula for the Gaussian discord in Eq. (5.98). In Fig. 7.5 we plot the dependence of the Gaussian discord D_G on the absolute values of the transmission coefficients from the mode k' to the modes l and m. Notice that the discord D is asymmetric against these coefficients

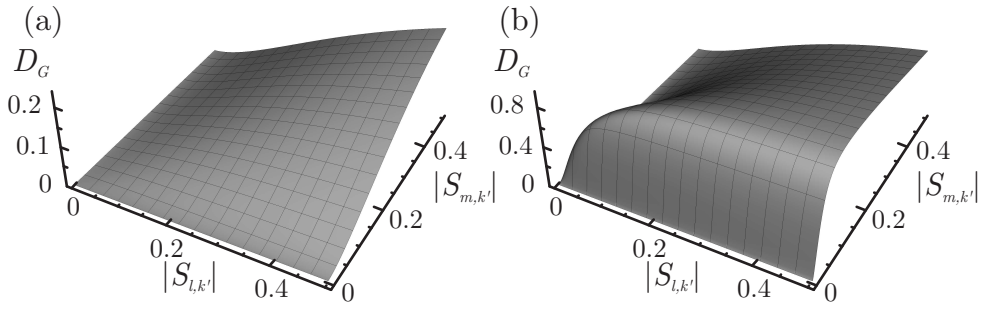

Figure 7.5: The dependence of the Gaussian discord D_G between modes l and m on the absolute values of the elements of the scattering matrix $|S_{l,k'}|$ and $|S_{m,k'}|$. The input mode, k', is in a thermal state with different average photon numbers (a) $\bar{n} = 1$, (b) $\bar{n} = 10^3$. The measurement is performed on the mode l.

since the measurement is performed on only one of the modes (on mode l in Fig. 7.5). The discord increases monotonously with $|S_{l,k'}|$, but there can be a maximum in its dependence on $|S_{m,k'}|$, the position of which is defined by the number of photons in the input mode (Fig. 7.5b). At low photon numbers there is no maximum, and in that case the discord increases monotonously (Fig. 7.5a).

To calculate the average amount of discord $\langle D_G \rangle$ of a pair of output modes, we make an ensemble average over the realizations of S. In a diffusive system the energy distributes equally among all the N possible channels, i.e. $\langle |S|^2 \rangle = 1/N$. Moreover, within the random matrix approximation [18, 222] the elements of the scattering matrix S follow a Rayleigh distribution

$$P(|S|) = \frac{2|S|}{\langle |S|^2 \rangle} \exp\left(-\frac{|S|^2}{\langle |S|^2 \rangle} \right), \tag{7.17}$$

which implies $\langle |S| \rangle = \sqrt{\pi \langle |S|^2 \rangle}/2 = \sqrt{\pi/4N}$ [8, 55, 83].

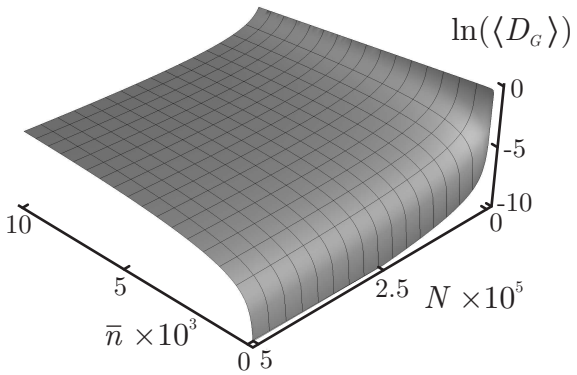

Figure 7.6: Dependence of the average Gaussian discord, $\langle D_G \rangle$, on the number of output modes, N, and the number of photons, $\bar{n}$, in the thermal input state.

Taking the average of Eq. (5.94) and using the above relation for the average value of $|S|$ we obtain $\langle D_G \rangle$ of a pair of output modes in this configuration. As shown in Fig. 7.6, $\langle D_G \rangle$ increases monotonically with $\bar{n}$, but decreases monotonically with N. As a consequence the best conditions to observe the discord generated by multiple scattering of a thermal state of light are obtained for an intense light signal scattering over a system with a small number of channels. Therefore we suggest that light scattering from systems showing Anderson localization [20, 55] will show a significant amount of quantum discord.

7.5 Correlation function

Classical correlations of scattered light are commonly described by a correlation function $\mathcal{C}_{l,m}$ that measures the correlations between intensity fluctuations of two different modes l and m [19, 22, 55],

$$\mathcal{C}_{l,m} = \frac{\langle I_l I_m \rangle}{\langle I_l \rangle \langle I_m \rangle}, \tag{7.18}$$

where $I = |E|^2$ is the light intensity and $\langle \cdot \rangle$ represents either a time or an ensemble average (if the system is ergodic the two are equivalent). $\mathcal{C}$ can be used beyond the classical case to study certain classes of quantum correlations by substituting I with the mode's number operator $\hat{n}$ [103, 109, 204, 225], and since classical light can never lead to $\mathcal{C} < 1$. A correlation value below 1 is considered a clear signature of quantumness [102], capturing, for example, the non-classical behavior of single photon states [226].

The intensity correlation $\mathcal{C}$ contains fourth order moments of the field distribution, and for Gaussian states these can always be written as a function of the second order moments, contained in the covariance matrix σ [148]. Substituting the mode's field operators (5.33) into Eq. (7.18) and using the definition of the elements of the covariance matrix in Eq. (7.8) we obtain:

$$\mathcal{C} = 1 + \frac{(2\gamma_x^2 + 2\gamma_p^2)}{(2\alpha - 1)(2\beta - 1)}. \tag{7.19}$$

From Eq. (7.19) we can see that Gaussian states always have $\mathcal{C} \geq 1$, as $\alpha, \beta \geq 1/2$ as a consequence of the commutation relations in Eq. (5.72).

The dependence of the correlation function on the parameters γ_x and γ_p is shown in Fig. 7.7. According to (7.19), $\mathcal{C}$ shows a parabolic dependence on these variables. The minimal value of $\mathcal{C}$ is 1 at $\gamma_x = \gamma_p = 0$, as expected for coherent states. The value of $\mathcal{C} = 2$ is maximal that can be achieved for a classical input state. However, when the

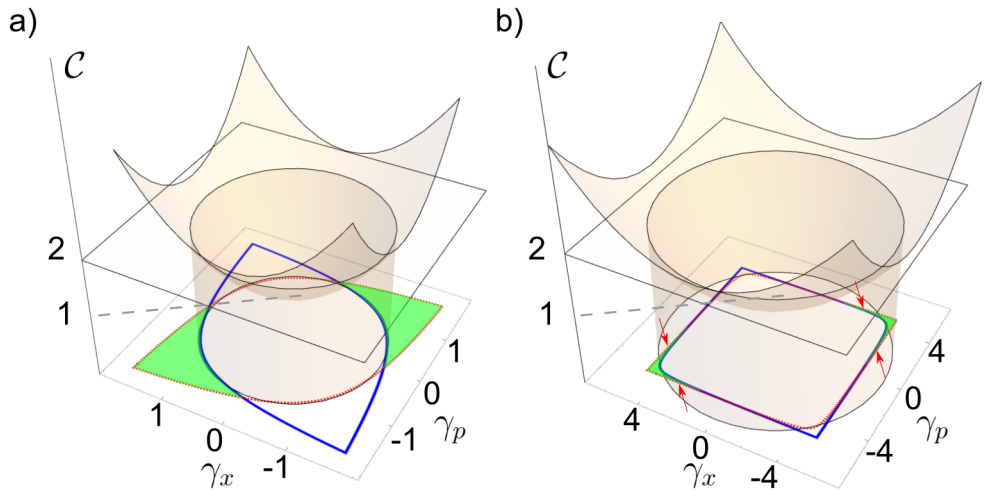

Figure 7.7: Dependence of the correlation function $\mathcal{C}$ (parabolic surface) on γ_x and γ_p for a) $a = b = 1$ b) $a = b = 5$. In the bottom plane we plot the region of valid states from Fig 7.2 with entangled states highlighted in green. The maximal level of $\mathcal{C}$ available for non-entangled states is 2. At low number of photons in the input mode $\mathcal{C}$ can indicate non-classicality as for all entangled states $\mathcal{C} \geq 2$ (the circle never reaches the highlighted areas), however at higher number of photons there are entangled states with $\mathcal{C} < 2$ (marked with red arrows).

output state is entangled, values greater than 2 are possible. For a squeezed state input, the maximal level of $\mathcal{C}$ is

$$\mathcal{C}^{\mathrm{sq}} = 2 + \frac{|S_{l,k'}|^2 + |S_{m,k'}|^2}{2\bar{n}|S_{l,k'}||S_{m,k'}|}, \tag{7.20}$$

where $\bar{n}$ is the average number of photons in the input mode. When $\bar{n} \to \infty$, $\mathcal{C}^{sq}$ approaches 2, which corresponds to the value expected for thermal states. The presence of entanglement allows to reach values of $\mathcal{C}$ inaccessible for thermal state input, and this is exploited in quantum imaging where it can allow faster recovery of information, especially in the low photon number regime [73]. However, this needs to be treated with some care. In fact, as it can be seen from Fig. 7.7b, with the increase of a and b the circle $\mathcal{C} = 2$ and the boundary of the green area (corresponding to the entangled states) cross, and therefore it is possible to find non-entangled states with higher intensity correlations than some entangled states.

7.6 Quantum tomography of a multimode field

Quantum tomography is a common name of a series of techniques aiming at reconstruction of the density matrix (or any equivalent representation) of a quantum state from the experimental measurements [104, 227, 228]. For continuous variable systems the

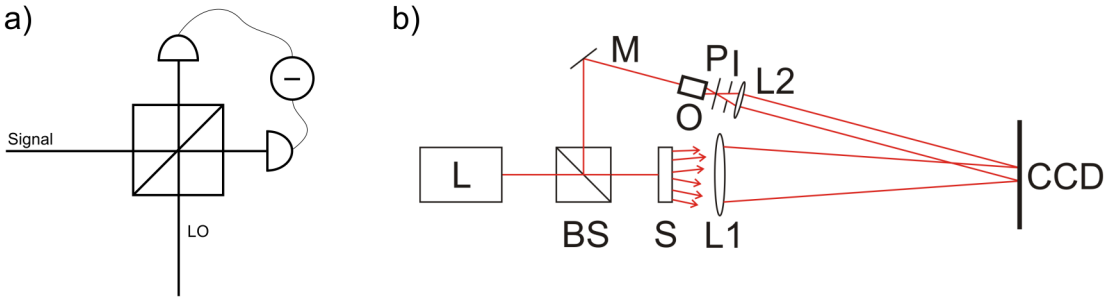

Figure 7.8: a) Schematic diagram of a balanced homodyne tomography setup. The difference between photocurrents in the two BS output arms is proportional to $\hat{a}e^{-i\theta_{LO}} + \hat{a}^{\dagger}e^{i\theta_{LO}}$, where θ_{LO} is the local oscillator phase. By changing θ_{LO} statistics of any quadrature can be measured b) Schematic diagram of the multimode array detector tomography setup based on the off-axis holography. The laser (L) light is split by a beam splitter (BS). The transmitted light is used as signal beam, which after passing through a multiply scatteting sample (S) becomes a multimode field with complex structure. It is focused onto the CCD array by the lens L1, where it interferes at some angle with the local oscillator, which is a Gaussian beam shaped by the objective (O), pinhole (P) and lens (L2). Simultaneous readings of the mode's quadratures can be obtained from the Fourier spectrum of the intensity profiles registered by the camera.

measured properties are usually the field quadratures, which can be accessed using optical homodyne/heterodyne detection or their derivatives [229]. These methods imply mixing of the measured signal field with a high amplitude coherent state mode (local oscillator) on a beam-splitter and measuring the difference of the photodiode currents in the beam-splitter output arms. By changing the phase of the local oscillator any combination of the quadratures can be obtained, see Fig. 7.8. The main difficulty of these methods is the requirement to achieve perfect spatial overlap of the signal mode with the local oscillator. Any mode mismatch between these two modes has the same effect as the photodiode detector losses, leading to the distortion of the measured quadrature distributions. The way to overcome this problem is to use the detector arrays instead of single photodetectors [230, 231]. Standard balanced array detection allows to analyse even multimode fields, however it does not provide mode selectivity, i.e. all the modes in the signal field are treated as one. The usual way to estimate the quantum state of a multimode field is a multiport generalization of the homodyne detection technique [232, 233], which can be quite challenging since it requires 2^N synchronized homodyne measurements (N is the number of analysed modes).

In [234, 235] a modification of the balanced detection technique was proposed, which allows mode selectivity without extensive complication of the measurement setup. This technique is based on the off-axis holography, which is a well-known method of measuring the amplitude and phase of a complex multimode field. In this method the signal beam

is overlapped at the detector array with a plane wave inclined at a non-zero angle θ_c with respect to the detector surface. The resulting intensity detected by the array is

$$I(x,y) = |E_{LO}|^2 + |E_s(x,y)|^2 + \left[E_{LO}E_s^*(x,y)e^{-ik_{LO}\sin(\theta_c x)} + \text{c.c.}\right], \tag{7.21}$$

where E_{LO} and E_s are the local oscillator and the signal field amplitudes, respectively, and k_{LO} is the local oscillator k-vector. The first term of this expression gives a constant displacement, while three others are the original signal itself and two of its copies shifted in spatial frequency by $\nu_c = \pm k\sin(\theta_c)/2\pi$. When ν_c is greater than any spatial frequency of the signal there is no overlap between the Fourier spectra of the signal and its copies. In that case we can take a Fourier transform of $I(x,y)$ and move either of these copies to 0 frequency, recovering the complex value of the field (up to a constant multiplier).

In [234–236] authors extended the method described above, taking into account the quantum nature of light. They have shown that the Fourier spectrum of $I(x,y)$ contains information about the quadratures of the signal field and as it comes in the form of a mode decomposition, the quadratures of a set of modes are measured simultaneously. As orthogonal quadratures do not commute, there is an uncertainty, which prevents from measuring the Wigner function of these modes directly, however reconstruction of the Q-function is still possible. In the case of Gaussian modes the covariance matrix can be obtained from the Q-function, which then can be analysed using any of the non-classicality criteria described in Sec. 5.4.1. When the modes are non-Gaussian, the covariance matrix does not fully describe their quantum state, therefore additional effort should be taken to estimate non-classical correlations. In [170, 171] a method for verifying quantum discord based on the joint quasiprobability distributions was proposed, which is based on checking whether the peaks of the conditional quasiprobability distributions corresponding to two different outcomes of heterodyne measurement coincide at the same point in the phase space. As the homodyne array detector measurements give the full quadrature statistics for a number of modes, one can obtain the conditional distribution from these measurements, and therefore directly verify the presence of quantum discord between these modes whether they are Gaussian or not.

7.7 Summary and outlook

The main original input described in this chapter is the first application of the rigorous quantum informational non-classicality criteria [145, 158, 159] to the quantum state of light scattered by the disordered materials. This approach allowed to study more subtle

quantum features, beyond entanglement. In particular, it was found that, surprisingly, quantum discord can be present in the output state even when the input is in a classical (thermal) state. In addition, we show that the correlation function between the modes, often treated as indicator of non-classicality is not always a reliable criterion.

An obvious extension of the results presented in the current chapter is an experiment, that would demonstrate the presence of quantum discord in multiple scattered light. It is a challenging task that involves quantum tomography of a highly multimode field. A method based on digital holography phase reconstruction [237] has been proposed for that purpose [235].

Publication status

Papers

[1] Starshynov I., Bertolotti J., Anders J. Quantum correlation of light scattered by disordered media. *Opt. Express* **24**, 4662 (2016).

[2] Starshynov I., Paniagua-Diaz A. M., Fayard N., Goetschy A., Pierrat R., Carminati R., Bertolotti J. Non-Gaussian Correlations between Reflected and Transmitted Intensity Patterns Emerging from Opaque Disordered Media. *Physical Review X* **8**, 021041 (2018).

[3] Starshynov I., Bertolotti J., Anders J. Non-classicality of coherent state mixtures http://arxiv.org/abs/1802.08486. (2018).

[4] Starshynov I., Paniagua-Diaz A. M., Fayard N., Goetschy A., Pierrat R., Carminati R., Bertolotti J. Blind Ghost Imaging *in preparation*

Conference proceedings

[1] Starshynov I., Bertolotti J., Anders J., Non-classical correlations of multiply scattered light in Quantum Information and Measurement (QIM) 2017, OSA Technical Digest (Optical Society of America, 2017), paper QT5C.3.

[2] Starshynov I., Paniagua-Diaz A. M., Fayard N., Goetschy A., Pierrat R., Carminati R., Bertolotti J. Ghost imaging through opaque scattering media, using reflection-transmission speckle correlations, in Imaging and Applied Optics 2018, OSA Technical Digest (Optical Society of America, 2018), paper JTu4A.41.

References

1. Hecht, J. The bandwidth bottleneck that is throttling the Internet. *Nature* **536,** 139–142 (2016).
2. Pérez-Delgado, C. A., Pearce, M. E. & Kok, P. Fundamental Limits of Classical and Quantum Imaging. *Physical Review Letters* **109,** 123601 (2012).
3. Tentrup, T. B. H. *et al.* Transmitting more than 10 bit with a single photon. *Optics Express* **25,** 2826 (2017).
4. Yeh, C.-H., Kang, L.-W., Lee, M.-S. & Lin, C.-Y. Haze effect removal from image via haze density estimation in optical model. *Optics Express* **21,** 27127 (2013).
5. Lu, H., Li, Y., Zhang, L. & Serikawa, S. Contrast enhancement for images in turbid water. *Journal of the Optical Society of America A* **32,** 886 (2015).
6. Vorontsov, M. A. & Sivokon, V. P. Stochastic parallel-gradient-descent technique for high-resolution wave-front phase-distortion correction. *Journal of the Optical Society of America A* **15,** 2745 (1998).
7. *The Mie Theory* (eds Hergert, W. & Wriedt, T.) (Springer Berlin Heidelberg, 2012).
8. Goodman, J. *Speckle Phenomena in Optics: Theory and Applications* (Roberts & Company, 2007).
9. Cover, T. M. & Thomas, J. A. *Elements of Information Theory* (John Wiley & Sons, Inc., Hoboken, NJ, USA, 2005).
10. Shannon, C. E. A Mathematical Theory of Communication. *Bell System Technical Journal* **27,** 379–423 (1948).
11. Shannon, C. E. A Mathematical Theory of Communication. *Bell System Technical Journal* **27,** 623–656 (1948).
12. Helstrom, C. W. Detection theory and quantum mechanics. *Information and Control* **10,** 254–291 (1967).
13. Hassani, M., Macchiavello, C. & Maccone, L. Digital Quantum Estimation. *Physical Review Letters* **119,** 1–6 (2017).
14. Fayard, N., Goetschy, A., Pierrat, R. & Carminati, R. Mutual Information between Reflected and Transmitted Speckle Images. *Physical Review Letters* **120,** 073901 (2018).
15. Kim, M. S., Son, W., Bužek, V. & Knight, P. L. Entanglement by a beam splitter: Nonclassicality as a prerequisite for entanglement. *Physical Review A* **65,** 032323 (2002).

16. Streltsov, A., Adesso, G. & Plenio, M. B. Quantum Coherence as a Resource. *Reviews of Modern Physics* **89,** 041003 (2016).

17. Starshynov, I. *et al.* Non-Gaussian Correlations between Reflected and Transmitted Intensity Patterns Emerging from Opaque Disordered Media. *Physical Review X* **8,** 021041 (2018).

18. Van Rossum, M. C. W. & Nieuwenhuizen, T. M. Multiple scattering of classical waves: microscopy, mesoscopy, and diffusion. *Reviews of Modern Physics* **71,** 313–371 (1999).

19. Berkovits, R. & Feng, S. Correlations in coherent multiple scattering. *Physics Reports* **238,** 135–172 (1994).

20. Ping, S. *Introduction to Wave Scattering, Localization and Mesoscopic Phenomena* (Springer Berlin Heidelberg, 2006).

21. Anderson, P. W. Absence of Diffusion in Certain Random Lattices. *Physical Review* **109,** 1492–1505 (1958).

22. Feng, S., Kane, C., Lee, P. a. & Stone, a. D. Correlations and fluctuations of coherent wave transmission through disordered media. *Physical Review Letters* **61,** 834–837 (1988).

23. Rogozkin, D. B. & Cherkasov, M. Y. Long-range intensity correlations in wave reflection from a disordered medium. *Physical Review B* **51,** 12256–12267 (1995).

24. Froufe-Perez, L., García-Martín, A., Cwilich, G. & Sáenz, J. Fluctuations and correlations in wave transport through complex media. *Physica A: Statistical Mechanics and its Applications* **386,** 625–632 (2007).

25. Fayard, N., Caze, A., Pierrat, R. & Carminati, R. Intensity correlations between reflected and transmitted speckle patterns. *Physical Review A* **92,** 033827 (2015).

26. Freund, I., Rosenbluh, M. & Feng, S. Memory Effects in Propagation of Optical Waves through Disordered Media. *Physical Review Letters* **61,** 2328–2331 (1988).

27. De Boer, J. F., van Albada, M. P. & Lagendijk, A. Transmission and intensity correlations in wave propagation through random media. *Physical Review B* **45,** 658–666 (1992).

28. Van Albada, M. P., de Boer, J. F. & Lagendijk, A. Observation of long-range intensity correlation in the transport of coherent light through a random medium. *Physical Review Letters* **64,** 2787–2790 (1990).

29. Scheffold, F., Härtl, W., Maret, G. & Matijević, E. Observation of long-range correlations in temporal intensity fluctuations of light. *Physical Review B* **56,** 10942–10952 (1997).

30. Genack, A. Z., Garcia, N. & Polkosnik, W. Long-range intensity correlation in random media. *Physical Review Letters* **65,** 2129–2132 (1990).

31. Garcia, N., Genack, A., Pnini, R. & Shapiro, B. Intensity correlation in waveguides. *Physics Letters A* **176,** 458–461 (1993).

32. Sarma, R., Yamilov, A., Neupane, P., Shapiro, B. & Cao, H. Probing long-range intensity correlations inside disordered photonic nanostructures. *Physical Review B* **90,** 014203 (2014).

33. Sarma, R., Yamilov, A., Neupane, P. & Cao, H. Using geometry to manipulate long-range correlation of light inside disordered media. *Physical Review B* **92,** 180203 (2015).

34. Ojambati, O. S., Hosmer-Quint, J. T., Gorter, K.-J., Mosk, A. P. & Vos, W. L. Controlling the intensity of light in large areas at the interfaces of a scattering medium. *Physical Review A* **94,** 043834 (2016).

35. Hsu, C. W., Liew, S. F., Goetschy, A., Cao, H. & Douglas Stone, A. Correlation-enhanced control of wave focusing in disordered media. *Nature Physics* **13,** 497–502 (2017).

36. Vimba: The SDK for Allied vision cameras - Allied Vision `https://www.alliedvision.com/en/products/software.html`.

37. Frigo, M. & Johnson, S. The Design and Implementation of FFTW3. *Proceedings of the IEEE* **93.** Special issue on "Program Generation, Optimization, and Platform Adaptation", 216–231 (2005).

38. Vynck, K., Pierrat, R. & Carminati, R. Polarization and spatial coherence of electromagnetic waves in uncorrelated disordered media. *Physical Review A - Atomic, Molecular, and Optical Physics* **89,** 013842 (2014).

39. Dogariu, A. & Carminati, R. Electromagnetic field correlations in three-dimensional speckles. *Physics Reports* **559,** 1–29 (2015).

40. Gorodnichev, E. E., Kuzovlev, A. I. & Rogozkin, D. B. Impact of wave polarization on long-range intensity correlations in a disordered medium. *Journal of the Optical Society of America A* **33,** 95 (2016).

41. Gorodnichev, E. E., Kuzovlev, A. I. & Rogozkin, D. B. Long-Range Correlations Between Transmitted and Reected Fluxes of Electromagnetic Waves. *Journal of Physics: Conference Series* **941,** 012045 (2017).

42. Lax, M. Multiple Scattering of Waves. II. The Effective Field in Dense Systems. *Physical Review* **85,** 621–629 (1952).

43. Draine, B. T. & Flatau, P. J. Discrete-Dipole Approximation For Scattering Calculations. *Journal of the Optical Society of America A* **11,** 1491 (1994).

44. Yurkin, M. A. & Hoekstra, A. G. The discrete dipole approximation: An overview and recent developments. *Journal of Quantitative Spectroscopy and Radiative Transfer* **106,** 558–589 (2007).

45. Yurkin, M. A., Maltsev, V. P. & Hoekstra, A. G. Convergence of the discrete dipole approximation. I. Theoretical analysis. *Journal of the Optical Society of America. A, Optics, image science, and vision* **23,** 2578–91 (2006).

46. Saad, Y. *Iterative Methods for Sparse Linear Systems* (PWS Publishing Company, 1996).

47. Maradudin, A. A. *Light Scattering and Nanoscale Surface Roughness* (ed Maradudin, A. A.) 496 (Springer US, 2007).

48. Carminati, R. Subwavelength spatial correlations in near-field speckle patterns. *Physical Review A - Atomic, Molecular, and Optical Physics* **81,** 1–5 (2010).

49. McGurn, A. R. & Maradudin, A. A. Computer simulation studies of the speckle correlations of light scattered from a random array of scatterers: Scalar wave approximation. *Physical Review B - Condensed Matter and Materials Physics* **64,** 1–14 (2001).

50. Danila, B. & McGurn, A. R. Computer simulation studies of the speckle correlations of light scattered from a random array of dielectric spheres of random radii or dielectric constants. *Physical Review B - Condensed Matter and Materials Physics* **73,** 1–13 (2006).

51. Landau, L. D. *The classical theory of fields* (Butterworth Heinemann, 2000).

52. Nair, V. P. *Quantum field theory : a modern perspective* (Springer Business+Science Media, 2005).

53. Osnabrugge, G., Leedumrongwatthanakun, S. & Vellekoop, I. M. A convergent Born series for solving the inhomogeneous Helmholtz equation in arbitrarily large media. *Journal of Computational Physics* **322,** 113–124 (2016).

54. Kubo, R. Generalized Cumulant Expansion Method. *Journal of the Physical Society of Japan* **17,** 1100–1120 (1962).

55. Akkermans, E. & Montambaux, G. *Mesoscopic Physics of Electrons and Photons* (Cambridge University Press, 2007).

56. Edwards, S. F. A new method for the evaluation of electric conductivity in metals. *Philosophical Magazine* **3,** 1020–1031 (1958).

57. Altshuler, B. L., Khmel'nitzkii, D., Larkin, A. I. & Lee, P. A. Magnetoresistance and Hall effect in a disordered two-dimensional electron gas. *Physical Review B* **22,** 5142–5153 (1980).

58. Akkermans, E., Wolf, P. E. & Maynard, R. Coherent Backscattering of Light by Disordered Media: Analysis of the Peak Line Shape. *Physical Review Letters* **56,** 1471–1474 (1986).

59. Hikami, S. Anderson localization in a nonlinear-sigma-model representation. *Physical Review B* **24,** 2671–2679 (1981).

60. Stephen, M. J. & Cwilich, G. Intensity correlation functions and fluctuations in light scattered from a random medium. *Physical Review Letters* **59,** 285 (1987).

61. Shapiro, B. Large Intensity Fluctuations for Wave Propagation in Random Media. *Physical Review Letters* **57,** 2168–2171 (1986).

62. Kane, C. L., Serota, R. A. & Lee, P. A. Long-range correlations in disordered metals. *Physical Review B* **37,** 6701–6710 (1988).

63. Shapiro, B. New Type of Intensity Correlation in Random Media. *Physical Review Letters* **83,** 4733–4735 (1999).

64. Skipetrov, S. E. & Maynard, R. Nonuniversal correlations in multiple scattering. *Physical Review B* **62,** 886–891 (2000).

65. Van Tiggelen, B. A. & Skipetrov, S. E. Fluctuations of local density of states and C0 speckle correlations are equal. *Physical Review E* **73,** 045601 (2006).

66. Moreau, P.-A., Toninelli, E., Gregory, T. & Padgett, M. J. Ghost Imaging Using Optical Correlations. *Laser & Photonics Reviews* **12,** 1700143 (2018).

67. Pittman, T. B., Shih, Y. H., Strekalov, D. V. & Sergienko, A. V. Optical imaging by means of two-photon quantum entanglement. *Phys. Rev. A* **52,** R3429–R3432 (5 1995).

68. Strekalov, D. V., Sergienko, A. V., Klyshko, D. N. & Shih, Y. H. Observation of Two-Photon "Ghost" Interference and Diffraction. *Physical Review Letters* **74,** 3600–3603 (1995).

69. Bennink, R. S., Bentley, S. J. & Boyd, R. W. "Two-Photon" Coincidence Imaging with a Classical Source. *Physical Review Letters* **89,** 113601 (2002).

70. Haner, A. B. & Isenor, N. R. Intensity Correlations from Pseudothermal Light Sources. *American Journal of Physics* **38,** 748–750 (1970).

71. Valencia, A., Scarcelli, G., D'Angelo, M. & Shih, Y. Two-Photon Imaging with Thermal Light. *Phys. Rev. Lett.* **94,** 063601 (6 2005).

72. Ferri, F. *et al.* High-Resolution Ghost Image and Ghost Diffraction Experiments with Thermal Light. *Physical Review Letters* **94,** 183602 (2005).

73. Gatti, A., Brambilla, E., Bache, M. & Lugiato, L. a. Ghost Imaging with Thermal Light: Comparing Entanglement and ClassicalCorrelation. *Physical Review Letters* **93,** 093602 (2004).

74. Ragy, S. & Adesso, G. Nature of light correlations in ghost imaging. *Scientific Reports* **2,** 651 (2012).

75. Shapiro, J. H., Venkatraman, D. & Wong, F. N. C. Ghost Imaging without Discord. *Scientific Reports* **3,** 1849 (2013).

76. Shapiro, J. H. Computational ghost imaging. *Physical Review A* **78,** 061802 (2008).

77. Duarte, M. F. *et al.* Single-Pixel Imaging via Compressive Sampling. *IEEE Signal Processing Magazine* **25,** 83–91 (2008).

78. Radwell, N. *et al.* Single-pixel infrared and visible microscope. *Optica* **1,** 285 (2014).

79. Watts, C. M. *et al.* Terahertz compressive imaging with metamaterial spatial light modulators. *Nature Photonics* **8,** 605–609 (2014).

80. Stantchev, R. I. *et al.* Noninvasive, near-field terahertz imaging of hidden objects using a single-pixel detector. *Science Advances* **2,** e1600190 (2016).

81. Greenberg, J., Krishnamurthy, K. & Brady, D. Compressive single-pixel snapshot x-ray diffraction imaging. *Optics Letters* **39,** 111–114 (2014).

82. Erkmen, B. I. & Shapiro, J. H. Signal-to-noise ratio of Gaussian-state ghost imaging. *Physical Review A* **79,** 023833 (2009).

83. Goodman, J. W. Speckle with a finite number of steps. *Applied Optics* **47,** A111–8 (2008).

84. Ferri, F., Magatti, D., Lugiato, L. A. & Gatti, A. Differential Ghost Imaging. *Physical Review Letters* **104,** 253603 (2010).

85. Penrose, R. & Todd, J. A. A generalized inverse for matrices. *Mathematical Proceedings of the Cambridge Philosophical Society* **51,** 406 (1955).

86. Donoho, D. Compressed sensing. *IEEE Transactions on Information Theory* **52,** 1289–1306 (2006).

87. Candes, E., Romberg, J. & Tao, T. Robust uncertainty principles: exact signal reconstruction from highly incomplete frequency information. *IEEE Transactions on Information Theory* **52,** 489–509 (2006).

88. Candes, E. & Wakin, M. An Introduction To Compressive Sampling. *IEEE Signal Processing Magazine* **25,** 21–30 (2008).

89. Orović, I., Papić, V., Ioana, C., Li, X. & Stanković, S. Compressive Sensing in Signal Processing: Algorithms and Transform Domain Formulations. *Mathematical Problems in Engineering* **2016,** 1–16 (2016).

90. Aharon, M., Elad, M. & Bruckstein, A. K-SVD: An Algorithm for Designing Overcomplete Dictionaries for Sparse Representation. *IEEE Transactions on Signal Processing* **54,** 4311–4322 (2006).

91. Rubinstein, B. R., Bruckstein, A. M. & Elad, M. Dictionaries for Sparse Representation Modeling. *Proceedings of the IEEE* **98,** 1045–1057 (2010).

92. Shaobing Chen & Donoho, D. *Basis pursuit* in *Proceedings of 1994 28th Asilomar Conference on Signals, Systems and Computers* **1** (IEEE Comput. Soc. Press, 1994), 41–44.

93. Tibshirani, R. Regression Shrinkage and Selection via the Lasso. *Journal of the Royal Statistical Society. Series B (Methodological)* **58,** 267–288 (1996).

94. Wright, S. J. *Primal-Dual Interior-Point Methods* (Society for Industrial and Applied Mathematics, 1997).

95. L1-MAGIC `https://statweb.stanford.edu/~candes/l1magic/`.

96. Zhang, Z. & Rao, B. D. Sparse Signal Recovery With Temporally Correlated Source Vectors Using Sparse Bayesian Learning. *IEEE Journal of Selected Topics in Signal Processing* **5,** 912–926 (2011).

97. Xu, Y.-K. *et al.* Is ghost imaging intrinsically more powerful against scattering? *Optics Express* **23,** 32993 (2015).

98. Gong, W. & Han, S. Correlated imaging in scattering media. *Optics Letters* **36,** 394–396 (2011).

99. Durán, V. *et al.* Compressive imaging in scattering media. *Optics Express* **23,** 14424 (2015).

100. Pullman, B. *The atom in the history of human thought* (Oxford University Press, 2001).

101. Dirac, P. A. M. The Quantum Theory of the Emission and Absorption of Radiation. *Proceedings of the Royal Society A: Mathematical, Physical and Engineering Sciences* **114,** 243–265 (1927).

102. Loudon, R. *The Quantum Theory of Light* (OUP Oxford, 2000).

103. Mandel, L. & Wolf, E. *Optical Coherence and Quantum Optics* (1995).

104. Leonhardt, U. *Measuring the quantum state of light* (Cambridge University Press, 2005).

105. Chuang, I. L. & Nielsen, M. A. Prescription for experimental determination of the dynamics of a quantum black box. *Journal of Modern Optics* **44,** 2455–2467 (1997).

106. Lahini, Y., Bromberg, Y., Christodoulides, D. N. & Silberberg, Y. Quantum correlations in two-particle Anderson localization. *Physical Review Letters* **105,** 163905 (2010).

107. Bromberg, Y., Lahini, Y., Small, E. & Silberberg, Y. Hanbury Brown and Twiss interferometry with interacting photons. *Nature Photonics* **4,** 721–726 (2010).

108. Gatti, A. & Lugiato, L. A. Quantum images and critical fluctuations in the optical parametric oscillator below threshold. *Physical Review A* **52,** 1675–1690 (1995).

109. Glauber, R. J. The Quantum Theory of Optical Coherence. *Physical Review* **130,** 2529–2539 (1963).

110. Sudarshan, E. C. G. Equivalence of Semiclassical and Quantum Mechanical Descriptions of Statistical Light Beams. *Physical Review Letters* **10,** 277–279 (1963).

111. Teich, M. C. & Saleh, B. E. A. Squeezed states of light. *Quantum Optics* **1,** 153–191 (1989).

112. Walls, D. F. Squeezed states of light. *Nature* **306,** 141–146 (1983).

113. Feynman, R. P. Space-Time Approach to Non-Relativistic Quantum Mechanics. *Reviews of Modern Physics* **20,** 367–387 (1948).

114. Bohm, D. A Suggested Interpretation of the Quantum Theory in Terms of "Hidden" Variables. I. *Physical Review* **85,** 166–179 (1952).

115. Born, M. Zur Quantenmechanik der Stossvorgänge. *Zeitschrift für Physik* **37,** 863–867 (1926).

116. Wigner, E. On the Quantum Correction For Thermodynamic Equilibrium. *Physical Review* **40,** 749–759 (1932).

117. Weyl, H. Quantenmechanik und Gruppentheorie. *Zeitschrift für Physik* **46,** 1–46 (1927).

118. Moyal, J. E. & Bartlett, M. S. Quantum mechanics as a statistical theory. *Mathematical Proceedings of the Cambridge Philosophical Society* **45,** 99 (1949).

119. Groenewold, H. On the principles of elementary quantum mechanics. *Physica* **12,** 405–460 (1946).

120. Olivares, S. Quantum optics in the phase space - A tutorial on Gaussian states. *The European Physical Journal Special Topics* **203,** 3–24 (2012).

121. Husimi, K. Some Formal Properties of the Density Matrix. *Proceedings of the Physico-Mathematical Society of Japan. 3rd Series* **22,** 264–314 (1940).

122. Leonhardt, U. & Paul, H. Phase measurement and Q function. *Physical Review A* **47,** R2460–R2463 (1993).

123. Adesso, G. *Entanglement of Gaussian States* PhD thesis (Università degli Studi di Salerno, 2006).

124. Anders, J. *Estimating the degree of entanglement of unknown Gaussian states* MA thesis (University of Potsdam, 2003).

125. Aspachs, M., Calsamiglia, J., Muñoz-Tapia, R. & Bagan, E. Phase estimation for thermal Gaussian states. *Physical Review A* **79,** 033834 (2009).

126. Marian, P. & Marian, T. A. Squeezed states with thermal noise. I. Photon-number statistics. *Physical Review A* **47,** 4474–4486 (1993).

127. Cooper, M., Wright, L. J., Söller, C. & Smith, B. J. Experimental generation of multi-photon Fock states. *Optics Express* **21,** 5309 (2013).

128. Ra, Y.-S., Jacquard, C., Dufour, A., Fabre, C. & Treps, N. Tomography of a Mode-Tunable Coherent Single-Photon Subtractor. *Physical Review X* **7,** 031012 (2017).

129. Yurke, B. Input states for enhancement of fermion interferometer sensitivity. *Physical Review Letters* **56,** 1515–1517 (1986).

130. Bužek, V., Vidiella-Barranco, A. & Knight, P. L. Superpositions of coherent states: Squeezing and dissipation. *Physical Review A* **45,** 6570–6585 (1992).

131. Hanbury Brown, R. & Twiss, R. Q. A Test of a New Type of Stellar Interferometer on Sirius. *Nature* **178,** 1046–1048 (1956).

132. Simon, D. S., Jaeger, G. & Sergienko, A. V. *Ghost Imaging and Related Topics* (2017).

133. Hanbury Brown, R. & Twiss, R. Q. Interferometry of the intensity fluctuations in light - I. Basic theory: the correlation between photons in coherent beams of radiation. *Proceedings of the Royal Society of London A: Mathematical, Physical and Engineering Sciences* **242,** 300–324 (1957).

134. Spreeuw, R. J. C. A classical analogy of entanglement. *Found. Phys.* **28,** 361–374 (1998).

135. Goldin, M. A., Francisco, D. & Ledesma, S. Simulating Bell inequalities violation with classical optics encoded qbits. *Journal of the Optical Society of America B* **27,** 15 (2009).

136. Einstein, A., Podolsky, B. & Rosen, N. Can Quantum-Mechanical Description of Physical Reality Be Considered Complete? *Physical Review* **47,** 777–780 (1935).

137. Bell, J. S. On the Einstein Podolsky Rosen paradox. *Physics* **1,** 195–200 (1964).

138. Aspect, A., Grangier, P. & Roger, G. Experimental Tests of Realistic Local Theories via Bell's Theorem. *Physical Review Letters* **47,** 460–463 (1981).

139. Nielsen, M. A. & Chuang, I. L. *Quantum Computation and Quantum Information* (Cambridge University Press, 2010).

140. Carteret, H. A., Higuchi, A. & Sudbery, A. Multipartite generalization of the Schmidt decomposition. *Journal of Mathematical Physics* **41,** 7932–7939 (2000).

141. Yu, C.-s. & Song, H.-s. Global entanglement for multipartite quantum states. *Physical Review A* **73,** 022325 (2006).

142. Gühne, O. & Tóth, G. Entanglement detection. *Physics Reports* **474,** 1–75 (2009).

143. Peres, A. Separability Criterion for Density Matrices. *Physical Review Letters* **77,** 1413–1415 (1996).

144. Horodecki, M., Horodecki, P. & Horodecki, R. Separability of mixed states: necessary and sufficient conditions. *Physics Letters A* **223,** 1–8 (1996).

145. Simon, R. Peres-Horodecki Separability Criterion for Continuous Variable Systems. *Physical Review Letters* **84,** 2726–2729 (2000).

146. Werner, R. F. Quantum states with Einstein-Podolsky-Rosen correlations admitting a hidden-variable model. *Physical Review A* **40,** 4277–4281 (1989).

147. Serafini, A., Illuminati, F. & Siena, S. D. Symplectic invariants, entropic measures and correlations of Gaussian states. *Journal of Physics B: Atomic, Molecular and Optical Physics* **37,** L21–L28 (2004).

148. Laurat, J. *et al.* Entanglement of two-mode Gaussian states: characterization and experimental production and manipulation. *Journal of Optics B: Quantum and Semiclassical Optics* **7,** S577–S587 (2005).

149. Fiurášek, J. & Mišta, L. Gaussian localizable entanglement. *Physical Review A* **75,** 060302 (2007).

150. Adesso, G. & Illuminati, F. Entanglement in continuous-variable systems: recent advances and current perspectives. *Journal of Physics A: Mathematical and Theoretical* **40,** 7821–7880 (2007).

151. Terhal, B. M. Bell inequalities and the separability criterion. *Physics Letters A* **271,** 319–326 (2000).

152. Henderson, L. & Vedral, V. Classical, quantum and total correlations. *Journal of Physics A: Mathematical and General* **34,** 6899–6905 (2001).

153. Ollivier, H. & Zurek, W. H. Quantum Discord: A Measure of the Quantumness of Correlations. *Physical Review Letters* **88,** 017901 (2001).

154. Datta, A. A Condition for the Nullity of Quantum Discord `http://arxiv.org/abs/1003.5256`. (2010).

155. Giorda, P., Allegra, M. & Paris, M. G. A. Quantum discord for Gaussian states with non-Gaussian measurements. *Physical Review A* **86,** 052328 (5 2012).

156. Giedke, G. & Ignacio Cirac, J. Characterization of Gaussian operations and distillation of Gaussian states. *Physical Review A* **66,** 032316 (2002).

157. Holevo, A. & Werner, R. Evaluating capacities of bosonic Gaussian channels. *Physical Review A* **63,** 032312 (2001).

158. Giorda, P. & Paris, M. G. A. Gaussian Quantum Discord. *Physical Review Letters* **105,** 020503 (2010).

159. Adesso, G. & Datta, A. Quantum versus classical correlations in gaussian states. *Physical Review Letters* **105,** 030501 (2010).

160. Mandel, L. Sub-Poissonian photon statistics in resonance fluorescence. *Optics Letters* **4,** 205 (1979).

161. Hudson, R. L. When is the wigner quasi-probability density non-negative? *Reports on Mathematical Physics* **6,** 249–252 (1974).

162. Richter, T. & Vogel, W. Nonclassicality of Quantum States: A Hierarchy of Observable Conditions. *Physical Review Letters* **89,** 283601 (2002).

163. Kenfack, A. & Yczkowski, K. Negativity of the Wigner function as an indicator of non-classicality. *Journal of Optics B: Quantum and Semiclassical Optics* **6,** 396–404 (2004).

164. Hillery, M. Nonclassical distance in quantum optics. *Physical Review A* **35,** 725–732 (1987).

165. Asbóth, J. K., Calsamiglia, J. & Ritsch, H. Computable Measure of Nonclassicality for Light. *Physical Review Letters* **94,** 173602 (2005).

166. Baumgratz, T., Cramer, M. & Plenio, M. B. Quantifying coherence. *Physical Review Letters* **113,** 140401 (2014).

167. Breuer, H. & Petruccione, F. *The Theory of Open Quantum Systems* (Oxford University Press, 2007).

168. Zhang, Y. R., Shao, L. H., Li, Y. & Fan, H. Quantifying coherence in infinite-dimensional systems. *Physical Review A* **93,** 012334 (2016).

169. Barnett, S. M. & Croke, S. Quantum state discrimination. *Advances in Optics and Photonics* **1,** 238–278 (2009).

170. Rahimi-Keshari, S., Caves, C. M. & Ralph, T. C. Measurement-based method for verifying quantum discord. *Physical Review A* **87,** 012119 (2013).

171. Hosseini, S. *et al.* Experimental verification of quantum discord in continuous-variable states. *Journal of Physics B: Atomic, Molecular and Optical Physics* **47,** 025503 (2014).

172. Choi, Y. *et al.* Generation of a non-zero discord bipartite state with classical second-order interference. *Opt. Express* **25,** 2540–2551 (2017).

173. Starshynov, I., Bertolotti, J. & Anders, J. Non-classicality of coherent state mixtures `http://arxiv.org/abs/1802.08486`. (2018).

174. Braunstein, S. L., Caves, C. M. & Milburn, G. Generalized Uncertainty Relations: Theory, Examples, and Lorentz Invariance. *Annals of Physics* **247,** 135–173 (1996).

175. Wittmann, C. *et al.* Demonstration of near-optimal discrimination of optical coherent states. *Physical Review Letters* **101,** 210501 (2008).

176. Cook, R. L., Martin, P. J. & Geremia, J. M. Optical coherent state discrimination using a closed-loop quantum measurement. *Nature* **446,** 774–777 (2007).

177. Becerra, F. E., Fan, J. & Migdall, A. Implementation of generalized quantum measurements for unambiguous discrimination of multiple non-orthogonal coherent states. *Nature Communications* **4,** 2028 (2013).

178. Rosati, M., Mari, A. & Giovannetti, V. Coherent-state discrimination via nonheralded probabilistic amplification. *Physical Review A* **93,** 062315 (6 2016).

179. Weir, G., Barnett, S. M. & Croke, S. Optimal discrimination of single-qubit mixed states. *Physical Review A* **96,** 022312 (2017).

180. Osaki, M., Ban, M. & Hirota, O. Derivation and physical interpretation of the optimum detection operators for coherent-state signals. *Physical Review A* **54,** 1691–1701 (1996).

181. Dolinar, S. J. An optimum receiver for the binary coherent state quantum channel. *MIT Research Laboratory of Electronics Quarterly Progress Report* **111,** 115 (1973).

182. Kennedy, R. S. A Near-Optimum Receiver for the Binary Coherent State Quantum Channel. *MIT Research Laboratory of Electronics Quarterly Progress Report* **108,** 219 (1973).

183. Sasaki, M. & Hirota, O. Optimum decision scheme with a unitary control process for binary quantum-state signals. *Physical Review A - Atomic, Molecular, and Optical Physics* **54,** 2728–2736 (1996).

184. Sych, D. & Leuchs, G. Practical receiver for optimal discrimination of binary coherent signals. *Physical Review Letters* **117,** 200501 (2016).

185. Ou, Z., Hong, C. & Mandel, L. Relation between input and output states for a beam splitter. *Optics Communications* **63,** 118–122 (1987).

186. Reck, M., Zeilinger, A., Bernstein, H. J. & Bertani, P. Experimental realization of any discrete unitary operator. *Physical Review Letters* **73,** 58–61 (1994).

187. Bouland, A. & Aaronson, S. Generation of universal linear optics by any beam splitter. *Physical Review A* **89,** 062316 (2014).

188. Feynman, R. *The Feynman lectures on physics* (Addison-Wesley Pub. Co, 1963).

189. Campos, R. A., Saleh, B. E. A. & Teich, M. C. Quantum-mechanical lossless beam splitter: SU (2) symmetry and photon statistics. *Physical Review A* **40,** 1371–1384 (1989).

190. Paris, M. G. Displacement operator by beam splitter. *Physics Letters A* **217,** 78–80 (1996).

191. Ma, Z., Chen, Z., Fanchini, F. F. & Fei, S.-M. Quantum Discord for dx2 Systems. *Scientific Reports* **5,** 10262 (2015).

192. Born, M. & Wolf, E. *Principles of optics: Electromagnetic Theory of Propagation, Interference and Diffraction of Light* (1994).

193. Streltsov, A., Singh, U., Dhar, H. S., Bera, M. N. & Adesso, G. Measuring Quantum Coherence with Entanglement. *Physical Review Letters* **115,** 020403 (2015).

194. Killoran, N., Steinhoff, F. E. & Plenio, M. B. Converting Nonclassicality into Entanglement. *Physical Review Letters* **116,** 080402 (2016).

195. Marvian, I., Spekkens, R. W. & Zanardi, P. Quantum speed limits, coherence, and asymmetry. *Physical Review A* **93,** 052331 (2016).

196. Hillery, M. Coherence as a resource in decision problems: The Deutsch-Jozsa algorithm and a variation. *Physical Review A* **93,** 012111 (2016).

197. Ferraro, A. & Paris, M. G. Nonclassicality criteria from phase-space representations and information-theoretical constraints are maximally inequivalent. *Physical Review Letters* **108,** 260403 (2012).

198. Starshynov, I., Bertolotti, J. & Anders, J. Quantum correlation of light scattered by disordered media. *Opt. Express* **24,** 4662–4671 (2016).

199. Duan, L.-M., Giedke, G., Cirac, J. I. & Zoller, P. Inseparability Criterion for Continuous Variable Systems. *Physical Review Letters* **84,** 2722–2725 (2000).

200. Beenakker, C. W. J. Thermal Radiation and Amplified Spontaneous Emission from a Random Medium. *Physical Review Letters* **81,** 1829–1832 (1998).

201. Patra, M. & Beenakker, C. Excess noise for coherent radiation propagating through amplifying random media. *Physical Review A* **60,** 4059–4066 (1999).

202. Patra, M. & Beenakker, C. W. J. Propagation of squeezed radiation through amplifying or absorbing random media. *Physical Review A* **61,** 063805 (2000).

203. Lodahl, P. & Lagendijk, A. Transport of Quantum Noise through Random Media. *Physical Review Letters* **94,** 153905 (2005).

204. Lodahl, P., Mosk, A. P. & Lagendijk, A. Spatial Quantum Correlations in Multiple Scattered Light. *Physical Review Letters* **95,** 173901 (2005).

205. Lodahl, P. Quantum noise frequency correlations of multiply scattered light. *Optics Letters* **31,** 110 (2006).

206. Smolka, S., Huck, A., Andersen, U. L., Lagendijk, A. & Lodahl, P. Observation of Spatial Quantum Correlations Induced by Multiple Scattering of Nonclassical Light. *Physical Review Letters* **102,** 193901 (2009).

207. Ott, J. R., Mortensen, N. A. & Lodahl, P. Quantum Interference and Entanglement Induced by Multiple Scattering of Light. *Physical Review Letters* **105,** 090501 (2010).

208. Smolka, S., Ott, J. R., Huck, A., Andersen, U. L. & Lodahl, P. Continuous-wave spatial quantum correlations of light induced by multiple scattering. *Physical Review A* **86,** 033814 (2012).

209. Crespi, A. *et al.* Anderson localization of entangled photons in an integrated quantum walk. *Nature Photonics* **7,** 322–328 (2013).

210. Beenakker, C. W. J., Venderbos, J. W. F. & van Exter, M. P. Two-Photon Speckle as a Probe of Multi-Dimensional Entanglement. *Physical Review Letters* **102,** 193601 (2009).

211. Peeters, W. H., Moerman, J. J. D. & van Exter, M. P. Observation of Two-Photon Speckle Patterns. *Physical Review Letters* **104,** 173601 (2010).

212. Gard, B. T., Motes, K. R., Olson, J. P., Rohde, P. P. & Dowling, J. P. in *From Atomic to Mesoscale* 167–192 (World Scientific, 2015).

213. Ralph, T. C. Boson sampling on a chip. *Nature Photonics* **7,** 514–515 (2013).

214. Aaronson, S. & Arkhipov, A. The Computational Complexity of Linear Optics. *Theory of Computing* **9,** 143–252 (2013).

215. Tillmann, M. *et al.* Experimental boson sampling. *Nature Photonics* **7,** 540–544 (2013).

216. Spring, J. B. *et al.* Boson Sampling on a Photonic Chip. *Science* **339,** 798–801 (2013).

217. Huisman, T. J., Huisman, S. R., Mosk, A. P. & Pinkse, P. W. Controlling single-photon Fock-state propagation through opaque scattering media. *Applied Physics B: Lasers and Optics* **116,** 603–607 (2014).

218. Wolterink, T. A. W. *et al.* Programmable two-photon quantum interference in 103 channels in opaque scattering media. *Physical Review A - Atomic, Molecular, and Optical Physics* **93,** 1–6 (2016).

219. Defienne, H. *et al.* Nonclassical light manipulation in a multiple-scattering medium. *Optics Letters* **39,** 6090 (2014).

220. Defienne, H., Barbieri, M., Walmsley, I. A., Smith, B. J. & Gigan, S. Two-photon quantum walk in a multimode fiber. *Science Advances* **2,** e1501054 (2016).

221. Dorokhov, O. On the coexistence of localized and extended electronic states in the metallic phase. *Solid State Communications* **51,** 381–384 (1984).

222. Beenakker, C. W. J. Random-matrix theory of quantum transport. *Reviews of Modern Physics* **69,** 731–808 (1997).

223. Marthaler, M. & Dykman, M. I. Switching via quantum activation: A parametrically modulated oscillator. *Physical Review A* **73,** 042108 (2006).

224. Paris, M. G. a. Entanglement and visibility at the output of a Mach-Zehnder interferometer. *Physical Review A* **59,** 1615–1621 (1999).

225. Kay, S. & Maitland, A. *Quantum Optics: Proceedings of the Tenth Session of the Scottish Universities' Summer School in Physics, 1969* (Academic Press, 1970).

226. Lvovsky, A. I. *et al.* Quantum State Reconstruction of the Single-Photon Fock State. *Physical Review Letters* **87,** 050402 (2001).

227. Altepeter, J., Jeffrey, E. & Kwiat, P. in, 105–159 (2005).

228. Lvovsky, A. I. & Raymer, M. G. Continuous-variable optical quantum-state tomography. *Reviews of Modern Physics* **81,** 299–332 (2009).

229. Dirk-Gunnar, W., Werner, V. & Tomas, O. in *Progress in Optics, Vol. XXXIX, ed. E. Wolf* 63–211 (Elsevier, Amsterdam, 1999).

230. Beck, M. Quantum State Tomography with Array Detectors. *Physical Review Letters* **84,** 5748–5751 (2000).

231. Dawes, a., Beck, M. & Banaszek, K. Mode optimization for quantum-state tomography with array detectors. *Physical Review A* **67,** 1–6 (2003).

232. Walker, N. Quantum Theory of Multiport Optical Homodyning. *Journal of Modern Optics* **34,** 15–60 (1987).

233. Takeda, S. *et al.* Generation and eight-port homodyne characterization of time-bin qubits for continuous-variable quantum information processing. *Physical Review A* **87,** 043803 (2013).

234. Dawes, A. M. & Beck, M. Simultaneous quantum-state measurements using array detection. *Physical Review A* **63,** 040101 (2001).

235. Harms, B. S., Anthony, B. E., Holte, N. T., Dassonville, H. a. & Dawes, A. M. C. Multimode quantum state tomography using unbalanced array detection. *Physical Review A* **90,** 053818 (2014).

236. Beck, M., Dorrer, C. & Walmsley, I. A. Joint Quantum Measurement Using Unbalanced Array Detection. *Physical Review Letters* **87,** 253601 (2001).

237. Huang, T. Digital holography. *Proceedings of the IEEE* **59,** 1335–1346 (1971).

238. Luo, S. Quantum discord for two-qubit systems. *Physical Review A* **77,** 042303 (2008).

239. Benedetti, C., Shurupov, A. P., Paris, M. G. a., Brida, G. & Genovese, M. Experimental estimation of quantum discord for a polarization qubit and the use of fidelity to assess quantum correlations. *Physical Review A* **87,** 052136 (2013).

240. Saguia, A., Rulli, C. C., de Oliveira, T. R. & Sarandy, M. S. Witnessing nonclassical multipartite states. *Physical Review A* **84,** 042123 (2011).

241. Passante, G., Moussa, O., Trottier, D. A. & Laflamme, R. Experimental detection of nonclassical correlations in mixed-state quantum computation. *Physical Review A* **84,** 044302 (2011).

242. Blandino, R. *et al.* Homodyne Estimation of Gaussian Quantum Discord. *Physical Review Letters* **109,** 180402 (2012).

243. Shi, M., Sun, C., Jiang, F., Yan, X. & Du, J. Optimal measurement for quantum discord of two-qubit states. *Physical Review A* **85,** 064104 (2012).

244. Jin, J., Zhang, F., Yu, C. & Song, H. Direct scheme for measuring the geometric quantum discord. *Journal of Physics A: Mathematical and Theoretical* **45,** 115308 (2012).

245. Cialdi, S., Smirne, A., Paris, M. G. A., Olivares, S. & Vacchini, B. Two-step procedure to discriminate discordant from classical correlated or factorized states. *Physical Review A* **90,** 050301 (2014).

246. Bengtsson, I. & Zyczkowski, K. *Geometry of quantum states : an introduction to quantum entanglement* (Cambridge University Press, Cambridge New York, 2008).

247. Hiai, F. & Petz, D. The proper formula for relative entropy and its asymptotics in quantum probability. *Communications in Mathematical Physics* **143,** 99–114 (1991).

248. Madhok, V. & Datta, A. Quantum discord as a resource in quantum communication. *International Journal of Modern Physics B* **27,** 1345041 (2013).

249. Dakic, B. *et al.* Quantum discord as resource for remote state preparation. *Nature Physics* **8,** 666–670 (2012).

Appendix A

In this appendix we show in details two examples of the quantum discord calculation. In the first example we consider the Werner state [146], which can be represented as a mixture of a two qubit maximally entangled state and a maximally mixed state. At a certain degree of mixing the entanglement of this state vanishes, however quantum discord changes monotonously becoming 0 only for a maximally mixed state, which shows that this quantity is suitable for characterization of quantum correlations beyond entanglement. In the second example we consider a simpler case of a mixed state that does not require any entanglement for its preparation. All the steps in this process are apparently classical, however as a result we get a state with non-zero discord.

Werner state

Werner states are a class of states with such a form:

$$\rho_{\mathrm{W}} = z\rho_{\mathrm{Bell}} + (1-z)\rho_{\mathrm{m.mix}}, \tag{A.1}$$

where ρ_{Bell} is the density matrix of a maximally entangled state, $\rho_{\mathrm{m.mix}}$ is a maximally mixed state and z is a mixing ratio. For two polarization qubits one of the variants of such a state is

$$\rho_{\mathrm{W}} = \frac{z}{2}\Big(|HH\rangle + |VV\rangle\Big)\Big(\langle HH| + \langle VV|\Big) + \frac{1-z}{4}\mathbb{I}_4, \tag{A.2}$$

where H and V are horizontal and vertical polarization respectively, $\mathbb{I}_4$ is a 4×4 identity matrix and $0 \leq z \leq 1$ is a mixing ratio. In the $|H\rangle, |V\rangle$ basis this state is

$$\rho_{\mathrm{W}} = \begin{pmatrix} \frac{z+1}{4} & 0 & 0 & \frac{z}{2} \\ 0 & \frac{1-z}{4} & 0 & 0 \\ 0 & 0 & \frac{1-z}{4} & 0 \\ \frac{z}{2} & 0 & 0 & \frac{z+1}{4} \end{pmatrix}. \tag{A.3}$$

It is easy to estimate its entanglement. The partial transpose (5.83) of this matrix is

$$\rho_{\mathrm{W}}^{\mathrm{PT}} = \begin{pmatrix} \frac{z+1}{4} & 0 & 0 & 0 \\ 0 & \frac{1-z}{4} & \frac{z}{2} & 0 \\ 0 & \frac{z}{2} & \frac{1-z}{4} & 0 \\ 0 & 0 & 0 & \frac{z+1}{4} \end{pmatrix}. \tag{A.4}$$

The smallest eigenvalue of the state $\rho_{\mathrm{W}}^{\mathrm{PT}}$ is $(1-3z)/4$, which means that ρ_{W} is entangled for $z > 1/3$ and separable otherwise.

Let's now calculate the discord, (5.94) of ρ_{W}.

$$D(\rho_{\mathrm{W}}) = S(\rho_{\mathrm{W}}^B) - S(\rho_{\mathrm{W}}) + \inf_{\Pi_j} \Big(\sum_j p_j S(\rho_{\mathrm{W}}^{A|\Pi_j}) \Big), \tag{A.5}$$

where ρ_{W}^A and ρ_{W}^B are the reduced states of the 1-st and the 2-nd qubit of ρ_{W} respectively, $p_j = \mathrm{Tr}[\rho_{\mathrm{W}}(\mathbb{I}^A \otimes \Pi_j^B)]$, $\rho_{\mathrm{W}}^{A|\Pi_j} = \mathrm{Tr}_B[\rho_{\mathrm{W}}(\mathbb{I}_2^A \otimes \Pi_j^B)]/p_j$ is the of the qubit A after obtaining the Π_j^B outcome on B (which happens with the probability p_j), and finally Π_j^B is a complete set of orthogonal projectors in the ρ_{W}^B subspace.

The first term in (A.5) is the entropy of the reduced state ρ_{W}^B. We can notice that ρ_{W} is symmetric and $\rho_{\mathrm{W}}^A = \rho_{\mathrm{W}}^B = \mathbb{I}_2/2$, therefore $S(\rho_{\mathrm{W}}^B) = \log 2$. The second term in (A.5) is the entropy of ρ_{W}

$$S(\rho_{\mathrm{W}}) = \frac{3(z-1)}{4} \log\left(\frac{1-z}{4}\right) - \frac{3z+1}{4} \log\left(\frac{3z+1}{4}\right) \tag{A.6}$$

The third term is the conditional entropy, of the A qubit depending on the possible outcomes of the projective measurement Π_j^B on the B qubit. A complete set of the orthogonal projectors Π_j^B for the second qubit can be parametrised as:

$$\begin{aligned} \Pi_0^B &= |\psi_0\rangle\langle\psi_0|; \quad |\psi_0\rangle = \cos(\theta)|H\rangle + e^{i\phi}\sin(\theta)|V\rangle, \\ \Pi_1^B &= |\psi_1\rangle\langle\psi_1|; \quad |\psi_1\rangle = -\sin(\theta)e^{-i\phi}|H\rangle + \cos(\theta)|V\rangle, \end{aligned} \tag{A.7}$$

where $\theta, \phi \in [0, 2\pi]$. The probability for Π_0^B to occur is

$$\begin{aligned} &p_0 = \mathrm{Tr}[\rho_{\mathrm{W}} \cdot (\mathbb{I}^A \otimes \Pi_0^B)] = \\ &= \mathrm{Tr}\left[\rho_{\mathrm{W}} \cdot \begin{pmatrix} 1 & 0 \\ 0 & 1 \end{pmatrix} \otimes \begin{pmatrix} \cos^2(\theta) & e^{i\phi}\cos(\theta)\sin(\theta) \\ e^{-i\phi}\cos(\theta)\sin(\theta) & \sin^2(\theta) \end{pmatrix}\right] = \frac{1}{2}. \end{aligned} \tag{A.8}$$

The state of the qubit A after Π_0^B was observed in B is

$$\rho_{\mathrm{W}}^{A|\Pi_0} = \frac{1}{p_0}\mathrm{Tr}_B\left[\rho_{\mathrm{W}}\cdot\begin{pmatrix}1&0\\0&1\end{pmatrix}\otimes\begin{pmatrix}\cos^2(\theta)&e^{i\phi}\cos(\theta)\sin(\theta)\\e^{-i\phi}\cos(\theta)\sin(\theta)&\sin^2(\theta)\end{pmatrix}\right] = \\ = \begin{pmatrix}\frac{1}{2}(z\cos(2\theta)+1)&e^{i\phi}z\cos(\theta)\sin(\theta)\\e^{-i\phi}z\cos(\theta)\sin(\theta)&\frac{1}{2}(1-z\cos(2\theta))\end{pmatrix}.$$

The eigenvalues of $\rho_{\mathrm{W}}^{A|\Pi_0}$ are $\left\{\frac{1-z}{2},\frac{z+1}{2}\right\}$ and therefore the entropy of this state

$$S(\rho_{\mathrm{W}}^{A|\Pi_0}) = \frac{1}{2}\left((z-1)\log\left(\frac{1-z}{2}\right)-(z+1)\log\left(\frac{z+1}{2}\right)\right) \tag{A.9}$$

Performing the same calculation for $\rho_{\mathrm{W}}^{A|\Pi_1}$ we can show that $p_1 = p_0 = 1/2$ and

$$\rho_{\mathrm{W}}^{A|\Pi_1} = \begin{pmatrix}\frac{1}{2}(1-z\cos(2\theta))&-e^{-i\phi}z\cos(\theta)\sin(\theta)\\-e^{i\phi}z\cos(\theta)\sin(\theta)&\frac{1}{2}(z\cos(2\theta)+1)\end{pmatrix}, \tag{A.10}$$

which has the same eigenvalues and entropy as $\rho_{\mathrm{W}}^{A|\Pi_0}$ and does not depend on θ and ϕ. Therefore, the last term in (A.5)

$$\inf_{\Pi_j}\Big(\sum_j p_j S(\rho_{\mathrm{W}}^{A|\Pi_j})\Big) = \frac{1}{2}\rho_{\mathrm{W}}^{A|\Pi_0}+\frac{1}{2}\rho_{\mathrm{W}}^{A|\Pi_1} = \\ = \frac{1}{2}\left((z-1)\log\left(\frac{1-z}{2}\right)-(z+1)\log\left(\frac{z+1}{2}\right)\right) \tag{A.11}$$

The discord is:

$$D(\rho_{\mathrm{W}}) = \frac{1}{4}(-(z-1)\log(1-z)-2(z+1)\log(z+1)+(3z+1)\log(3z+1)), \tag{A.12}$$

this expression is plotted in Fig. A.1 together with the total mutual information (5.91)

$$I^q(\rho_{\mathrm{W}}) = S(\rho_{\mathrm{W}}^A)+S(\rho_{\mathrm{W}}^B)-S(\rho_{\mathrm{W}}), \tag{A.13}$$

and the classical part of the mutual information (5.93)

$$J^q(\rho_{\mathrm{W}}) = S(\rho_{\mathrm{W}}^A)-\sum_j p_j S(\rho_{\mathrm{W}}^{A|\Pi_j}), \tag{A.14}$$

Let's discuss the physical meaning of the behaviour we observe. At $z=1$ the state of the qubits A and B is maximally entangled. The total correlation is equally shared

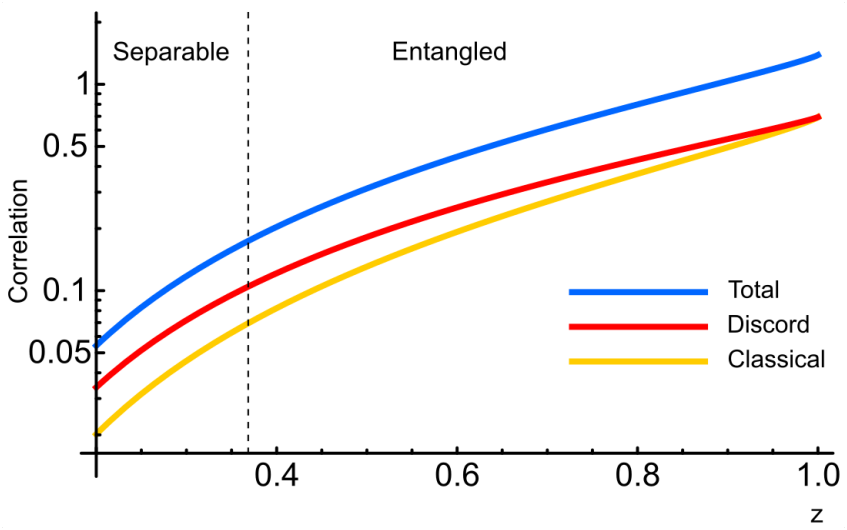

Figure A.1: Correlations of the state ρ_{W}: blue line, total correlations (A.13); yellow line, classical correlations (A.14); red line, quantum discord (A.12).

between the quantum and classical ones, which is a common feature of the maximally entangled states [238]. When $z \to 0$, ρ_{W} approaches a maximally mixed two-qubit state. In such a state there is no correlation (neither quantum nor classical) between A and B qubits as shown in Fig. A.1. Interestingly, there is a region of z in which the ρ_{W} becomes separable, however quantum discord still indicates presence of non-classical correlations.

Classically prepared state with non-zero discord

The state ρ_{W} from the previous example was convenient for the theoretical analysis. First of all the reduces states its subsystems were the same, making ρ_{W} symmetric. Also, both elements of the mixture, i.e. the maximally entangled and the maximally mixed state were invariant under the local transformations, which eliminated the dependence of the conditional entropy on the measurement basis, making the minimization in (5.94) redundant. On the other hand such a state is not easy to prepare, since it requires a non-classical source of photons. One may argue that it is not surprising to get non-classical correlations in that scenario even if the mixing is strong. In this section we consider an example of a state, which does not require an apparent non-classical resources in its preparation, however demonstrates non-zero discord.

Let's look at how to prepare the state (A.2). The most obvious setup for that is shown in Fig. A.2. Two independent sources produce two mode states ρ^A and ρ^B and each of that states enters a mixing device M. This device should effectively be an optical multiplexer, which at any moment of time connects one of its inputs to the output and discards the other. If now we drive both of these mixers by pseudorandom signals from

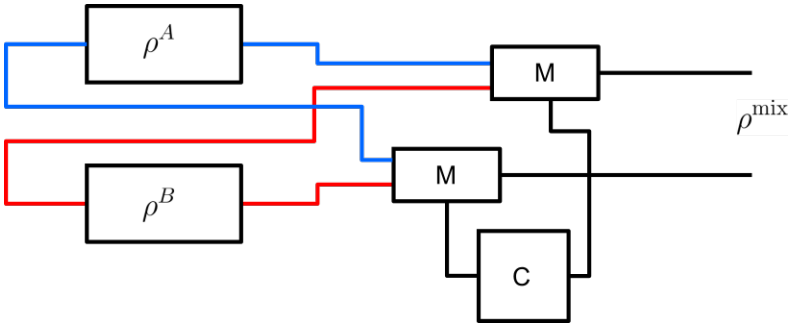

Figure A.2: Classical mixing of two mode states.

the controller C, to switch each of the mixers simultaneously but in a random way, we get the state as in (A.2), with the parameter z being the average "duty cycle" of the random signal. In the previous example we considered a situation when ρ^A was an entangled (in polarizaton) state, and ρ^B was just a source of depolarized uncorrelated photons and any correlation in the output state was from ρ^A.

Let's now consider a situation when $\rho^A = |HH\rangle\langle HH|$ and $\rho^B = |VD\rangle\langle VD|$, where $|D\rangle = (|H\rangle + |V\rangle)/\sqrt{2}$. Both of these states are completely classical. The first one is just a source of horizontally polarized light divided into two beams, and the second one is a source that emits vertically polarized light in on of the output modes and diagonally polarized into another. In the $|H\rangle, |V\rangle$ basis the resulting output state is

$$\rho_C = \begin{pmatrix} \frac{1}{2} & 0 & 0 & 0 \\ 0 & 0 & 0 & 0 \\ 0 & 0 & \frac{1}{4} & \frac{1}{4} \\ 0 & 0 & \frac{1}{4} & \frac{1}{4} \end{pmatrix}. \tag{A.15}$$

We can see that the state ρ_C fails to follow the criterion of the discord absence, (5.95), since the states corresponding to Ψ^i in that formula are $|H\rangle, |D\rangle$ and are not orthogonal.

Let's calculate the discord of this state. From now on we will use base 2 in the logarithms to have all the entropies in bits. The reduced states of the subsystems of ρ_C are

$$\rho^A = \begin{pmatrix} \frac{1}{2} & 0 \\ 0 & \frac{1}{2} \end{pmatrix}, \quad \rho^B = \begin{pmatrix} \frac{3}{4} & \frac{1}{4} \\ \frac{1}{4} & \frac{1}{4} \end{pmatrix}. \tag{A.16}$$

The entropies are: $S(\rho^A) = S(\rho_C) = 1$ and

$$S(\rho^B) = 2 - \frac{\left(\sqrt{2}+2\right)\log_2\left(\sqrt{2}+2\right) + \left(\sqrt{2}-2\right)\log_2\left(2-\sqrt{2}\right)}{4} \approx 0.6$$

We now need to calculate the conditional entropy in (5.94). The probabilities to get

Π_0^B or Π_1^B by analogy to (A.8) are

$$p_0 = \frac{1}{8}\left(4\sin(\theta)\cos(\theta)\cos(\phi) + 2\cos^2(\theta) + \cos(2\theta) + 3\right), \tag{A.17}$$

$$p_1 = \frac{1}{4}\left(-2\sin(\theta)\cos(\theta)\cos(\phi) + \sin^2(\theta) - \cos^2(\theta) + 2\right). \tag{A.18}$$

The post-measurement states are:

$$\rho_{\mathrm{C}}^{A|\Pi_0} = \begin{pmatrix} \frac{2\cos^2(\theta)}{\cos(2\theta)+\cos(\phi)\sin(2\theta)+2} & 0 \\ 0 & \frac{2(\sin(2\theta)\cos(\phi)+1)}{4\sin(\theta)\cos(\theta)\cos(\phi)+2\cos^2(\theta)+\cos(2\theta)+3} \end{pmatrix} \tag{A.19}$$

$$\rho_{\mathrm{C}}^{A|\Pi_1} = \begin{pmatrix} -\frac{2\sin^2(\theta)}{\cos(2\theta)+\cos(\phi)\sin(2\theta)-2} & 0 \\ 0 & \frac{\sin(2\theta)\cos(\phi)-1}{\sin(2\theta)\cos(\phi)-\sin^2(\theta)+\cos^2(\theta)-2} \end{pmatrix} \tag{A.20}$$

It is possible to see, that these states are different. For example for $\theta = \phi = 0$, in which case $\Pi_0^B = |H\rangle\langle H|$, $\Pi_1^B = |V\rangle\langle V|$, the conditional states are

$$\rho_{\mathrm{C}}^{A|\Pi_0(\theta=0,\phi=0)} = \begin{pmatrix} \frac{2}{3} & 0 \\ 0 & \frac{1}{3} \end{pmatrix} \tag{A.21}$$

$$\rho_{\mathrm{C}}^{A|\Pi_1(\theta=0,\phi=0)} = \begin{pmatrix} 0 & 0 \\ 0 & 1 \end{pmatrix} \tag{A.22}$$

This effect has the same nature as for the entangled states. The measurement performed on one of the arms leads to a non-local change of the global state and leads to different conditional distributions for the second system. In contrast to the entanglement scenario, this change is not enough to violate the Bell's inequalities, however it is still an observable effect.

Interestingly, the global state after $\Pi_0^B = |H\rangle\langle H|$, $\Pi_1^B = |V\rangle\langle V|$ projective measurement is

$$\begin{aligned} \rho'_C = {} & p_0(\theta=0,\phi=0)\begin{pmatrix} \frac{2}{3} & 0 \\ 0 & \frac{1}{3} \end{pmatrix} \otimes \begin{pmatrix} 1 & 0 \\ 0 & 0 \end{pmatrix} \\ & + p_1(\theta=0,\phi=0)\begin{pmatrix} 0 & 0 \\ 0 & 1 \end{pmatrix} \otimes \begin{pmatrix} 0 & 0 \\ 0 & 1 \end{pmatrix} = \begin{pmatrix} \frac{1}{2} & 0 & 0 & 0 \\ 0 & 0 & 0 & 0 \\ 0 & 0 & \frac{1}{4} & 0 \\ 0 & 0 & 0 & \frac{1}{4} \end{pmatrix}, \end{aligned} \tag{A.23}$$

which is identical to ρ_C with removed off-diagonal elements.

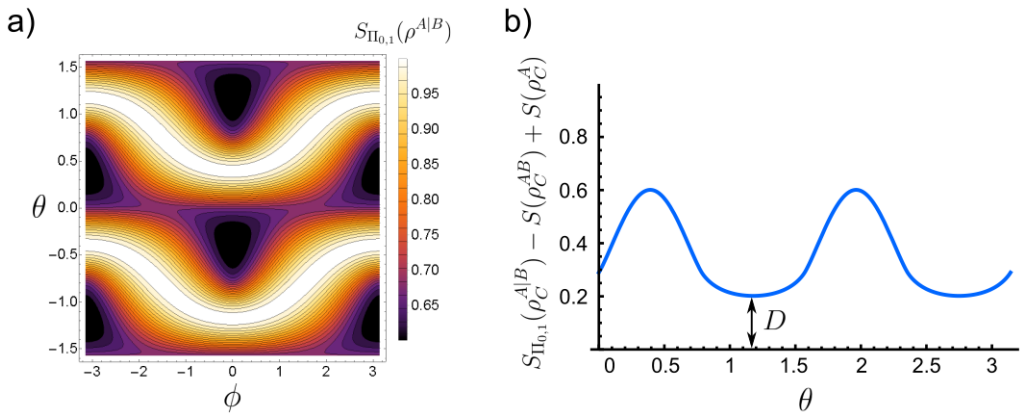

Figure A.3: a) Conditional entropy of the state ρ_C, Eq. (A.15). b) The expression for quantum discord (A.5), without minimization. Due to the invariance of the shape of this dependence along ϕ we take $\phi = 0$ and minimize only over θ. Quantum discord is the minimum of this curve, as indicated.

The conditional entropy is

$$S_{\Pi_{0,1}}(\rho^{A|B}) = p_0 S(\rho_{\mathrm{C}}^{A|\Pi_0}) + p_1 S(\rho_{\mathrm{C}}^{A|\Pi_1}) \tag{A.24}$$

We plot this quantity in Fig. A.3a, depending on θ and ϕ, and in Fig. A.3b we plot the dependence of $S_{\Pi_{0,1}}(\rho_C^{A|B}) - S(\rho_C^{AB}) + S(\rho_C^A)$ on θ, the minimization of which gives us the discord of $D \approx 0.2$ bit.

As we already discussed in Ch. 6 presence of discord in the states commonly considered classical was demonstrated experimentally [171, 172]. The most straightforward way of showing non-classical correlations in a generic state is a full tomographic reconstruction of its density matrix [172, 239]. This method, however is accompanied with practical difficulties, as for a 2×2 system it requires $2^2 \times 2^2$ measurements and implies a reconstruction procedure sensitive to measurement errors [104]. There are several methods allowing to surpass these difficulties and detect or measure quantum discord directly [240–245], however often such schemes require generalized measurements, which are hard to implement experimentally.

The main difficulty in estimation of quantum discord is related to building a measurement that maximizes the mutual information between the correlated systems. The classical mutual information Eq. (5.93) can be extracted from simple projective measurements. We can introduce a set of projectors on the A subsystem similarly to Eq. (A.7), parameterized by the angles θ_0, ϕ_0, and construct a classical probability distribution

from the measurement outcomes of four projectors:

$$\begin{array}{|c|c|}\hline p\big[\Pi_1^A(\theta_0,\phi_0)\Pi_1^B(\theta,\phi)\big] & p\big[\Pi_1^A(\theta_0,\phi_0)\Pi_2^B(\theta,\phi)\big] \\ \hline p\big[\Pi_2^A(\theta_0,\phi_0)\Pi_1^B(\theta,\phi)\big] & p\big[\Pi_2^A(\theta_0,\phi_0)\Pi_2^B(\theta,\phi)\big] \\ \hline\end{array} \tag{A.25}$$

One can calculate the mutual information between A and B subsystems from this distribution, using Eq. (6.55) or Eq. (5.91) (once the quantum part of the mutual information is extracted, these two are equivalent). Measuring the total mutual information is less straightforward. A method, allowing to estimate the total mutual information without the tomographic reconstruction of the state relies on following identity [139]:

$$I(\rho^{AB}) = S(\rho^{AB}||\rho^A \otimes \rho^B), \tag{A.26}$$

where $S(\rho||\sigma) = \mathrm{Tr}\big[\rho\log(\rho) - \rho\log(\sigma)\big]$ is the relative entropy. This quantity characterizes the distinguishability of ρ and σ. It can be estimated using the following procedure [246]:

- N copies of the original state ρ^{AB} are prepared: $\rho^{AB\,N} = \otimes^N \rho^{AB}$
- From the results of the protective measurements $\{E\}$ on a tensor product state we obtain
$$S_N = \frac{1}{N}\sum_i p_i \log\left(\frac{p_i}{q_i}\right), \tag{A.27}$$
where $p_i = \mathrm{Tr}[\rho E_i]$ and $q_i = \mathrm{Tr}[\sigma E_i]$
- Finally, taking a limit of $N \to \infty$ and optimizing over all possible $\{E\}$ we obtain [247]
$$S(\rho||\sigma) = \lim_{N\to\infty}\max_{\{E\}} S_N \tag{A.28}$$

In the measurement procedure described above, the state σ is $\rho^A \otimes \rho^B$. It is not directly available experimentally, however q_i can be obtained from the measurements on ρ_{AB} by randomizing the measurement outcomes on both subsystems with respect to each other and thus erasing the correlations between them. The main difficulty, however lies in the optimization over all possible $\{E\}$. The optimal measurement is not necessarily of the type $\Pi^A \otimes \Pi^B$. A general set of projectors in the 2×2 Hilbert space is parametrized by 16 real numbers, which makes the optimization procedure cumbersome. The same applies to finding a measurement procedure that maximally utilizes the total mutual information. Despite a clear role of quantum correlations in the improvement over classical procedures [248, 249], finding a general method of how this improvement can be implemented is still an opened question.

Appendix B

In this appendix we calculate the integrals from the expression for $\langle O_p^2 \rangle$, (4.9) and $\mathrm{Cov}\left[O_p, \Delta\widetilde{R}_p\right]$, (4.19), required for the Ghost Imaging SNR estimation.

$$\begin{aligned}
&\frac{1}{N_{\mathrm{r}}^2}\int_0^\infty \left[\sum_i^{N_{\mathrm{r}}}\sum_{j\neq p}^{N_{\mathrm{p}}} R_{ij}R_{ip}\Lambda_j\right]^2 P(\mathbf{R})d\mathbf{R} = \\
&= \frac{1}{N_{\mathrm{r}}^2}\int_0^\infty \left[\sum_i^{N_{\mathrm{r}}}\sum_{j\neq p}^{N_{\mathrm{p}}} R_{ij}^2R_{ip}^2\Lambda_j^2 + \sum_i^{N_{\mathrm{r}}}\sum_{j\neq l\neq p}^{N_{\mathrm{p}}} R_{ip}^2R_{ij}R_{il}\Lambda_j\Lambda_l + \right. \\
&\left. + \sum_{i\neq k}^{N_{\mathrm{r}}}\sum_{j\neq p, l\neq p}^{N_{\mathrm{p}}} R_{ip}R_{ij}R_{kp}R_{kl}\Lambda_j\Lambda_j\right] P(\mathbf{R})d\mathbf{R} = \\
&= \begin{cases} \overline{R}^4 N_{\mathrm{r}}\left(N_{\mathrm{w}}-1\right)\left[(N_{\mathrm{w}}-1)(N_{\mathrm{r}}-1)+2N_{\mathrm{w}}\right], & \text{if } \Lambda_p = 1 \\ \overline{R}^4 N_{\mathrm{r}}N_{\mathrm{w}}\left[N_{\mathrm{w}}(N_{\mathrm{r}}+1)+2\right], & \text{if } \Lambda_p = 0. \end{cases}
\end{aligned} \tag{B.1}$$

$$\begin{aligned}
&\frac{2\Lambda_p}{N_{\mathrm{r}}^2}\int_0^\infty \left(\sum_i^{N_{\mathrm{r}}} R_{ip}^2\right)\left(\sum_k^{N_{\mathrm{r}}}\sum_{j\neq p}^{N_{\mathrm{p}}} R_{kj}R_{kp}\Lambda_j\right) P(\mathbf{R})d\mathbf{R} = \\
&= \frac{2\Lambda_p}{N_{\mathrm{r}}^2}\left[\frac{1}{\overline{R}^2}\int_0^\infty \sum_i^{N_{\mathrm{r}}}\sum_{j\neq p}^{N_{\mathrm{p}}} R_{ip}^3R_{ij}\Lambda_j e^{-(R_{ip}+R_{ij})/\overline{R}}dR_{ip}dR_{ij} + \right. \\
&\left. + \frac{1}{\overline{R}^3}\int_0^\infty \sum_{i\neq k}^{N_{\mathrm{r}}}\sum_{j\neq p}^{N_{\mathrm{p}}} R_{kp}^2R_{ij}R_{ip}\Lambda_j e^{-(R_{kp}+R_{ij}+R_{ip})/\overline{R}}dR_{kp}dR_{ip}dR_{ij}\right] = \\
&= \begin{cases} 4\overline{R}^4\left(N_{\mathrm{w}}-1\right)\left[1+\dfrac{2}{N_{\mathrm{r}}}\right], & \text{if } \Lambda_p = 1 \\ 0, & \text{if } \Lambda_p = 0. \end{cases}
\end{aligned} \tag{B.2}$$

$$\frac{\Lambda_p^2}{N_{\rm r}^2}\int_0^\infty\left[\sum_i^{N_{\rm r}} R_{ip}^2\right]^2 P(\mathbf{R})d\mathbf{R}=\frac{\Lambda_p^2}{N_{\rm r}^2\overline{R}}\int_0^\infty\sum_i^{N_{\rm r}} R_{ip}^4 e^{-R_{ip}/\overline{R}}dR_{ip}+$$
$$+\frac{\Lambda_p^2}{N_{\rm r}^2\overline{R}^2}\int_0^\infty\sum_i^{N_{\rm r}}\sum_k^{j-1} R_{ip}^2R_{kp}^2 e^{-(R_{ip}+R_{kp})/\overline{R}}dR_{ip}dR_{kp}=$$
$$=4\overline{R}^4\Lambda_p^2\left(1+\frac{5}{N_{\rm r}}\right). \tag{B.3}$$

$$\int_0^\infty O_p\,\widetilde{R}_p\,P(\mathbf{R})d\mathbf{R}=\frac{1}{N_{\rm r}^3}\int_0^\infty\sum_{ik}^{N_{\rm r}}\sum_j^{N_{\rm p}} R_{ij}R_{ip}R_{kp}\Lambda_j P(\mathbf{R})d\mathbf{R}=$$
$$=\frac{1}{N_{\rm r}^3}\int_0^\infty\left[\sum_{ik}^{N_{\rm r}} R_{ip}^3\Lambda_p+\sum_{i\neq k}^{N_{\rm r}} R_{ip}^2R_{kp}\Lambda_p+\sum_i^{N_{\rm r}}\sum_{j\neq p}^{N_{\rm p}} R_{ij}R_{kp}\Lambda_j+\right.$$
$$\left.+\sum_{i\neq k}^{N_{\rm r}}\sum_{j\neq p}^{N_{\rm p}} R_{ij}R_{ip}R_{kp}\Lambda_j\right]P(\mathbf{R})d\mathbf{R}=$$

$$=\frac{\overline{R}^3}{N_{\rm r}^2}\begin{cases}(N_{\rm w}+1)(N_{\rm r}+1)+2, & \text{if } \Lambda_p=1\\ \\ N_{\rm r}+1, & \text{if } \Lambda_p=0.\end{cases} \tag{B.4}$$

Appendix C

In this appendix we show that the shape of the object, reconstructed using the blind ghost imaging technique is the convolution of the original object shape with the average reflection-transmission correlation function.

We start with the expression for the correlation function (1.4)

$$\overline{C_i^{RT}}(\Delta\mathbf{r}) = \delta R_i(\mathbf{r}) \star \delta T_i(\mathbf{r}), \tag{C.1}$$

where $\star$ is the correlation product. In the experiment we measure

$$\langle\overline{C^{RT}}(\Delta\mathbf{r})\rangle = \frac{1}{N}\sum_i \overline{C_i^{RT}}(\Delta\mathbf{r}) \tag{C.2}$$

From (C.1) we can get

$$\overline{C_i^{RT}}(\Delta\mathbf{r}) \star \delta T_i(\mathbf{r}) = \delta R_i(\mathbf{r}) \star \delta T_i(\mathbf{r}) \star \delta T_i(\mathbf{r}) = \delta R_i(\mathbf{r}), \tag{C.3}$$

where in the last step we used the property $\delta T_i(\mathbf{r}) \star \delta T_i(\mathbf{r}) = \delta(\mathbf{r})$. Using the expression above we rewrite the ghost imaging observable G (4.22) as

$$G = \frac{1}{N}\sum_i^{N_\mathrm{r}} \delta R_i t_i = \frac{1}{N}\sum_i^{N_\mathrm{r}} \overline{C_i^{RT}} \star \delta T_i t_i = \int \langle\overline{C_i^{RT}}(\Delta\mathbf{r})\delta T_i(\mathbf{r}+\Delta(\mathbf{r}))t_i\rangle d\mathbf{r} \tag{C.4}$$

Using the expression for the mean value of the product $\langle AB\rangle = \langle A\rangle\langle B\rangle - \mathrm{Cov}[AB]$, we

rewrite G as

$$
\begin{aligned}
G = \int \Bigg[& \langle \overline{C_i^{RT}}(\Delta\mathbf{r}) \rangle \langle \delta T_i(\mathbf{r}+\Delta(\mathbf{r})) t_i \rangle - \\
& \frac{1}{N} \sum_i^{N_\mathrm{r}} \left(\delta T_i(\mathbf{r}+\Delta(\mathbf{r})) t_i - \langle \delta T_i(\mathbf{r}+\Delta(\mathbf{r})) t_i \rangle \right) \left(\overline{C_i^{RT}}(\Delta\mathbf{r}) - \langle \overline{C_i^{RT}}(\Delta\mathbf{r}) \rangle \right) \Bigg] d\mathbf{r} = \\
& \Lambda \langle \overline{C^{RT}} \rangle - \frac{1}{N} \sum_i^{N_\mathrm{r}} \int \Big[\overline{C_i^{RT}}(\Delta\mathbf{r}) \delta T_i(\mathbf{r}+\Delta(\mathbf{r})) t_i - \delta T_i(\mathbf{r}+\Delta(\mathbf{r})) t_i \langle \overline{C_i^{RT}} \rangle + \\
& + \Lambda(\mathbf{r}+\Delta(\mathbf{r})) \langle \overline{C^{RT}} \rangle - \Lambda(\mathbf{r}+\Delta(\mathbf{r})) \overline{C_i^{RT}} \Big] d\mathbf{r} = \\
& = \frac{1}{N} \sum_i^{N_\mathrm{r}} \left[\delta T_i t_i \langle \overline{C_i^{RT}} \rangle - \delta T_i t_i \overline{C_i^{RT}} + \Lambda \langle \overline{C_i^{RT}} \rangle \right] = 2\Lambda \langle \overline{C_i^{RT}} \rangle - G. \qquad \text{(C.5)}
\end{aligned}
$$

Therefore we can state that

$$G = \Lambda \star \langle \overline{C^{RT}} \rangle, \qquad \text{(C.6)}$$

and the measured average correlation acts effectively as a point-spread function in our imaging technique.

Acknowledgements

I am thankful to many people, without whom this thesis would never have been achievable. First of all, I want to express my sincere gratitude to my supervisors, Jacopo Bertolotti and Janet Anders for all the valuable comments and constant feedback they gave me during past four years. I will always remember our discussions, that often went over schedule, going into the very depth of the fundamental aspects of how we describe Nature and reaching the topics where physics meets philosophy. I would like to thank the directors of the Centre of Doctoral Training in Metamaterials, Prof. Roy Sambles and Prof. Alastair Hibbins for choosing me among many other candidates, despite my unconventional profile. I am indebted to them, because their decision allowed me to continue working in science, which is the occupation I always dreamed about.

I am thankful to the people I worked closely with on the project of the reflection-transmission correlations. First of all this is Alba Paniagua, with whom we did most of the measurements. I am grateful to her for bearing with me for all the hours we spent in the dark basement aligning optics and debugging the code. I also thank Nikos Fayard for answering my often naive questions regarding the theory and explaining complex ideas in the way I could digest. I am also grateful to Prof. Remi Carminati and his group for their input into this project.

I would like to acknowledge the groups of Prof. Euan Hendry, Prof. Bill Barnes and Prof. Geoff Nash for their valuable comments during our regular group meetings. I am also grateful to all the participants of the Theory Group Meetings, but particularly I would like to thank Dr. Thomas Philbin and Dr. Simon Horsley for their comments and suggestions. One of the chapters of this thesis emerged from the discussions with them. I thank all my peers from the CDT for providing a friendly atmosphere, full of events and fun activities. I am grateful to the administrative staff Anja, Rosie and Deborah, and also to the finance and workshop teams for dealing with all my requests and queries.

Among the people who are most close to me, I would first of all thank my first supervisor, Igor Oleksandrovich Melnichuk, who is no longer with us. He showed me the way to the experimental physics and taught me a rational and consistent approach to obtaining scientific knowledge that I could apply across disciplines and research topics. I thank my mother for giving me an opportunity to become who I am. Finally, I wish to thank my wife, for her love and support. She always had faith in me and my capabilities, even in the moments when I questioned those myself.

Thank you all again! Ilya Starshynov.